Multiscale Modelling of Sintering in Thermal Barrier Coatings

Kumar Shanmugam
Linacre College

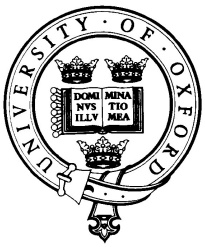

Supervisor: Professor Alan Cocks

Solid Mechanics and Materials Engineering
Department of Engineering Science
University of Oxford

A thesis submitted for the degree
Doctor of Philosophy
Trinity Term 2010

Multiscale Modelling of Sintering in Thermal Barrier Coatings

Kumar Shanmugam

Abstract

submitted for the degree of
Doctor of Philosophy
Trinity Term 2010

Multiscale (analytical and computational) models have been developed based on a thermodynamic variational principle (TVP) to model sintering and eventual mud-cracking in thermal barrier coatings (TBCs) made using the electron beam physical vapour deposition (EB-PVD) process. It is assumed that the sintering occurs by interfacial diffusion at local contacts between columns and driven by changes in interface free energy and elastic stored energy of the coating. The models link diffusional processes at the scale of contacting feathery columns with the macroscopic deformation and sintering response. In service, the columns can come into contact and sinter together. As sintering progresses there is a build up of strain energy in the system which reduces the driving force for sintering and leads to either complete or incomplete sintering of the TBC depending on the magnitude of effective modulus (E) of the coating. By seeding the coating with initial imperfections, different types of behaviour are observed depending on the value of E and the spacing between imperfections. For compliant coatings, the response is insensitive to the presence of imperfections and the coating fully sinters. At higher values of E, strain energy is released by the development of intercolumnar cracks in the coating, which can propagate to the interface with the TGO (thermally grown oxide), deflect into the interface and propagate, leading to spallation of regions of the coating and loss of thermal protection. It is observed that cracks develop at initial imperfections in the structure. The greater the spacing between imperfections the faster the development of cracks at these locations. If a TBC contains a distribution of imperfections there is progressive formation of cracks, with the average spacing decreasing with time, after an initial incubation period. The crack density eventually saturates to a constant value, which depends on the mechanical properties of the TBC.

Initially, a crack spacing, CS, in the range $1.5H \leq CS \leq 3H$ has been predicted based on trapezoidal contact models. Here H is the thickness of the coating. Crack spacing predicted using this model is consistent in the lower range of experimentally observed crack spacing. However, axisymmetric contact models predict a crack spacing, CS, in the range $4H \leq CS \leq 8H$, which is in good agreement with experimentally observed crack spacing range $3H \leq CS \leq 10H$ reported in the literature. Compared to the trapezoidal contact models, axisymmetric contact models more accurately predict the sintering response.

Acknowledgements

At the outset, I would like to express my profound appreciation and gratitude to my advisor **Prof. Alan Cocks**, for his direction and support throughout my DPhil. He has been constantly enthusiastic about this work, and inspired me with many ideas! I admire him as a teacher, as a leader, and above all, as a great human being. It is a great privilege to have worked with him.

My sincere thanks to **Dr. John Huber** and **Prof. Fionn Dunne** who initially provided me an opportunity to tutor a variety of courses during the second year of my DPhil. I also take this opportunity to thank **Prof. David Hills** for having given me opportunities of lab demonstrations.

I would also like to thank my doctoral committee members **Prof. A M Korsunsky** and **Dr. Z You**. I had opportunities to have a number of fruitful discussions with many of our group members. Many have provided helpful hints and criticisms on this thesis and throughout the project. Thanks must also go to all my many friends and colleagues in the lab over the last 4 years: lab lunches, and 'cake club' were always a welcome distraction while I was writing up. I would like to express my sincere thanks in particular to the following researchers of our group: Paynter, Joshi, Michael, Aurelio, Lucas, Mario, Gao, Arezoo, Memhet, Willem, Matthew, Prasant, Daniel, Sara, Ben, Walter, and Liang. Thanks to all other members of the Solid Mechanics and Materials Engineering Group in Oxford.

I must thank my medical friend **Dr Raja Jayaram** and other friends in Oxford for their moral support which in turn indirectly helped me to complete my thesis successfully. I am indebted to my Dad, Wife and the rest of my family members for their tireless and loving support. Many thanks to my loving children, ***Eshwer*** and ***Harish*** , who are longing for my presence. I would like to dedicate this thesis to hollowed memory of my mother

Contents

List of Figures

Chapter 1

Introduction

1.1 Gas Turbine Development

The development of today's gas turbine engines has been the result of continual improvements in a wide variety of engineering skills including turbine design, combustion, and materials [1]. Nevertheless, ever increasing business competition for both aircraft and industrial gas turbine engines constrains engine manufacturers to produce more efficient engines with near zero harmful emissions. The thermal efficiency of the gas turbine engines is primarily governed by the maximum pressure and temperature i.e. turbine entry temperature (TET) of the gas in the engine. The TET of today's gas turbine engines is as high as 1500°C. This means that the hot-section components of the engine are required to operate in harsh environments significantly in excess of their melting temperatures, requiring extensive cooling coupled with heat resistant and protective coatings. Although the highly loaded blades and vanes in the high pressure turbine (HPT) are heavily cooled, today's substrate materials are unable to provide sufficient strength in the temperature range beyond 1500°C [2]. If thermal barrier coatings (TBCs) are applied on superalloy turbine blades which are gas cooled, a substantial temperature drop of the order of 100-300°C of the components can be achieved [3]. Use of TBCs result not only in increased thermodynamic efficiency of the engine but also they prolong the durability of hot-section turbine components: whether from environmental attack, creep rupture, or fatigue. The necessity of a close control of material temperatures can be expressed by the simple rule

that creep blade life is halved for every 10 to 15°C increase in temperature [2]. The resulting increase in efficiency comes from reduced cooling flow requirement and/or increased gas TET of upto 150°C [2]. Fig. 1.1 shows how TET has increased over the years [1]. TBCs reduce the cooling air requirements, making more air available for the combustion process with a consequential reduction in NO_x emissions. As a result, TBCs have been increasingly used in turbines. Further, it is anticipated that a TET as high as 1800°C will be achieved within the next five years. There is no doubt that this ambitious goal can only be met if one or more of the following occurs [4].

- Use of advanced substrate materials (e.g ceramic matrix composites)
- Cooling technologies that imparts a very low performance penalty
- Development of high performance thermal barrier coating (TBC) systems.

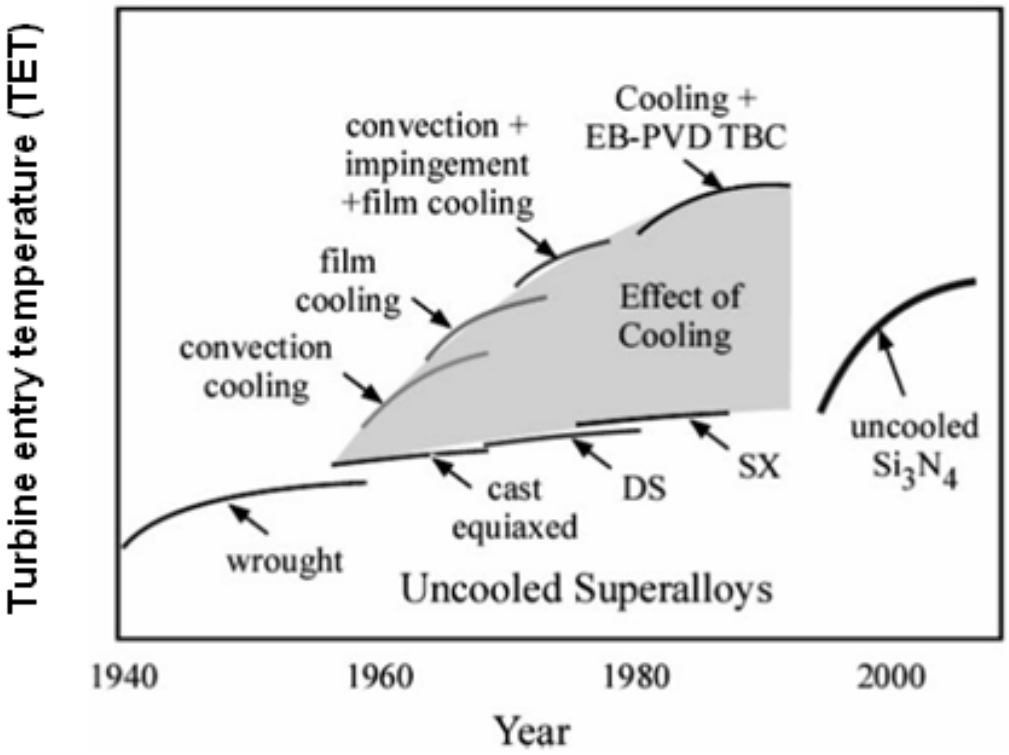

Figure 1.1: Increase in TET over the past 60 years through combinations of material advances and associated developments in cooling techniques [1].

Materials development: The revolution in high temperature gas turbine materials technology from heat resisting steels to today's Ni-base superalloys led to a significant improvement in energy efficiency of gas turbine systems (Fig. 1.1). Extruded blades were replaced by equiaxed, cast turbine blades which offered much more design flexibility for the internal cooling configuration in the early 1970s. However, the resulting material structure had a large number of grain boundaries, with a random crystal orientation. In the late 1970s directionally solidified cast blades were introduced, in which the crystals are grown along the axis of the blade in order to align the maximum strength capability with the direction of centrifugal stress. In these blades, there are significantly fewer grain boundaries and they are all aligned approximately with the radial direction. To further enhance the high temperature creep resistance, single crystal blades were introduced in the early 1990s . These blades have no grain boundaries and, as with the directionally solidified casting process, the crystal is aligned with the direction of radial centrifugal stresses. Though second generation single crystal materials are in use today, engine manufactures are currently developing third generation blade materials, to further increase the alloys temperature capability. Future advances may see the use of ceramic matrix composites in turbines which has the potential to withstand even higher temperatures.

Air cooling technology: Alongside these advances in materials, significant improvements have been made to the cooling technology. The early extruded and cast equiaxed blades introduced in the 1970s had single pass cooling configurations. However, the latest generation of blades use a multi-pass configuration (1.2a), where the flow passes through a long passage before being exhausted. This maximizes the heat pick-up of the cooling air, enabling increases to the main stream gas temperatures and reductions in required cooling flow. The advances in alloy design and cooling tecnology have been reviewed extensively elsewhere [5].

1.2 Thermal Barrier Coatings

Thermal Barrier Coatings(TBCs) comprise thermally insulating materials having sufficient thickness and durability that they can sustain an appreciable temperature difference between the load bearing alloy and the coating surface [6]. TBCs are also being used, to some extent, in diesel engines, where higher operating temperatures translate into increased fuel economy and cleaner exhaust. Further, improvements in TBCs will require a better understanding of the complex changes in their structures and properties that occur under operating conditions that lead to their failure.

1.2.1 Anatomy of TBC

TBCs comprise several layers as shown in Fig. 1.2b, having markedly different properties. They are designed to simultaneously provide thermal and oxidation protection [4, 7]. They are: the TBC, which provides thermal insulation; the superalloy substrate which sustains the structural loads; an aluminum containing bond-coat (BC) between the substrate and the TBC, providing a surface to which the TBC can adhere; and a thermally grown oxide (TGO), predominantly alumina, that forms between the TBC and BC, which provides oxidation protection. Each of these elements is dynamic and all interact to control the performance and durability [6]. Although the number and severity of TBC applications have dramatically increased in the past decade, premature spallation-failure of TBCs during service, which can expose the bare metal to dangerously hot gases, is still an overriding concern [8]. This possibility of premature failure of a coating prevents the design engineers from fully utilising them [9]. Successful implementation requires comprehensive testing protocols, facilitated by engineering models. Expanded applications to more demanding scenarios (Fig. 1.1) requires that their basic thermo-mechanical characteristics be understood and quantified [6].

Substrate: The superalloy component is investment-cast in single-crystal or polycrystalline form, and it contains as many as 5 to 12 additional elements that are added for the enhancement of specific properties such as high-temperature strength, ductil-

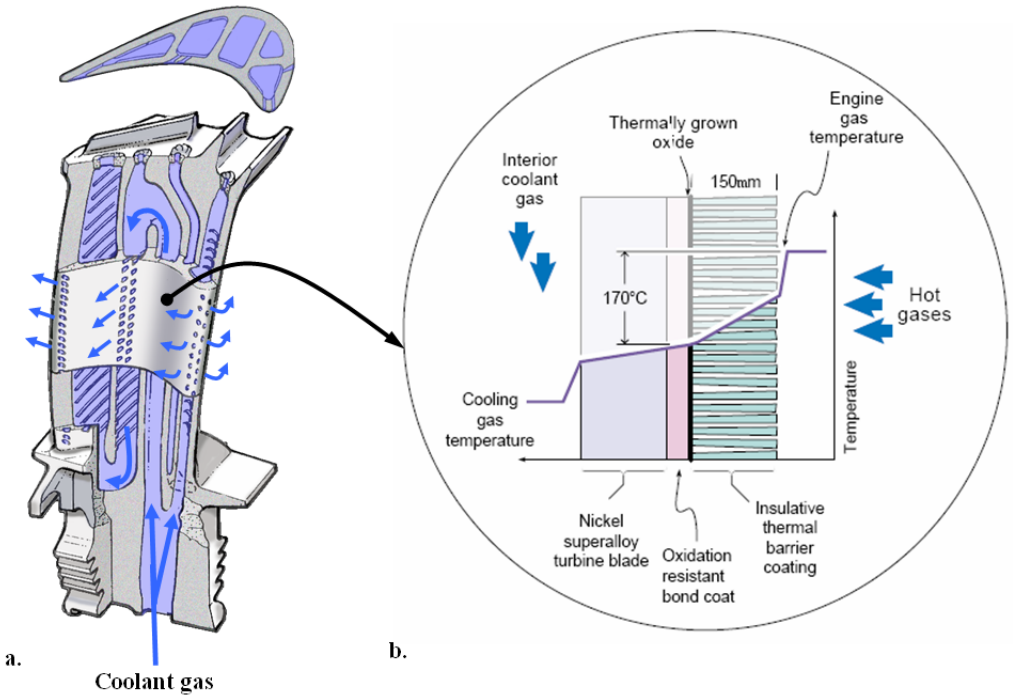

Figure 1.2: a. Thermally coated, internally cooled gas turbine blade. b. A schematic illustration of a modern TBC system comprising of a thermally insulating thermal barrier coating (TBC), a thermally grown oxide (TGO) and an aluminum rich bond-coat. The temperature profile across the TBC during engine operation is superimposed.

ity, oxidation resistance, hot-corrosion resistance, and castability [10]. At the high temperature of operation in gas-turbine engines, diffusion of elements of high relative concentration can occur between the superalloy substrate and the bond-coat. These diffusing elements can occasionally be found in the TGO and the TBC as well. This interdiffusion can have a profound influence on the spallation failure of the TBC [8].

Bond-coat (BC) and thermally grown oxide (TGO): The bond-coat is an oxidation-resistant metallic layer, 75 to 150 μm in thickness, and it essentially dictates the spallation failure of a TBC [8]. At peak operating conditions the bond-coat temperature in gas-turbine engines typically exceeds 700°C, resulting in bond-coat oxidation and the inevitable formation of the TGO layer- between the BC and TBC [11]. The energy density in the TGO and imperfections in its vicinity govern durability [6].

TBC: A TBC is a thermally insulating, strain tolerant oxide. zirconia has emerged

as the preferred material, stabilized into its cubic/tetragonal forms by the addition of yttria in solid solution [6]. This yttria stabilized zirconia (YSZ) material has low thermal conductivity ($\sim$ 2.3 W/m K at $1000°C$ for a fully dense material) with minimal temperature sensitivity [12]. The TBC is likely to have a thermal expansion coefficient ($\sim 11 \times 10^{-6}/°C$) that differs from the substrate ($\sim 14 \times 10^{-6}/°C$) to which it is attached. A TBC should therefore have a high in-plane compliance to accommodate this thermal expansion misfit with the substrate. Usually, strain tolerance is designed into the material to avoid instantaneous delamination from thermal expansion misfit [6]. YSZ has a relatively low density ($\sim 6.4 Mg/m^3$), which is important for parasitic weight considerations in rotating engine components [8, 13]. YSZ has a hardness ($\sim$ 14 GPa), which makes it resistant to erosion and foreign object impact. The important feature of TBC is stability of their thermal properties as a function of time at service conditions. A TBC should have a low sintering rate. Levi provided a comprehensive review on the emerging materials and processes for thermal barrier systems [14]. The coatings can be formed by different methods, but invariably the properties are dependent on the coating process. The two most important methods used for top-coat deposition to produce strain tolerant TBCs are:

- Electron beam physical vapour deposition (EB-PVD)
- Air plasma spraying (APS)

1.2.2 EB-PVD Coatings

EB-PVD evaporates the oxide from an ingot and directs the vapor onto the preheated component. The deposition conditions are designed to create a columnar grain structure (2 to 10 μm diameter) with multiscale porosity as depicted in Fig. 1.3. The disconnected columns impart 'strain tolerance' to the TBC because they can separate at high temperatures, accommodating thermal expansion misfit stresses [15]. EB-PVD TBCs are more durable than APS TBCs due to its unique columnar structure, but are expensive, and are primarily used in severe applications [8, 16]. The porosity and the channels separating the columnar grains help reduce thermal conductivity ($\sim$1.5

to 2 W/mK) but to a lesser extent than APS TBCs, because the channels are parallel to the direction of heat flow [2]. Wadley's group described the method of deposition of coatings on substrates by the physical vapour deposition process [17].

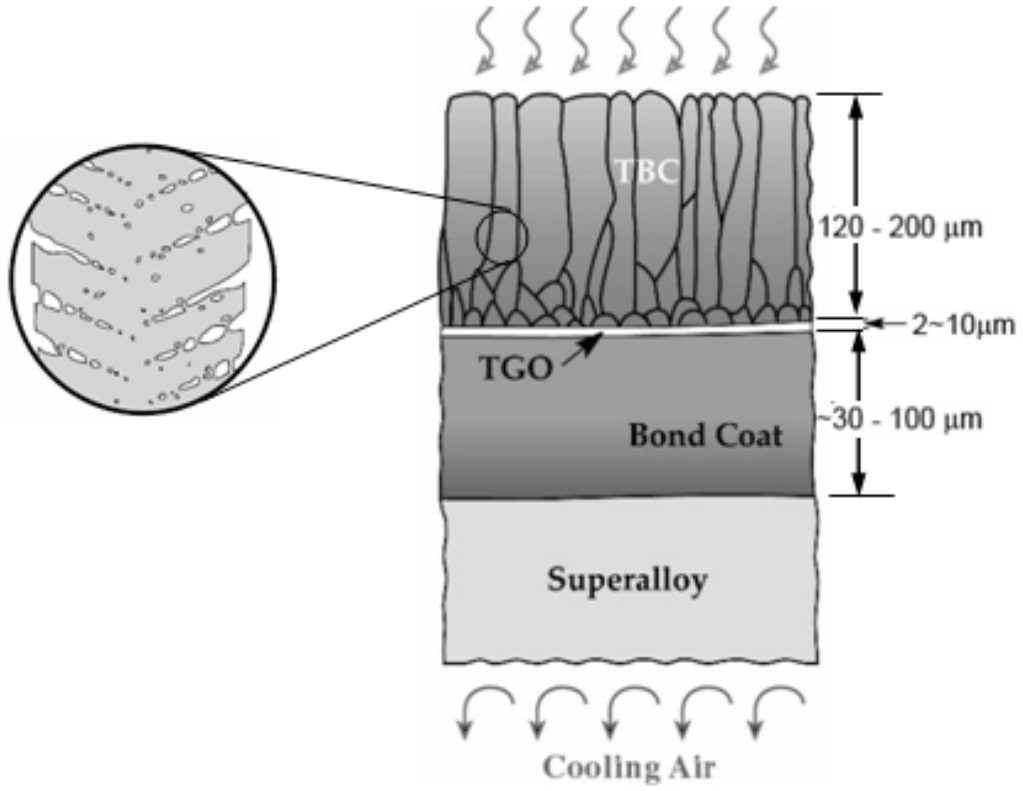

Figure 1.3: EB-PVD TBC: Columnar structure with multiscale porosity

1.2.3 APS Coatings

In the APS process ceramic materials are fed in powder or wire form, heated to a molten or semimolten state by plasma in ambient air and accelerated towards substrates in the form of micrometer-size particles. APS can provide thick coatings (approx. thickness range is 20 μm to several mm), over a large area at higher deposition rates than physical vapour deposition. Plasma sprayed TBC is designed to have: a 'splat' grain morphology (1 to 5 μm thick, 200 to 400 μm diameter) with inter-splat boundaries and cracks parallel to the metal/ceramic interface for low thermal conductivity; and 15 to 20 vol% porosity for both low elastic modulus (high

strain tolerance) and low thermal conductivity [6, 8] as depicted in Fig. 1.4. The thickness of an APS top-coat ranges from 300 to 600 μm depending on the application. The orientation of cracks and pores normal to the heat flow reduces the thermal conductivity of the top-coat from $\sim$ 2.3 W/m K for a fully dense material to a more typical 0.8 to 1.7 W/m K.

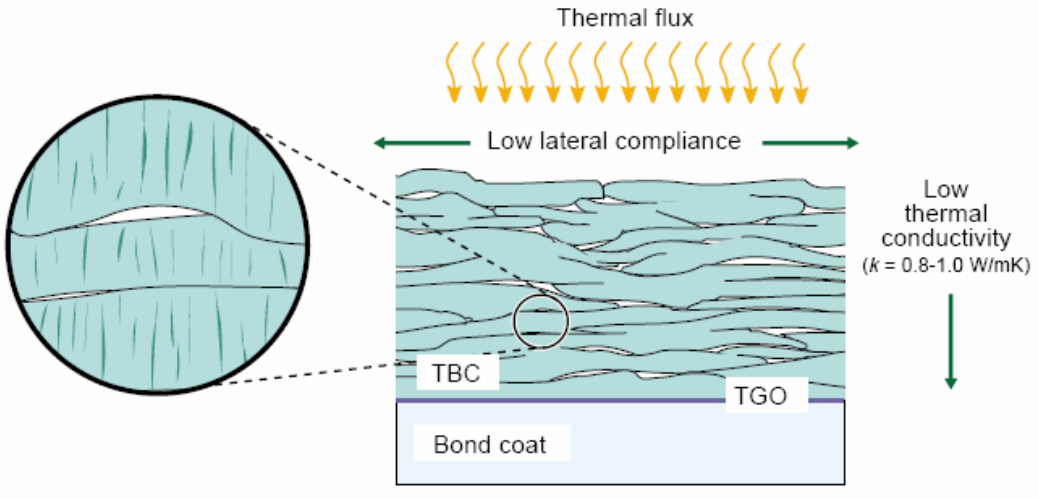

Figure 1.4: APS TBC with inter-splat boundaries and cracks parallel to metal/ceramic interface

The undulating nature of the metal/ceramic interface, which is required for better interlocking adhesion, produces out-of-plane stresses responsible for in-service failure of APS TBCs [8]. While APS is lower in cost, EB-PVD leads to superior strain and thermal shock tolerant coatings. Furthermore, in EB-PVD TBCs cooling hole closure of turbine blades and vanes is prevented and aerodynamic design maintained [2]. Because of the proliferation of microstructural defects parallel to the interface and the roughness of the interface, APS TBCs generally have shorter thermal-cycling lives than EB-PVD TBCs. This makes APS TBC suitable for less exacting applications [8].

1.3 Failure Mechanisms

Under service conditions TBCs can fail. The mechanisms by which TBCs fail are numerous, depending on the processing methods, applications and operating scenarios, the most important among them are: thermal stresses in the coating systems; the oxidation of the bond-coat and substrate [18]; and the continuously changing compositions, microstructures, interfacial morphologies and properties of the TBC system [8]. Failure in TBCs almost always occurs by TBC spallation typically on cooling to room temperature [1, 19]. The failure is ultimately connected to the large residual compression in the TGO through its roles in amplifying imperfections near the interface. This amplification induces an energy release rate at cracks emanating from the imperfections that eventually buckle and spall the TBC [6, 20].

Graded interlayers have been extensively used to mitigate thermal stresses induced by thermomechanical mismatch between top-coat and substrate. Closed form analytical solutions for thermo-elastic stress distribution in a graded TBC sytem is given in [21]. Clyne et. al., developed an analytical model to predict the residual stress distributions in progressively deposited coatings based on the misfit strain caused by the deposition stress or by differential thermal contraction between substrate and coating during cooling [22]. Mao et. al., recently developed a two-dimensional analytical solution under the condition of non-linear coupled effects of temperature gradient, thermal fatigue, deposited residual stress, TGO thickening, elasto-plastic and creep deformations [23]. Effective anisotropic elastic stiffness and thermal conductivities of the plasma sprayed ceramic coating were calculated in terms of the relevant microstructural parameters [24]. Vasinonta et. al., developed models based on a simple indentation test to measure the interfacial toughness of a TBC system [25]. Evans et. al., analyzed delamination and spalling of compressed films or coatings using a combination of fracture mechanics and post-buckling theory [26]. Evans and his coworkers addressed edge-delamination and buckling-delamination issues of EB-PVD multilayered TBCs [27]. Mercer et al, proposed a delamination mechanism for TBCs subject to calcium-magnesium-alumino-silicate (CMAS) infiltration [28].

Sintering in TBCs: Though, failure prediction and performance improvements of TBCs require a system approach, there are critical issues closely related to ceramic TBC and the bond-coat respectively. One of the most critical issues for the development of advanced TBCs is sintering of ceramic TBC and the corresponding microstructural changes under high heat flux conditions. At operating temperatures, the ceramic TBC will densify by the reduction in surface energy associated with the excess surface area of pores. This process is commonly referred to as sintering. It has long been recognized that at high temperatures sintering and creep effects of the coating are pronounced, and they are detrimental to coating performance [29, 30]. Sintering and creep result in considerable coating thermal conductivity and elastic-modulus increase that will lead to reduced thermal insulation and increased thermal stresses respectively. The increase in the thermal conductivity of the TBC [31], results in a higher metal surface temperature and the attendant enhancement of bond-coat oxidation. The increased thermal cyclic stresses and accumulated creep strains provide the major driving force for shrinkage-cracking that originate at the TBC surface, eventually leading to TBC spallation [31].

Golo et. al., developed an analytical model for the simulation of heat flow in plasma-sprayed thermal barrier coatings to predict their thermal conductivity as a function of microstructural parameters [32]. Many investigators proposed different ways of reducing the thermal conductivity of TBCs [33, 34]. However, thermal conductivity reductions have largely been achieved by engineered micropores and microcracks within the ceramic coating systems. The thermal conductivity reduction provided by the microporosity may not persist because of the ceramic coating sintering at high temperatures [30, 31, 35, 36, 37].

Sintering in EB-PVD TBCs: Sintering in EB-PVD TBC results in the partial healing of the gaps between columns and a reduction in porosity. It also accelerates TBC failure by making the top-coat less 'strain tolerant' [30]. At a given temperature, the sintering rate of the ceramic coating typically changes with time. Higher temperatures and compressive stresses will lead to a higher sintering/creep rate. High electron

beam power and low substrate rotation speed results in increase of Young's modulus due to sintering of YSZ during deposition [38]. The thermal conductivity increase due to micro-pore sintering and the decrease due to coating micro-delaminations in the EB-PVD coating have been evaluated experimentally [39]. The long-term thermal conductivity increase observed in EB-PVD TBC by the laser conductivity tests is attributed to the sintering of both the inter-columnar and intra-columnar microporosity [39]. It was shown that the strain tolerance in as-deposited samples decreased with an increase in deposition temperature [38]. In a sample deposited at $973°C$ and $995°C$, with a high temperature aging treatment at $1000°C$ for 10 h, remarkably reduced strain tolerance due to the formation of the TGO beneath the TBC. The TGO-layer growth was observed even in as-deposited samples, thickness being dependent on deposition temperature. It suggests that the oxidation resistance of TBC systems can be improved by controlling the processing parameters [38]. Eventually, the growth of highly stressed TGO leads to coating spallation [7]. Lughi et al., performed isothermal experiments on EB-PVD TBCs and found that the initial feathery microstructure evolves to a smoother surface within hours and with longer times at this temperature, the columns developed pronounced surface undulations over their surfaces and subsequently leading to formation of mud-cracks after 50 h at $1200°C$ [40].

In fact, it is quite likely that the densification of plasma-sprayed and EB-PVD TBCs might be quite different from one another and also from bulk zirconia ceramics on account of constraint imposed by the underlying alloy [1]. Two possible factors appear to affect densification of coatings. One is the geometric constraint on the lateral shrinkage of the coating by the rigid alloy as the coating tries to densify to lower its overall surface area. This classic problem of constrained sintering in ceramic coating was addressed initially by Bordia et. al [41]. The other factor is the effect of stress produced by thermal expansion mismatch between coating and the alloy. In 2006, Hutchinson et. al, have developed micromechanical sintering model for EB-PVD TBCs constrained by the rigid substrate [42]. Clyne's group has recently developed

a sintering model for plasma sprayed zirconia thermal barrier coatings [43, 44] using the variational principle of Cocks et al [45]. Cocks and Fleck very recently developed multiscale models to study constrained sintering of an air-plasma-sprayed thermal barrier coating [46, 47].

The erosion-resistance of EB-PVD 8% YSZ coatings both at room temperature and $910°C$ were found to be more than the equivalent plasma spray coating [48]. Wellman et al., studied the effect of TBC morphology, aging and sintering on the erosion rate of EB-PVD TBCs and found that the erosion rate decreases with decrease in column diameter, while the aging results in increase of erosion rate, dependent on the aging temperature and time [49]. Sintering enables cracks to propagate into neighboring columns, as opposed to stopping at column boundaries and increases erosion rate [49]. The impact of larger particles on the top-coat was numerically investigated considering the columnar structure and the friction between them [50]. The densification and deformation occuring in TBCs at operating temperatures involves stress- and thermally activated diffusion and mechanical compaction processes [30, 31] and will become of even greater significance in the design of future coatings for higher temperature applications [1]. In order to understand the failures, it is important to correlate experiments and theoretical evolutions by conducting careful experiments and develop mechanics based models. The mechanics based models must incorporate the relevant physics governing the evolution of failures [6, 8, 15, 18, 42].

As a coating sinters vertical cracks can form in the coating and penetrate to the TGO, where they are deflected into the TBC/TGO interface, leading to spallation of large section of the coating. In practice families of vertical cracks are often observed, forming a 2D pattern on the surface similar to that observed in drying mud. These are commonly referred to as 'mud-cracks'. Formation of these mud cracks is an important pre-cursor to spallation. There have been limited studies of the processes that lead to mud cracking in TBCs and this forms the central theme of the thesis.

1.3.1 Review of mud-cracking

When natural and engineered systems are subjected to applied strain-often driven by cooling or evaporation-the resulting stresses may lead to formation of cracks. In many cases these cracks may form patterns which exhibit distinct length scales [51]. This cracking pattern occurs in different situations. The drying of mud is perhaps the classical natural example of this phenomenon (As water evaporates from the mud it shrinks creating a tensile stress that eventually results in mud cracking).

Similarly, ceramic TBCs during service exhibit mud-cracking due to sintering. Though formation of mud-cracks in a TBC does not mean complete loss of structural integrity of the coating system, it would eventually lead to TBC spallation. Therefore, it is indispensable to study how mud-cracks evolve in a TBC during cyclic operation of the gas turbine engine and lead to spallation of the coating. To understand this, let us first consider a simple case where a TBC is subjected to uniform temperature independent of time. At temperature, sintering occurs in the TBC as a function of time. Progressive sintering leads to build up of in-plane tension in the TBC. If the magnitude of this tension is sufficiently high it may lead to the formation of initial set of mud-cracks. Further, the mud-cracked TBC layer continues to sinter causing formation of a subsequent set of mud-cracks. Evolution of mud-cracks continues until the crack density attains a saturated value. Upon cool-down, under isothermal conditions, the TBC experiences in-plane compression and therefore further mud-cracks do not occur. Nonetheless, in-plane compression of the TBC induces high mode II stress intensity at the mud crack tips already touching the interface/TGO. This may cause coating delamination and eventual spallation. On the other hand, upon cool down, under non-isothermal conditions (where temperature gradients are present), a mud cracked TBC may be subjected to residual tension which may cause further mud-cracking and extension of existing mud-cracks to reach the interface. In-plane tension in the TBC and the in-plane compression at the interface creates a mode II stress intensity at the mud crack tips already touching the interface/TGO. Again, these mud cracks may propagate and lead to spallation of the TBC.

Ultimate shear strength of a metal-ceramic interface was obtained based on the tensile fracture strength of the ceramic film and the largest spacing between the cracks; both of these quantities are measured experimentally [52]. Hsueh et. al., observed multiple film cracking in SiOx films on polyethylene terephthalate substrates systems with residual stresses and unidirectional loading. Guided by experiments, analytical models based on strength and the energy criteria were proposed for crack density [53]. Hseuh continued work to obtain a master curve by normalizing the crack density and the applied strain, respectively, by the coating thickness and the critical applied strain required to initiate cracking [54].

Thouless [55] initially presented an approximate analytical solution for the minimum spacing that can exist between a series of parallel cracks propagating in a thin film, applicable to a case where the film and substrate have identical elastic properties. In a subsequent study, Thouless et.al., [56] presented an analysis which relates the crack spacing in a brittle film on an elastic substrate to the stress in the film, its thickness and fracture toughness. The critical stress as a function of film thickness, the residual stress, the substrate yield strength, the ratio of elastic moduli and the mode I fracture toughness of the film for the steady-state cracking of adherent thin films on a ductile substrate has been investigated for thin Cr films on Al and stainless steel [57]. Evans et. al., [58] explored the thermo-mechanical integrity of thin films and multilayers in detail considering the residual and intrinsic stresses. An accurate closed-form solution for the strain energy release rate for a given rectangular film loaded by a centre line force using a pull-off test is derived in the presence of a tensile residual stress [59].

Suo's group developed the extented finite element method (XFEM) to evolve patterns of mud cracks, in a brittle thin film bonded to an elastic substrate [60]. They recently studied an electronic system consisting of a polymeric substrate and an array of stiff islands, on which devices are fabricated. It was found that the islands debonded when the substrate was stretched provided the islands size reached a critical value. It was also shown that a thin layer of polymer coating, covering the islands

and the substrate, can markedly increase the critical island size [61]. A very recent study proposes an energy model for segmentation cracking of thin films [62]

Beuth proposed analytical solutions for two elastic plane strain problems relevant to the cracking of a thin film in residual tension bonded to a dissimilar semi-infinite substrate material. The first problem is that of a crack in the film oriented perpendicular to the film/substrate interface with the crack tip touching the interface. The second problem is that of a crack of the same geometry, but with length less than the film thickness, so that the crack tip is within the film [63]. In a subsequent study, Beuth et al. [64] performed numerical plane strain fracture analyses to investigate the channel cracking of elastic thin films in residual tension considering yielding in the substrate material. Hutchinson et al. [42] employed Beuth's analysis to determine the initiation of mud-cracking in a sintering thermal barrier coating and used energy considerations to obtain the density of mud-cracks formed by a cleavage process. Bazant et al., initially studied the instability and spacing of cooling or shrinkage cracks in an elastic half-plane and later investigated the initiation of parallel cracks from the surface of an elastic half-plane [65, 66]. Fleck's group initially studied thermal shock resistance of a brittle solid orthotropic plate containing a distribution of flaws such as pores and another case where the plate had a single dominant crack in the through-thickness direction [67]. Later this group analysed crack channeling and spalling in a plate due to cold shock [67, 68]. Kachanov proposed a simple method of stress analysis in elastic solids with many cracks [69]. In a subsequent study, Kachanov et al., analysed elastic interactions between holes of diverse eccentricities, as well as between holes and cracks [70].

There are numerous investigations on mud-cracking of elastic solids in general though there are only a few on mud-cracking of TBCs. In all these investigations, mud-crack prediction is based either on critical strain or energy. In contrast, we currently focus on micromechanical models to understand the evolution of mud cracks in TBCs, arising as the result of instabilities in the sintering process.

1.4 Multiscale Modelling Methods

In order to model the sintering and mud-cracking processes in TBCs, we need to consider and model the material behaviour across number of different scales. Multiscale modelling is the field of solving physical problems which have important features at multiple scales, particularly multiple spatial and(or) temporal scales. In cases where an understanding of the dual nature of the structure of matter (continuous when viewed at large length scales and discrete when viewed at an atomic scale) and its interdependencies are crucial, multiscale materials modelling approaches are required to complement continuum and atomistic analysis methods. On transitional (or microstructure) scales (in between continuum and atomistic), continuum approaches begin to breakdown, and atomistic methods reach inherent time and length-scale limitations [71]. Multiscale modeling aims to calculate material properties or system behaviour on one level using information or models from different levels. On each level, particular approaches are used for description of a system. Each level addresses a phenomenon over a specific window of length and time. The different methods for modelling nano and microsystems are: quantum mechanics (QM) (information about electrons , i.e states is included), molecular dynamics (MD) (information about individual atoms is included), Monte Carlo (MC) method, dislocation dynamics (DD), statistical mechanics (SM), microstructure evolution modelling (either phase field method (PFM) or thermodynamic variational principle (TVP)) and, finally continuum mechanics (CM). Structural features of materials at a number of different scales can alter the macroscopic response of materials to external stimuli. The dominant processes in sintering occur at the microstructural scale. In order to study mud-cracking we need to link the material response at this scale with continuum scale observations. There are two typical modelling approaches that can be employed to model microstructure evolution: the phase field method or the variational approach developed by Cocks and co-workers.

1.4.1 Phase-Field Method (PFM)

The Phase-Field method is a mathematical technique, based on thermodynamics, for solving interfacial problems. The phase-field approach has become one of the powerful computational methods for simulating microstructure evolution for a variety of different material processes, such as solidification, solid state phase transformations, etc. This method has been successfully applied to solidification dynamics [72]. It has also been applied to other situations such as fracture dynamics [73], viscous fingering, vesicle dynamics etc. The main feature of the phase field approach is that the interface between phases is regarded to be diffuse. This method usually is constructed in such a way that in the limit of small interface width (the so-called sharp interface limit) it recovers the correct interfacial dynamics. This method allows the problem by integrating a set of partial differential equations for all the system to be solved, thus avoiding the explicit treatment of the boundary conditions at the interface.

It has also been applied to model microstructural evolution during sintering of materials. The effective treatment of particle translation and rotation is the key step in developing a phase-field sintering model. Wang has recently developed a sintering model accounting for multiple simultaneous physical processes, including various diffusion paths (along surface and grain boundary, through bulk lattice), vapour transport, particle rigid body motions (translation and rotation), and grain growth through boundary migration without explicitly tracking the surfaces and grain boundaries or imposing boundary conditions [74].

1.4.2 Thermodynamic Variational Principle (TVP)

There has been growing interest in modelling the microscopic processes that occur within a material under service conditions. The microstructure of the material can continue to evolve during service, eventually leading to failure of the components. Variational techniques developed by Cocks and co-workers [45] can be employed to link events at the micro structural scale with the continuum response. TVP is ideally suited for modelling systems whose internal geometry change during the process.

The approach is based on a fundamental variational principle which considers the competition between all possible dissipative processes that are driven by a number of thermodynamic driving forces. The variational principle allows the rate of evolution of the microstructure to be determined. The objective of the current study is to model the way in which microstructure evolves in EB-PVD TBCs during in-service sintering. We seed the microstructure with imperfections to study the influence of imperfections on sintering response. These simulations can be evaluated again using the variational principle to provide simple macroscopic models of the way in which the microstructure evolves.

1.4.3 Modelling of Sintering

There has been long history of modelling the sintering of particulate systems. In the 1980s, Ashby and his co-workers consolidated all the sintering models available at that time and constructed sintering mechanism maps which has been widely referred to in the literature [75]. Following this work, isotropic constitutive laws for finite element analysis of sintering were critically reviewed by Cocks [76] and Olevsky [77]. In the 1990s apart from development of finite element modelling of sintering, robust numerical schemes for the computer modelling of microstructural evolution [78] were also developed. Cocks and his co-workers proposed a variational technique for computational modelling of nonuniform microstructural evolution during sintering [45]. In 2003, Pan critically reviewed the existing sintering models at various length scales [79]. In early 2000s a method based on cubic spline elements for modelling microstructural evolution during sintering of particulate systems was developed [80, 81]. Of late, Olevsky and his co-workers provided a comprehensive review on multiscale study of sintering [82]. Recent key development in the area of modelling of sintering is the establishment of anisotropic constitutive laws for sintering bodies [83, 84]. Green et al, recently critically reviewed the continuum theories for modelling constrained sintering [85]. Martin and Bordia studied the effect of substrate on the sintering of constrained films [86]. In this thesis, we focus on modelling constrained sintering of

TBC films.

1.5 Structure of Thesis

Chapters 2 and 3: Initially, the effect of mud-cracking on intercolumnar sintering rate of a constrained TBC was studied assuming a fully developed square pattern of mud-cracks with pre-defined spacing. Based on this, it was found that the reduced elastic constraint of the mud-cracked layer leads to full sintering between columns in a relatively short time for the same choice of Young's modulus (E), for which the sintering was switched off in an equivalent uncracked layer. Now, naturally, a question arises as to how do these mud-cracks evolve in space and time during service in TBCs. In order to explore the evolution of mud-cracks in TBCs, a multi-scale model is formulated for the evolution of microstructure, sintering and deformation of columnar EB-PVD thermal barrier coatings. Initially, computational studies have been performed to study sintering of a coating constrained by a rigid substrate. It is demonstrated that the sintering process can become unstable when the in plane stiffness exceeds a critical value. Imperfections in the coating can develop into cracks, which propagate through the thickness of the coating, creating a pattern of "mud cracks". The simulations have motivated the development of simplified models of this process which describe the sintering response and the development of mud cracks in terms of the evolution of a small number of degrees of freedom. These simple models capture the major features of the more detailed computational simulations. They also allow the conditions under which imperfections grow into cracks to be readily identified and predict a density of mud cracks that is consistent with experimental observations.

Chapters 4 and 5: We developed another set of models by releasing some key assumptions of models presented earlier. One of the demerits of the models described in chapters 3 and 4 is that the modulus of the TBC is assumed to be constant throughout the sintering process, while the contact modulus indeed changes with sintering time. Moreover, in the models described in previous chapters, we assume a simple

but continuous 2-D contact geometry to keep the number of independent variables as small as possible. Therefore, the TBC behaves like a stiff system. In these models, we account for this time dependent nature of contact modulus as a function of sintering strain, and assume a widely spaced axisymmetric contact geometry that is more consistent with experimental observations [40]. We also assume that the columns are inextensible both elastically and plastically in the coating thickness direction to determine the displacement field which is more realistic assumption than assuming elastic incompressibilty condition of columns. Again, the variational principle has been used in two ways. It has provided the framework to construct an inelastic constitutive law expressed in terms of internal state variables which describe the structure. We use this improved constitutive model to perform finite element studies in order to determine the effect of imperfections on the sintering process. These studies have been complimented by the development of Rayleigh-Ritz type models, which model the sintering response in terms of a small number of degrees of freedom. The numerical predictions are in good agreement with the micromechanical mathematical models.

Chapter 6: We summarise the work that has been described in this thesis and the main contributions. We describe future work that we propose in the area of modelling of sintering and mud-cracking in TBCs.

Chapter 2

Trapesoidal Contact Computational Models

2.1 Abstract

In this study we focus on the sintering response of an EB-PVD top coat and examine the conditions under which inter-columnar cracks can develop within the coating. Hutchinson et al. [42] have recently developed a micromechanical model for constrained sintering of EB-PVD TBCs and modelled the growth of tunneling cracks in the coating by a cleavage mechanism . Here we explore an alternative mechanism of crack formation, which arises from instabilities in the sintering process. We rework the sintering model of Hutchinson et al [42] to provide a macroscopic sintering constitutive law, which we employ in a series of finite element calculations to evaluate the sensitivity of the sintering response to imperfections in the coating.

2.2 Problem Statement

TBCs comprise several layers as shown in Fig. 2.1, with each performing a specific function and exhibiting markedly different properties. In this study, we focus on the behaviour of the top coat. In turbine applications the top coat is generally deposited using an EB-PVD process. The main objective of this study is to identify the conditions under which mud-cracks can develop in an EB-PVD thermal barrier coating. In service, a temperature gradient will exist across the coating. Here, however, we

focus on the simpler problem of isothermal sintering as employed in the experimental study of Lughi et al [40]. The methodology described here can be readily extended to non-isothermal situations, but it is important to fully understand the behaviour under isothermal first before addressing the full practical problem.

Following Hutchinson et al [42] we idealise the top coat as a regular array of parallelepiped columnar grains of square cross-section with dimensions $d \times d$, as illustrated in Fig. 2.2a. We describe the response in terms of a Cartesian co-ordinate system in which the x_1 and x_2 directions lie in the plane of the coating and are parallel to the sides of the columnar grains. The x_3 direction is perpendicular to the plane, with its origin at the interface with the substrate. The columns have a surface roughness of characteristic wavelength, λ. Asperities on the columns can come into contact. At elevated temperature, sintering occurs as a result of the diffusional flow of material away from the contact regions. This gives rise to macroscopic sintering strains, $\varepsilon^s_{11}, \varepsilon^s_{22}$. By considering the response of a representative volume element, we develop a constitutive model below for the sintering rate in terms of the geometry of the internal contacts and the macroscopic stress experienced by the element. Finite element studies are undertaken of intercolumnar sintering of a constrained homogeneous film (Fig. 2.2.a) and progressive sintering of a set of columns within a mud cracked square cluster of size 2R (Fig. 2.2b.). These results are compared directly with the analyses of Hutchinson et al [42]. We then use the model to evaluate the influence of imperfections (where the initial contact geometry of the asperities is slightly different to that experienced in the remainder of the coating) on the sintering process. This is conducted in 2 stages. First we model the evolution of microstructure for a set of arbitrary equi-spaced imperfections. We then consider the response for a square grid of imperfections, with the objective of identifying the conditions under which a square grid of cracks can develop from these initial imperfections. The resulting mud-cracked pattern is an idealisation of the patterns observed experimentally, for example by Lughi et al [40], see Fig. 2.2b. These simulations are used to guide the development of a two state variable Rayleig-Ritz model, which we validate against

the detailed finite element calculations, as described in chapter 3. Use of this simpler model allows a wide range of geometric and material conditions to be evaluated and the conditions under which cracking occurs to be identified, but these calculations are unable to provide information about the average spacing of the mud cracks. This requires a three state variable model in which we follow the evolution of two families of imperfections. This is described in chapter 3. In all the problems, the TBC layer is of height H and it is assumed that the TBC film is perfectly bonded to the substrate.

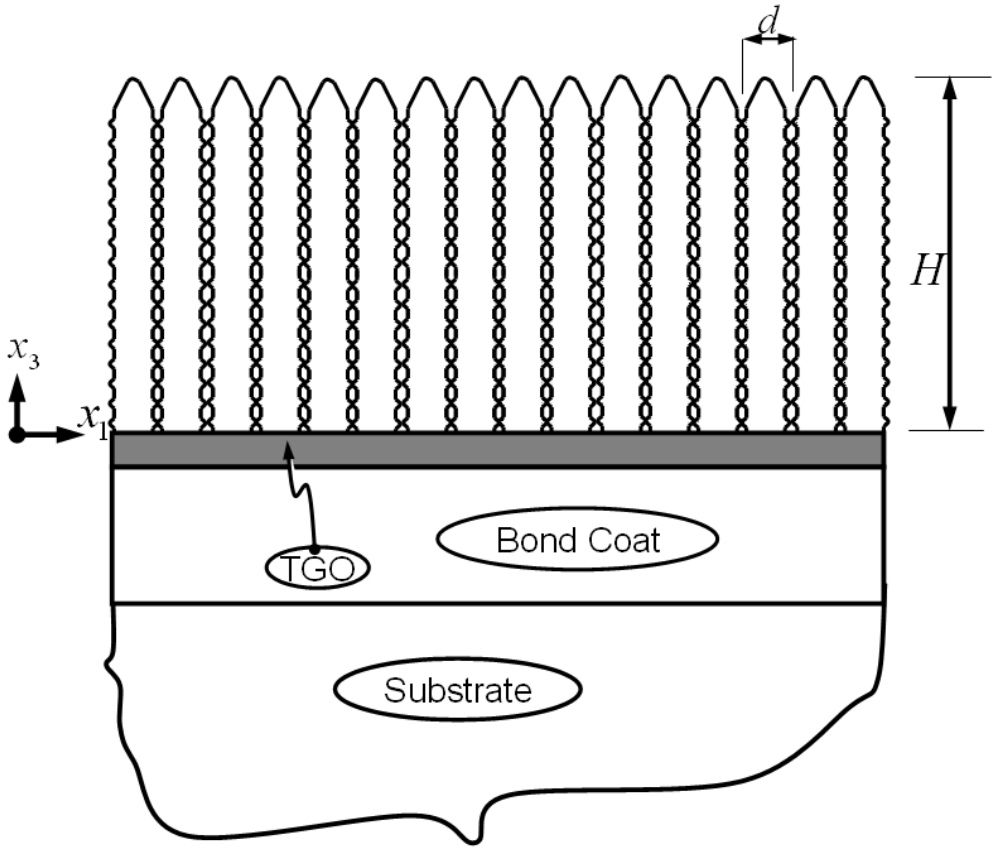

Figure 2.1: A TBC system comprising a thermally insulating top layer of columnar YSZ, a TGO layer of alumina, an aluminium containing bond coat and an underlying superalloy substrate.

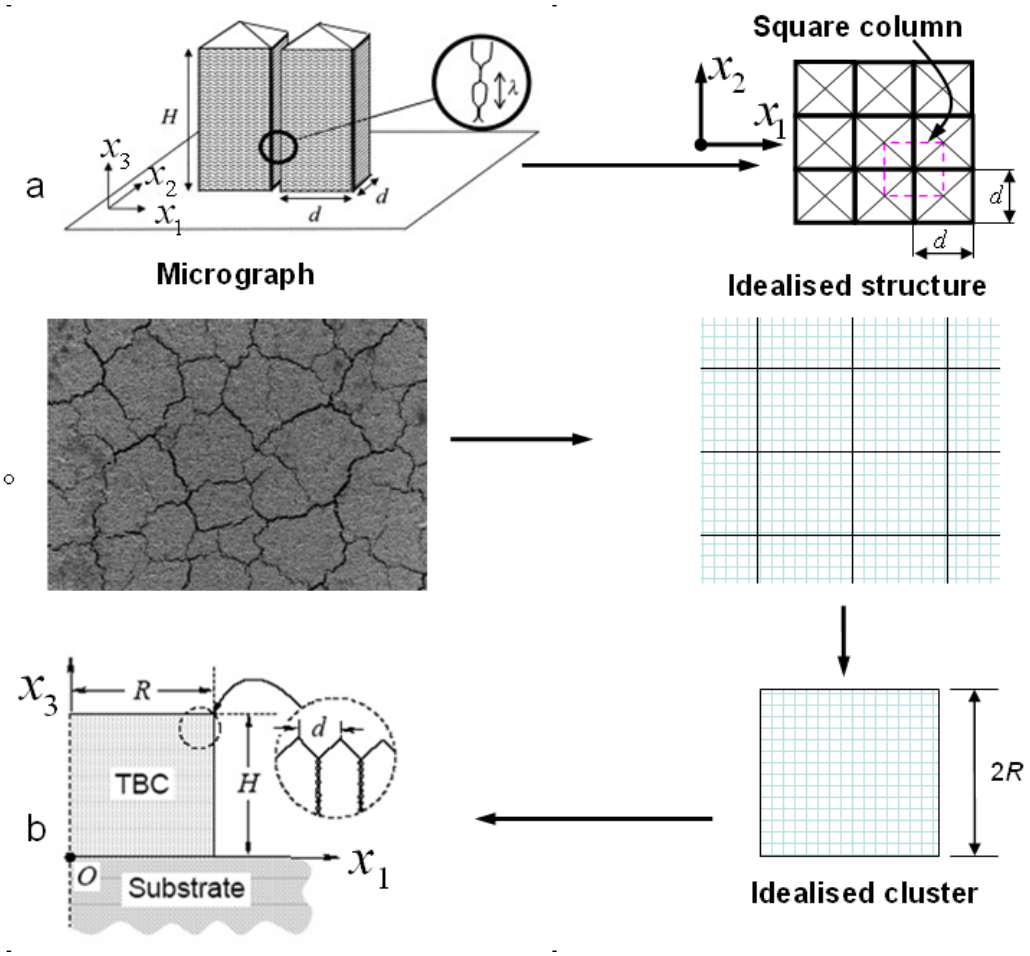

Figure 2.2: a. Sintering of neighbouring TBC columns, each of cross-section $d \times d$ perfectly bonded to the substrate. The local roughness at contacts is of wavelength λ. b. The mud-cracked TBC layer is idealized as an assembly of square clusters, each of height H and size $2R$. The clusters comprise columns which progressively sinter together

2.3 Computational Model

A representative macroscopic volume element of the coating is shown in Fig. 2.3. The element has a square cross section $d \times d$, made up of 4 quarter columns which are in contact along lines that bisect the element along two mutually perpendicular planes, parallel to the x_1 and x_2 axes. The height of the element is equal to the wavelength of the undulations on the surface of the columns. Following Hutchinson et al [42], we assume that the elastic response does not depend on the detailed structure across

the interface between the columns (the effect of asperity contact stiffness on the constitutive response is examined in chapters 4 and 5). Inelastic deformation results from sintering and sliding between the asperities. We assume a simple linear viscous response for the sliding deformation. For the situations examined here the results are not sensitive to the magnitude of the viscosity. The inelastic strain-rates $\dot{\varepsilon}^s_{11}, \dot{\varepsilon}^s_{22}$ arise from diffusional rearrangement at the asperity scale on two independent planes. We can therefore model these processes independently and superimpose the results to give the full constitutive response. We assume simple shapes for the evolving

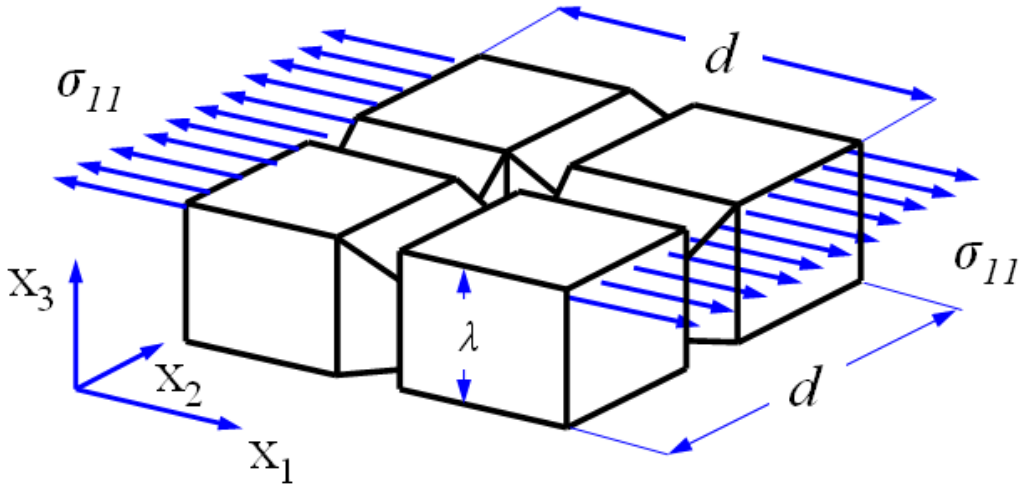

Figure 2.3: A representative macroscopic volume element of the coating. The element has a square cross section $d \times d$, made up of 4 quarter columns which are in contact. The height of the element is equal to the wavelength λ of the undulations on the surface of the columns

asperities and develop the constitutive model within the framework of the variational principle described by Cocks et al [45] and Suo [87]. This requires an identification of the different contributions to the functional

$$\Phi \;=\; \psi + \dot{G} \tag{2.1}$$

where ψ is a rate potential and $\dot{G}$ is the rate of change of Gibbs free energy of the system. Each of these quantities are expressed in terms of geometric rate quantities that describe the rate of evolution of the microstructure (ie the change in shape of the

asperities). The functional Φ is purely a mathematical construct, and has no clear physical meaning. Of all the virtual velocity distribution, the actual combination of rates is that which minimises the functional Φ. The proof of the principle is given by Suo [87]. It can be shown that the minimisation of Φ leads to determination of actual velocity distribution which would otherwise be obtained by solving the partial differential equation of the moving interface [87]. However, solving the partial differential equation which governs the motion of interface exactly is always not possible and hence we use the TVP to analyse the problem approximately. Formulation of a PDE is not a good way to look at a general problem for several reasons [87].

We focus on the local sintering between contacting columns on a length scale λ (less than 1μm) and neglect the much slower diffusion over larger length scales of the order of the column size d (5-10μm) and column height H (100-200μm). Consequently, we can solve for the evolution of the sintering strains ε^s_{11} and ε^s_{22} in the x_1 and x_2 directions respectively under fixed temperature T.

2.3.1 Contact geometry

Consider the situation where the element of Fig. 2.3 is subjected to a stress σ_{11}. Following Hutchinson et al [42] we associate all the surface roughness with one of the contacting surfaces, while the other surface is treated as perfectly flat. We assume the idealised saw-toothed contact geometry shown in Fig. 2.4. It proves convenient to define a reference configuration as illustrated in Fig. 2.4a. Note that the reference configuration is introduced for algebraic convenience only and may not be realized in practice. The geometry of the contacting asperities at a given instant can be characterised by the geometric parameters (u_1, w_1) as shown in Fig. 2.4b.

This simplification of contact geometry allows us to reduce the number of independent geometric variables and to formulate an analytical micromechanical model for the evolution of contact geometry. Further, it is assumed that the wavelength λ of the undulations is of the order of the length scale of the feathery arms of the TBC columns. This assumption is justified by the fact that surface roughness is smoothed

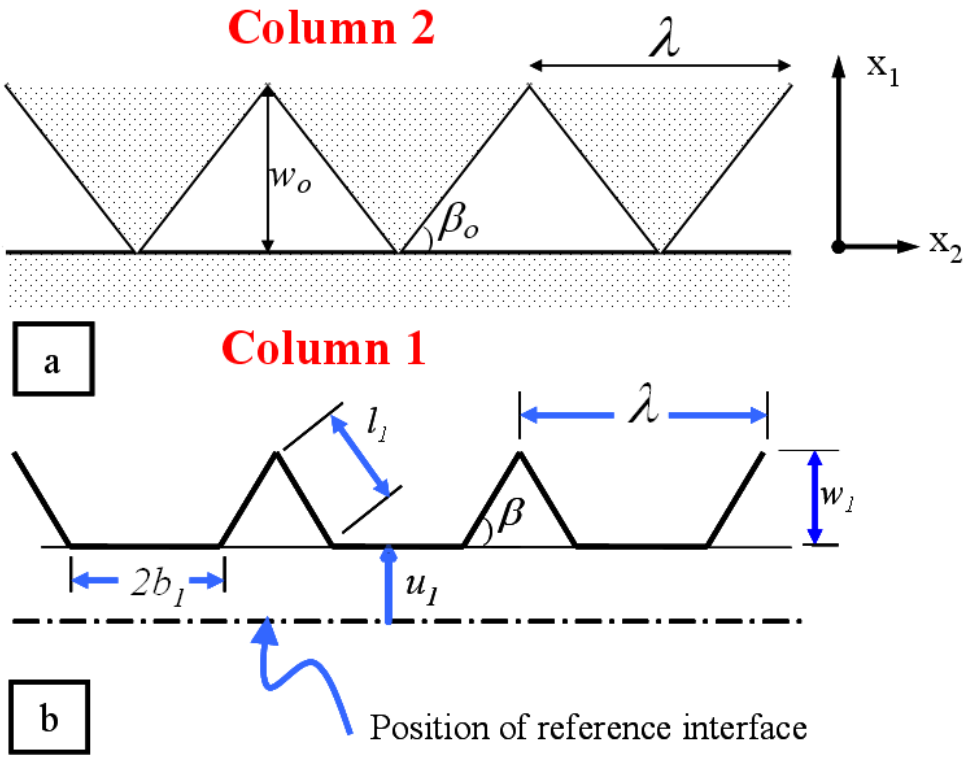

Figure 2.4: . Idealisation of surface undulations. a. Reference configuration, where sintering strain is zero. b. Current configuration, where column 1 has displaced an amount u_1 with respect to column 2 from the reference configuration.

within a few hours of deposition as reported by Lughi et al [40]. As sintering proceeds, the contact width $2b_1$ increases and the combined peak-to-peak amplitude of the undulations w_1 decreases, while the wavelength λ remains the same.

The objective of the problem is to solve for the local evolution of surface profile as characterized by (u_1, w_1) due to the interfacial diffusion of matter from the contacts into the gaps of peak-to-peak amplitude w_1. Interfacial diffusion is driven by the combined driving forces of the net reduction in interfacial energy, and the change in potential energy of the system. It has been observed from numerical simulations over a wide range of parameters that the pore profile angle β quickly settles down to a constant value. This steady-state angle β can be given in terms of interface energy γ_g and surface energy γ_s at contacts as

$$\beta \;=\; \arccos\left[\frac{1}{4}\left(\frac{\gamma_g}{\gamma_s}-1\right)+\sqrt{\left(\frac{\gamma_g}{\gamma_s}-1\right)^2+8}\right] \tag{2.2}$$

Adopting this equilibrium pore profile angle β for the contact geometries, we can express all the geometric variables that define the contact geometry (b_1, w_1, l_1) as a function of u_1. As a result, we have only one independent variable. Considering constancy of volume of the contacting asperities, we can express b_1, w_1 and l_1 as functions of u_1:

$$b_1 = \frac{\lambda}{2}-\frac{1}{2}\sqrt{\lambda^2-4\lambda u_1\cot\beta};\;\; w_1 = \frac{\tan\beta}{2}\sqrt{\lambda^2-4\lambda u_1\cot\beta};\;\; l_1 = \frac{\sec\beta}{2}\sqrt{\lambda^2-4\lambda u_1\cot\beta} \tag{2.3}$$

The macroscopic sintering strain in the x_1 direction ε^s_{11} can be expressed in terms of the state variable u_1.

$$\varepsilon^s_{11} \;=\; \frac{u_0^1-u_1}{d} \tag{2.4}$$

Note that u_0^1 is the initial value of state variable u_1.

2.3.2 Local sintering at contacts

At all contacts between columns, it is assumed that matter diffuses along the interface from the contacts, labelled OA in Fig. 2.5, and deposits along the free surface AB. Ficks first law states that the interfacial volumetric flux j per unit thickness (in units of m^2/s) is related to the gradient of chemical potential (J/m^3) by

$$j \;=\; D\frac{\partial\mu}{\partial s} \tag{2.5}$$

where s is the arc length and D is the interfacial diffusivity (in units of $m^6/J/s$) and is given by the following expression in terms of a reference diffusivity D_o , atomic volume Ω , interface thickness δ , thermal activation energy q and Boltzmann constant k.

$$D \;=\; \frac{\delta\Omega}{kT}D_o\exp\left(\frac{-q}{kT}\right) \tag{2.6}$$

Continuity of mass at an interface dictates the following relationship between the

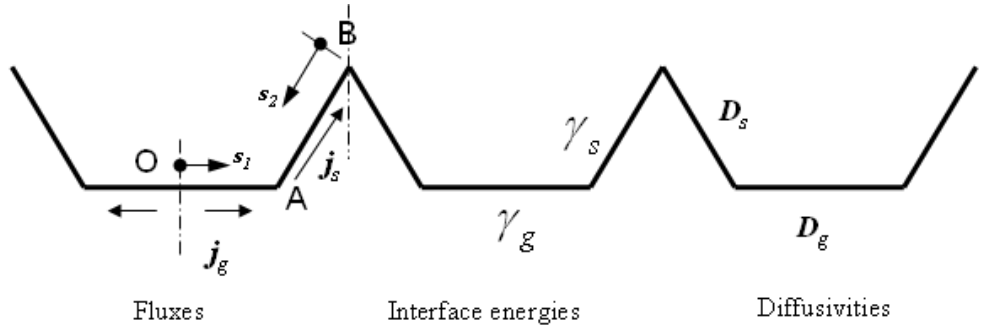

Figure 2.5: Definition of fluxes, surface energies and diffusivities at the contact geometry.

normal velocity of evolving surface v_n and the flux j

$$v_n + \frac{\partial j}{\partial s} \;=\; 0 \tag{2.7}$$

2.3.3 Thermodynamic variational principle (TVP)

At a given instant the state of the material can be expressed in terms u_1. In order to complete the constitutive description we need to determine the rate of change of u_1 , ie $\dot{u}_1$. We do this by using the variational principle given by eqn. 2.1, which requires expressing ψ and $\dot{G}$ in terms of $\dot{u}_1$.

Determination of Gibbs free energy

Consider a slice of thickness λ of the repeating cell $d \times d$ subjected to a stress σ_{11} as shown in Fig. 2.3. The Gibbs free energy has contributions from the interface energy and the potential energy of the applied stress and is given by

$$G_T \;=\; G_\lambda + \sigma_{11} d\lambda u_1 \tag{2.8}$$

G_λ is the interface energy and is given by

$$G_\lambda \;=\; d\left[2b_1\gamma_g + 2l_1\gamma_s + (\lambda - 2b_1)\gamma_s\right] \tag{2.9}$$

Substituting for b_1 and l_1 using eqn. 2.3 we obtain G_λ as a function of u_1:

$$G_\lambda(u_1) \;=\; d\left[(\lambda - \sqrt{\lambda^2 - 4\lambda u_1 \cot\beta})\gamma_g + \gamma_s(\sec\beta + 1)\sqrt{\lambda^2 - 4\lambda u_1 \cot\beta}\right] \tag{2.10}$$

The Gibbs free energy density (G) is obtained by dividing the Gibbs free energy by the volume of the representative volume element of Fig. 2.3.

$$G = \frac{G_\lambda(u_1)}{d^2\lambda} + \frac{\sigma_{11} d\lambda u_1}{d^2\lambda} \tag{2.11}$$

Then $\dot{G}$ is obtained by differentiating eqn. 2.11 with respect to time:

$$\dot{G} = \left[\frac{2\lambda \cot\beta(\gamma_g - \gamma_s \sec\beta - \gamma_s)}{d\sqrt{\lambda^2 - 4\lambda u_1 \cot\beta}} + \frac{\sigma_{11}}{d} \right] \dot{u}_1 \tag{2.12}$$

Determination of rate potential

We now introduce the rate potential ψ_λ arising from diffusional flow of material over the asperities for the representative volume element of Fig. 2.3. The potential is expressed in terms of the volumetric flux per unit depth j as given below. This interfacial flux is a function of the local co-ordinate along the contact OA, and of the local co-ordinate along the contact AB, as shown in Fig. 2.5.

$$\psi_\lambda = \frac{d}{D_g} \int_0^{b_1} j^2(s_1)\, ds_1 + \frac{d}{D_s} \int_0^{l_1} j^2(s_2)\, ds_2 \tag{2.13}$$

where D_g and D_s are the diffusion coefficients for interfacial diffusion along OA and surface diffusion along the free surface AB, respectively, as specified by eqn. 2.6. The flux on OA and on AB can be obtained by considering mass conservation (eqn. 2.7)and this requires normal velocity of the contact surface OA and the free surface AB respectively. From the contact geometry, we can readily find the normal velocity of surface OA and normal velocity of free surface AB as

$$v_n = \begin{cases} \dot{u}_1 & \text{on} \quad OA; \\ -(\dot{u}_1 + \dot{w}_1)\cos\beta + \frac{s_2}{l_1}\left(\dot{b}_1 \sin\beta + \dot{w}_1 \cos\beta\right) & \text{on} \quad AB. \end{cases}$$

Upon invoking eqn. 2.7, flux on interface OA and free surface AB can be obtained as

$$j = \begin{cases} -\dot{u}_1 s_1 & \text{on} \quad OA; \\ s_2(\dot{u}_1 + \dot{w}_1)\cos\beta - \frac{s_2^2}{2l_1}\left(\dot{b}_1 \sin\beta + \dot{w}_1 \cos\beta\right) & \text{on} \quad AB. \end{cases}$$

Continuity of flux at A is satisfied because j at $s_1 = b_1$ on OA is equal to j at $s_2 = l_1$ on AB. The macroscopic potential per unit volume of the TBC is given by

$$\psi = \frac{\psi_\lambda}{d^2\lambda} \tag{2.14}$$

An explicit expression can be obtained for ψ by integration of eqn. 2.13, using expressions for the fluxes to give

$$\psi(\dot{u}_1) = \frac{\dot{u}_1^2}{24d\lambda D_g \cos\beta}\left[\lambda - \sqrt{\lambda^2 - 4\lambda u_1 \cot\beta}\right]^2\left[\cos\beta - \left(\lambda\cos\beta - \frac{D_g}{D_s}\right)\sqrt{\lambda^2 - 4\lambda u_1\cot\beta}\right] \tag{2.15}$$

Constitutive model

Substituting $\dot{G}$ given by eqn. 2.12 and ψ given by eqn. 2.15 into eqn. 2.1 and choosing the value of $\dot{u}_1$ that minimises the resulting functional gives the rate of evolution of the microstructure as a function of the current state and applied stress. It proves convenient to write the resulting relationships in dimensionless form. All the length scales are normalised by the wavelength of undulation λ, such that

$$\bar{u}_1 = \frac{u_1}{\lambda}; \quad \bar{w}_1 = \frac{w_1}{\lambda}; \quad \bar{b}_1 = \frac{b_1}{\lambda}; \quad \bar{l}_1 = \frac{l_1}{\lambda}; \quad \bar{d} = \frac{d}{\lambda}; \tag{2.16}$$

and the non-dimensional material properties are

$$\bar{D}_g = \frac{D_g}{D_s}; \quad \bar{\gamma}_g = \frac{\gamma_g}{\gamma_s}; \quad \bar{E} = \frac{E\lambda}{(1-\nu)\gamma_s}; \tag{2.17}$$

And the non-dimensional stress is

$$\bar{\sigma}_{11} = \frac{\sigma_{11}\lambda}{(1-\nu)\gamma_s} \tag{2.18}$$

These normalisations are consistent with the normalised time measure

$$\bar{t} = \frac{D_s\gamma_s t}{\lambda^4} \tag{2.19}$$

Minimisation of the functional gives

$$\dot{\bar{u}}_1 = -\left[\frac{a(\bar{u}_1) + \frac{\bar{\sigma}_{11}(1-\nu)}{\bar{d}}}{A(\bar{u}_1)}\right] \tag{2.20}$$

where,

$$a(\bar{u}_1) = \frac{2\cot\beta(\bar{\gamma}_g - \sec\beta - 1)}{\bar{d}\sqrt{1 - 4\bar{u}_1\cot\beta}} \tag{2.21}$$

$$A(\bar{u}_1) \;=\; \frac{1}{24\bar{d}\bar{D}_g\cos\beta}\left[1-\sqrt{1-4\bar{u}_1\cot\beta}\right]^2\left[\cos\beta-\left(\cos\beta-\bar{D}_g\right)\sqrt{1-4\bar{u}_1\cot\beta}\right] \tag{2.22}$$

The strain-rate $\dot{\varepsilon}^s_{11}$ can be obtained by differentiating eqn. 2.4 with respect to time, ie

$$\dot{\varepsilon}^p_{11} \;=\; -\frac{\dot{\bar{u}}_1}{\bar{d}} \tag{2.23}$$

Combining eqns. 2.20 and 2.23 gives

$$\dot{\varepsilon}^p_{11} \;=\; \left[\frac{a(\bar{u}_1)+\frac{\bar{\sigma}_{11}(1-\nu)}{\bar{d}}}{\bar{d}A(\bar{u}_1)}\right] \equiv\; g_{11} \tag{2.24}$$

Repeating this analysis for a stress σ_{22} applied in the x_2 direction, we obtain

$$\dot{\varepsilon}^p_{22} \;=\; \left[\frac{a(\bar{u}_2)+\frac{\bar{\sigma}_{22}(1-\nu)}{\bar{d}}}{\bar{d}A(\bar{u}_2)}\right] \equiv\; g_{22} \tag{2.25}$$

We assume that $\varepsilon^p_{33}=\gamma^p_{13}=\gamma^p_{23}=0$. We complete the model by specifying relationship for the shear strain rate in 1-2 plane as

$$\dot{\gamma}^p_{12}=\frac{\sigma_{12}}{\eta} \tag{2.26}$$

Where η is the shear viscosity. $\dot{\gamma}^p_{12}$ is non-dimensionalised taking $\bar{\eta}=\frac{\eta D_s}{(1-\nu)\lambda^3}$ and is given by

$$\dot{\gamma}^p_{12}=\frac{\bar{\sigma}_{12}}{\bar{\eta}} \tag{2.27}$$

These equations have been coded into ABAQUS using the UMAT facility. The Newton-Raphson scheme employed to solve the system of equations is detailed in the following section. The resulting code has been used to simulate the sintering response of a constrained TBC as detailed in the following sections.

Integration scheme for constitutive model

The constitutive relationships of eqns. 2.24, 2.25 and 2.27 can be written in incremental form as follows

$$\bar{G}_{ij}=\Delta\varepsilon^p_{ij}-\Delta\bar{t}\;g_{ij}\left(\bar{\sigma}_{ij}+\theta\Delta\bar{\sigma}_{ij},\varepsilon^p_{ij}+\theta\Delta\varepsilon^p_{ij}\right)=0 \qquad 0<\theta\leq 1; \tag{2.28}$$

where $\Delta\varepsilon^p_{ij}$ is the increment of sintering strain over the time increment $\Delta\bar{t}$, with the rates determined at an instant $\theta\Delta\bar{t}$ in the increment. $\bar{G}_{ij}$ is the difference in sintering strain increments in a typical time step. In the simulations presented here a value of $\theta = 0.5$ was chosen to ensure that the solution is unconditionally stable. The stress and strain increments must satisfy the elastic constitutive law:

$$\bar{H}_{ij} = \Delta\bar{\sigma}_{ij} - \bar{D}_{ijkl}\left(\Delta\varepsilon_{ij} - \Delta\varepsilon^p_{ij}\right) = 0 \tag{2.29}$$

Here we assume that the elastic stiffness matrix $\bar{D}_{ijkl}$ is not a function of state (ie inelastic strain). $\bar{H}_{ij}$ is the difference between stress increments in a typical time step. Eqns. 2.28 and 2.29 represent a set of non-linear equations in unknowns $(\Delta\varepsilon^p_{ij}, \Delta\bar{\sigma}_{ij})$. This system of equations can be solved using Newton's method. After i iterations within the increment the values of $(\Delta\varepsilon^p_{ij}, \Delta\bar{\sigma}_{ij})^i$ are given by

$$\begin{bmatrix} \Delta\varepsilon^p_{kl} \\ \Delta\bar{\sigma}_{kl} \end{bmatrix}^i = \begin{bmatrix} \Delta\varepsilon^p_{kl} \\ \Delta\bar{\sigma}_{kl} \end{bmatrix}^{i-1} - \left[\begin{bmatrix} \delta_{ik}\delta_{jl} - \Delta\bar{t}\theta\frac{\partial g_{ij}}{\partial\varepsilon^p_{kl}} & -\Delta\bar{t}\theta\frac{\partial g_{ij}}{\partial\bar{\sigma}_{kl}} \\ \bar{D}_{ijkl} & \delta_{ik}\delta_{jl} \end{bmatrix}^{i-1}\right]^{-1} \begin{bmatrix} \bar{G}_{ij} \\ \bar{H}_{ij} \end{bmatrix}^{i-1}$$

Where the superscript $i-1$ indicates that all functions are determined using quantities determined at the end of the $(i-i)^{th}$ iteration. The iterative process is continued until a prescribed tolerance in $\Delta\varepsilon^p_{kl}, \Delta\bar{\sigma}_{kl}$ is reached. Explicit forms of eqns. 2.28 and 2.29 are given below.

$$\bar{G}_{11} = \Delta\varepsilon^p_{11} - \Delta\bar{t}\; g_{11}\left(\bar{\sigma}_{11} + \theta\Delta\bar{\sigma}_{11}, \varepsilon^p_{11} + \theta\Delta\varepsilon^p_{11}\right) = 0 \tag{2.30}$$

$$\bar{G}_{22} = \Delta\varepsilon^p_{22} - \Delta\bar{t}\; g_{22}\left(\bar{\sigma}_{22} + \theta\Delta\bar{\sigma}_{22}, \varepsilon^p_{22} + \theta\Delta\varepsilon^p_{22}\right) = 0 \tag{2.31}$$

$$\bar{H}_{11} = \Delta\bar{\sigma}_{11} - \frac{\bar{E}}{(1+\nu)(1-2\nu)}\left[(1-\nu)(\Delta\varepsilon_{11} - \Delta\varepsilon^p_{11}) + \nu(\Delta\varepsilon_{22} - \Delta\varepsilon^p_{22}) + \nu(\Delta\varepsilon_{33})\right] = 0 \tag{2.32}$$

$$\bar{H}_{22} = \Delta\bar{\sigma}_{22} - \frac{\bar{E}}{(1+\nu)(1-2\nu)}\left[\nu(\Delta\varepsilon_{11} - \Delta\varepsilon^p_{11}) + (1-\nu)(\Delta\varepsilon_{22} - \Delta\varepsilon^p_{22}) + \nu(\Delta\varepsilon_{33})\right] = 0 \tag{2.33}$$

$$\bar{H}_{33} = \Delta\bar{\sigma}_{33} - \frac{\bar{E}}{(1+\nu)(1-2\nu)}\left[\nu(\Delta\varepsilon_{11} - \Delta\varepsilon^p_{11}) + \nu(\Delta\varepsilon_{22} - \Delta\varepsilon^p_{22}) + (1-\nu)(\Delta\varepsilon_{33})\right] = 0 \tag{2.34}$$

$$\bar{G}_{33} = \Delta\gamma^p_{12} - \frac{\Delta\bar{t}}{\bar{\eta}}\left(\bar{\sigma}_{12} + \theta\Delta\bar{\sigma}_{12}\right) = 0 \tag{2.35}$$

$$\bar{H}_{44} = \Delta\bar{\sigma}_{12} - \frac{\bar{E}}{2(1+\nu)}\left[(\Delta\gamma_{12} - \Delta\gamma^p_{12})\right] = 0 \tag{2.36}$$

$$\bar{H}_{55} = \Delta\bar{\sigma}_{13} - \frac{\bar{E}}{2(1+\nu)}\left[\Delta\gamma_{13}\right] = 0 \tag{2.37}$$

$$\bar{H}_{66} = \Delta\bar{\sigma}_{23} - \frac{\bar{E}}{2(1+\nu)}\left[\Delta\gamma_{23}\right] = 0 \tag{2.38}$$

The above integration scheme has been coded as a UMAT routine in ABAQUS. ABAQUS also reqires specification of the Jacobian for use in the solution for the next increment. This can be determined using a procedure originally proposed by Benallal et al [88] as described below.

Determination of Jacobian

We now need to determine the Jacobian within the UMAT routine.

$$J_{ijkl} = \frac{\partial\Delta\bar{\sigma}_{ij}}{\partial\Delta\varepsilon_{kl}} \tag{2.39}$$

Note that $(\Delta\varepsilon^p_{ij}, \Delta\bar{\sigma}_{ij})$ are functions of the total strain increment $\Delta\varepsilon_{ij}$. Differentiating eqns. 2.28 and 2.29 with respect to $\Delta\varepsilon_{ij}$ then gives

$$\begin{bmatrix} \delta_{ik}\delta_{jl} - \Delta\bar{t}\theta\frac{\partial g_{ij}}{\partial\varepsilon^p_{kl}} & -\Delta\bar{t}\theta\frac{\partial g_{ij}}{\partial\bar{\sigma}_{kl}} \\ \bar{D}_{ijkl} & \delta_{ik}\delta_{jl} \end{bmatrix} \begin{bmatrix} \frac{\partial\Delta\varepsilon^p_{kl}}{\partial\Delta\varepsilon_{mn}} \\ J_{klmn} \end{bmatrix} = \begin{bmatrix} 0 \\ \bar{D}_{ijmn} \end{bmatrix}$$

J_{klmn} in the above equation is the Jacobian. While computing the Jacobian using the above equation, all the quantities within the leading square matrices are determined using the values computed in the final iteration for the determination of stress increment, thus the Jacobian can be determined in a single step by inverting the above system of linear equations.

2.4 Constrained sintering of a perfect TBC

In this section, we model the sintering of a perfect intact coating using the constitutive model described above and demonstrate that the results are in exact agreement with the results of Hutchinson et al [42]. The FE model is constructed with C3D8 8-noded linear brick elements. Symmetry conditions are imposed at all boundaries

perpendicular to the x_1 and x_2 directions. An initial condition of $\bar{u}_0^1 = \bar{u}_0^2 = 0.07$ is taken for all the elements. Unless otherwise stated, we assume that $\nu = 0.3, \bar{d} = 20, \bar{D}_g = 1, \bar{\gamma}_g = 0.68, \beta = 0.8871$ and $\bar{\eta} = 25$ in the simulations presented in this chapter. FE analysis indicates that for smaller values of $\bar{E}$(say, 500), the perfect film fully densifies ($\bar{b}_1 \simeq 0.5$). On the other hand, sintering gets arrested ($\bar{b}_1 \simeq 0.153$) for larger values of $\bar{E}$(say, 1000). It should be noted that the sintering strain evolves uniformly in x_1 and x_2 directions for the perfect film. The computational results of the sintering response of a perfect film are compared with solutions obtained from direct integration of eqns. 2.24 and 2.25 for different modulus values in Figs. 2.6 and 2.7. These simulations demonstrate the accuracy of the finite element scheme described above. It was also observed through a series of computational simulations that the sintering response of the TBC is not influenced by the choice of Poisson's ratio (ν) and viscosity ($\bar{\eta}$).

2.5 Influence of Imperfections on the sintering of a constrained TBC

Here we concentrate on the behaviour of coatings that contain defects. We start by examining the situation where the coating contains a set of fully developed mud cracks considered by Hutchinson et al [42]. We demonstrate that the simple analysis presented by Hutchinson et al [42] provides a good description of the more detailed computations presented here. We then consider the response of coatings which contain small imperfections and explore the conditions under which these can develop into cracks.

2.5.1 Progressive sintering of columns within a mud cracked cluster

Here we explore the inter-columnar sintering of the mud-cracked TBC shown in Fig. 2.2b. The mud cracked TBC is idealized as an assembly of square clusters of columns as shown in Fig. 2.2b. We take a single square cluster of side length $2R$

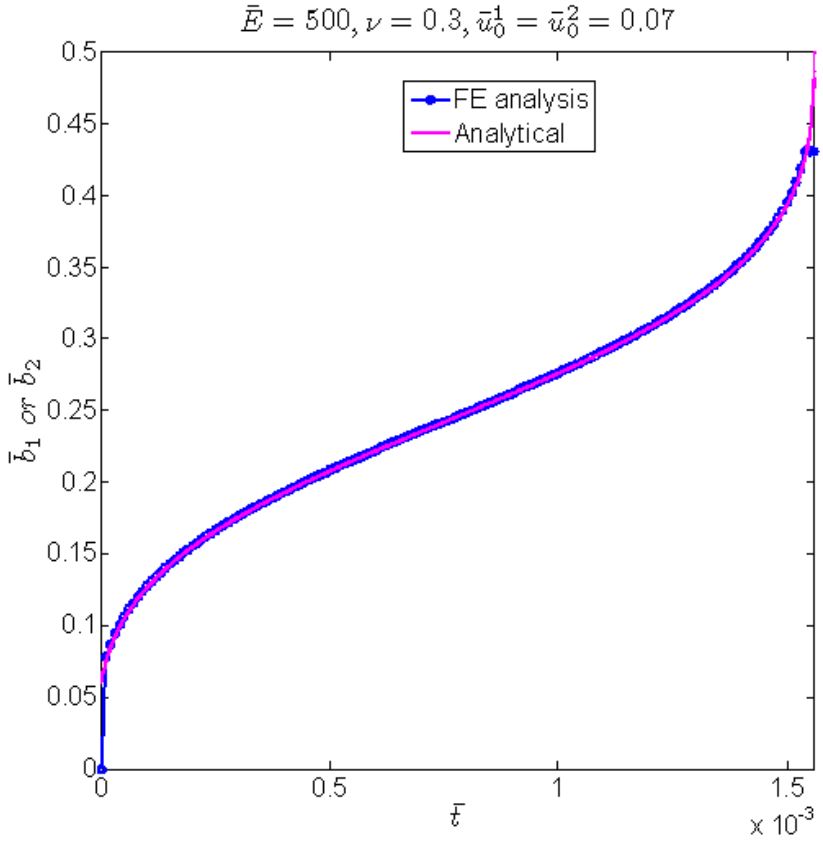

Figure 2.6: Comparison of analytical and computational solution of sintering response of a perfect constrained film: Full sintering occurs for $\bar{E} = 500$.

and height H, perfectly bonded to the underlying substrate. The geometric model of the island cluster is shown in Fig. 2.8. The FE model is fixed at the bottom in all three directions and all other faces are traction free. The FE model is constructed with C3D8 8-noded linear brick elements. An initial condition of $\bar{u}_0^1 = \bar{u}_0^2 = 0.05$ is taken for all the elements. The FE analysis shows that full sintering occurs within the square cluster for smaller values of $\bar{E}$. Fig. 2.9 shows the semi-contact width $\bar{b}_2$ in the x_2-direction at a time $\bar{t} = 7.8 \times 10^{-4}$ for $\bar{E} = 1500$. It is evident that sintering is non-uniform in the cluster. In their analytical model, Hutchinson et al [42] assumed that the sintering strains, ie $\bar{b}_1, \bar{b}_2$, are uniform in the cluster. With this assumption they demonstrate that the sintering response of the cluster can be determined by the analytical expressions for a perfect fully constrained layer, but using a modified value of

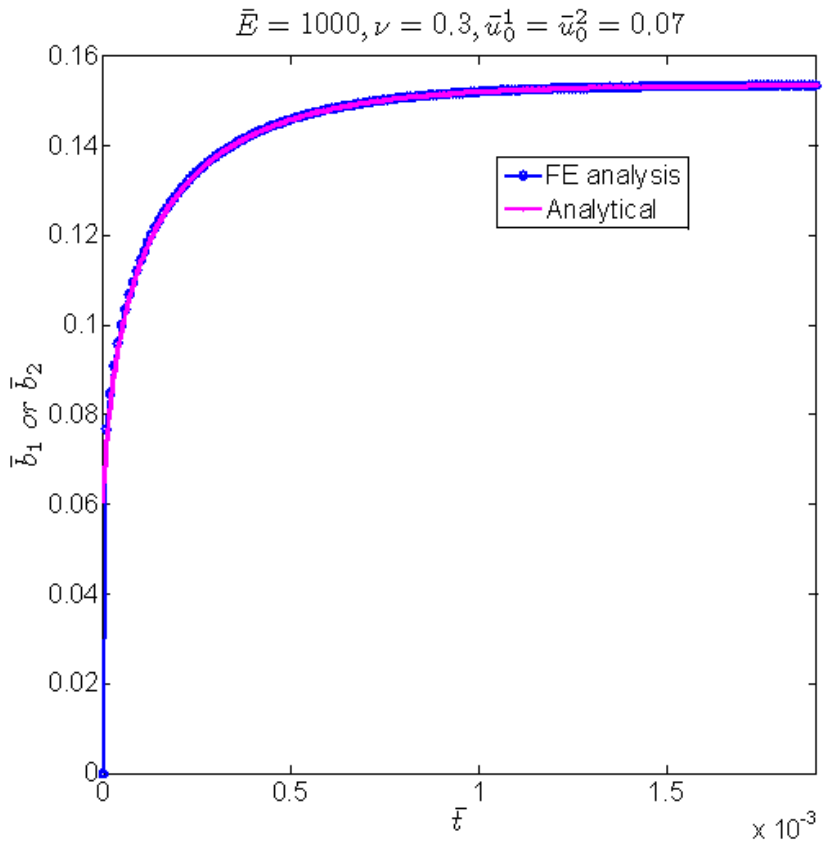

Figure 2.7: Comparison of analytical and computational solution of sintering response of a perfect constrained film: Sintering gets arrested for $\bar{E} = 1000$.

Young's modulus. The elastic stored energy density of a mud-cracked, incompressible TBC (derived in chapter 3) is given by

$$U_{sq} = \frac{4}{3\sqrt{6}} E \left(\frac{R}{H}\right) (\varepsilon_s + \varepsilon_T)^2 \tag{2.40}$$

The strain energy density in a perfect constrained film is

$$U_{pf} = \frac{E_{eff}}{(1-\nu)} (\varepsilon_s + \varepsilon_T)^2 \tag{2.41}$$

Equating eqns. 2.40 and 2.41, and taking $\nu = 1/2$ for an elastically incompressible film, we find the effective modulus ($\bar{E}_{eff}$) of a perfect film equivalent to a mud-cracked island cluster to be

$$\bar{E}_{eff} = \frac{2}{3\sqrt{6}} \bar{E} \left(\frac{R}{H}\right) \tag{2.42}$$

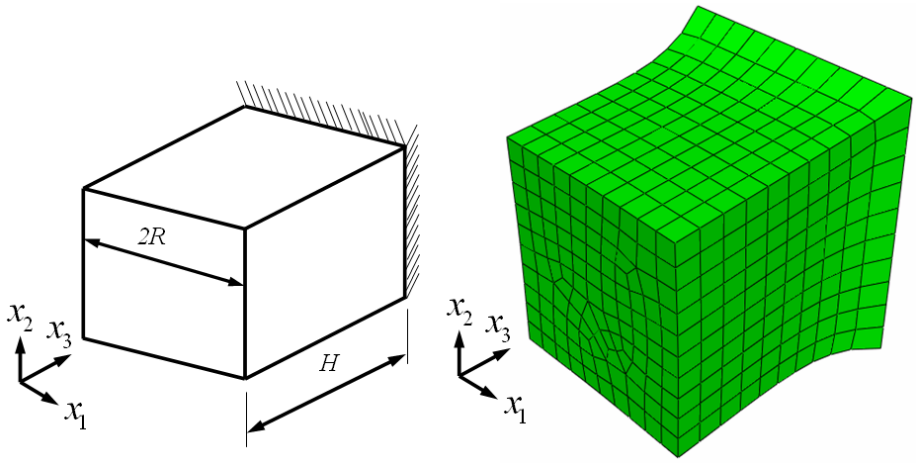

Figure 2.8: Model of a mud-cracked island cluster. a. The model is of size $2R \times 2R \times H$ and is constrained at the bottom in all the three directions. b. Deformed FE model of a mud-cracked cluster

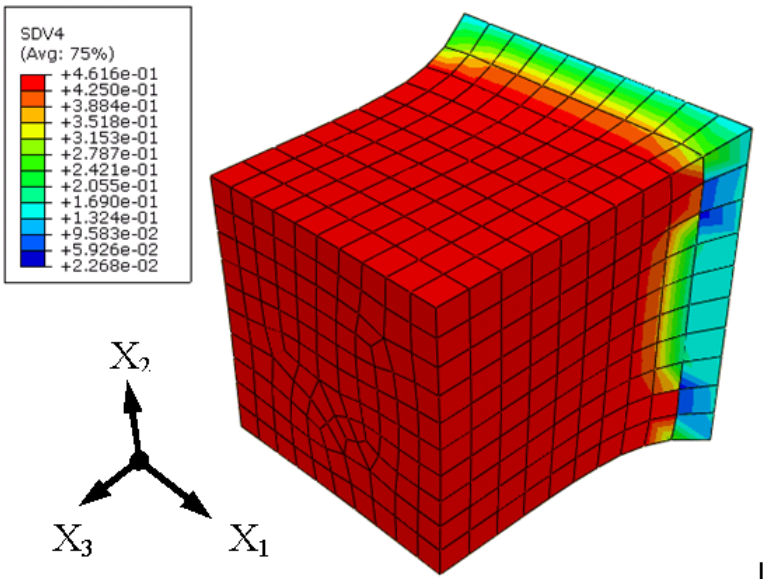

Figure 2.9: Deformed FE model of defect free island cluster. The model is of size $2R \times 2R \times H$ and is constrained at the bottom($X_3 = 0$) in all directions. Its faces are traction free. It shows the semi-contact width $\bar{b}_2$ in X_2 direction for $\bar{E} = 1500$ and $\bar{R} = 1/2$.

Fig. 2.10 shows the evolution of the average value of $\bar{b}_2$ within the cluster compared with the prediction for a perfect film using the modified modulus of eqn. 2.42. It is evident from Fig. 2.10 that the simplified model provides a reasonably accurate

description of the overall sintering response, both in terms of timescale for the sintering process and the overall extent of the sintering behaviour. Also, it is evident that the constraint of the coating is experienced over a height $H/4$, within which there is significant shear deformation (evidenced by the exaggerated distorted shape of the mesh in Fig. 2.9). Above this height sintering is reasonably uniform within the cluster. Both these observations are consistent with the assumptions made in the model of Hutchinson et al [42]. We make use of these observations in developing analytical models in the next chapter, where we use a similar approximations to model the growth of imperfections in the coating.

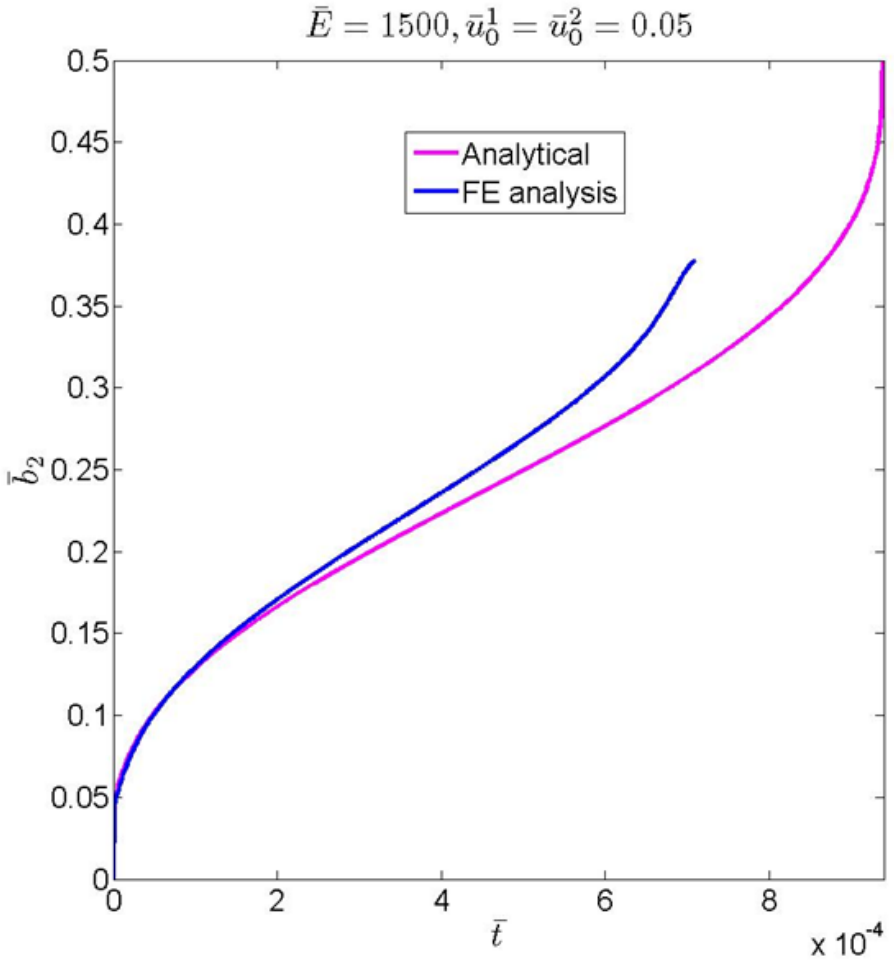

Figure 2.10: Evolution of semi-contact width $\bar{b}_2$ in x_2 direction of analytical model is compared with average semi-contact width $\bar{b}_2$ of finite element model for $\bar{E} = 1500$ and $\bar{R} = 1/2$.

2.5.2 Influence of an arbitrarily placed imperfection

We now consider an arbitrarily placed imperfection within the constrained TBC and study the influence of this imperfection on the sintering response. Within the imperfection, an initial condition which differs from that in the remainder of the coating is specified. All other geometric and material parameters are kept the same. We have demonstrated in the previous section that a compliant coating without an imperfection can fully densify. Further, here it is shown that the sintering response of the compliant coating is not sensitive to the presence of small variations in the initial conditions and the entire coating fully densifies. A completely different type of behaviour is observed for stiff coatings. Now let us examine a compliant coating with an imperfection. A FE model of a representative material volume is shown in Fig. 2.11. Symmetry conditions are imposed at all boundaries perpendicular to the x_1 and x_2 directions. Initial condition ($\bar{u}_0^1 = \bar{u}_0^2 = 0.07$) of defective elements within a cluster of elements which extends down the entire height (x_3-direction) of the TBC is slightly less than that in the remainder of the coating ($\bar{u}_0^1 = \bar{u}_0^2 = 0.08$). Figs. 2.12

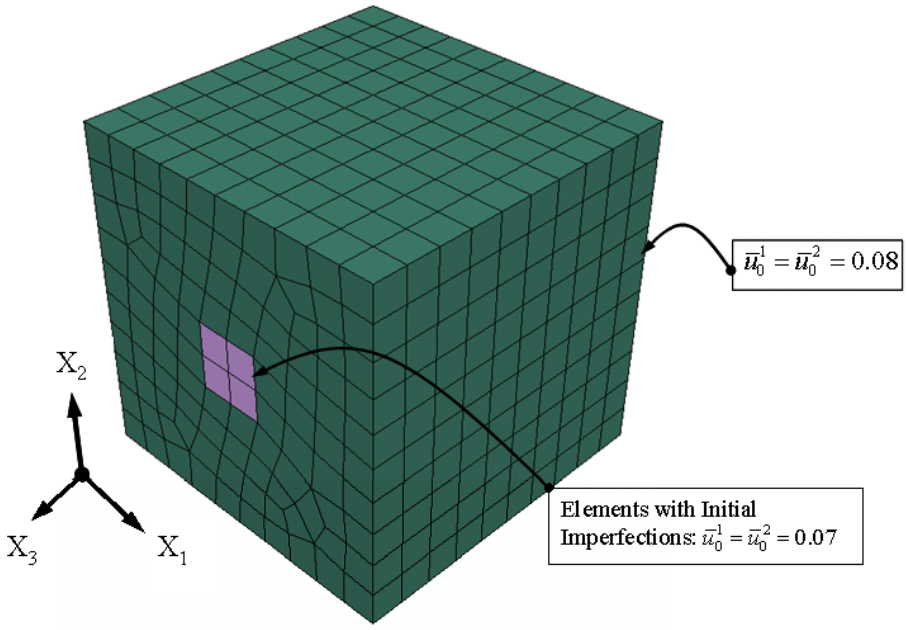

Figure 2.11: Finite element model of constrained film with imperfections. Imperfections exist over the entire height of the TBC (x_3-direction).

2.13 show the sintering response of a compliant coating with imperfection. It is clear from these figures that complete sintering of the coating occurs at and away from the imperfection and the sintering response of the TBC for this small value of modulus ($\bar{E} = 500$) is insensitive to the presense of imperfections.

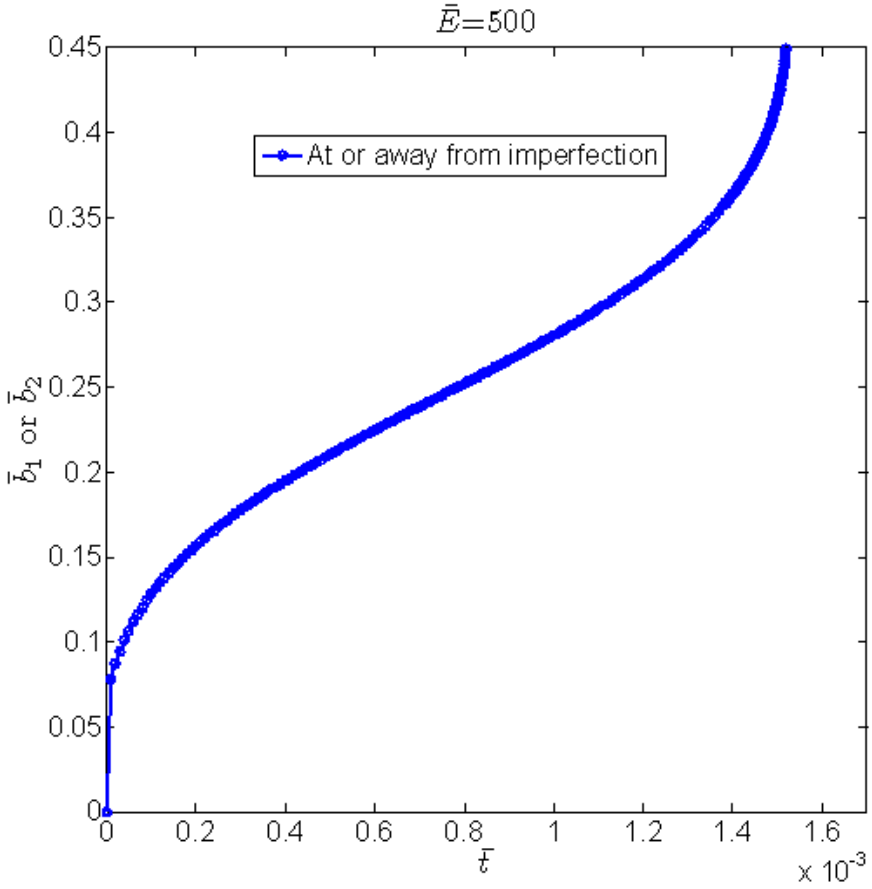

Figure 2.12: Evolution of semi-contact width ($\bar{b}_2$) at imperfection or away from imperfection for $\bar{E} = 500$.

For larger values of the modulus, eg ($\bar{E} = 1000$), the FE analysis indicates that the imperfection and surrounding material densify initially at a rate similar to that for the perfect film. As the in plane tensile stress builds up due to generation of elastic strain to accommodate the sintering strain, the rate of sintering slows. As sintering is about to be arrested, as in the case of the perfect coating, we observe a divergence in the response between that at the imperfection and remainder of the coating. This is illustrated in Fig. 2.14 which shows the evolution of ($\bar{b}_2$) within the

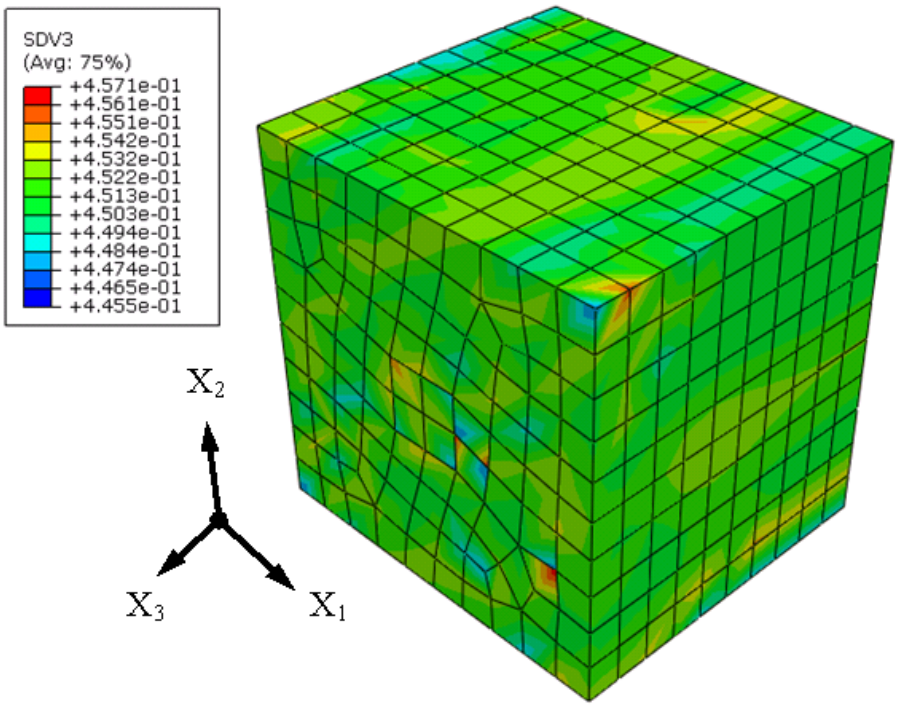

Figure 2.13: Full sintering ($\bar{b}_2 \simeq 0.5$) of constrained film with a defect for $\bar{E} = 500$.

imperfection and surrounding material, compared with that for the perfect coating. Desintering occurs at the location of the initial imperfection, ie $\bar{b}_2$ decreases, for $\bar{t} > 1.2 \times 10^{-3}$. As it does so, the constraint on the remaining material is relaxed allowing the surrounding material to sinter faster. Eventually, $\bar{b}_2 = 0$ at the site of the imperfection. This occurs initially at the surface of the TBC. The desintered zone then spreads vertically towards the substrate and horizontally towards the axis of symmetry, where it meets with an equivalent zone spreading from the adjacent imperfection to form a band of desintered material. This localised desintering reduces the constraint on the surrounding material allowing it to sinter faster. Fig. 2.15 shows the semi-contact width ($\bar{b}_2$) in the x_2-direction following the spread of the desintering region from the initial imperfection (ie at $\bar{t} = 4{\times}10^{-3}$). A negative value of $\bar{b}_2$ indicates separation between the columns of the TBC. For this value of $\bar{E}$ the constraint on elements away from the defect is not relaxed sufficiently to allow them to reach full density and sintering is arrested when $\bar{b}_2 = 0.2461$. Simulations were also carried

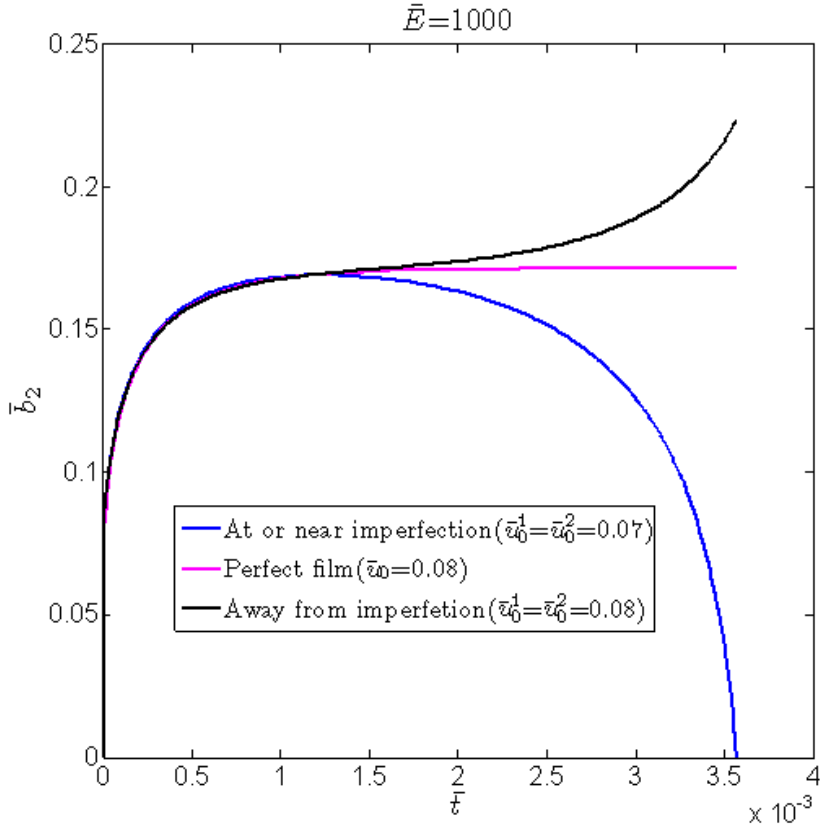

Figure 2.14: Evolution of semi-contact width ($\bar{b}_2$) at the imperfection and away from imperfection compared with perfect film for $\bar{E} = 1000$.

out considering imperfection only at the top of the coating and found that the same pattern of cracks form as in the case of coating with imperfection over its entire height, and this will be further explored in chapter 4.

2.5.3 Influence of a family of imperfections

The analysis of the previous sub-section indicates that in compliant systems the sintering response is not sensitive to the presence of small imperfections, but if the system is stiff small imperfections can eventually develop into cracks, which propagate through the coating. We explore this further by examining the sintering response when the coating contains a regular pattern of imperfections. Fig. 2.16 shows the idealized TBC structure with a primary set of imperfections running along the boundaries of the cluster. These imperfections are assigned a slightly different contact condition

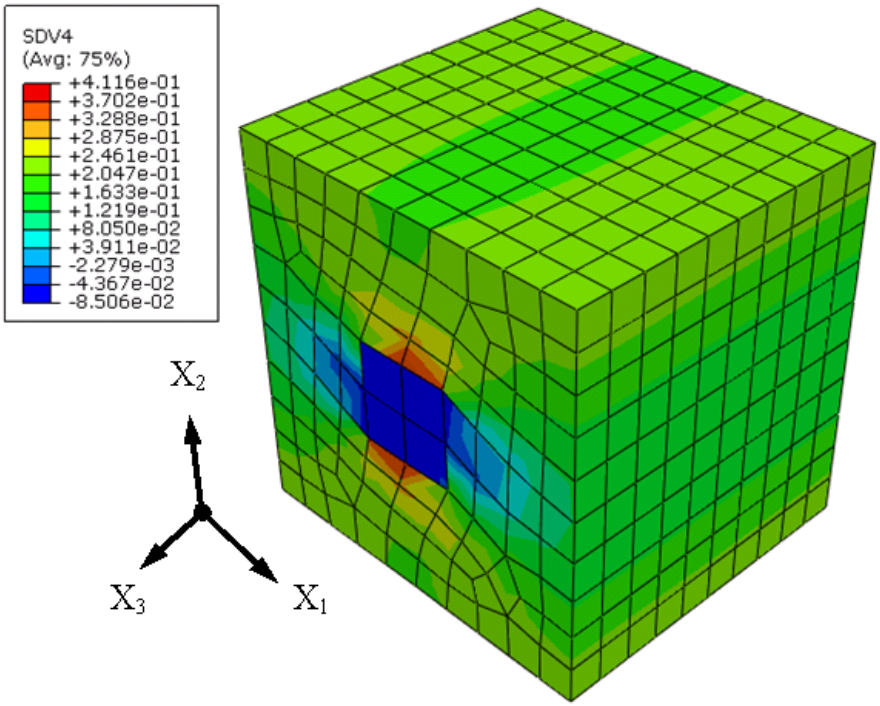

Figure 2.15: Semi-contact width ($\bar{b}_2$) at the imperfection and away from imperfection for $\bar{E} = 1000$ at $\bar{t} = 4 \times 10^{-3}$.

than within the cluster. We consider a repeating cluster of size $2R \times 2R$ which has a primary imperfection on its boundary as shown in Fig. 2.17.

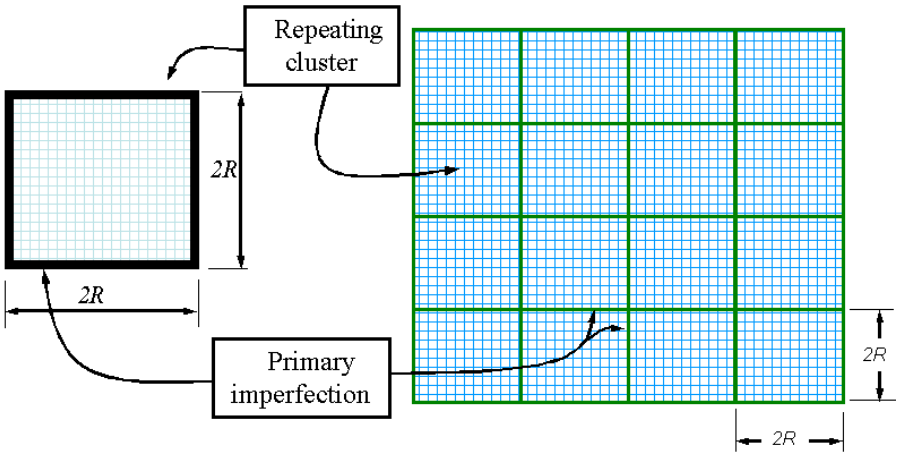

Figure 2.16: Idealization of mud-cracked TBC as an assembly of square clusters of size $2R \times 2R$ with a family of primary imperfections on the boundaries of clusters.

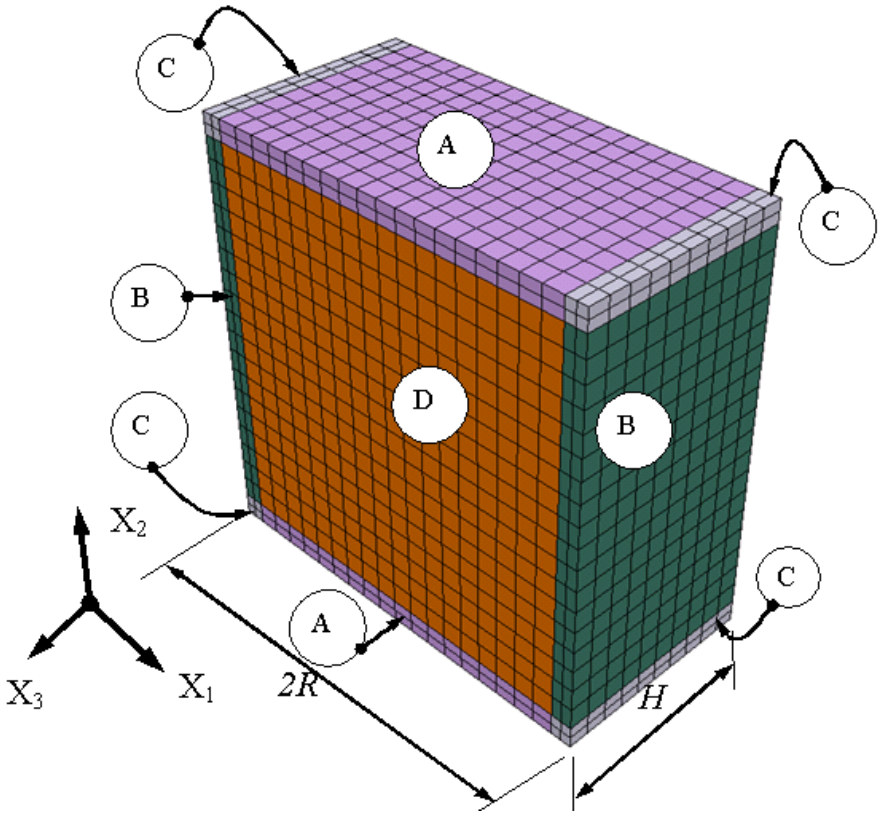

Figure 2.17: Finite element model of a repeating cluster with primary imperfection on its boundary: A-C elements with imperfection, D-Defect free elements, A: $\bar{u}_0^1 = 0.05, \bar{u}_0^2 = 0.045$; B: $\bar{u}_0^1 = 0.045, \bar{u}_0^2 = 0.05$; C: $\bar{u}_0^1 = 0.045, \bar{u}_0^2 = 0.045$; D: $\bar{u}_0^1 = 0.05, \bar{u}_0^2 = 0.05$.

The imperfection exists over the entire height (x_3-direction) of the TBC. In the simulations presented here $R = H$. The FE model of this cluster consists of C3D8 uniform brick 8 noded elements. The FE model is fixed at its base in all three directions and constrained around the vertical boundaries. The defect free elements are marked by D and their initial condition is $\bar{u}_0^1 = 0.05, \bar{u}_0^2 = 0.05$. The elements with imperfections at the boundary of the FE model are shown in different colours and are marked by A, B and C. The initial condition for elements marked by A is $\bar{u}_0^1 = 0.05, \bar{u}_0^2 = 0.045$, for elements marked by B it is $\bar{u}_0^1 = 0.045, \bar{u}_0^2 = 0.05$ and for elements marked by C it is $\bar{u}_0^1 = 0.045, \bar{u}_0^2 = 0.045$. For small values of $\bar{E}$ the response is not sensitive to the imperfections and the entire coating fully sinters i.e full sintering occurs both at the imperfections and within the cluster for small values

of $\bar{E}$, regardless of the cluster size. For instance, Figs. 2.18a and 2.18b show the semi-contact width $\bar{b}_1$ and $\bar{b}_2$ respectively for $\bar{E} = 300$ and $\bar{R} = 1$. From these figures, it should be noted that both $\bar{b}_1$ and $\bar{b}_2$ reach close to 0.5 everywhere in the FE model. For values of $\bar{E} > 600$ desintering occurs at the imperfections which develop into cracks. This reduces the constraint on the surrounding material allowing it to sinter faster and to a greater extent than that experienced in a perfect coating. For $\bar{E} = 1000$ and the same cluster size ($\bar{R} = 1$), the primary imperfections develop into cracks ($\bar{b}_1 = \bar{b}_2 \leq 0$) as shown in Figs. 2.19a and 2.19b. Because of the physical separation at the primary imperfections, constraint on the adjacent material within the cluster is relaxed, allowing it to reach full density quickly as shown in these figures. For large value of $\bar{E}$ sintering within the cluster is eventually arrested and the terminal state is almost exactly the same as that for the isolated cluster considered earlier. Increasing $\bar{R} = 2$ increases the constraint on the sintering process and prevents full sintering being achieved in the cluster. This is shown in Figs. 2.20a and 2.20b for $\bar{E} = 1000$. Arrest of sintering within the cluster might lead to formation of a further set of cracks. A more detailed discussion of these computational models are presented in the next chapter along with analytical models.

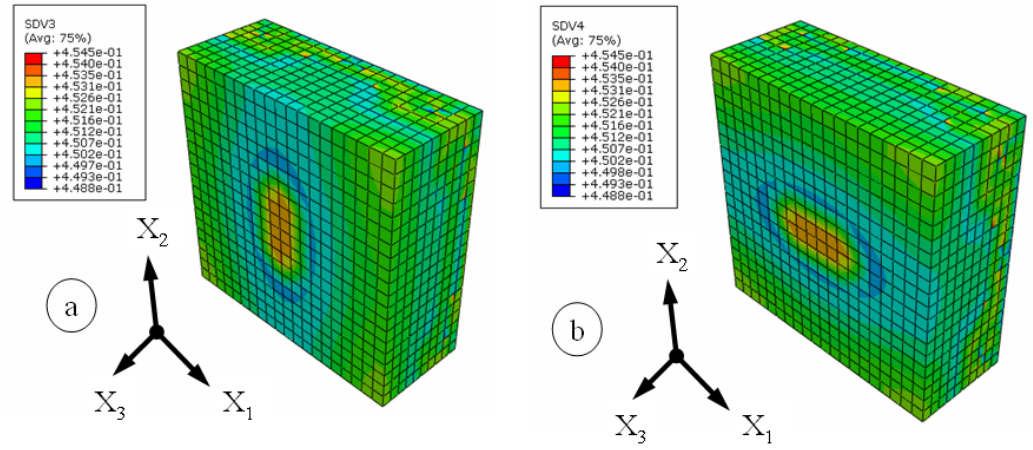

Figure 2.18: Full sintering both at imperfection and within cluster for a choice of $\bar{E} = 300$ and $\bar{R} = 1$. a. Semi-contact width $\bar{b}_1$ b. Semi-contact width $\bar{b}_2$

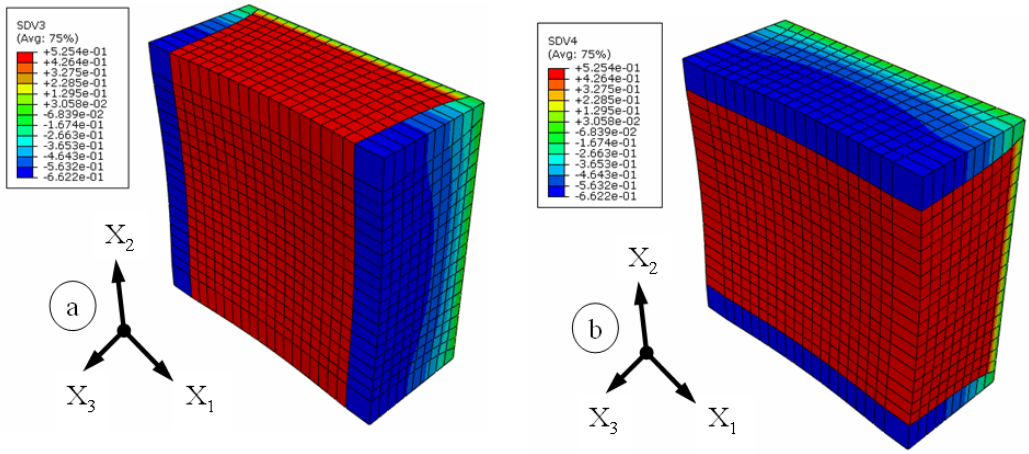

Figure 2.19: Fully developed primary crack at imperfection and complete sintering of cluster for a choice of $\bar{E} = 1000$ and $\bar{R} = 1$. a. Semi-contact width $\bar{b}_1$ b. Semi-contact width $\bar{b}_2$.

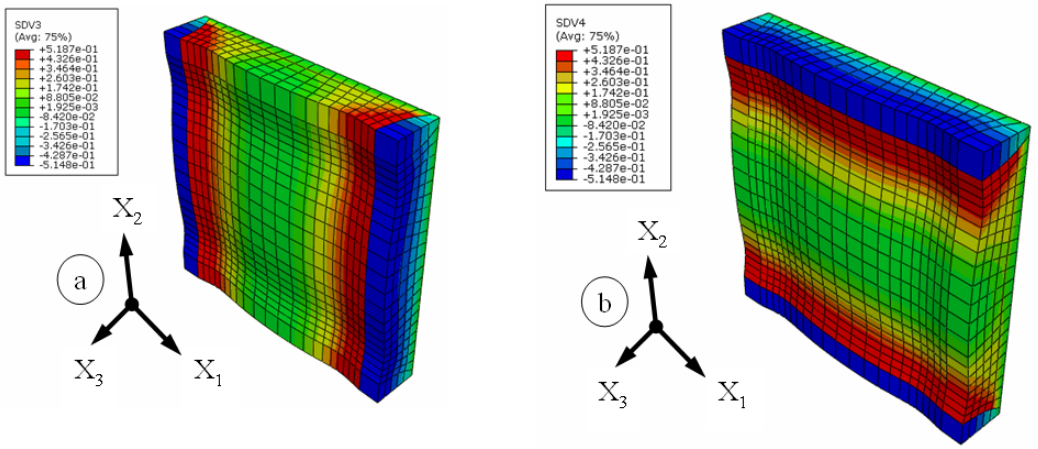

Figure 2.20: Fully developed primary crack at imperfection and incomplete sintering of cluster for a choice of $\bar{E} = 1000$ and $\bar{R} = 2$. a. Semi-contact width $\bar{b}_1$ b. Semi-contact width $\bar{b}_2$.

2.6 Conclusion

In this chapter computational approaches have been presented for determining the sintering response of an ePVD columnar thermal barrier coating and for identifying the conditions under which instabilities can develop in the sintering process, leading to the formation of cracks. A simple constitutive model is developed which has been used in conventional finite element studies to model the sintering response and assess the

sensitivity of the response to the presence of imperfections in the coating. Initially, we modelled the sintering of a perfect intact coating using the constitutive model described above and demonstrated that the results are in exact agreement with the results of Hutchinson et al [42]. Then, we explored progressive sintering of columns within a mud cracked cluster and compared the results with analytical solutions. We went on to study the influence of an arbitrarily placed imperfection within the constrained TBC on the sintering response. This analysis indicates that in compliant systems the sintering response is not sensitive to the presence of small imperfections, but if the system is stiff small imperfections can eventually develop into cracks, which propagate through the coating. We explored this further by examining the sintering response when the coating contains a regular pattern of imperfections and identified conditions under which imperfection grow into cracks. In the following chapter we use these results to motivate a simple analytical model which captures the major features of the effect of imperfections on the sintering response. These simpler models allow a wider range of conditions to be evaluated than can be achieved with computational models, and they can be readily extended to more complex distributions of initial imperfections.

Chapter 3

Trapesoidal Contact Analytical Models

3.1 Abstract

Analytical multi-scale models are presented for the evolution of microstructure, sintering and deformation of columnar EB-PVD thermal barrier coatings. Studies are presented of the sintering of a coating constrained by a rigid substrate. It is demonstrated that the sintering process can become unstable when the in-plane stiffness exceeds a critical value. Imperfections in the coating can develop into cracks, which propagate through the thickness of the coating, creating a pattern of "mud cracks". The computational simulations discussed in the previous chapter have motivated the development of simplified models of this process which describe the sintering response and the development of mud cracks in terms of the evolution of a small number of degrees of freedom. These simple models capture the major features of the more detailed computational simulations presented in the previous chapter. They also allow the conditions under which imperfections grow into cracks to be readily identified and predict a density of mud cracks that is consistent with experimental observations.

3.2 Problem description

In this chapter we focus on the sintering response of an EB-PVD top coat and examine the conditions under which inter columnar cracks can develop within the coat-

ing. Hutchinson et al.[42] have recently developed a micromechanical model for constrained sintering of EB-PVD TBCs and modelled the growth of tunneling cracks in the coating by a cleavage mechanism . Here we explore an alternative mechanism of crack formation, which arises from instabilities in the sintering process. The FE simulations presented in the previous chapter guide us to develop 2DOF and 3DOF Rayleigh-Ritz models, which capture the physics of the growth of imperfections, and identify the conditions under which they develop into cracks. Use of 2DOF simpler model allows a wide range of geometric and material conditions to be evaluated and the conditions under which cracking occurs to be identified, but these calculations are unable to provide information about the average spacing of the mud cracks. This requires a three state variable model in which we follow the evolution of two families of imperfections.

Initially, we explore the sintering response of a constrained perfect EB-PVD TBC.

Problem A Progressive sintering of an infinite TBC layer of columns upon a half-space, as shown schematically in Fig.2.2a.

Problem B Progressive sintering of a set of columns within a mud-cracked square cluster of size $2R$, as shown schematically in Fig.2.2b.

In order to capture the essential physics of the mud cracking phenomenon in EB-PVD TBCs due to in-service sintering between neighboring columns, the following two models have been developed in this study.

Problem C A model for the evolution of a set of arbitrarily equi-spaced primary imperfections in an infinite TBC layer upon a half-space.

Problem D A model for the evolution of two sets of equi-spaced imperfections in an infinite TBC layer upon a half-space.

In all the problems, the TBC layer is of height H and it is assumed that the TBC film is perfectly bonded to the substrate. The layer contains columns of square cross-section, of dimension $d \times d$, aligned with the in-plane axes (x_1, x_2). The wavelength

of the local roughness between columns is λ. The layer thickness is along the x_3 direction, with the origin located at the bottom of the columnar layer.

3.3 Problem A: Intercolumnar sintering of a constrained film

In the previous chapter, we compared the computational results of sintering of a perfect film with the analytical results to calibrate the computational model. We now develop the analytical model. We assume elastic incompressibility condition of columns of the TBC, ie, Poisson's ratio $\nu = 0.5$, following Hutchinson et al [42]. For this choice of ν, we have simple form of displacement field. For other value of ν, the fields are more complex. The Finite Element calculations of chapter 2 demonstrate that the sintering response of the TBC is not very sensitive to ν. So limiting the analysis to $\nu = 0.5$ allows us to capture the major physical processes, without over complicating the model. The effect of compressibility in context of modelling the growth of nanostructure has been evaluated by Gill and Cocks [89].

The analysis is based on an idealized contact geometry between columns of a TBC as shown in Fig. 3.1. Here, indeed, we reduce the 2DOF (u, w) sintering model of Hutchinson et al. [42] to 1DOF problem by noting that the pore profile angle β of the contact geometry (see Fig. 3.1) quickly settles down to a constant value given by eqn. 2.2. By fixing β, from geometrical arguments, we can express all geometric variables, (l, w, u) in terms of a single unknown b. As sintering proceeds, the contact size $2b$ increases and the height of the the asperity w decreases, while the wavelength λ remains constant. With further sintering, the neck size b, grows until it reaches the limiting value, ie, $b \to \frac{\lambda}{2}$. This is the state at which full densification occurs in the coating. As the columns sinter together, and the in-plane sintering strain, ε_s, evolves, overall strain compatibility with the substrate dictates the build-up of in-plane tensile stress. Note that the uniform macroscopic sintering strain, ε_s is related to the local

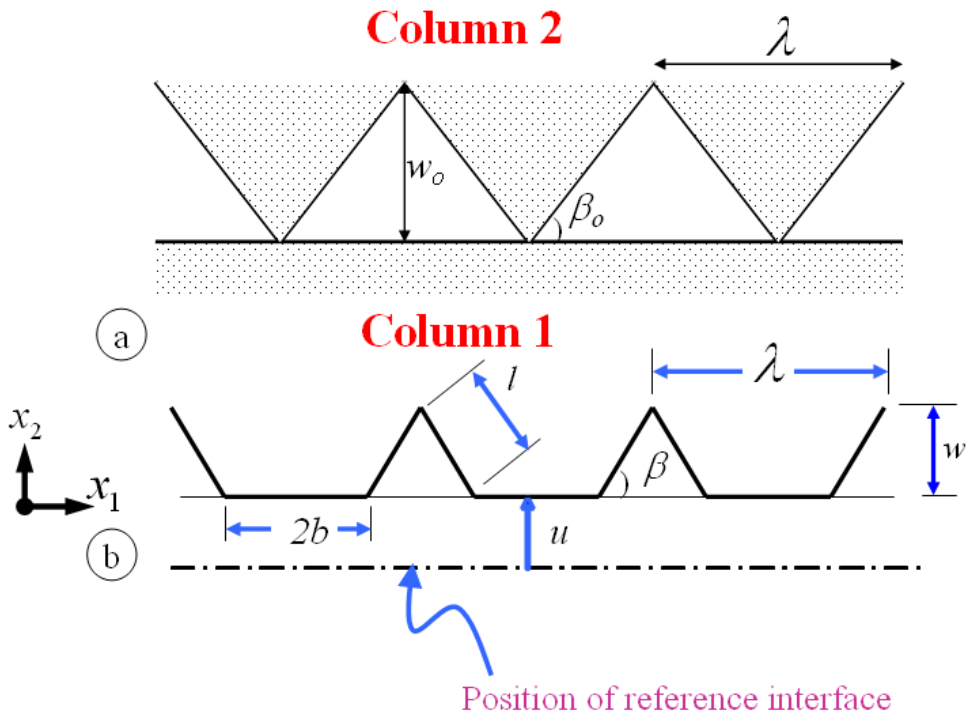

Figure 3.1: Idealisation of surface undulations. a Reference configuration, where sintering strain is zero. b Current configuration, where column 1 has displaced an amount u with respect to column 2 from the reference configuration.

approach of two neighbouring columns by

$$\varepsilon_s = \frac{u_1 - u}{d} \tag{3.1}$$

here, u_1 is the initial value of u after deposition. Consider a RVE of size $d \times d$ and thickness, λ, in the x_3 direction as shown in Fig. 3.2 subjected to an equi-biaxial stress state, σ. Now we can write the Gibbs free energy density in the coating, G as

$$G = \frac{1}{d\lambda}\left\{2b\left(\gamma_g - \gamma_s \sec\beta - \gamma_s\right) + \gamma_s\lambda(\sec\beta + 1) + \sigma\frac{(\lambda^2 - (\lambda - 2b)^2)}{4\cot\beta}\right\} \tag{3.2}$$

We can now differentiate G with respect to time. The resulting expression for $\dot{G}$ is given below in non-dimensional form following the normalisation procedure discussed earlier and also normalising σ such that

$$\bar{\sigma} = \frac{2\sigma\lambda}{\gamma_s} \tag{3.3}$$

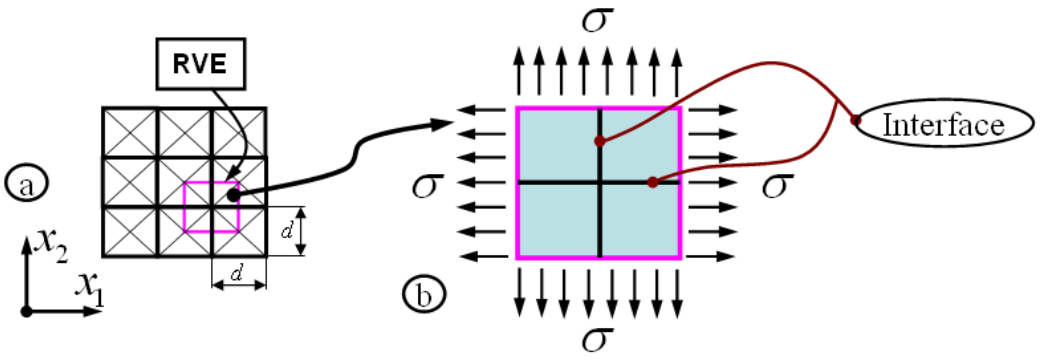

Figure 3.2: a. Array of columns of TBC, each of size $d \times d$. b. A RVE of size $d \times d \times \lambda$ subjected to an equi-biaxial stress state σ.

$$\dot{G} = \frac{1}{\bar{d}}\frac{\gamma_s}{\lambda}\left[2\left(\bar{\gamma}_g - \sec\beta - 1\right) + \frac{\bar{\sigma}}{2\cot\beta}(1-2\bar{b})\right]\dot{\bar{b}} \tag{3.4}$$

We can also write the macroscopic rate potential per unit volume of the TBC as

$$\psi(\dot{b}) = \frac{(\lambda-2b)^2 b^2}{6d\lambda^3 D_g \cot^2\beta\cos\beta}\left[\lambda\cos\beta - \left(\cos\beta - \frac{D_g}{D_s}\right)(\lambda-2b)\right]\dot{b}^2 \tag{3.5}$$

ψ in non-dimensional form is given by

$$\psi(\dot{\bar{b}}) = \frac{(1-2\bar{b})^2\bar{b}^2}{6\bar{d}\bar{D}_g\cot^2\beta\cos\beta}\frac{\lambda^3}{D_s}\left[\cos\beta - \left(\cos\beta - \bar{D}_g\right)(1-2\bar{b})\right]\dot{\bar{b}}^2 \tag{3.6}$$

We make use of the TVP in order to calculate the time evolution of the neck size b. For a given geometry of the TBC columns it is shown below that the rate of evolution of the microstructure is given by the kinematic rate ($\dot{b}$) at any contacts between columns that minimises the functional

$$\Phi(\dot{b}) = \psi(\dot{b}) + \dot{G}(\dot{b}) \tag{3.7}$$

Using $\psi(\dot{\bar{b}})$ given by eqn. 3.6 and $\dot{G}(\dot{b})$ given by the eqn. 3.4 in the above functional and performing variational calculus, we get $\dot{\bar{b}}$

$$\dot{\bar{b}} = -\frac{1}{f(\bar{b})}\left\{\frac{2}{\bar{d}}(\bar{\gamma}_g - \sec\beta - 1) + \frac{\bar{\sigma}}{2\bar{d}\cot\beta}(1-2\bar{b})\right\} \tag{3.8}$$

where, $f(\bar{b})$ is

$$f(\bar{b}) = \frac{(1-2\bar{b})^2\bar{b}^2}{3\bar{d}\bar{D}_g\cot^2\beta\cos\beta}\left[\cos\beta - \left(\cos\beta - \bar{D}_g\right)(1-2\bar{b})\right] \tag{3.9}$$

Note that the non-dimensional time scale $\bar{t}$ turns out to be the same as given by eqn. 2.19. The value of $\dot{\bar{b}}$ given by eqn. 3.8 can be cast in the following form

$$\dot{\bar{b}} = \; f_1(\bar{b}) \left[\bar{\sigma}_s(\bar{b}) - \bar{\sigma}\right] \tag{3.10}$$

In the above equation, $\bar{\sigma}_s(\bar{b})$ is the sintering potential and is given by

$$\bar{\sigma}_s(\bar{b}) = \; - \frac{4 \cot\beta(\bar{\gamma}_g - \sec\beta - 1)}{(1 - 2\bar{b})} \tag{3.11}$$

In order to assess the sintering response of a coating, we can compare the sintering potential with the in-plane stress generated in the coating for different choices of modulus of the coating. We now determine the in-plane stress generated in the coating. The total strain at any position in the plane of the TBC is zero.

$$\varepsilon^e + \varepsilon^T + \varepsilon^s = 0 \tag{3.12}$$

Here, ε^e is the elastic strain in the x_1 or x_2 direction, ε^s is the sintering strain given by eqn. 3.1 and ε^T is the thermal mismatch strain. Noting that ε^T is constant and differentiating the above equation with respect to time we get

$$\dot{\varepsilon}^e + \dot{\varepsilon}^s = 0 \tag{3.13}$$

$\dot{\varepsilon}^e$ is the elastic strain rate and $\dot{\varepsilon}^s$ is the sintering strain rate. The elastic strain in the repeating cell (see Fig. 3.2) subjected an equi-biaxial stress state σ, is

$$\varepsilon^e = \frac{\bar{\sigma}}{2\bar{E}} \tag{3.14}$$

Note that the elastic field ε^e, is uniform in the coating. We can get $\dot{\varepsilon}^e$ by differentiating ε^e given by eqn. 3.14 and $\dot{\varepsilon}^s$ by differentiating ε^s given by eqn. 3.1.

$$\dot{\varepsilon}^e = \frac{1}{2}\frac{\dot{\bar{\sigma}}}{\bar{E}}; \qquad \dot{\varepsilon}^s = -\frac{\dot{\bar{u}}}{\bar{d}}; \tag{3.15}$$

Note that $\bar{E}$ of the coating is assumed to be constant during sintering. However, it evolves during the sintering process. The change of coating stiffness is included in the subsequent studies presented in chapters 4 and 5. From geometry we can write

$$u = \frac{\lambda^2 - (\lambda - 2b)^2}{4\lambda \cot\beta} \tag{3.16}$$

Non-dimensionaling the above and differentiating with respect to time we get $\dot{\bar{u}}$ and using this in $\dot{\varepsilon}^s$, we have

$$\dot{\varepsilon}^s = -\frac{(1-2\bar{b})}{\bar{d}\cot\beta}\dot{\bar{b}} \tag{3.17}$$

Substituting $\dot{\varepsilon}^e$ given by eqn. 3.15 and $\dot{\varepsilon}^s$ given by eqn. 3.17 into eqn. 3.13, we get $\dot{\bar{\sigma}}$ as

$$\dot{\bar{\sigma}} = \frac{2\bar{E}(1-2\bar{b})}{\bar{d}\cot\beta}\dot{\bar{b}} \tag{3.18}$$

The $\dot{\bar{b}}$ given by eqn. 3.8 and $\dot{\bar{\sigma}}$ given by eqn. 3.18 can be together integrated forward to obtain the evolution $\bar{b}$ and $\bar{\sigma}$ noting the initial conditions ($\bar{\sigma} = 0$ at $\bar{t} = 0$ and $\bar{b} = \bar{b}_1(\bar{u}_1)$ at $\bar{t} = 0$). In the simulations presented here, we assume $\bar{d}$=20, $\bar{\gamma}_g$=0.68 and $\bar{D}_g$=1 unless otherwise stated. For the initial choice of u in non-dimensional form $\bar{u}_1 = 0.05$, two types of behaviour are observed, depending upon the magnitude of effective modulus of the TBC ($\bar{E}$). The evolution of surface profile and the sintering strain are plotted (solid lines) in Fig. 3.3, for $\bar{E} = 500$ for this 1DOF problem for vanishing thermal strain ($\varepsilon^T = 0$). Full sintering occurs over a finite time scale. It means that the the neck size $\bar{b}$ reaches 0.5 and the magnitude of the sintering strain ε^s increases to a saturated finite value (-1.3%) with increasing time. We have also analysed the 2DOF (u, w) model of Hutchinson et al [42] with initial conditions ($\frac{u_1}{\lambda} = 0.05, \frac{w_1}{\lambda} = 0.5615$ with $\bar{w}_0 = 1/2\tan(\beta)$. Here, β is the equilibrium pore profile angle given by eqn. 2.2 and $\bar{w}_1$ is same as in 1DOF problem. The results of the 2DOF model are also shown in Fig. 3.3 in dotted lines, for the same $\bar{E}$ (500). It can be seen from Fig. 3.3 that both the models predict full sintering of the coating for $\bar{E} = 500$ and the terminal state is the same. Note from the results of 2DOF problem that the roughness amplitude $\bar{w}$ decreases monotonically to zero and the pore profile angle β (see Fig. 3.1) quickly settles down to a constant value as the void shrinks.

For sufficiently large values of $\bar{E}$, say 1000, the build-up of elastic strain energy within the TBC layer prevents the later stages of sintering, and the neck size $\bar{b}$ asymptotes to a value of less than 0.5 as shown in Fig. 3.4. As a result, the asymptotic value of sintering strain does not attain the limiting value of (-1.3%). Again, the results of the 2DOF model are shown in dotted lines. Note that the early stages of

the sintering response are qualitatively similar for the choices $\bar{E} = 500$ and 1000, with the equilibration of pore profile angle β. However, the higher modulus leads to an arrest of the sintering process prior to full densification. If the magnitude of this tensile stress is sufficiently large it may lead to inter-columnar mud-cracking. The

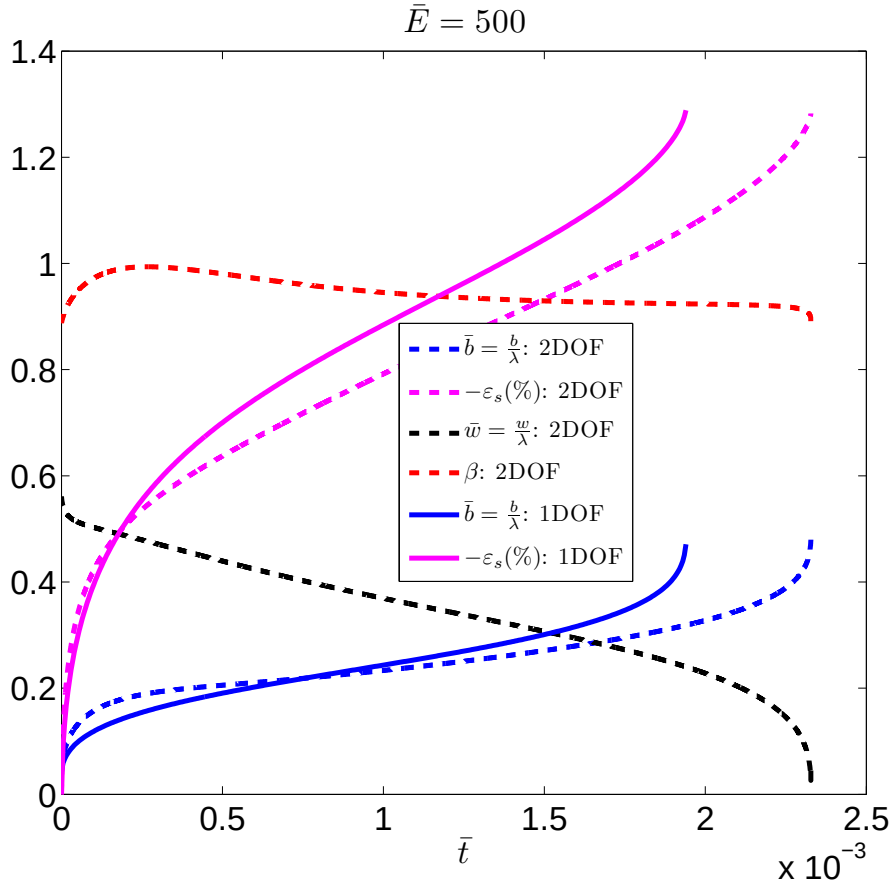

Figure 3.3: Perfect film: Evolution of contact geometry and sintering strain (%) for $\bar{E} = 500$. The inclination β is in radians. $\bar{t}$ is non-dimensional time.

sintering potential of this coating, $\bar{\sigma}_s$ is shown in Fig. 3.5 as a function of neck size, $\bar{b}$. Note that $\bar{\sigma}_s$ monotonically increases with the increase of contact size, $\bar{b}$ and is maximum at the point of full densification of the coating ($\bar{b} = 0.5$). The sintering potential is compared with the stress generated in the coating for different choices of $\bar{E}$ as shown in Fig. 3.6 for a given initial neck size, $\bar{b}_1 = 0.0425(\bar{u}_1 = 0.05)$. It can be seen from this figure that for the choice of $\bar{E} = 500$, $\sigma < \sigma_s$ throughout and therefore

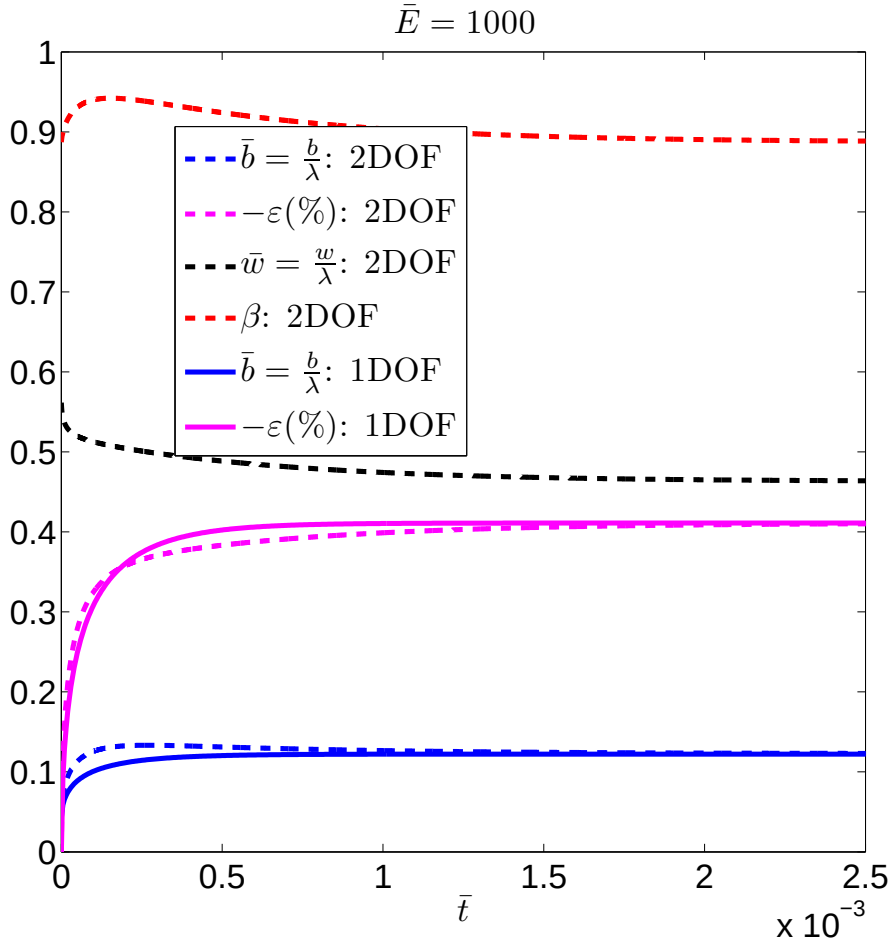

Figure 3.4: Perfect film: Evolution of contact geometry and sintering strain (%) for $\bar{E} = 1000$. The inclination β is in radians. $\bar{t}$ is non-dimensional time.

full sintering occurs in the coating as shown in Fig 3.3. On the contrary, for higher modulus of the coating, say $\bar{E} = 1000$, σ reaches the value of sintering potential early during the sintering process and therefore sintering gets arrested as shown in Fig. 3.4. It has also been observed that the for a fixed $\bar{E}$, sintering gets arrested earlier for smaller initial neck size $\bar{b}_1$. The approach adopted here is slightly different to that employed by Hutchinson et al [42]. When determining the Gibbs free energy they consider directly the problem of a constrained film and instead of considering the potential energy of an applied stress or traction, they express the Gibbs free energy in terms of elastic stored energy at zero net displacement of the boundary of the RVE.

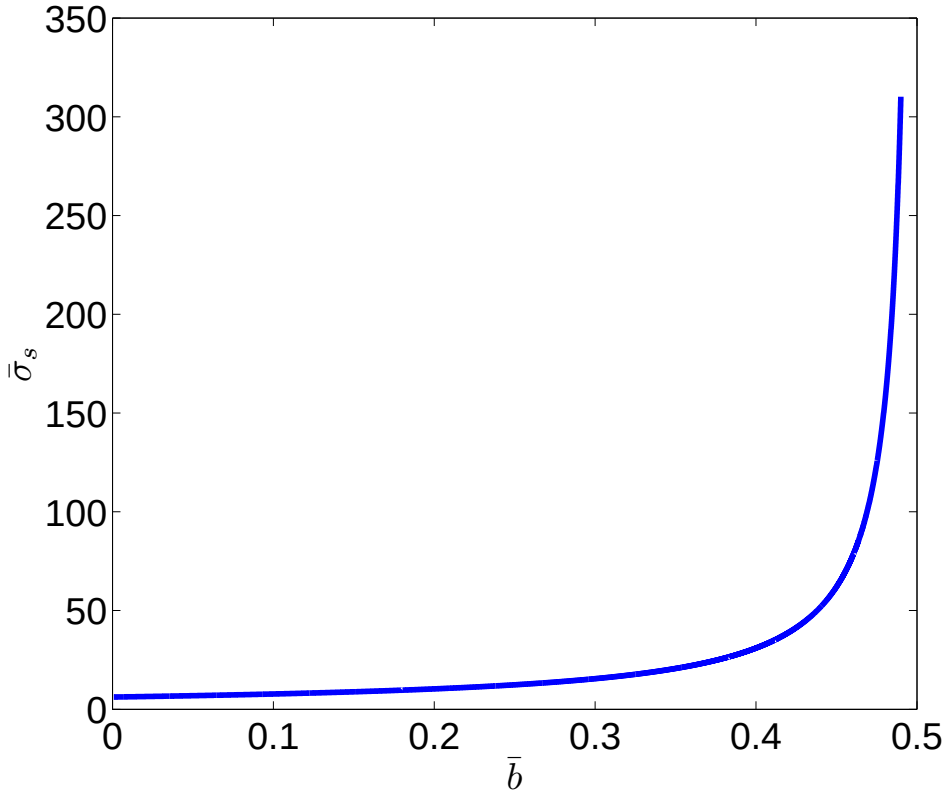

Figure 3.5: Sintering potential of the EB-PVD coating with the trapezoidal contacts as a function of the contact size, $\bar{b}$.

In this case, Gibbs energy density takes the form

$$G = \frac{2}{d\lambda}\left\{2b\left(\gamma_g - \gamma_s \sec\beta - \gamma_s\right) + \gamma_s\lambda(\sec\beta + 1)\right\} + 2E(\varepsilon^s)^2 \tag{3.19}$$

Differentiating G given by eqn. 3.19 with respect to time, we get rate of Gibbs free energy density in the perfect film

$$\dot{G} = \frac{2}{d\lambda}\left\{2\dot{b}\left(\gamma_g - \gamma_s \sec\beta - \gamma_s\right)\right\} + 4E\varepsilon^s\dot{\varepsilon}^s \tag{3.20}$$

Noting that

$$\sigma = -2E\varepsilon^s; \qquad \dot{\varepsilon}^s = -\frac{\dot{b}(\lambda - 2b)}{d\lambda\cot\beta}; \tag{3.21}$$

the expression for rate of Gibbs free energy density in normalised form turns out to be the same form of eqn. 3.4.

$$\dot{G} = \frac{2}{\bar{d}}\frac{\gamma_s}{\lambda}\left[2\left(\bar{\gamma}_g - \sec\beta - 1\right) + \frac{\bar{\sigma}}{2\cot\beta}(1 - 2\bar{b})\right]\dot{\bar{b}} \tag{3.22}$$

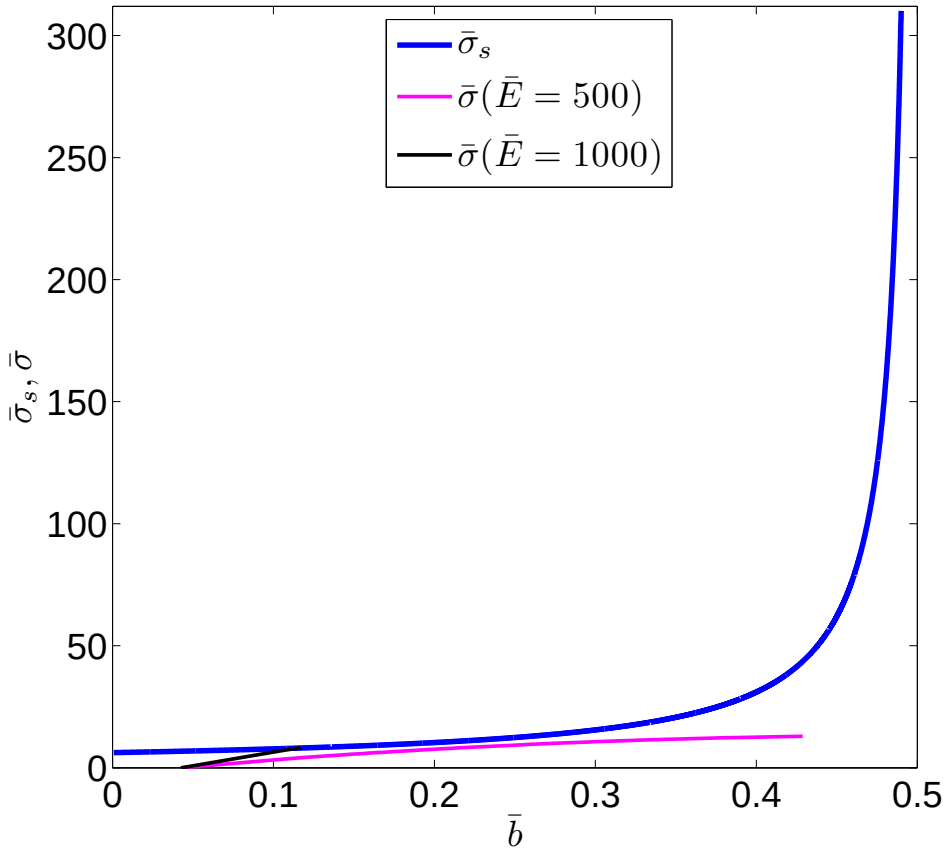

Figure 3.6: Sintering potential, $\bar{\sigma}_s$ and the in-plane stress $\bar{\sigma}$ generated in the coating as a function of the contact size, $\bar{b}$ for different choices of $\bar{E}$.

Therefore, in the subsequent sections, we follow the later approach to express G in terms of the elastic stored energy in order to develop Raleigh-Ritz type models.

3.4 Problem B: Sintering within a mud-cracked layer

Following the analysis of Hutchinson et al. [42], we have modelled the progressive sintering of a set of columns in a mud-cracked TBC layer under isothermal conditions. We assume that a fully developed mud-cracking pattern has been developed, with TBC columns grouped into a square arrangement of clusters as shown in Figs. 2.2

and 3.7. The cluster is of size $2R \times 2R \times H$. The only difference here is that we assume

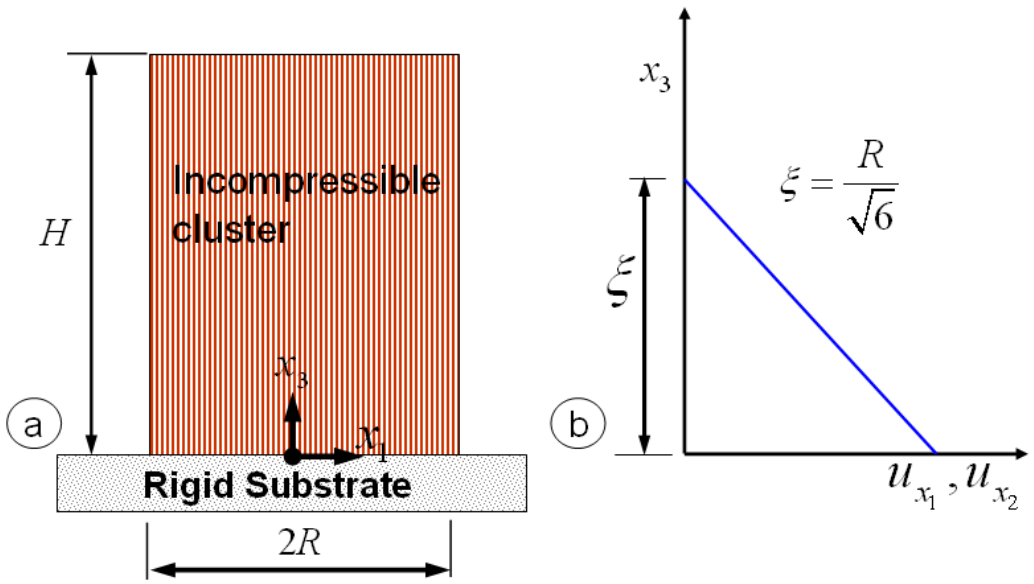

Figure 3.7: a. Mud-cracked incompressible square cluster of size $2R \times 2R \times H$ on a rigid substrate. b. In-plane elastic deformation of the cluster over height ξ.

square clusters instead of cylindrical clusters and therefore the elastic stored energy changes. The elastic strain energy density in the square cluster U_{sq} is estimated by assuming that the cluster is given a uniform in-plane, stress-free transformation strain of ε_s, with full constraint against in-plane motion imposed along the bottom surface, $x_3 = 0$. An Eshelby-type cut-and-paste procedure implies that the elastic component of in-plane displacements at the base of the column, $x_3 = 0$, are

$$u_{x_1} = -\varepsilon_s \, x_1 \tag{3.23}$$

$$u_{x_2} = -\varepsilon_s \, x_2 \tag{3.24}$$

where x_1 and x_2 are the in-plane co-ordinates from the centreline of the cluster. In order to estimate the stored elastic strain energy in the cluster it is envisaged that elastic straining occurs over a height ξ of the TBC coating from the rigid substrate. A simple kinematically admissible displacement field is assumed within the cluster which satisfies the boundary condition shown in Fig. 3.7.

$$u_{x_1}(x_1, x_3) = \begin{cases} -\varepsilon_s \left(1 - \frac{x_3}{\xi}\right) x_1 & \text{if} \quad 0 \leq x_3 \leq \xi; \\ 0 & \text{if} \quad \xi < x_3 \leq H. \end{cases}$$

and

$$u_{x_2}(x_2, x_3) = \begin{cases} -\varepsilon_s \left(1 - \frac{x_3}{\xi}\right) x_2 & \text{if} \quad 0 \leq x_3 \leq \xi; \\ 0 & \text{if} \quad \xi < x_3 \leq H. \end{cases}$$

The elastic displacement in the x_3 direction is obtained using the elastic incompressibility condition ($\varepsilon^e_{kk} = 0$).

$$u_{x_3}(x_3) = \begin{cases} \varepsilon_s \left(2x_3 - \frac{(x_3)^2}{\xi}\right) & \text{if} \quad 0 \leq x_3 \leq \xi; \\ \varepsilon_s \, \xi & \text{if} \quad \xi < x_3 \leq H. \end{cases}$$

The elastic stored energy in the square cluster is given by

$$U_C = \frac{8}{3} E R^2 \left(\varepsilon_s + \varepsilon_T\right)^2 \left(\xi + \frac{R^2}{6\xi}\right) \tag{3.25}$$

The optimal height $\xi = \frac{R}{\sqrt{6}}$, and therefore the elastic stored energy density in the mud-cracked TBC is given by

$$U_{sq} = \frac{4}{3\sqrt{6}} E \left(\frac{R}{H}\right) \left(\varepsilon_s + \varepsilon_T\right)^2 \tag{3.26}$$

Now this local sintering between columns within a cluster is same as that of the perfect TBC, and can be described in terms of rate of state variable $\dot{b}$. We analysed this problem for $\bar{E} = 1000$ using the same initial condition and found that the reduced elastic constraint of the mud-cracked layer leads to full sintering between columns in a relatively short time, whereas sintering is switched-off in the perfect TBC layer for the same $\bar{E}$. Having analyzed the aforementioned problems, naturally these questions arise: how do mud-cracks evolve or form in TBCs? and what is their average spacing? We address these questions in the following sections.

3.5 Problem C: Modelling evolution of primary imperfections

The simulations presented in the previous chapter provide insight into situations where mud cracking might occur in practice, but in order to map out the role of the

different geometric and material parameters it would be necessary to undertake a wide range of computer simulations. The ability of the simplified model developed by Hutchinson et al. [42] in simulating the response of an isolated cluster as described above motivates us to develop a model with a similar degree of complexity for the growth of imperfections. The simulations presented in the last chapter will allow us to assess the validity of any assumptions made in the model.

In this section we develop a two state variable Rayleigh-Ritz type model. It can be observed from the micrograph of mud cracked TBC film (see Fig. 3.8) that mud cracked islands are equiaxed, e.g. hexagonal or square. We therefore idealise the structure of a TBC as an assembly of square clusters of square columns as shown schematically in Fig. 3.8. Imperfections exist along the boundary of the clusters, which initially have slightly different contact conditions than the within cluster. Some or all of these imperfections grow during in-service sintering of the TBC, depending upon geometric and material properties of the coating, and can potentially lead to mud cracking of the TBC. A representative repeating cell is chosen that has a primary imperfection within it as shown in Fig. 3.8. For the computational studies the imperfection extended throughout a continuum element. Within the model developed in this chapter we assume that the defect exists along a single line of contacts between adjacent columns. This is a more realistic assumption. Isothermal conditions are imposed within the repeating cell which may be greater than or less than the deposition temperature T_D. Though TBCs experience thermal cycling under service conditions, isothermal experiments with T independent of location x_3 and of time t are not uncommon in accelerated testing [42]. The objective is to determine the time evolution of the sintering of clusters and primary imperfections and to determine under what condition a fully developed crack forms due to the imposed thermal mismatch associated with T. The restraint of the substrate is included in the analysis.

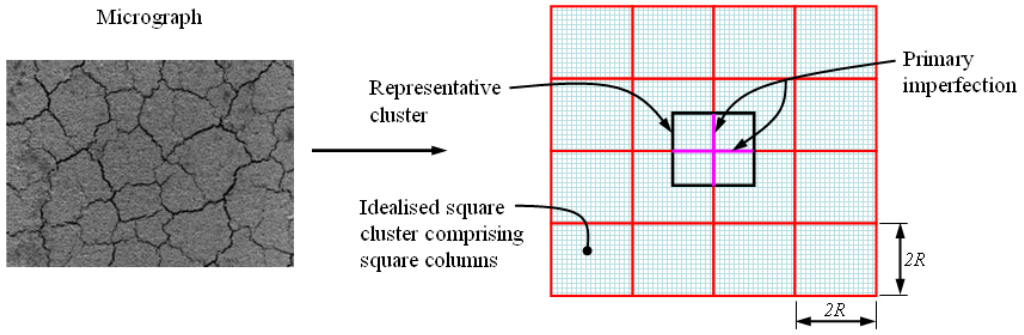

Figure 3.8: Idealisation of mud-cracked TBC as a assembly of square clusters of dimension $2R \times 2R$ with a regular, equi-spaced distribution of primary imperfections.

3.5.1 Global considerations

The idealised square clusters with an imperfection can be regarded as a continuum with an in-plane isotropic thermal expansion mismatch strain $\varepsilon^T_{ij} = \varepsilon^T \delta_{ij}$ relative to the underlying substrate, where i and j independently range over 1,2. Here, δ_{ij} is the usual two-dimensional Kronecker delta symbol and the thermal expansion mismatch strain ε^T is given by

$$\varepsilon^T \;=\; \alpha_c \left[T - T_D\right] - \alpha_s \left[T - T_D\right] \tag{3.27}$$

where, α_c and α_s are the coefficients of thermal expansion of the TBC and substrate, respectively. The deposition temperature T_D is taken as the reference temperature and defines the initial stress-free condition of the TBC. As inter-columnar sintering proceeds, an equi-biaxial sintering strain ε^s_{ij} evolves with time. $\varepsilon^s_{ij} = \varepsilon^s \delta_{ij}$,where i and j independently range over 1,2. Following Hutchinson et al [42] we assume that the sintering strain is uniform within the cluster. ε^s_{ij} can be conveniently split into two fields, one analogous to progressive sintering of columns in a perfect constrained TBC film with sintering strain ε^1_s and thermal mismatch strain ε^T and the other corresponding to intercolumnar sintering of an isolated cluster with sintering strain ε^2_s as shown in Fig. 3.9.

$$\varepsilon^s \;=\; \varepsilon^1_s + \varepsilon^2_s \tag{3.28}$$

A thermodynamic variational approach is employed here in order to calculate

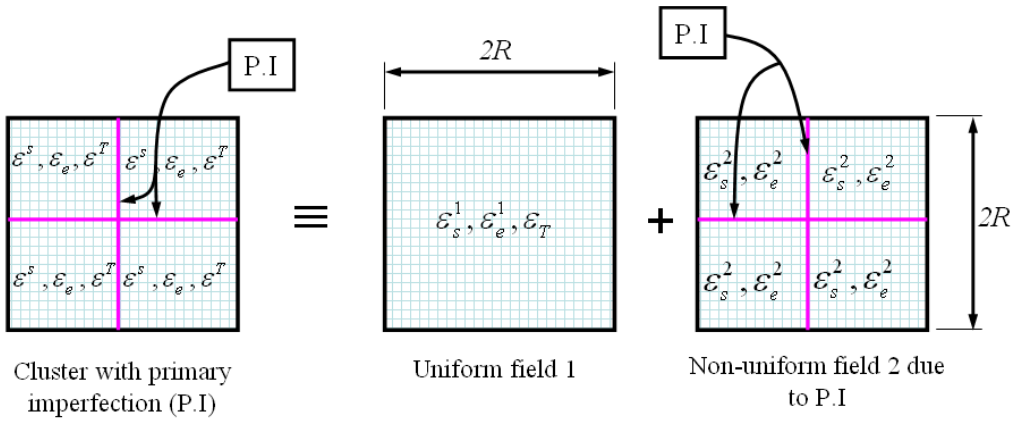

Figure 3.9: Decomposition of fields in the square cluster with primary imperfection. Field 1: analogous to progressive sintering of columns in a perfect constrained TBC film with sintering strain ε_s^1 and thermal mismatch strain ε^T and Field 2: Corresponding to intercolumnar sintering of an isolated cluster with sintering strain ε_s^2.

the time evolution of ε_s^1 and ε_s^2 based upon an assumed contact geometry between neighboring TBC columns within a cluster (see Fig. 3.10b) and at the primary imperfections as shown in Fig.3.10c. The subscripts $'cl'$ and $'cr'$ characterise the geometric parameters within cluster and imperfection respectively. The substrate is taken to be much thicker than the TBC layer, such that the in-plane strain in the TBC layer relative to the substrate is zero. Consequently, the elastic strain $\varepsilon_{ij}^e(x_3)$ in field 1 of the cluster is uniform as illustrated in Fig. 3.13a and is given by

$$\varepsilon_{ij}^{e_1} = -\left(\varepsilon_{ij}^T + \varepsilon_{ij}^{s1}\right) \tag{3.29}$$

In field 2 of the cluster, we consider elastic constraint of the substrate up to height ξ in the x_3 direction from the substrate (see Fig. 3.13b). The following compatibility condition needs to be satisfied in field 2. The detailed form of field 2 is given later.

$$\left(\varepsilon_{ij}^{e_2}(x_3) + \varepsilon_{ij}^{s_2}\right) 2R - \Delta u_s(x_3) = 0 \tag{3.30}$$

Here, $\Delta u_s(x_3)$ is the net displacement across the primary imperfection. The elastic field exists and varies in the bottom portion of a cluster. The elastic constraint of the substrate alters the local contact condition along the primary imperfection.

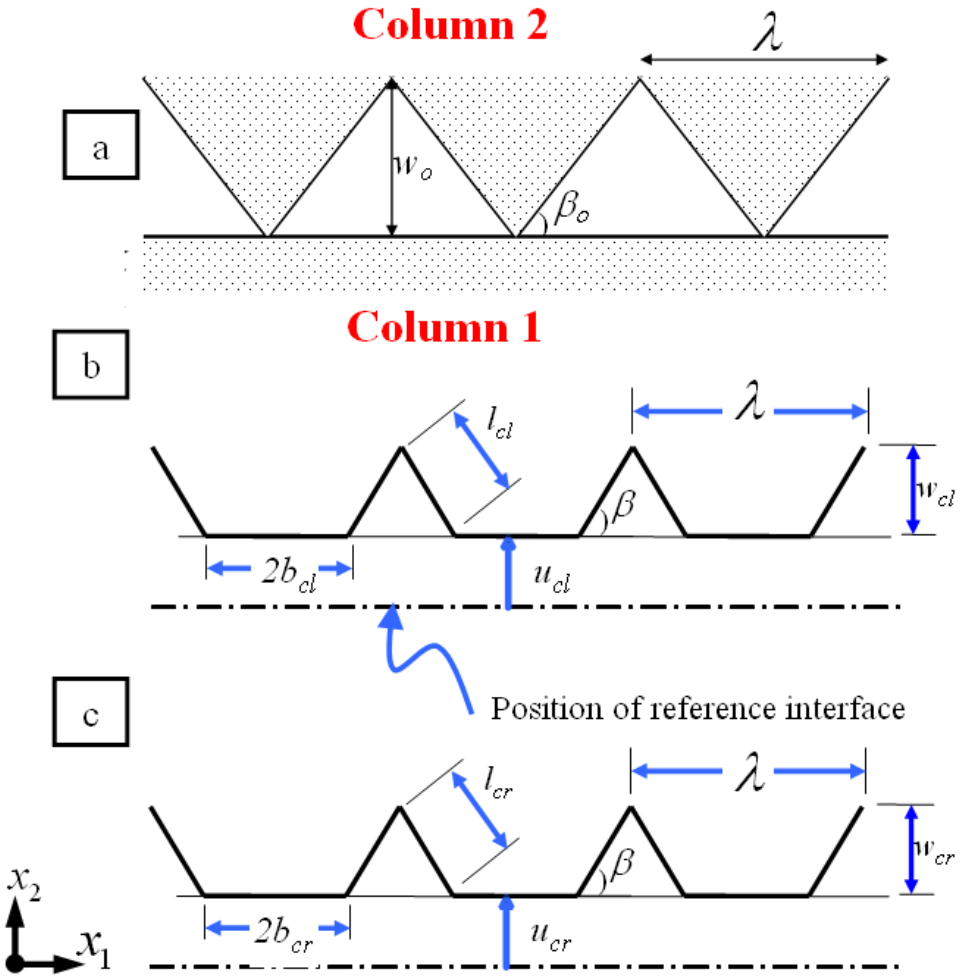

Figure 3.10: Idealisation of surface undulations. a. Reference configuration b. Current configuration, where column 1 has displaced an amount u_{cl} with respect to column 2 from the reference configuration. c. Current configuration at a primary imperfection (defect), where column 1 has displaced an amount u_{cr} with respect to column 2.

3.5.2 Local considerations

Contact geometry

The undulation of both surfaces at contacts is combined into a single wavy surface of saw tooth profile while the other surface is treated as perfectly flat. The idealised contact geometry is shown in Fig. 3.10. The reference configuration is given

in Fig. 3.10a. The geometry at a typical instant between columns within a cluster can be characterised by the geometric parameters (u_{cl}, w_{cl}) as shown in Fig. 3.10b. Similarly, the geometry at a typical instant between columns along an imperfection can be characterized by the geometrical parameters (u_{cr}, w_{cr}) as shown in Fig. 3.10c. This simplification of contact geometry allows us to reduce the number of independent geometric variables and to formulate an analytical micromechanical model for the evolution of contact geometry in the clusters and along the imperfections. As sintering proceeds, the contact widths $2b_{cl}$ and $2b_{cr}$ increase and the combined peak-to-peak amplitude of the undulations w_{cl} and w_{cr} decrease, while the wavelength λ remains the same.

The objective of the problem is to solve for the local evolution of surface profile within the repeating cluster as characterized by (u_{cl}, w_{cl}) and (u_{cr}, w_{cr}). Interfacial diffusion is driven by the combined driving forces of the net reduction in interfacial energy, and the bulk elastic strain energy of the TBC. Now, we have four primary unknowns, two (u_{cl}, w_{cl}) within cluster and the other two (u_{cr}, w_{cr}) at the imperfection. The geometric variables associated with the columns within the cluster and that associated with the imperfection are depicted in Fig. 3.11a and Fig. 3.11b respectively. In problems A and B, it has been observed from numerical simulations over a wide range of parameters that the pore profile angle β quickly settles down to a constant value. Adopting, the equilibrium pore profile angle β [42], for the contact geometries both at the imperfection and elsewhere in the cluster, we can express all variables along the imperfection as a function of u_{cr} and that in the cluster as a function of u_{cl}. As a result, we have only two independent variables (u_{cr}, u_{cl}). Considering constancy of volume of the contacting asperities, we can express w_{cr}, b_{cr} and l_{cr} as functions of u_{cr} as

$$b_{cr} = \frac{\lambda}{2} - \frac{1}{2}\sqrt{\lambda^2 - 4\lambda u_{cr}\cot\beta};\;\; w_{cr} = \frac{\tan\beta}{2}\sqrt{\lambda^2 - 4\lambda u_{cr}\cot\beta};\;\; l_{cr} = \frac{\sec\beta}{2}\sqrt{\lambda^2 - 4\lambda u_{cr}\cot\beta} \tag{3.31}$$

The incompressibility condition between columns within the cluster give similar expressions for w_{cl}, b_{cl} and l_{cl} as functions of u_{cl}.

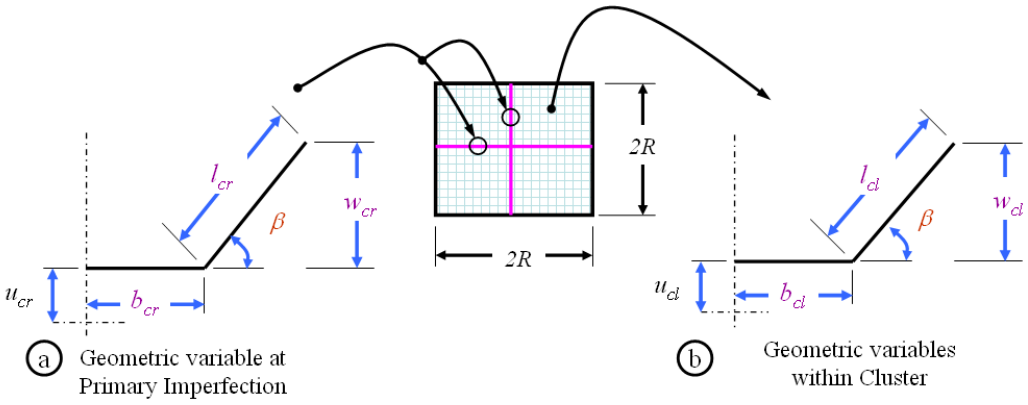

Figure 3.11: Geometric variables associated with local contacts between columns. a. Geometric variables at interfaces between columns within cluster. b. Geometric variables at interfaces between columns on primary imperfection.

3.5.3 Geometric coupling between local and global scales

The macroscopic sintering strain in field 1, ε_s^1 and in field 2, ε_s^2 are expressed in terms of the state variables with their appropriate initial guesses. The sintering strains in both fields are uniform over the entire cluster. Following Hutchinson et al [42], we assume a kinematically admissible in-plane elastic deformation field that is compatible with ε_s^2. This deformation field varies linearly with height up to $x_3 = \xi$. This gives rise to a displacement across the primary imperfection (see Fig. 3.13).

$$\Delta u_s(x_3) = \begin{cases} 2R\varepsilon_s^2 \frac{x_3}{\xi} & \text{if} \quad 0 \le x_3 \le \xi; \\ 2R\varepsilon_s^2 & \text{if} \quad \xi \le x_3 \le H. \end{cases}$$

The primary unknown at contacts within cluster u_{cl} can be expressed as

$$u_{cl} \;=\; u_1 - \left(\varepsilon_s^1 + \varepsilon_s^2\right) d \tag{3.32}$$

The local approach at the primary imperfection is given by

$$u_{cr}(x_3) \;=\; u_1^{cr} - \left(\varepsilon_s^1 + \varepsilon_s^2\right) d + \Delta u_s(x_3) \tag{3.33}$$

$u_{cr}(x_3)$ at $x_3 = \xi$ is u_{cr}, which is defined as the state variable associated with the imperfection. Now manipulating the resulting expression for u_{cr} with u_{cl} given by eqn. 3.32, we can express the sintering strains in the two fields as functions of two

state variables (u_{cr}, u_{cl}) as follows

$$\varepsilon_s^1 = \frac{u_1 - u_{cl}}{d} - \left[\frac{(u_{cr} - u_1^{cr}) - (u_{cl} - u_1)}{2R}\right] \tag{3.34}$$

and

$$\varepsilon_s^2 = \left[\frac{(u_{cr} - u_1^{cr}) - (u_{cl} - u_1)}{2R}\right] \tag{3.35}$$

Note that u_1 and u_1^{cr} are the initial values of the kinematic variables u_{cl} and u_{cr} respectively created soon after deposition.

3.5.4 Thermodynamic variational principle(TVP)

In this problem, we focus on the local sintering between contacting columns, both at the primary imperfection and within the clusters, on a length scale λ (less than 1 μm)and neglect the much slower diffusion over larger length scales of the order of the column size d (5−10 μm) and column height H (100−200 μm). Consequently, we can solve for the evolution of the sintering strains $\varepsilon_s^1(t)$ and $\varepsilon_s^2(t)$ in field 1 and field 2 respectively under fixed T. Our task now is to solve for the time evolution of geometric variables (u_{cr}, u_{cl}) between adjacent TBC columns under a uniform temperature T.

To solve this local sintering problem in a cluster with an imperfection, the thermodynamic variational principle of Cocks et al. [45] is used to obtain the time evolution of (u_{cr}, u_{cl}) and this requires a knowledge of the Gibbs free energy density of coating G, and density of the rate potential ψ arising from the local flux of matter at contacts. Gibbs free energy is derived as an explicit function of state variables (u_{cr}, u_{cl}) and used below. The rate potential ψ is a quadratic functional of the diffusion flux, and can be re-expressed as an explicit quadratic function of the rates of kinematic variables $(\dot{u}_{cr}, \dot{u}_{cl})$.

For a given geometry of TBC clusters and initial microstructure described by (u_1^{cr}, u_1), the rate of evolution of the microstructure is given by the set of kinematic rates $(\dot{u}_{cr}, \dot{u}_{cl})$ that minimise the functional Φ.

$$\Phi(\dot{u}_{cr}, \dot{u}_{cl}) = \dot{G}(\dot{u}_{cr}, \dot{u}_{cl}) + \psi(\dot{u}_{cr}, \dot{u}_{cl}) \tag{3.36}$$

The optimal choice for $(\dot{u}_{cr}, \dot{u}_{cl})$ is obtained by rendering the functional Φ stationary

$$\delta\Phi(\dot{u}_{cr}, \dot{u}_{cl}) \ = 0 \tag{3.37}$$

for arbitrary variations in $(\dot{u}_{cr}, \dot{u}_{cl})$. This gives a set of following simultaneous equations.

$$\frac{\partial \dot{G}}{\partial \dot{u}_{cr}} + \frac{\partial \psi}{\partial \dot{u}_{cr}} \ = \ 0 \tag{3.38}$$

and

$$\frac{\partial \dot{G}}{\partial \dot{u}_{cl}} + \frac{\partial \psi}{\partial \dot{u}_{cl}} \ = \ 0 \tag{3.39}$$

Here $\dot{G}$ is linear and ψ is quadratic in the rates $(\dot{u}_{cr}, \dot{u}_{cl})$. Hence, this set of equations can be cast in matrix form as

$$\begin{bmatrix} \frac{\partial^2 \psi}{\partial \dot{u}_{cr}^2} & \frac{\partial^2 \psi}{\partial \dot{u}_{cr} \partial \dot{u}_{cl}} \\ \frac{\partial^2 \psi}{\partial \dot{u}_{cr} \partial \dot{u}_{cl}} & \frac{\partial^2 \psi}{\partial \dot{u}_{cl}^2} \end{bmatrix} \begin{bmatrix} \dot{u}_{cr} \\ \dot{u}_{cl} \end{bmatrix} = - \begin{bmatrix} \frac{\partial \dot{G}}{\partial \dot{u}_{cr}} \\ \frac{\partial \dot{G}}{\partial \dot{u}_{cl}} \end{bmatrix}$$

This matrix can be inverted algebraically to obtain $(\dot{u}_{cr}, \dot{u}_{cl})$ as a function of the current state (u_{cr}, u_{cl}). The time evolution of (u_{cr}, u_{cl}) follows by time integration of a set of nonlinear ODEs using either a forward Euler or a fourth-order Runge-Kutta (R-K4) method.

3.6 Evolution of imperfection in two kinematic variable system

3.6.1 Determination of Gibbs free energy

The Gibbs free energy has contributions from the interfacial free energy and elastic stored energy and is given by

$$G \ = \ G_\lambda + U \tag{3.40}$$

where, G is the Gibbs free energy density, G_λ is the interfacial energy density and U is the elastic strain energy density of the TBC.

Determination of interface free energy

We will now determine the interface energy density of the the TBC. The interfacial energy of the TBC has contributions from bulk contacts associated with u_{cl} within a cluster, and contacts associated with the primary imperfection u_{cr}. Let G_λ^{cl} be the interface energy density associated with bulk contact and G_λ^{cr} be the interface energy density associated with primary imperfection of the TBC. Thus G_λ of the TBC becomes

$$G_\lambda \;=\; G_\lambda^{cl} + G_\lambda^{cr} \tag{3.41}$$

It can be seen from Fig. 3.13.b that the local contact at the primary imperfection characterized by u_{cr} is not uniform over the entire height of the cluster. The value of u_{cr} varies linearly with x_3 from the substrate up to a height ξ and remains constant thereafter over the rest of the TBC height.

$$u_{cr} = \begin{cases} u_{cr}^b = (u_1^{cr} - u_1 + u_{cl})\left(1 - \frac{z}{\xi}\right) + u_{cr}\ \frac{z}{\xi} & \text{if} \quad 0 \le z \le \xi; \\ u_{cr}^t = u_{cr} & \text{if} \quad \xi \le z \le H. \end{cases}$$

Accordingly, G_λ^{cr} is the sum of the interface energy density associated with the linearly varying contact displacement $u_{cr}(x_3)$ in the bottom portion of cluster and that associated with uniform displacement u_{cr} in the top portion of cluster. G_λ^{cr} now becomes

$$G_\lambda^{cr} \;=\; \int_0^\xi G_\lambda^{cr^b}\, dx_3 + G_\lambda^{cr^t} \tag{3.42}$$

Considering a slice of thickness λ of the repeating cell of size $2R \times 2R$ in the x_3 direction as shown in Fig. 3.12.a and a typical contact geometry over its thickness λ as shown in Fig. 3.12b, the interfacial energy density associated with bulk contact G_λ^{cl} of the entire cluster can be written in terms of the surface energy γ_s and interfacial energy at the contacts γ_g (see Fig.3.12b) as

$$G_\lambda^{cl} \;=\; \frac{8R\left(\frac{R}{d} - \frac{1}{2}\right)}{4R^2 H}\left(\frac{H}{\lambda}\right)\Big[2b_{cl}\gamma_g + 2l_{cl}\gamma_s + (\lambda - 2b_{cl})\gamma_s\Big] \tag{3.43}$$

Where, b_{cl} and l_{cl} in the above equation are

$$b_{cl} \;=\; \frac{\lambda}{2} - \sqrt{\frac{\lambda^2}{4} - \lambda u_{cl}\cot\beta}; \quad l_{cl} \;=\; \sec\beta\sqrt{\frac{\lambda^2}{4} - \lambda u_{cl}\cot\beta} \tag{3.44}$$

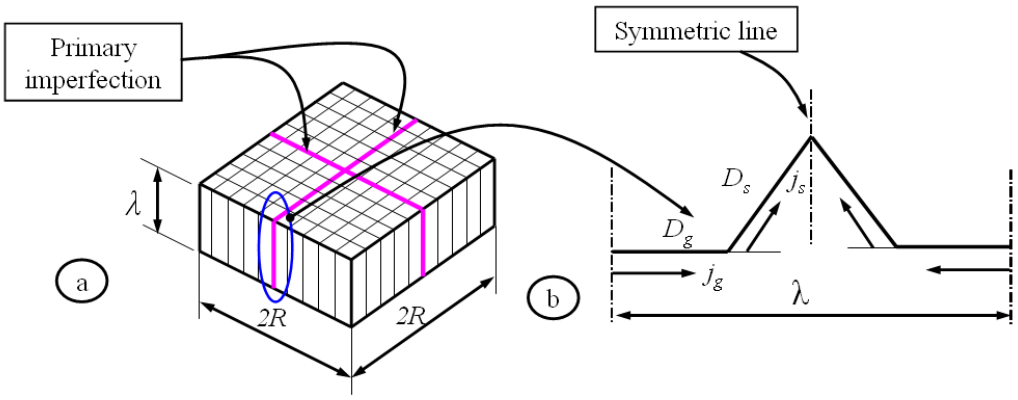

Figure 3.12: a. Repeating element of slice thickness λ in x_3 direction. b. Symmetric contact geometry over λ thickness.

The interfacial energy density at an imperfection in the bottom portion of a cluster is given by

$$G_\lambda^{cr^b} = \frac{4R}{\lambda 4R^2 H}\int_0^\xi \left[\left(\lambda - \sqrt{\lambda^2 - 4\lambda u_{cr}^b \cot\beta}\right)(\gamma_g - \gamma_s) + \gamma_s\left(\sec\beta\sqrt{\lambda^2 - 4\lambda u_{cr}^b\cot\beta} + \lambda\right)\right] dx_3 \tag{3.45}$$

and, the interfacial energy density at the imperfection in the top portion of a cluster, where there is uniform contact, is given by

$$\begin{aligned} G_\lambda^{cr^t}(u_{cr}) \;=\; & \frac{4R}{4R^2H}\frac{(H-\xi)}{\lambda}\left[\left(\lambda - \sqrt{\lambda^2 - 4\lambda u_{cr}\cot\beta}\right)(\gamma_g - \gamma_s)\right. \\ & \left. +\gamma_s\left(\sec\beta\sqrt{\lambda^2 - 4\lambda u_{cr}\cot\beta} + \lambda\right)\right] \end{aligned} \tag{3.46}$$

Now the total interface energy density of the TBC, G_λ is obtained by adding equations 3.43, 3.45 and 3.46

$$G_\lambda(u_{cr}, u_{cl}) \;=\; G_\lambda^{cl}(u_{cl}) + G_\lambda^{cr^b}(u_{cr}, u_{cl}) + G_\lambda^{cr^t}(u_{cr}) \tag{3.47}$$

Estimation of elastic stored energy within the cluster

The elastic strain energy in the potential cluster has contributions from field 1, field 2 and the interaction between them. The total elastic strain energy U_C in the cluster for an incompressible material can be written as

$$U_C \;=\; \int \frac{E}{3}\varepsilon_{ij}\varepsilon_{ij}\; dV \tag{3.48}$$

Here, i and j independently range over 1-3. The total elastic strain tensor ε_{ij} can be decomposed into strain tensors in field 1 and field 2 as given below.

$$\varepsilon_{ij} = \varepsilon_{ij}^{e_1} + \varepsilon_{ij}^{e_2} \tag{3.49}$$

Inserting ε_{ij} in the expression for U_C,

$$\begin{array}{rcl} U_C & = & \frac{E}{3}\int \varepsilon_{ij}^{e_1}\varepsilon_{ij}^{e_1}\ dV + \frac{E}{3}\int \varepsilon_{ij}^{e_2}\varepsilon_{ij}^{e_2}\ dV + \frac{2E}{3}\int \varepsilon_{ij}^{e_1}\varepsilon_{ij}^{e_2}\ dV \\ & = & U^{e_1} + U^{e_2} + U^{e_1 e_2} \end{array} \tag{3.50}$$

The first two terms in the above expression U^{e_1} and U^{e_2} are the strain energy in field 1 and field 2 respectively. The elastic strain tensor in field 1 is obtained using the compatibility condition given by eqn. 3.29 and the incompressibility condition $\varepsilon_{kk}^{e_1} = 0$.

$$\varepsilon_{ij}^{e_1} = \begin{bmatrix} -(\varepsilon_s^1 + \varepsilon^T) & 0 & 0 \\ 0 & -(\varepsilon_s^1 + \varepsilon^T) & 0 \\ 0 & 0 & 2(\varepsilon_s^1 + \varepsilon^T) \end{bmatrix}$$

Consequently, the stored elastic strain energy in field 1 of the TBC cluster is given by

$$U^{e_1} \ = \ 8ER^2H\left(\varepsilon^T + \varepsilon_s^1\right)^2 \tag{3.51}$$

The elastic strain energy in field 2 of the square cluster U^{e_2} is estimated by assuming a kinematically admissible in-plane elastic displacement field following the analysis of mud-cracked cluster (Problem B of this chapter). It is envisaged that elastic straining occurs over a height ξ of the TBC coating from the rigid substrate as shown in Fig. 3.13. The elastic strain tensor in field 2 in the bottom portion of a cluster becomes

$$\varepsilon_{ij}^{e_2} = \begin{bmatrix} -\varepsilon_s^2(1-\frac{x_3}{\xi}) & 0 & \varepsilon_s^2\frac{x_1}{2\xi} \\ 0 & -\varepsilon_s^2(1-\frac{x_3}{\xi}) & \varepsilon_s^2\frac{x_2}{2\xi} \\ \varepsilon_s^2\frac{x_1}{2\xi} & \varepsilon_s^2\frac{x_2}{2\xi} & 2\varepsilon_s^2(1-\frac{x_3}{\xi}) \end{bmatrix}$$

and strain energy is given by

$$U^{e_2} \ = \ \frac{E}{2}\int_{-R}^{R}\int_{-R}^{R}\int_0^{\xi}(\varepsilon_s^2)^2\left[4\left(1-\frac{x_3}{\xi}\right)^2 + \frac{1}{3}\left(\frac{(x_1)^2}{\xi^2} + \frac{(x_2)^2}{\xi^2}\right)\right]\ dx_1\ dx_2\ dx_3 \tag{3.52}$$

The third term in eqn. 3.50 is the energy due to interaction between two strain fields.

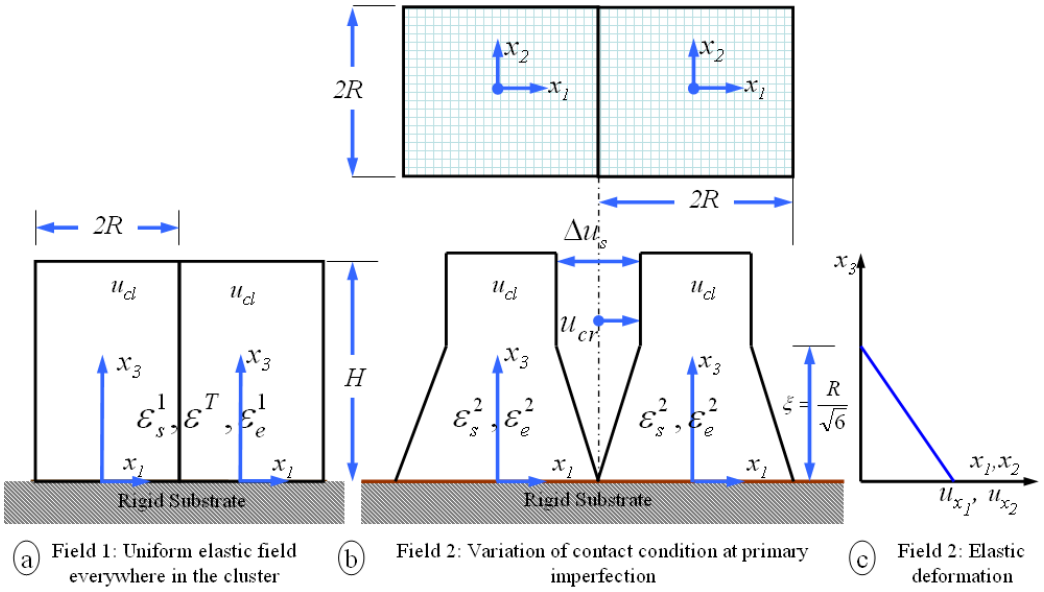

Figure 3.13: Variation of elastic field in the cluster. a. Field 1: Uniform elastic field exists over entire height H of the cluster. b. Field 2: Non-uniform elastic field in the bottom portion of cluster up to a height ξ from the substrate. c. Field 2: Elastic deformation in the bottom portion of cluster

$$U^{e_1e_2} = 4E \int_{-R}^{R} \int_{-R}^{R} \int_{0}^{\xi} \varepsilon_s^2 \left(1 - \frac{x_3}{\xi}\right) dx_1\, dx_2\, dx_3 \tag{3.53}$$

Now the total stored elastic strain energy in the cluster is the sum of U^{e_1}, U^{e_2} and $U^{e_1e_2}$ given by eqns. 3.51, 3.52 and 3.53 respectively.

$$U_C = 8ER^2H\left(\varepsilon^T + \varepsilon_s^1\right)^2 + \frac{8}{3}ER^2(\varepsilon_s^2)^2\left(\xi + \frac{R^2}{6\xi}\right) + 8ER^2\,\xi\left(\varepsilon^T + \varepsilon_s^1\right)\,\varepsilon_s^2 \tag{3.54}$$

The optimal height ξ that minimises the total strain energy U_C is a function of ε_s^1 and ε_s^2. However, we take $\xi = \frac{R}{\sqrt{6}}$ which minimises the strain energy in field 2, in order to keep the description of the evolving crack geometry simple. Therefore, the total strain energy density of the TBC becomes

$$U = 2E\left(\varepsilon^T + \varepsilon_s^1\right)^2 + \frac{4}{3\sqrt{6}}\frac{ER}{H}(\varepsilon_s^2)^2 + \frac{2}{\sqrt{6}}\frac{ER}{H}\left(\varepsilon^T + \varepsilon_s^1\right)\,\varepsilon_s^2 \tag{3.55}$$

The expressions for ε_s^1 given by eqn. 3.34 and ε_s^2 given by eqn. 3.35 in terms of state variables (u_{cr}, u_{cl}) can now be used in eqn. 3.55 to express the strain energy density U in terms of state variables (u_{cr}, u_{cl}). Now the Gibbs energy density of the TBC, G

given by eqn. 3.40 can be re-written by adding U to G_λ given by eqn. 3.47

$$G(u_{cr}, u_{cl}) \;=\; G_\lambda^{cl}(u_{cl}) + G_\lambda^{cr^b}(u_{cr}, u_{cl}) + G_\lambda^{cr^t}(u_{cr}) + U(u_{cr}, u_{cl}) \tag{3.56}$$

3.6.2 Determination of dissipation potential at primary imperfection and in the cluster

We now introduce the rate potential ψ_λ per unit length of contact between columns, for a slice of thickness λ of the repeating cluster shown in Fig. 3.12a. The potential ψ_λ is expressed in terms of the volumetric flux per unit depth j as given below. This interfacial flux is a function of the local co-ordinate s_1 along the contact OA, and of the local co-ordinate s_2 along the contact AB, as shown in Fig. 2.5.

$$\psi_\lambda \;=\; \frac{1}{D_g}\int_0^b j^2(s_1)\,ds_1 + \;\frac{1}{D_s}\int_0^l j^2(s_2)\,ds_2 \tag{3.57}$$

Knowing the flux and the bulk contact length L_{cl}^λ, we now can express the rate potential from bulk contacts characterized by u_{cl} in the whole cluster

$$\begin{aligned}\psi^{cl} = L_{cl}^\lambda \left(\frac{H}{\lambda}\right) \Bigg[& \frac{1}{D_g}\int_0^{b_{cl}} (-\dot{u}_{cl} s_1)^2\, ds_1 \\ & + \frac{1}{D_s}\int_0^{l_{cl}} \left(s_2(\dot{u}_{cl} + \dot{w}_{cl})\cos\beta - \frac{s_2^2}{2l_{cl}}\left(\dot{b}_{cl}\sin\beta + \dot{w}_{cl}\cos\beta\right)\right)^2 ds_2 \Bigg]\end{aligned} \tag{3.58}$$

After performing integration of eqn. 3.58, we have ψ^{cl} as a function of $(\dot{u}_{cl}, \dot{w}_{cl}, \dot{b}_{cl}, b_{cl}, l_{cl})$. Using appropriate expressions for w_{cl}, u_{cl}, b_{cl}, $\dot{w}_{cl}$, $\dot{b}_{cl}$ and L_{cl}^λ in ψ^{cl} and dividing by the volume of the cluster $4R^2H$, yields the following expression.

$$\psi_{cl}(\dot{u}_{cl}) = K_1 \dot{u}_{cl}^2 \left[\lambda - \sqrt{\lambda^2 - 4\lambda u_{cl}\cot\beta}\right]^2 \left(D_s\lambda\cos\beta + (D_g - D_s\cos\beta)\sqrt{\lambda^2 - 4\lambda u_{cl}\cot\beta}\right) \tag{3.59}$$

Where K_1 is

$$K_1 \;=\; \frac{(2R-d)}{24Rd\lambda D_g D_s\cos\beta} \tag{3.60}$$

The expression for ψ^{cl} given by eq. 3.59 gives the dissipation from bulk contacts in the whole cluster per unit volume as a quadratic function of $\dot{u}_{cl}$. The dissipation from

contacts in the bottom portion of the imperfection is

$$\psi^b_{cr} = \frac{4R}{\lambda}\int_0^{\xi}\left[\frac{1}{D_g}\int_0^{b^b_{cr}}(-\dot{u}^b_{cr}s_1)^2\,ds_1 + \frac{1}{D_s}\int_0^{l^b_{cr}}\left(s_2(\dot{u}^b_{cr}+\dot{w}^b_{cr})\cos\beta - \frac{s_2^2}{2l^b_{cr}}\left(\dot{b}^b_{cr}\sin\beta + \dot{w}^b_{cr}\cos\beta\right)\right)^2 ds_2\right] dx_3 \tag{3.61}$$

where, $\dot{u}^b_{cr}$ is the time derivative of $u^b_{cr}(x_3)$. b^b_{cr} and l^b_{cr} are the interface and free surface length at a typical contact in the bottom portion of an imperfection, which are functions of position x_3. Using appropriate expressions for $\dot{u}^b_{cr}$, b^b_{cr}, w^b_{cr} and l^b_{cr} (differentiating b^b_{cr} with respect to time (gives $\dot{b}^b_{cr}$) and differentiating w^b_{cr} with respect to time (gives $\dot{w}^b_{cr}$)) in eqn. 3.61 and dividing by the cluster volume gives

$$\psi^b_{cr} = \int_0^{\xi}\psi^b_{cr}(\dot{u}_{cr},\dot{u}_{cl},x_3)\,dx_3 \tag{3.62}$$

The function given by eqn. 3.62 needs to be integrated numerically. Further, the dissipation in the top portion of an the imperfection over height $(H-\xi)$ is given by

$$\psi^t_{cr} = \rho\left[\frac{1}{D_g}\int_0^{b_{cr}}(-\dot{u}_{cr}s_1)^2\,ds_1 + \frac{1}{D_s}\int_0^{l_{cr}}\left(s_2(\dot{u}_{cr}+\dot{w}_{cr})\cos\beta - \frac{s_2^2}{2l_{cr}}\left(\dot{b}_{cr}\sin\beta + \dot{w}_{cr}\cos\beta\right)\right)^2 ds_2\right] \tag{3.63}$$

where, $\rho = \frac{4R(H-\xi)}{\lambda}$. Integrating eqn. 3.63 and using appropriate expressions for $(\dot{u}_{cr},\dot{w}_{cr},\dot{b}_{cr},b_{cr},l_{cr})$ and dividing by the volume of the cluster $4R^2H$, we obtain

$$\psi^t_{cr}(\dot{u}_{cr}) = K_2\dot{u}^2_{cr}\left[\lambda - \sqrt{\lambda^2 - 4\lambda u_{cr}\cot\beta}\right]^2\left(D_s\lambda\cos\beta + (D_g - D_s\cos\beta)\sqrt{\lambda^2 - 4\lambda u_{cr}\cot\beta}\right) \tag{3.64}$$

Where K_2 is

$$K_2 = \frac{(H-\xi)}{144RH\lambda D_g D_s\cos\beta} \tag{3.65}$$

Eqn. 3.64 gives the dissipation per unit volume of the TBC for the contacts along the imperfection in the top portion of the cluster. Now the total dissipation per unit volume of the TBC is given as the sum of eqns. 3.59, 3.62 and 3.64.

$$\psi(\dot{u}_{cr},\dot{u}_{cl}) = \psi_{cl}(\dot{u}_{cl}) + \int_0^{\xi}\psi^b_{cr}(\dot{u}_{cr},\dot{u}_{cl},x_3)\,dx_3 + \psi^t_{cr}(\dot{u}_{cr}) \tag{3.66}$$

3.6.3 Numerical solution of two kinematic variable system

It is useful to non-dimensionalise parameters of the problem in order to minimise the number of variables. All length scales are normalised by the wavelength of the undulations λ except R, such that

$$\bar{u}_{cl} = \frac{u_{cl}}{\lambda}; \quad \bar{w}_{cl} = \frac{w_{cl}}{\lambda}; \quad \bar{b}_{cl} = \frac{b_{cl}}{\lambda}; \quad \bar{l}_{cl} = \frac{l_{cl}}{\lambda}; \tag{3.67}$$

$$\bar{u}_{cr} = \frac{u_{cr}}{\lambda}; \quad \bar{w}_{cr} = \frac{w_{cr}}{\lambda}; \quad \bar{b}_{cr} = \frac{b_{cr}}{\lambda}; \quad \bar{l}_{cr} = \frac{l_{cr}}{\lambda}; \tag{3.68}$$

$$\bar{d} = \frac{d}{\lambda}; \quad \bar{x_3} = \frac{x_3}{\lambda}; \quad \bar{H} = \frac{H}{\lambda}; \quad \bar{R} = \frac{R}{H}; \tag{3.69}$$

and the non-dimensional material properties are

$$\bar{D}_g = \frac{D_g}{D_s}; \quad \bar{\gamma}_g = \frac{\gamma_g}{\gamma_s}; \quad \bar{E} = \frac{E\lambda}{(1-\nu)\gamma_s}; \tag{3.70}$$

Now the non-dimensional time scale turns out to be

$$\bar{t} \;=\; \frac{D_s \gamma_s t}{\lambda^4} \tag{3.71}$$

Note from the eqn. 3.71 that the sintering time is very sensitive to wavelength of undulation λ and consistent with the fact that interfacial diffusion-controlled sintering rates scale with grain size to the power of -4. Taking $\xi = \frac{R}{\sqrt{6}}$, the non-dimensional form of $\dot{G}$ and ψ is given by

$$\dot{\bar{G}}(\dot{\bar{u}}_{cr}, \dot{\bar{u}}_{cl}) \;=\; \dot{\bar{G}}^{cl}_{\lambda}(\dot{\bar{u}}_{cl}) + \dot{\bar{G}}^{cr^b}_{\lambda}(\dot{\bar{u}}_{cr}, \dot{\bar{u}}_{cl}) + \dot{\bar{G}}^{cr^t}_{\lambda}(\dot{\bar{u}}_{cr}) + \dot{\bar{U}}(\dot{\bar{u}}_{cr}, \dot{\bar{u}}_{cl}) \tag{3.72}$$

$$\bar{\psi}(\dot{\bar{u}}_{cr}, \dot{\bar{u}}_{cl}) \;=\; \bar{\psi}_{cl}(\dot{\bar{u}}_{cl}) + \int_0^{\frac{\bar{R}\bar{H}}{\sqrt{6}}} \bar{\psi}^b_{cr}(\dot{\bar{u}}_{cr}, \dot{\bar{u}}_{cl}, \bar{x_3})\, d\bar{x_3} + \bar{\psi}^t_{cr}(\dot{\bar{u}}_{cr}) \tag{3.73}$$

The second term of eqn. 3.73 represents the contribution to the rate potential from the bottom portion of the imperfection. This needs to be numerically evaluated at each time step

$$\bar{\psi}^b_{cr} \;=\; \int_0^{\frac{\bar{R}\bar{H}}{\sqrt{6}}} \bar{\psi}^b_{cr}(\dot{\bar{u}}_{cr}, \dot{\bar{u}}_{cl}, \bar{x_3})\, d\bar{x_3} \tag{3.74}$$

We use a Gaussian quadrature rule to get an approximation for the definite integral of this function. The integral over $[0, \frac{\bar{R}\bar{H}}{\sqrt{6}}]$ must be changed into an integral over $[-1, 1]$ before applying the Gaussian quadrature rule. In order to do that, replace $\bar{x}_3$ and $d\bar{x}_3$ in the above function by

$$\bar{x}_3 \;=\; \frac{\bar{R}\bar{H}}{2\sqrt{6}}\;(\eta+1)\,, \quad d\bar{x}_3 \;=\; \frac{\bar{R}\bar{H}}{2\sqrt{6}}\,d\eta \tag{3.75}$$

Now the function takes the following form

$$\bar{\psi}^b_{cr} \;=\; \int_0^{\frac{\bar{R}\bar{H}}{\sqrt{6}}} \bar{\psi}^b_{cr}(\dot{\bar{u}}_{cr}, \dot{\bar{u}}_{cl}, \bar{x}_3)\, d\bar{x}_3 = M \int_{-1}^{1} \bar{\psi}^b_{cr}(\dot{\bar{u}}_{cr}, \dot{\bar{u}}_{cl}, \eta)\, d\eta \tag{3.76}$$

The resulting polynomial function for η is of degree 3 and therefore a two point (η_i with weights c_i) Gauss-Legendre formula will be good enough to exactly integrate it.

$$\bar{\psi}^b_{cr} \;=\; M \int_{-1}^{1} \bar{\psi}^b_{cr}(\dot{\bar{u}}_{cr}, \dot{\bar{u}}_{cl}, \eta)\, d\eta \;=\; M \sum_{i=1}^{2} c_i \bar{\psi}^b_{cr}(\dot{\bar{u}}_{cr}, \dot{\bar{u}}_{cl}, \eta_i)\, d\eta \tag{3.77}$$

We now can set up the equations in non-dimensional form and solve them numerically. We determine the values of D_g and D_s from the eqn. 2.6 knowing the thermal activation energy q. However, the values of q reported in the literature differ by orders of magnitude. To circumvent this uncertainty in the values of D_g and D_s, we take $\bar{D_g} = 1$. From the micrograph of the EB-PVD coatings, one can observe that the wavelength, λ is in the range of 0.2-2μm and the size of the columnar grains is in the range of 2-10μm. Therefore, $\bar{d}$ can vary from 1-50. In the following calculations we take $\bar{d} = 20$, $\bar{D_g} = 1$, $\bar{\gamma_g} = 0.68$ and $\bar{H} = 200$. It has been observed from the simulations (presented in the subsequent sections) that the choice of $\bar{d}$ influences the sintering response of the coating slightly but it does change the overall failure behaviour.

3.6.4 Full development of mud cracks from a primary imperfection

The system of nonlinear ODEs are solved with initial contact conditions $\bar{u}_1^{cr} = \frac{u_1^{cr}}{\lambda} = 0.045$ and $\bar{u}_1 = \frac{u_1}{\lambda} = 0.05$. Other geometric and material parameters are the same as

those used in the computational study. In order to simulate the primary imperfections, the initial condition at the primary imperfections is deliberately chosen different from the initial conditions within the clusters. Four different types of behavior are observed depending upon the magnitude of $\bar{E}$ and the cluster size $\bar{R}$ as shown in Fig. 3.14. As before, for low values of $\bar{E}$ complete sintering occurs both in the clus-

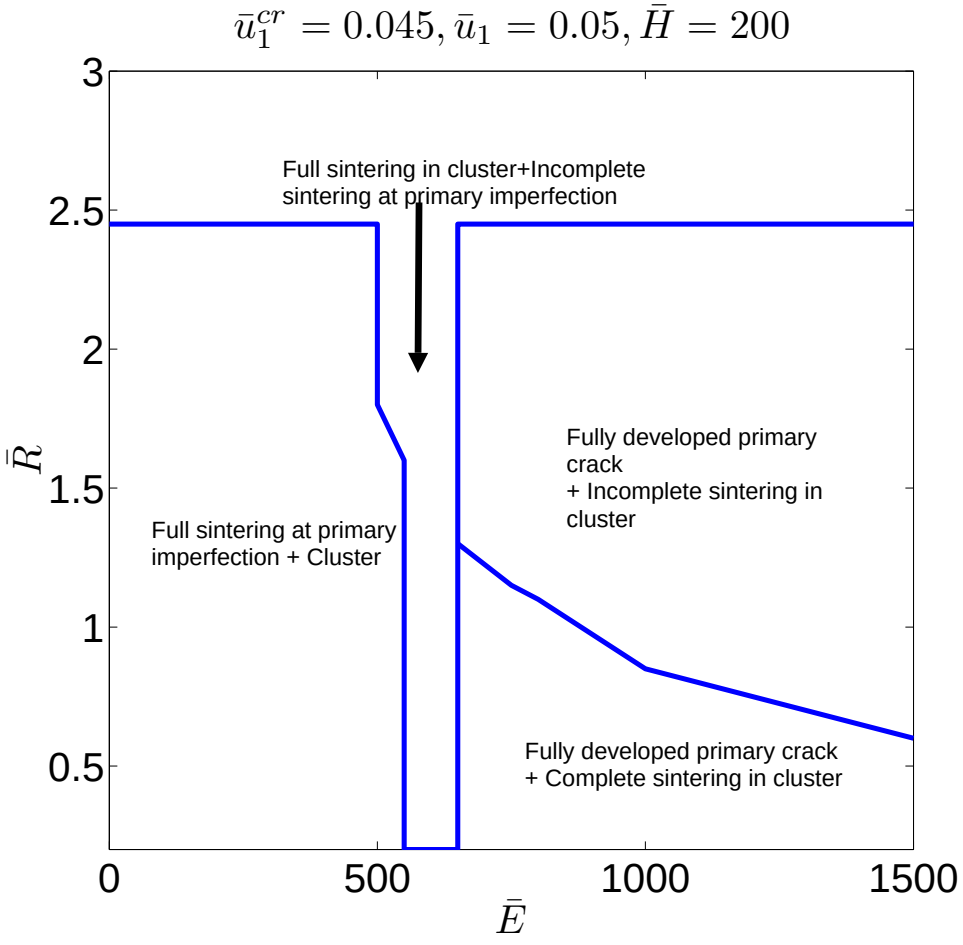

Figure 3.14: Map showing different types of sintering behaviour of TBC

ter and at the primary imperfections regardless of the cluster size and the sintering response is the same as that for a perfect coating. An example of this situation is shown in Fig. 3.15 for $\bar{E} = 300$ and $\bar{R} = 1$.

The displacement field that we assume for the imperfection varies linearly up to a height ξ, and then is constant with increasing height. This results in a variation of the

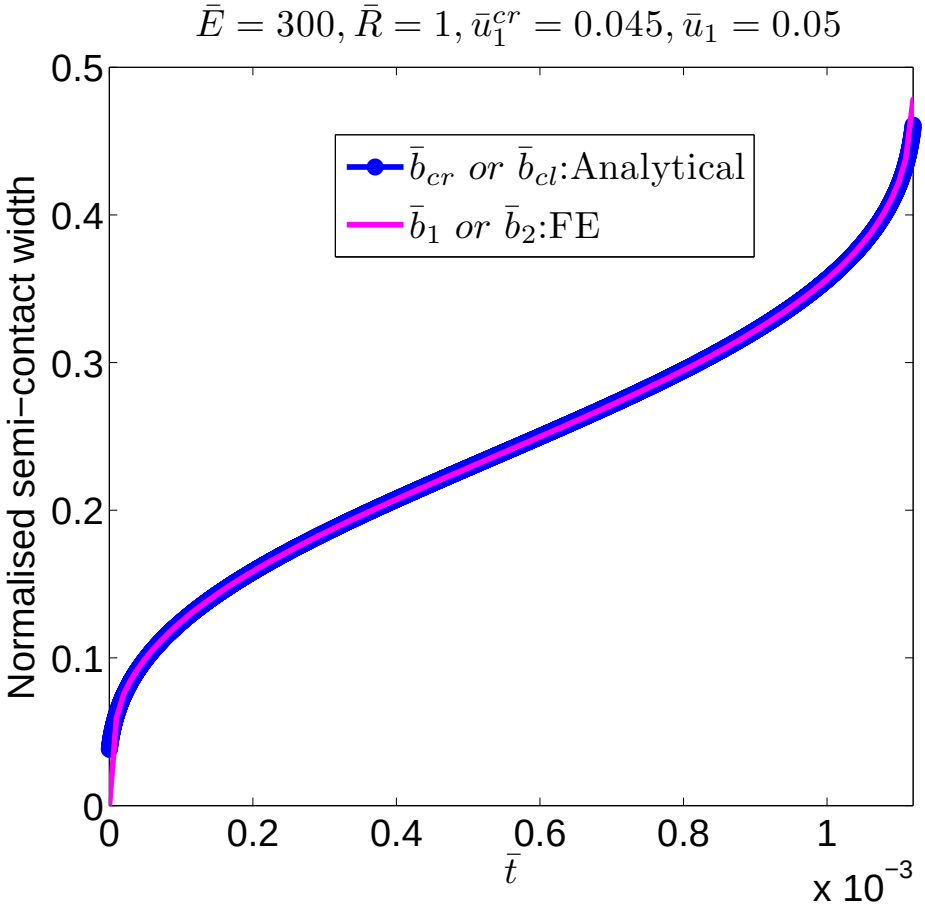

Figure 3.15: Complete sintering everywhere in the TBC layer

half contact width along the height of the imperfection. In this and subsequent figures the value of $\bar{b}$ in the uniform top section of the imperfection is plotted. We obtain the solution in terms of the primary unknowns $(\bar{u}_{cr}, \bar{u}_{cl})$. Negative value of $\bar{u}_{cr}$ means the physical separation of an interface. However, we plot the graphs here in terms of $(\bar{b}_{cr}, \bar{b}_{cl})$ for the sake of convenience. It should be noted that when the semi-contact width, $\bar{b}_{cr} \to 0$, a fully developed crack forms at the interface. Physically, $\bar{b}_{cr}$ can not be less than zero. Nevertheless, negative value $\bar{b}_{cr}$ means the measure of physical separation at the top portion of an imperfection. For moderate values of $\bar{E}$, elastic constraint of the TBC layer is just sufficient to switch off sintering at the primary imperfections, while full sintering occurs in the cluster. This is true for any cluster size $\bar{R}$. In contrast, when $\bar{E}$ is large, significant tensile stress develops in the TBC

which almost arrests sintering, the constraint is then relieved by desintering at the imperfections and by the development of cracks along the lines of the imperfections. Complete sintering occurs in the clusters if the cluster size $\bar{R}$ is relatively small. The evolution of the semi-contact width, $\bar{b}$ for the cluster and imperfection are shown in Fig. 3.16 for $\bar{E} = 1000$ and $\bar{R} = 1$ and compared with FE results. It can be seen

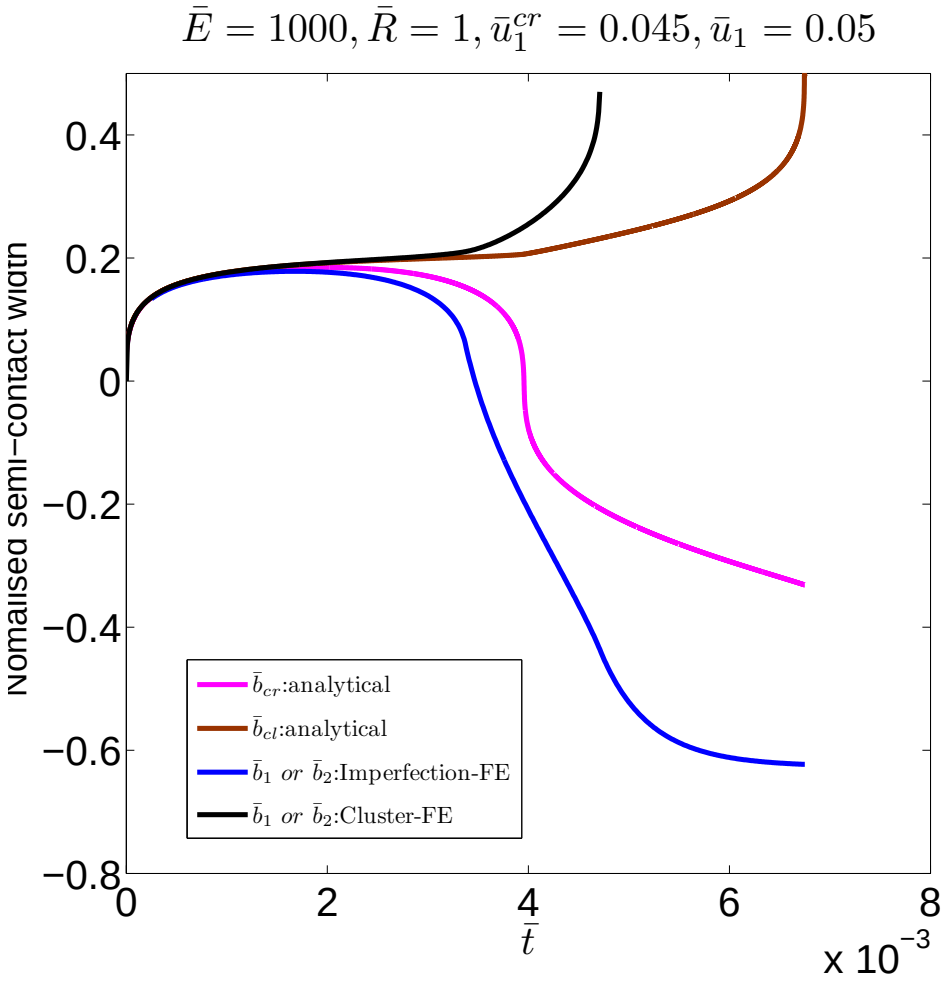

Figure 3.16: Fully developed primary crack and complete sintering in cluster

that the analytical model captures the essential physics, with the timescales for the development of the imperfections and form of behaviour being comparable with the computational simulations. The differences arise in part from the approximations employed in the analytical model, but it should also be noted that the imperfections are treated in a different way in the two situations. In the analytical model the

imperfection is a line defect, while in the computations the defect has a width equal to the element size. Increasing $\bar{R}$ increases the constraint on the sintering process and prevents full sintering being achieved in the cluster. This is shown in Fig. 3.17 for $\bar{E} = 1000$ and $\bar{R} = 2$. Again, the analytical results agree closely with the FE results.

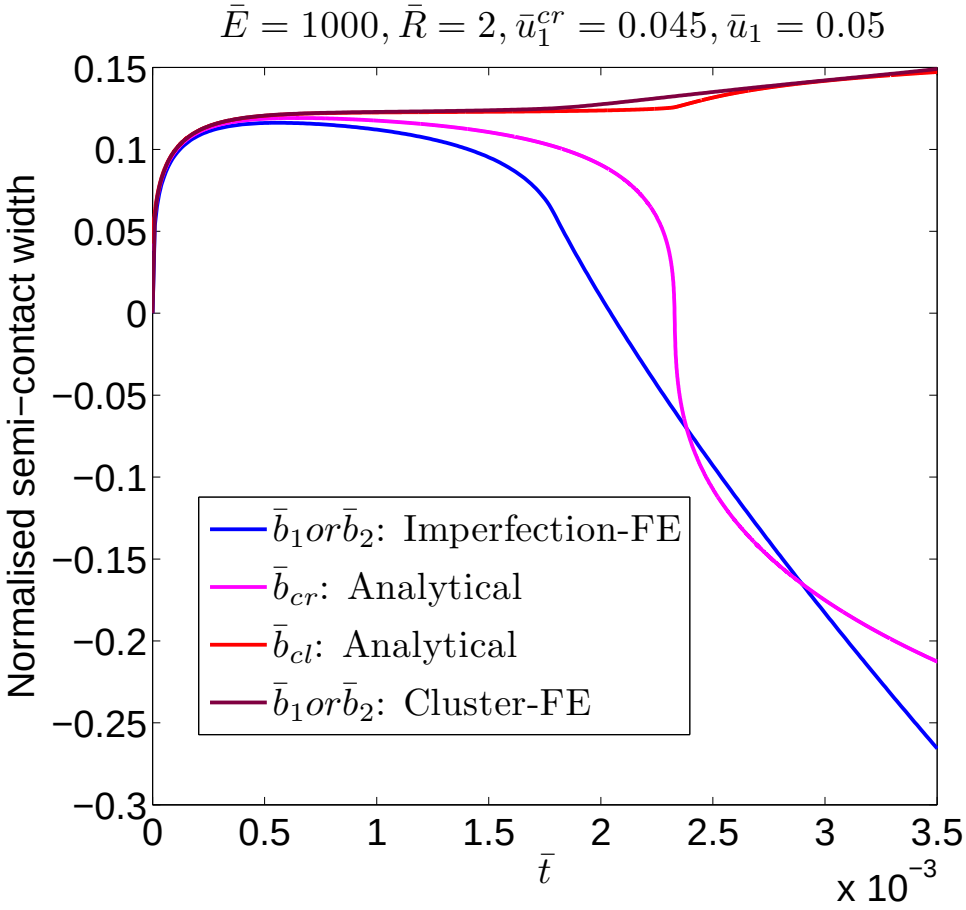

Figure 3.17: Fully developed primary crack and incomplete sintering in cluster

From a series of simulations of this type we can determine how different characteristics of the sintering behaviour depend on the geometric and material parameters. Fig. 3.18 shows how the time for the initiation of desintering at the imperfections depends on the spacing of the imperfections for $\bar{E} = 1500$ and $\bar{H} = 200$. This reflects a general trend with instabilities occuring initially at the most widely spaced imperfections. Fig. 3.19 shows the time at which primary cracks fully develop (i.e the columns loose contact at the top of imperfection) as a function of cluster size for $\bar{E} = 1500$ and

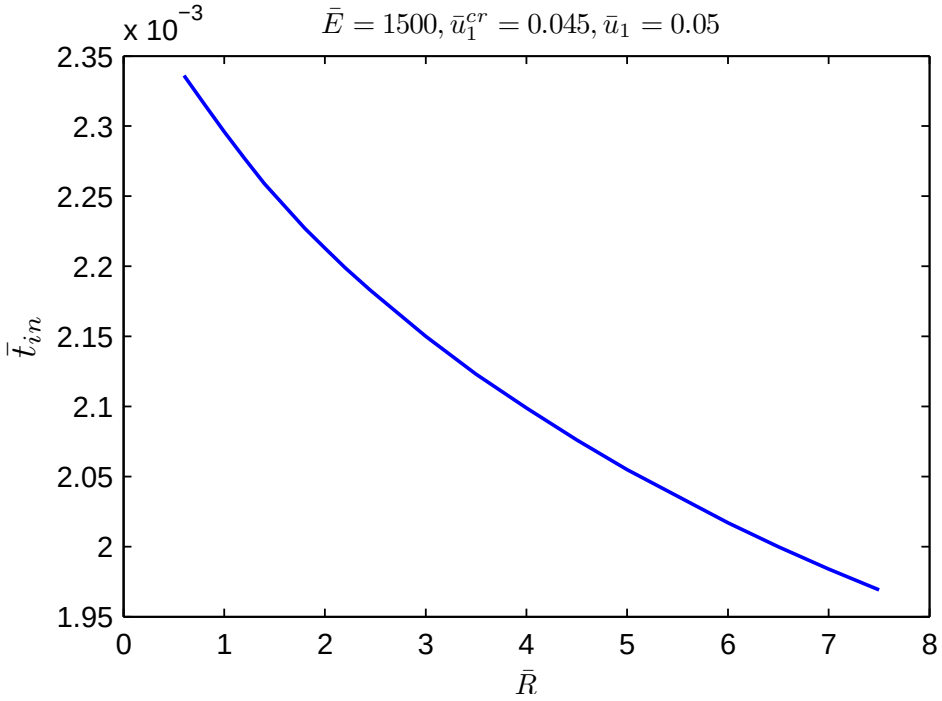

Figure 3.18: Time at primary crack inception with the variation of cluster size

$\bar{H} = 200$. It is clear from this plot that mud-cracking time t_{crack} is a minimum for a particular cluster size ($\bar{R}$=3). The simulations presented here allow the conditions under which mud cracks will develop in a coating to be identified, but they do not provide any information about the mud crack pattern. In order to do this we need to consider the response of a body which contains a number of different types of imperfections. This is the subject of the next section.

3.7 Problem D: Modelling evolution of P.I and S.I in TBC layer

In problem C, we have modelled the development of a primary set of mud cracks in the TBC layer during progressive sintering. The analysis identifies the conditions under which mud cracks can form, but it does not provide any information about the final pattern of cracks in the coating. The analysis suggests that the wider the spacing of the imperfections the faster they develop into cracks, see Fig. 3.18.

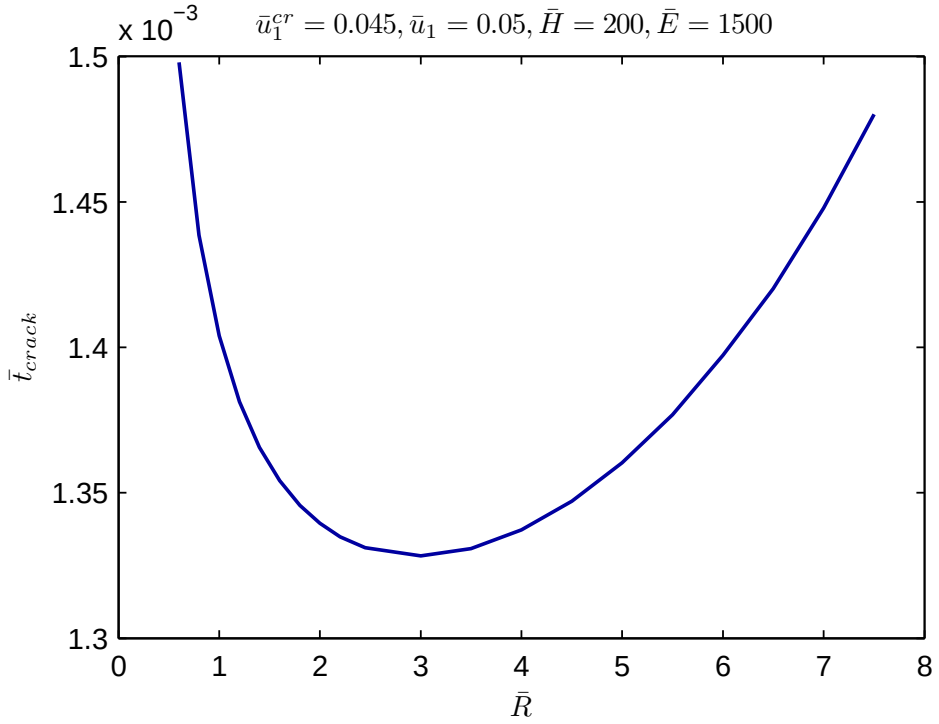

Figure 3.19: Time at which fully developed primary crack forms as a function of cluster size

This suggests that the initial cracks that form will be widely spaced. We might, however, expect imperfections at intermediate positions to subsequently develop into cracks, with this process repeated until the crack density saturates. The question now is "what is the final steady state spacing of the cracks?". In order to answer this, another problem has been formulated considering an equi-spaced distribution of another set of imperfections, in addition to the primary imperfections considered in previous section. The primary imperfections are at the junctions of clusters in the idealized TBC layer, while the secondary imperfections run across the clusters as shown in Fig. 3.20. The primary imperfections form a square grid of spacing $2R$ as before. Superimposed on top of this is a square grid of secondary imperfections, also of spacing $2R$, whose lines bisect the sides of the grid of primary imperfections as shown in Fig. 3.20. We can identify a representative square cell of side $2R$, with secondary imperfections forming the boundary of the cell and primary imperfections

bisecting the cell to form four equal square sub-cells of side R.

3.7.1 Global considerations

We can analyse this problem in a similar way to problem C. During progressive sintering of columns of the TBC under isothermal conditions with primary and secondary defects, an equi-biaxial sintering strain $\varepsilon^s_{ij} = \varepsilon^s \delta_{ij}$ evolves with time in the TBC which is uniform over the entire height of the TBC layer. Here i and j independently range over 1-2. ε^s_{ij} can be conveniently decomposed into three fields.

$$\varepsilon^s \;=\; \varepsilon^1_s + \varepsilon^2_s + \varepsilon^3_s \tag{3.78}$$

Field 1 is the same as that for inter-columnar sintering of columns in a perfect constrained TBC film with sintering strain ε^1_s and thermal mismatch strain ε^T. Field 2 is similar to that for progressive sintering of columns of an isolated cluster as described earlier with sintering strain ε^2_s and field 3 in each sub-cluster is analogous to progressive sintering of columns of an isolated cluster with sintering strain ε^3_s as shown in Fig. 3.21. Field 3 is similar in form to Field 2, but is associated with each sub-cluster.

Time evolution of ε^1_s, ε^2_s and ε^3_s is obtained based upon an assumed initial contact

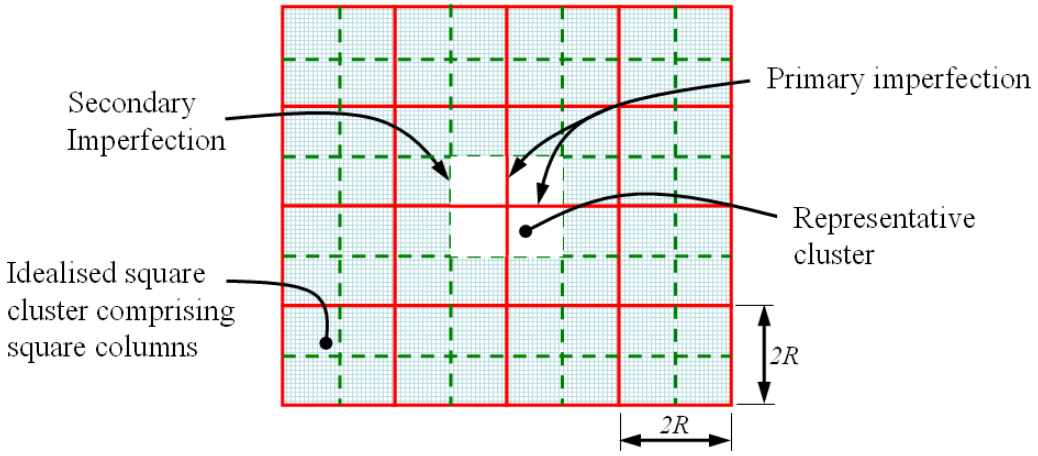

Figure 3.20: Idealisation of mud-cracked TBC as a assembly of square clusters of dimension $2R \times 2R$ with primary and secondary imperfections.

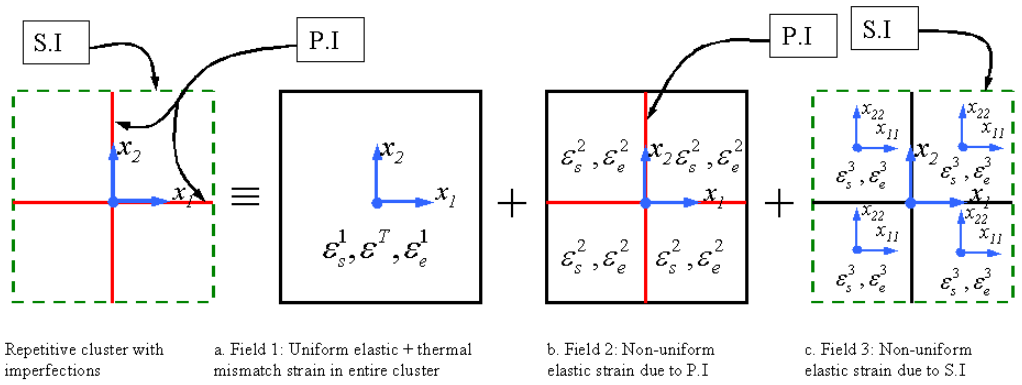

Figure 3.21: Decomposition of fields in the square cluster with primary and secondary imperfections. a: Field 1 associated with uniform sintering strain ε_s^1 in a defect free cluster. b. Field 2 associated with uniform sintering strain ε_s^2 and primary imperfection. c. Field 3 associated with uniform sintering strain ε_s^3 and secondary imperfection.

geometry between neighboring TBC columns as before. The subscripts $'cr'$, $'cl'$ and $'cr_2'$ are used to characterize the geometric parameters at primary imperfection, bulk contacts in the cluster and secondary imperfection respectively, see Fig. 3.22. The compatibility conditions given by eqs. 3.29 and 3.30 are still valid for field 1 and field 2 respectively in this problem. The following compatibility condition needs to be satisfied in each sub-cluster of field 3.

$$\left(\varepsilon_{ij}^{e_3}(x_3) + \varepsilon_{ij}^{s_3}\right) R - \Delta u_s^{cr_2}(x_3) = 0 \tag{3.79}$$

Here, $\Delta u_s^{cr_2}(x_3)$ is the net displacement across the secondary imperfection. Further, we consider elastic constraint of the substrate up to height ξ on each sub-cluster in the x_3 direction from the substrate (see Fig. 3.23.b). The elastic constraint of the substrate alters the local contact condition at the secondary imperfection to vary linearly from the substrate up to ξ.

3.7.2 Local considerations

Contact geometry

The objective of the problem is to solve for the local evolution of surface profile within the repeating cluster as characterized by (u_{cr}, w_{cr}), (u_{cl}, w_{cl}) and (u_{cr_2}, w_{cr_2}) (see Fig.

3.22). Now, we have six primary unknowns. Assuming an equilibrium pore profile angle β as before, the problem reduces to three independent variables $(u_{cr}, u_{cl}, u_{cr2})$.

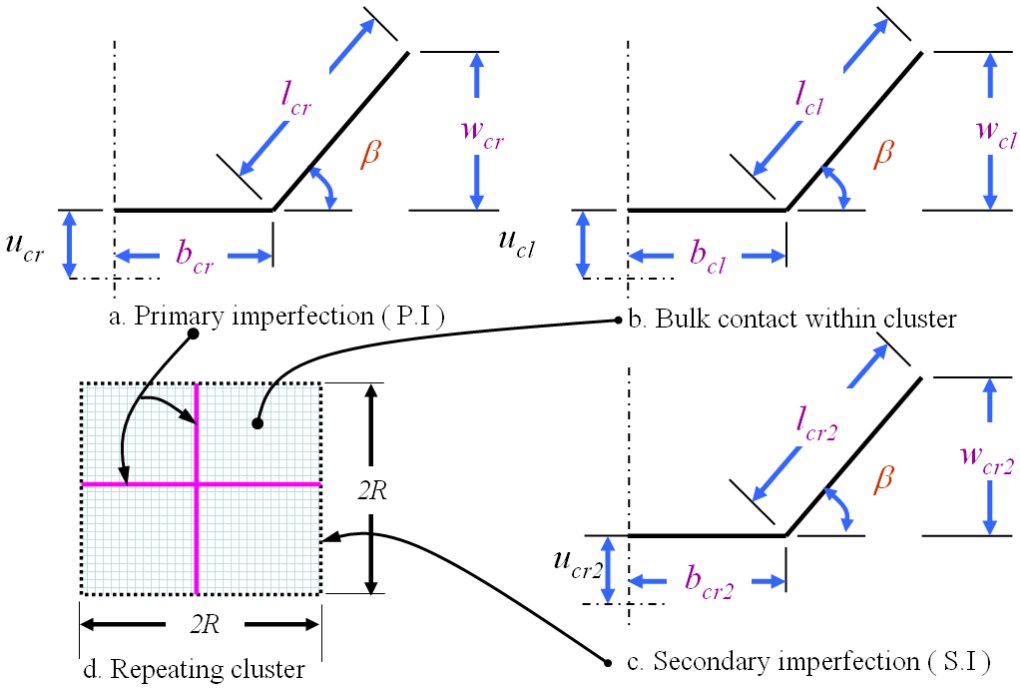

Figure 3.22: Contact geometries. a. Contact geometry at P.I. characterized by u_{cr} b. Geometry at bulk contacts within cluster characterized by u_{cl} c. Contact geometry at S.I. characterized by u_{cr_2}

3.7.3 Thermodynamic variational principle(TVP)

Again, employing the variational method described earlier, it is shown below that the rate of evolution of microstructure is given by the set of kinematic rates $(\dot{u}_{cr}, \dot{u}_{cl}, \dot{u}_{cr2})$ that minimise the following functional Φ.

$$\Phi(\dot{u}_{cr}, \dot{u}_{cl}, \dot{u}_{cr2}) \;=\; \dot{G}(\dot{u}_{cr}, \dot{u}_{cl}, \dot{u}_{cr2}) + \psi(\dot{u}_{cr}, \dot{u}_{cl}, \dot{u}_{cr2}) \tag{3.80}$$

The optimal choice for $(\dot{u}_{cr}, \dot{u}_{cl}, \dot{u}_{cr2})$ is obtained by minimising the functional Φ, ie

$$\delta\Phi(\dot{u}_{cr}, \dot{u}_{cl}, \dot{u}_{cr2}) \;= 0 \tag{3.81}$$

for arbitrary variations in $(\dot{u}_{cr}, \dot{u}_{cl}, \dot{u}_{cr2})$. This gives a set of simultaneous equations that can be cast in matrix form as

$$\begin{bmatrix} \frac{\partial^2\psi}{\partial\dot{u}_{cr}^2} & \frac{\partial^2\psi}{\partial\dot{u}_{cr}\partial\dot{u}_{cl}} & \frac{\partial^2\psi}{\partial\dot{u}_{cr}\partial\dot{u}_{cr2}} \\ \frac{\partial^2\psi}{\partial\dot{u}_{cr}\partial\dot{u}_{cl}} & \frac{\partial^2\psi}{\partial\dot{u}_{cl}^2} & \frac{\partial^2\psi}{\partial\dot{u}_{cl}\partial\dot{u}_{cr2}} \\ \frac{\partial^2\psi}{\partial\dot{u}_{cr}\partial\dot{u}_{cr2}} & \frac{\partial^2\psi}{\partial\dot{u}_{cl}\partial\dot{u}_{cr2}} & \frac{\partial^2\psi}{\partial\dot{u}_{cr2}^2} \end{bmatrix} \begin{bmatrix} \dot{u}_{cr} \\ \dot{u}_{cl} \\ \dot{u}_{cr2} \end{bmatrix} = - \begin{bmatrix} \frac{\partial\dot{G}}{\partial\dot{u}_{cr}} \\ \frac{\partial\dot{G}}{\partial\dot{u}_{cl}} \\ \frac{\partial\dot{G}}{\partial\dot{u}_{cr2}} \end{bmatrix}$$

This set of nonliear ODEs are solved numerically to calculate the time evolution of $(u_{cr}, u_{cl}, u_{cr2})$ using a fourth order Runga-Kutta (R-K4) integration scheme.

3.8 Evolution of state in three kinematic variable system

Uniform macroscopic sintering strains, ε_s^1 in field 1, ε_s^2 in field 2 and ε_s^3 in field 3 of the cluster are formulated as functions of primary unknowns $(u_{cr}, u_{cl}, u_{cr2})$. The unknown variable at bulk contacts in the cluster u_{cl} can be written as

$$u_{cl} \;=\; u_1 - \left(\varepsilon_s^1 + \varepsilon_s^2 + \varepsilon_s^3\right) d; \qquad 0 \le x_3 \le H \tag{3.82}$$

The state variable u_{cr} at the primary imperfection is given by

$$u_{cr} \;=\; u_1^{cr} - \left(\varepsilon_s^1 + \varepsilon_s^2 + \varepsilon_s^3\right) d + \Delta u_s(x_3) + \Delta u_s^{cr2}(x_3); \qquad \xi \le x_3 \le H \tag{3.83}$$

Now the state variable at the secondary imperfection u_{cr2} becomes

$$u_{cr2} \;=\; u_2^{cr} - \left(\varepsilon_s^1 + \varepsilon_s^2 + \varepsilon_s^3\right) d + \Delta u_s^{cr2}(x_3); \qquad \xi \le x_3 \le H \tag{3.84}$$

Using the compatibility condition in the sub-cluster given by eqn. 3.79 and considering kinematically admissible linearly varying displacement field in each of the sub-clusters, we find

$$\Delta u_s^{cr2}(x_3) = \begin{cases} R\varepsilon_s^3 \frac{x_3}{\xi} & \text{if} \quad 0 \le x_3 \le \xi; \\ R\varepsilon_s^3 & \text{if} \quad \xi \le x_3 \le H. \end{cases}$$

Now using $\Delta u_s^{cr}(x_3)$ and $\Delta u_s^{cr2}(x_3)$ in eqns. 3.83 and 3.84 at $x_3 = \xi$ and manipulating the resulting equations for u_{cr} and u_{cr2} equations with u_{cl} given by eqn. 3.82, we

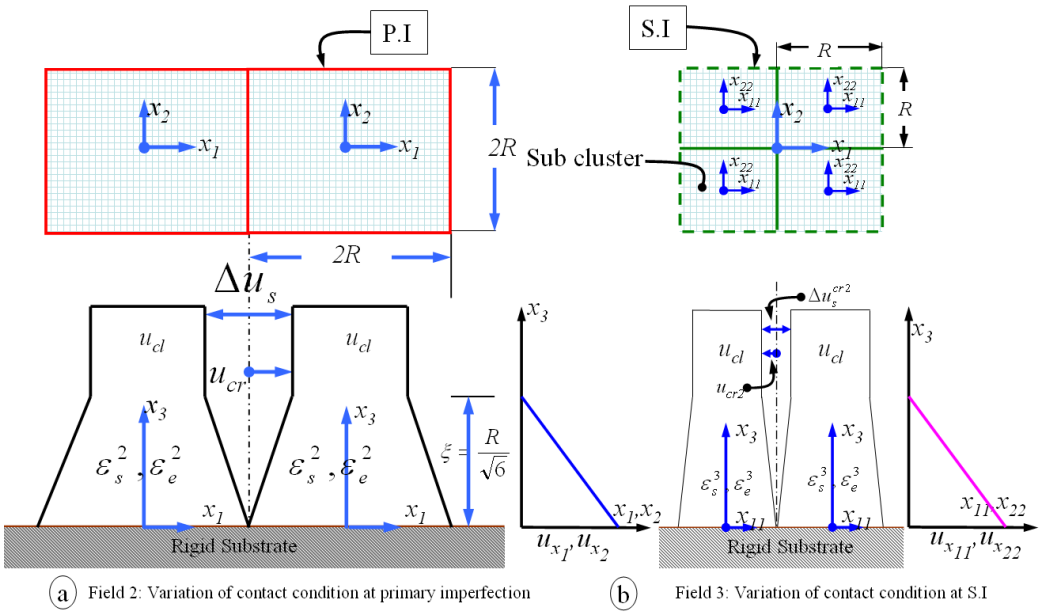

Figure 3.23: Variation of contact condition in the representative cluster. a. Field 2: Variation of contact condition at P.I; In-plane elastic deformation in the bottom portion of cluster up to a height ξ from the substrate. b. Field 3: Variation of contact condition at S.I; In-plane elastic deformation in the bottom portion of cluster up to a height ξ from the substrate.

can express the sintering strains as functions of three state variables $(u_{cr}, u_{cl}, u_{cr2})$ as follows

$$\varepsilon_s^1 = \frac{u_1 - u_{cl}}{d} - \left[\frac{(u_{cr} - u_{cr2}) - (u_1^{cr} - u_2^{cr})}{2R} + \frac{(u_1 - u_2^{cr}) - (u_{cl} - u_{cr2})}{R}\right] \tag{3.85}$$

and

$$\varepsilon_s^2 = \left[\frac{(u_{cr} - u_{cr2}) - (u_1^{cr} - u_2^{cr})}{2R}\right] \tag{3.86}$$

$$\varepsilon_s^3 = \left[\frac{(u_1 - u_2^{cr}) - (u_{cl} - u_{cr2})}{R}\right] \tag{3.87}$$

Note that u_1, u_1^{cr} and u_2^{cr} are the initial values of the kinematic variables u_{cl}, u_{cr} and u_{cr2} respectively immediately after deposition.

3.8.1 Determination of interface free energy

We will now determine the interface energy density G_λ of the TBC with primary and secondary imperfections. Let G_λ^{cl} be the interface energy density of bulk contacts,

G_λ^{cr} be the interface energy density of primary imperfections and G_λ^{cr2} be the interface energy density of secondary imperfections of the TBC. Thus G_λ becomes

$$G_\lambda \;=\; G_\lambda^{cl} + G_\lambda^{cr} + G_\lambda^{cr2} \tag{3.88}$$

G_λ^{cr} in the eqn. 3.88 is same as G_λ^{cr} in two DOF problem. It can be seen from the Fig. 3.23a and b, that the local contact at the secondary imperfection characterized by u_{cr2} also varies linearly with x_3 from the substrate up to a height ξ and remains constant thereafter over the rest of the TBC height as described below.

$$u_{cr2} = \begin{cases} u_{cr2}^b = (u_2^{cr} - u_1 + u_{cl})\left(1 - \frac{x_3}{\xi}\right) + u_{cr2}\,\frac{x_3}{\xi} & \text{if} \quad 0 \le x_3 \le \xi; \\ u_{cr2}^t = u_{cr2} & \text{if} \quad \xi \le x_3 \le H. \end{cases}$$

Accordingly, G_λ^{cr2} is the sum of interface energy density associated with linearly varying contact in the bottom of the imperfection characterized by u_{cr2}^b and that associated with uniform contact in the top of the imperfection characterized by u_{cr2}^t. G_λ^{cr2} now becomes

$$G_\lambda^{cr2} \;=\; \int_0^\xi G_\lambda^{cr2^b}(u_{cr2}, u_{cl})\; dx_3 + G_\lambda^{cr2^t}(u_{cr2}) \tag{3.89}$$

Consider a slice of thickness λ of the repeating cell of size $2R \times 2R$ in the x_3 direction as shown in Fig. 3.24a and a typical contact geometry over its thickness λ as shown in Fig. 3.24b. The interfacial energy density associated with bulk contacts of the entire

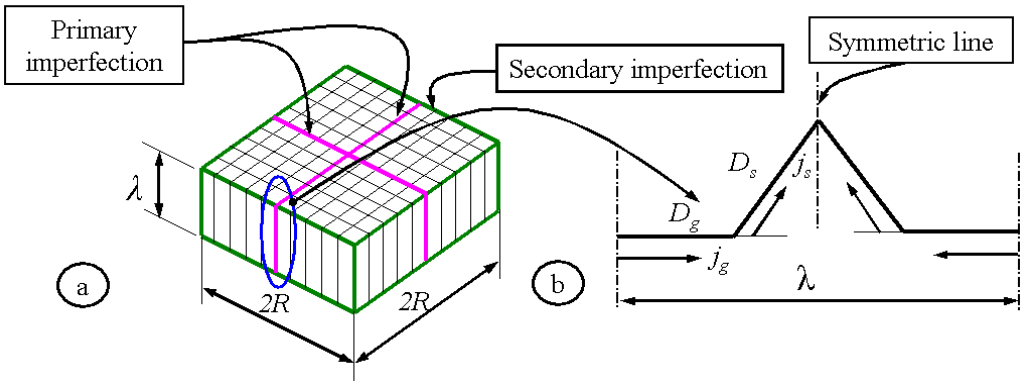

Figure 3.24: a. Repeating element of slice thickness λ in x_3 direction. b. Symmetric contact geometry over λ thickness.

cluster can be written (see Fig. 3.24b) as

$$G_\lambda^{cl} = \frac{2}{\lambda R}\left(\frac{R}{d}-1\right)\left[\left(\lambda-\sqrt{\lambda^2-4\lambda u_{cl}\cot\beta}\right)(\gamma_g-\gamma_s)+\gamma_s\left(\sec\beta\sqrt{\lambda^2-4\lambda u_{cl}\cot\beta}+\lambda\right)\right] \tag{3.90}$$

The effective contact length at the secondary imperfection over a thickness λ of the cluster is $4R$. The interfacial energy density at the secondary imperfection in the bottom portion of the imperfection is now

$$\begin{aligned} G_\lambda^{cr2^b} =& \frac{4R}{\lambda 4R^2H}\int_0^\xi\left[\left(\lambda-\sqrt{\lambda^2-4\lambda u_{cr2}^b\cot\beta}\right)(\gamma_g-\gamma_s)\right. \\ &\left.+\gamma_s\left(\sec\beta\sqrt{\lambda^2-4\lambda u_{cr2}^b\cot\beta}+\lambda\right)\right]dx_3 \end{aligned} \tag{3.91}$$

Inserting u_{cr2}^b in eqn. 3.91 and performing integration yields an explicit analytical expression for $G_\lambda^{cr2^b}$ as a function of (u_{cr2}, u_{cl}). Again, the interfacial energy density at the secondary imperfection $G_\lambda^{cr2^t}$ in the top portion of the imperfection is

$$\begin{aligned} G_\lambda^{cr2^t} =& \frac{4R}{4R^2H}\frac{(H-\xi)}{\lambda}\left[\left(\lambda-\sqrt{\lambda^2-4\lambda u_{cr2}\cot\beta}\right)(\gamma_g-\gamma_s)\right. \\ &\left.+\gamma_s\left(\sec\beta\sqrt{\lambda^2-4\lambda u_{cr2}\cot\beta}+\lambda\right)\right] \end{aligned} \tag{3.92}$$

Now the total interface energy density of the TBC is obtained by adding eqns. 3.90, 3.45, 3.46, 3.91 and 3.92,

$$G_\lambda(u_{cr},u_{cl},u_{cr2}) = G_\lambda^{cl}(u_{cl})+G_\lambda^{cr^b}(u_{cr},u_{cl})+G_\lambda^{cr^t}(u_{cr})+G_\lambda^{cr2^b}(u_{cr2},u_{cl})+G_\lambda^{cr2^t}(u_{cr2}) \tag{3.93}$$

3.8.2 Estimation of elastic stored energy within the cluster

The elastic strain energy in the potential cluster has contributions from field 1, field 2 and field 3 and the interaction between them. The total elastic strain energy U_C in an elastically incompressible cluster can be written as

$$U_C = \frac{E}{3}\int \varepsilon_{ij}\varepsilon_{ij}\ dV \tag{3.94}$$

Here, i and j independently range over 1-3. The total elastic strain tensor ε_{ij} can be decomposed into strain tensors in field 1, field 2 and field 3 as

$$\varepsilon_{ij} = \varepsilon_{ij}^{e_1}+\varepsilon_{ij}^{e_2}+\varepsilon_{ij}^{e_3} \tag{3.95}$$

Inserting ε_{ij} in the expression for U_C,

$$\begin{aligned} U_C =& \frac{E}{3}\int \varepsilon_{ij}^{e_1}\varepsilon_{ij}^{e_1}\,dV + \frac{E}{3}\int \varepsilon_{ij}^{e_2}\varepsilon_{ij}^{e_2}\,dV \\ &+\frac{E}{3}\int \varepsilon_{ij}^{e_3}\varepsilon_{ij}^{e_3}\,dV + \frac{2E}{3}\int \varepsilon_{ij}^{e_1}\varepsilon_{ij}^{e_2}\,dV + \frac{2E}{3}\int \varepsilon_{ij}^{e_2}\varepsilon_{ij}^{e_3}\,dV + \frac{2E}{3}\int \varepsilon_{ij}^{e_3}\varepsilon_{ij}^{e_1}\,dV \end{aligned} \tag{3.96}$$

The terms 1, 2 and 3 in the eqn. 3.96 are the elastic strain energy due to fields 1, 2 and 3 respectively. The fourth, fifth and sixth terms in eqn. 3.96 are the energy due to interaction between strain fields 1-2, 2-3 and 3-1 respectively. The variation of elastic deformation in fields 2 and 3 are shown in Fig. 3.23. The elastic strain tensors in field 1 and field 2 of this problem are exactly same as the strain tensors in field 1 and field 2 of two DOF problem. The elastic strain energy due to field 1 of the cluster U^{e_1}, elastic strain energy due to field 2 of the cluster U^{e_2} and the energy due to interaction between these two strain fields $U^{e_1e_2}$ are given by eqns. 3.51, 3.52 and 3.53 respectively. Now, we need to find the strain tensor of field 3, $\varepsilon_{ij}^{e_3}$, in each sub-cluster in order to find the elastic energy due to field 3 in the cluster U^{e_3} and the energies due to its interaction with field 1 and 2. The elastic strain tensor in the bottom of each sub-cluster of field 3 which contributes to elastic stored energy is given by

$$\varepsilon_{ij}^{e_3}(x_1,x_2,x_3) = \begin{bmatrix} -\varepsilon_s^3\,(1-\frac{x_3}{\xi}) & 0 & \varepsilon_s^3\,\frac{\left(x_1-\frac{R}{2}\right)}{2\xi} \\ 0 & -\varepsilon_s^3\,(1-\frac{x_3}{\xi}) & \varepsilon_s^3\,\frac{\left(x_2-\frac{R}{2}\right)}{2\xi} \\ \varepsilon_s^3\,\frac{\left(x_1-\frac{R}{2}\right)}{2\xi} & \varepsilon_s^3\,\frac{\left(x_2-\frac{R}{2}\right)}{2\xi} & 2\varepsilon_s^3\,(1-\frac{x_3}{\xi}) \end{bmatrix}$$

The stored elastic strain energy due to field 3 in the cluster is

$$U^{e_3} \;=\; \frac{2}{3}ER^2(\varepsilon_s^3)^2\left(4\xi+\frac{R^2}{6\xi}\right) \tag{3.97}$$

The strain energy due to interaction between fields 2 and 3 is

$$U^{e_2e_3} \;=\; \frac{2}{9}ER^2\varepsilon_s^2\varepsilon_s^3\left(24\xi+\frac{R^2}{\xi}\right) \tag{3.98}$$

The strain energy due to interaction between fields 3 and 1 is

$$U^{e_3e_1} \;=\; 8ER^2\xi\left(\varepsilon^T+\varepsilon_s^1\right)\varepsilon_s^3 \tag{3.99}$$

Now, the total stored elastic strain energy U_C in the cluster is

$$\begin{aligned} U_C \quad &= \quad 8ER^2H\left(\varepsilon^T+\varepsilon_s^1\right)^2+\tfrac{8}{3}ER^2(\varepsilon_s^2)^2\left(\xi+\tfrac{R^2}{6\xi}\right)+\tfrac{2}{3}ER^2(\varepsilon_s^3)^2\left(4\xi+\tfrac{R^2}{6\xi}\right) \\ &+ \quad 8ER^2\,\xi\left(\varepsilon^T+\varepsilon_s^1\right)\,\varepsilon_s^2+\tfrac{2}{9}ER^2\varepsilon_s^2\varepsilon_s^3\left(24\xi+\tfrac{R^2}{\xi}\right)+8ER^2\xi\left(\varepsilon^T+\varepsilon_s^1\right)\varepsilon_s^3 \end{aligned} \tag{3.100}$$

Setting $\xi = \frac{R}{\sqrt{6}}$, the strain energy density of the TBC becomes

$$\begin{aligned} U =& 2E\left(\varepsilon^T+\varepsilon_s^1\right)^2+\frac{ER}{H}\left[\frac{2\sqrt{6}}{9}(\varepsilon_s^2)^2+\frac{5\sqrt{6}}{36}(\varepsilon_s^3)^2\right. \\ &\left.+\sqrt{\frac{2}{3}}(\varepsilon^T+\varepsilon_s^1)\varepsilon_s^2+\frac{5\sqrt{6}}{18}\varepsilon_s^2\varepsilon_s^2+\frac{2}{\sqrt{6}}(\varepsilon^T+\varepsilon_s^1)\varepsilon_s^3\right] \end{aligned} \tag{3.101}$$

The expressions for ε_s^1 given by eqn. 3.85, ε_s^2 given by eqn. 3.86 ε_s^3 given by eqn. 3.87 in terms of state variables can now be used in eqn. 3.101 to express the strain energy density U in terms of state variables $(u_{cr}, u_{cl}, u_{cr2})$. Now the Gibbs energy density G of the TBC can be obtained by adding U to G_λ given by eqn. 3.93

$$\begin{aligned} G(u_{cr},u_{cl},u_{cr2}) \;&= G_\lambda^{cl}(u_{cl})+G_\lambda^{cr^b}(u_{cr},u_{cl})+G_\lambda^{cr^t}(u_{cr})+G_\lambda^{cr2^b}(u_{cr2},u_{cl}) \\ &+G_\lambda^{cr2^t}(u_{cr2})+U(u_{cr},u_{cl},u_{cr2}) \end{aligned} \tag{3.102}$$

3.8.3 Determination of rate potential ψ

Similar to the 2DOF problem, we can now find the rate potential ψ per unit volume of the TBC (see Fig. 3.24a.). The dissipation from bulk contacts in the whole cluster per unit volume is given by

$$\psi_{cl}(\dot{u}_{cl}) = K_3\dot{u}_{cl}^2\left[\lambda-\sqrt{\lambda^2-4\lambda u_{cl}\cot\beta}\right]^2\left(D_s\lambda\cos\beta+(D_g-D_s\cos\beta)\sqrt{\lambda^2-4\lambda u_{cl}\cot\beta}\right) \tag{3.103}$$

Where K_3 is

$$K_3 \;=\; \frac{(R-d)}{12Rd\lambda D_gD_s\cos\beta} \tag{3.104}$$

The rate potential per unit volume of the TBC at the primary imperfection is exactly the same as the sum of eqns. 3.62 and 3.64 in the two DOF problem. The dissipation

from contacts at the secondary imperfection in the bottom portion of the cluster can be obtained similar to that of a primary imperfection as

$$\psi^b_{cr2} \;=\; \int_0^{\xi} \psi^b_{cr2}(\dot{u}_{cr2}, \dot{u}_{cl}, x_3)\, dx_3 \tag{3.105}$$

Further, the contribution to the rate potential in the top portion of the cluster at the secondary imperfection where there is uniform contact over height $(H - \xi)$ is given by

$$\begin{aligned}\psi^t_{cr2}(\dot{u}_{cr2}) =& K_2 \dot{u}^2_{cr2} \left[\lambda - \sqrt{\lambda^2 - 4\lambda u_{cr2} \cot\beta}\right]^2 (D_s \lambda \cos\beta \\ &+ (D_g - D_s \cos\beta)\sqrt{\lambda^2 - 4\lambda u_{cr2}\cot\beta}\Big)\end{aligned} \tag{3.106}$$

Now the rate potential per unit volume of the TBC is given as the sum of eqns. 3.103, 3.62, 3.64, 3.105 and 3.106.

$$\begin{aligned}\psi(\dot{u}_{cr}, \dot{u}_{cl}, \dot{u}_{cr2}) \;=& \psi_{cl}(\dot{u}_{cl}) + \int_0^{\xi} \psi^b_{cr}(\dot{u}_{cr}, \dot{u}_{cl}, x_3)\, dx_3 \\ &+ \psi^t_{cr}(\dot{u}_{cr}) + \int_0^{\xi} \psi^b_{cr2}(\dot{u}_{cr2}, \dot{u}_{cl}, x_3)\, dx_3 + \psi^t_{cr2}(\dot{u}_{cr2})\end{aligned} \tag{3.107}$$

The second and third terms in eqn. 3.107 are to be numerically integrated at each time step during the solution process.

3.8.4 Numerical solution of three kinematic variables system

The additional set of non-dimensional parameters in this problem are

$$\bar{u}_{cr2} = \frac{u_{cr2}}{\lambda}; \quad \bar{w}_{cr2} = \frac{w_{cr2}}{\lambda}; \quad \bar{b}_{cr2} = \frac{b_{cr2}}{\lambda}; \quad \bar{l}_{cr2} = \frac{l_{cr2}}{\lambda}; \tag{3.108}$$

Considering elastic constraint up to $\xi = \frac{R}{\sqrt{6}}$ in the cluster and the sub-cluster, the non-dimensional form of $\dot{G}$ and ψ are

$$\begin{aligned}\dot{\bar{G}}(\dot{\bar{u}}_{cr}, \dot{\bar{u}}_{cl}, \dot{\bar{u}}_{cr2}) =& \dot{\bar{G}}^{cl}_{\lambda}(\dot{\bar{u}}_{cl}) + \dot{\bar{G}}^{cr^b}_{\lambda}(\dot{\bar{u}}_{cr}, \dot{\bar{u}}_{cl}) + \dot{\bar{G}}^{cr^t}_{\lambda}(\dot{\bar{u}}_{cr}) + \dot{\bar{G}}^{cr2^b}_{\lambda}(\dot{\bar{u}}_{cr2}, \dot{\bar{u}}_{cl}) \\ &+ \dot{\bar{G}}^{cr2^t}_{\lambda}(\dot{\bar{u}}_{cr2}) + \dot{\bar{U}}(\dot{\bar{u}}_{cr}, \dot{\bar{u}}_{cl}, \dot{\bar{u}}_{cr2})\end{aligned} \tag{3.109}$$

$$\begin{aligned}\bar{\psi}(\dot{\bar{u}}_{cr}, \dot{\bar{u}}_{cl}, \dot{\bar{u}}_{cr2}) =& \bar{\psi}_{cl}(\dot{\bar{u}}_{cl}) + \int_0^{\frac{\bar{R}\bar{H}}{\sqrt{6}}} \bar{\psi}^b_{cr}(\dot{\bar{u}}_{cr}, \dot{\bar{u}}_{cl}, \bar{x_3})\, d\bar{x_3} + \bar{\psi}^t_{cr}(\dot{\bar{u}}_{cr}) \\ &+ \int_0^{\frac{\bar{R}\bar{H}}{\sqrt{6}}} \bar{\psi}^b_{cr2}(\dot{\bar{u}}_{cr2}, \dot{\bar{u}}_{cl}, \bar{x_3})\, d\bar{x_3} + \bar{\psi}^t_{cr2}(\dot{\bar{u}}_{cr2})\end{aligned} \tag{3.110}$$

We can now set up the equations in non-dimensional form and solve solve numerically.

3.8.5 Results and discussion

The set of nonlinear ODEs are solved and time integrated by a fourth order Runge-Kutta(RK-4) scheme from an initial state of $\bar{u}_1^{cr} = 0.045$, $\bar{u}_1 = 0.055$ and $\bar{u}_1^{cr2} = 0.05$. If $\bar{E} < 600$ complete sintering of the cluster and imperfections occurs independent of the choice of geometric and other material parameters, including the initial values of $\bar{u}$ in the cluster and along the two families of imperfections. For larger values of $\bar{E}$ we observe two major different types of mud cracking behaviour, depending on the magnitude of $\bar{E}$ and the size of the cluster $\bar{R}$. For $\bar{E} = 3000$ and $\bar{R} = 1.2$, cracks fully develop at the primary imperfections, while the secondary imperfections fully densify, and sintering is arrested in the cluster before full density is achieved as shown in Fig. 3.26. Full sintering of the secondary imperfections appears counter intuitive. One might expect sintering to be arrested in a similar way to that observed in the cluster. It is interesting to note, however, that for situations where an initial imperfection is introduced into a coating such that $\bar{u}_1^{cr} > \bar{u}_1$ full densification can occur at the site of the imperfection, while the cluster only partially sinters. This illustrates that depending on the magnitude of the imperfection we can either get cracking or localised densification. In the context of Fig. 3.26, this suggests that it is not energetically favourable for a secondary crack to form, but it is possible for local densification to occur, promoted by small differences in the sintering response at these locations with increasing time.

Increasing $\bar{R}$ to 1.4, the primary and secondary imperfections develop into cracks as shown in Fig. 3.27. As before the cluster does not fully densify, but formation

of the secondary cracks reduces the constraint on the sintering process and a higher density is achieved than for the situation $\bar{R} = 1.2$ shown in Fig. 3.27. From a series of simulations of this type where we systematically change $\bar{E}$ and $\bar{R}$ we can map out the conditions under which the different types of behaviour typified by Figs 3.26 and 3.27 occur. The resulting map is shown in Fig. 3.25. As $\bar{E}$ is increased the value of $\bar{R}$ at the transition between the two types of behaviour (ie the limiting crack spacing) increases. This reflects the fact that the larger the value of $\bar{E}$, the greater the constraint on sintering, which results in a smaller build up of elastic strain energy in the coating to drive the desintering and cracking process. These calculations correspond to an idealised geometric situation, but Fig. 3.25 suggests that once the crack spacing has reduced to that represented by the solid line on the figure, no further cracking can occur. Thus the line provides an indication of the value of $\bar{R}$ at which saturation of cracks occurs. Consider the case where $\bar{E} = 3000$. Fig. 3.25 then gives the transition between the two cracking patterns at $\bar{R} \approx 1$. Thus for a primary spacing of the imperfections slightly less than this value cracks will form with a spacing $2\bar{R} \approx 2$, while for a slightly larger value of $\bar{R}$ cracks will form at both the secondary and primary imperfections giving a crack spacing $\bar{R} \approx 1$. Thus in practice we would expect to see a pattern of cracks with spacing, CS , in the range $\bar{R} \leq CS \leq 2\bar{R}$. This gives, CS, in the range $1.5H \leq CS \leq 3H$, in terms of thickness, H, of the coating.

3.8.6 Mud-cracked cluster with secondary set of imperfections

In order to validate the 3DOF analytical mode described above, a number of computational studies have been undertaken. Here, we consider the situation where there is a fully developed primary set of cracks in the TBC and examine whether a secondary set of imperfections develop into cracks. Fig. 3.28a shows a mud-cracked cluster with secondary imperfection. Fig. 3.28b shows the geometric model of one-fourth of a mud-cracked cluster with secondary imperfections for FE analysis. We consider the

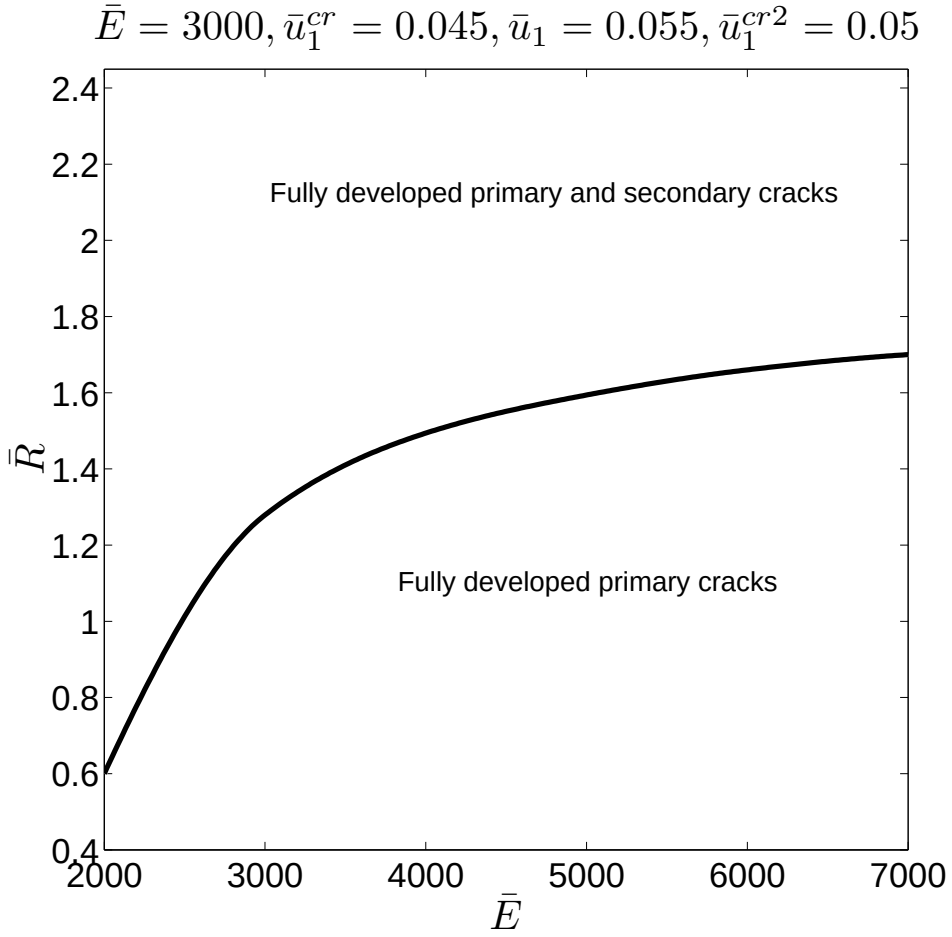

Figure 3.25: Failure map as a function of cluster size and modulus of coating

situations where $\bar{E} = 3000$ and $\bar{R}$=1 or 2. These two situations indicate the two types of cracking patterns as observed in the analytical model indicating that the secondary imperfections should not develop into cracks when $\bar{R} = 1$, but secondary cracking is expected when $\bar{R} = 2$. In these simulations an initial imperfection exists over the entire height (x_3-direction) of the TBC. We use the same initial conditions as for the 3DOF analytical model. In the defect free elements the initial condition is $\bar{u}_0^1 = 0.055, \bar{u}_0^2 = 0.055$. For the elements with imperfections the initial condition $\bar{u}_0 = 0.05$, for contacts parallel to the line of the defect and $\bar{u}_0 = 0.055$ perpendicular to the defect (see Fig. 3.29).

First consider the case with $\bar{E} = 3000$ and $\bar{R} = 1$. Contours of constant $\bar{b}_2$ are

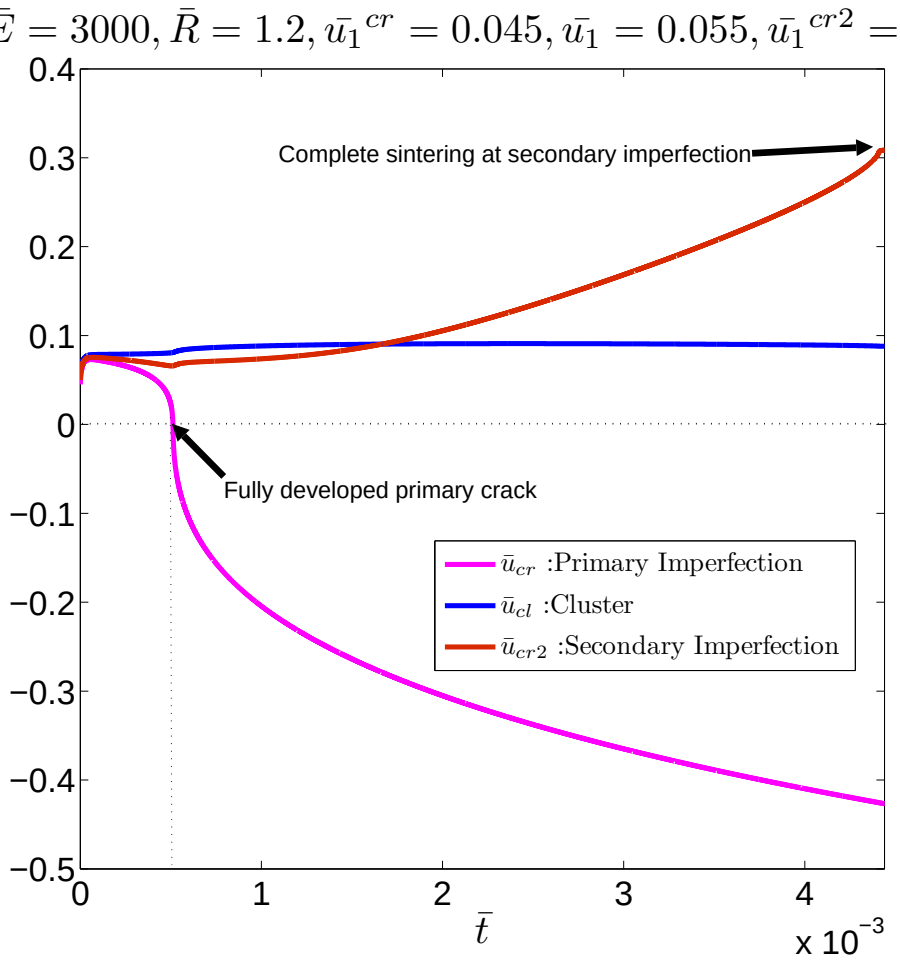

Figure 3.26: A typical plot showing the formation of primary crack

shown in Figs. 3.30a and 3.30b after a time $\bar{t} = 7.8 \times 10^{-3}$, after which no further sintering occurs. Towards the top of the coating, the columns have fully sintered throughout the cluster and across the initial imperfections. In this region the cluster does not experience any constraint from the coating (as predicted by the Rayleigh Ritz analysis of an isolated cluster). Towards the bottom of the coating sintering within the cluster is incomplete and desintering occurs along the imperfections leading to a crack which grows to 1/4th of the height of the column. However, this analysis does not provide any information about the final pattern of cracks in the coating.

The terminal state for the situation where $\bar{R} = 2$ is shown in Figs. 3.31a and 3.31b. A crack now forms at the secondary imperfection and propagates through the height

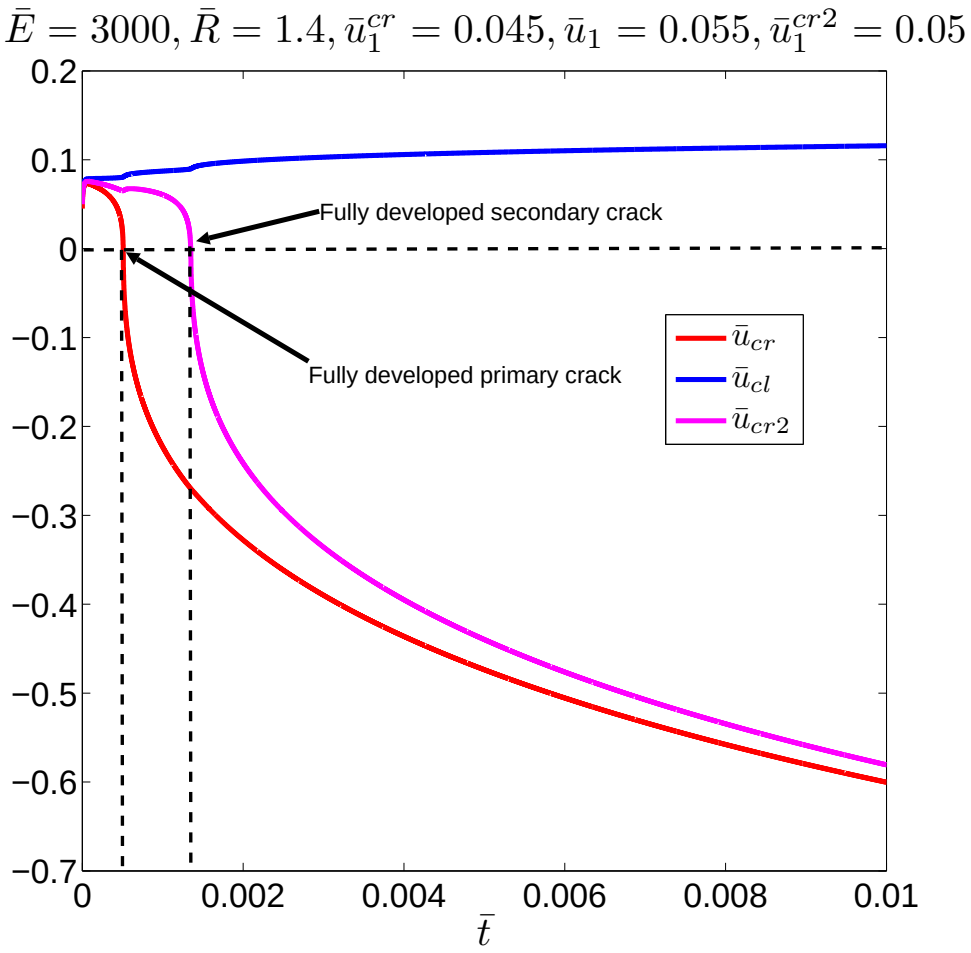

Figure 3.27: Formation of primary and secondary cracks

of the coating. This is consistent with the simplified 3DOF model which correctly identifies when a secondary crack can grow through the thickness of the coating.

3.9 Conclusions

Two micro-mechanical sintering models have been developed to capture the essential physics of the mud-cracking phenomenon in EB-PVD TBCs under isothermal conditions based on the information provided by computational models described in chapter 2. Mud-cracks can form in a coating under conditions where sintering in a perfect coating would be arrested before full density is achieved. As sintering is

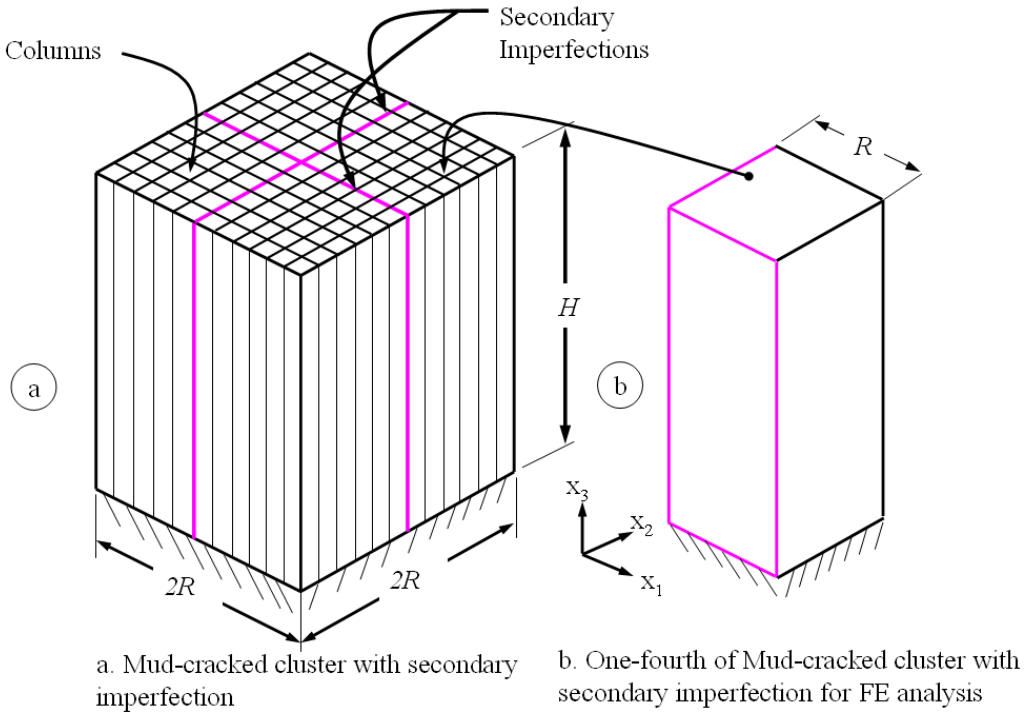

Figure 3.28: a. Mud-cracked cluster with secondary imperfection b. One-fourth of mud-cracked cluster with secondary imperfection for FE analysis.

arrested, desintering can occur at the site of small imperfections within the coating, relaxing the constraint on the remaining material allowing it to sinter towards a lower energy state. A coating can contain a large number of imperfections of different intensity, with cracks forming at different locations at different times during the sintering process. Eventually, the density of cracks will saturate. An assessment of the final crack density has been made using a three degree of freedom model, which follows the evolution of a body which contains two families of imperfections. The transition from one family of imperfections developing into cracks to both families cracking is used to estimate the final density of mud cracks in a coating. The density depends on the stiffness of the coating and results in a crack spacing that scales with the thickness of the coating.

In the 2DOF problem, it was observed that the build-up of in-plane tensile stress with progressive sintering triggers the development of a primary set of mud-cracks. Formation of a primary set of mud-cracks in turn partially relieves this stress and

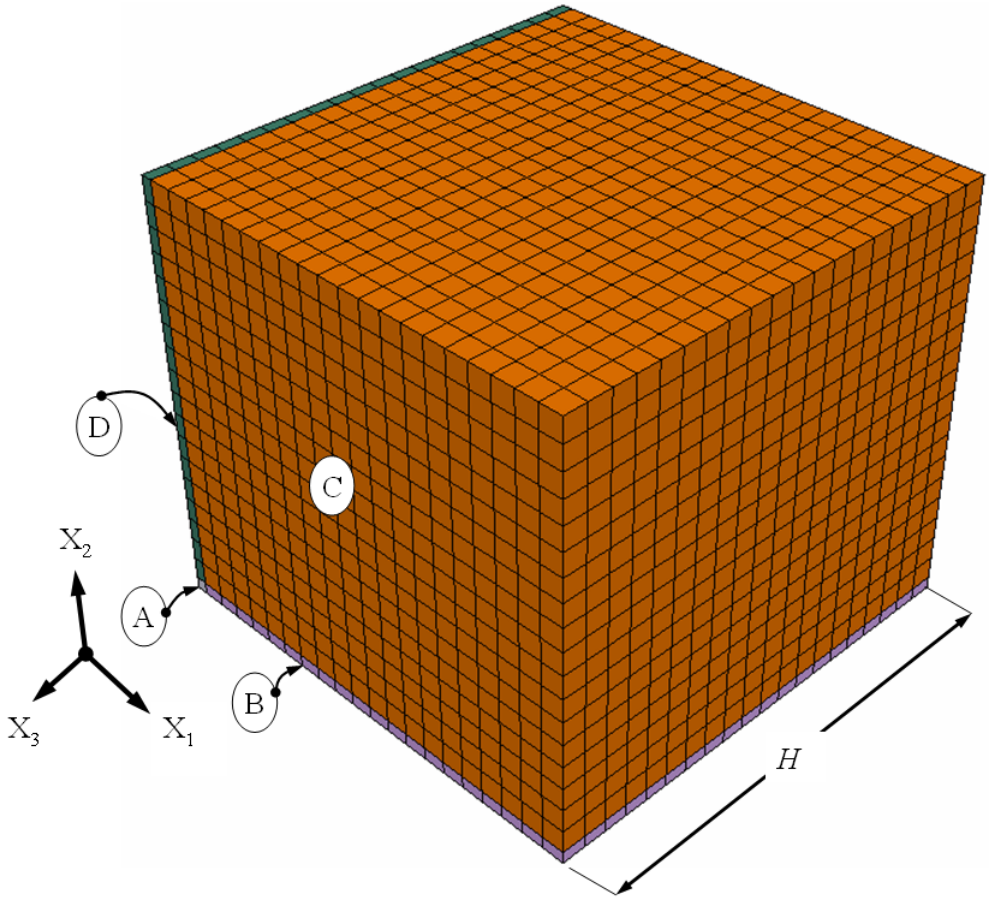

Figure 3.29: Finite element model of one-fourth of the mud-cracked cluster with secondary imperfection: A,B and D are elements with imperfection, D-Defect free elements, A: $\bar{u}_0^1 = 0.05, \bar{u}_0^2 = 0.05$; B: $\bar{u}_0^1 = 0.055, \bar{u}_0^2 = 0.05$; D: $\bar{u}_0^1 = 0.05, \bar{u}_0^2 = 0.055$; C: $\bar{u}_0^1 = 0.055, \bar{u}_0^2 = 0.055$;

accelerates subsequent sintering within the mud-cracked island clusters. From the 3DOF problem, it was found that the build of tensile stress within island clusters leads to further mud-cracking within mud-cracked clusters. This process continues until sintering is completely switched off in the mud-cracked sub-islands. From these models, it was observed that the primary cracks can develop early if the spacing considered between the primary set of imperfections is larger. After the formation of a primary set of cracks, a subsequent set of secondary cracks form within the mud cracked cluster-islands of the TBC. This process of mud-cracking continues and eventually the crack density saturates to a constant value for given initial conditions

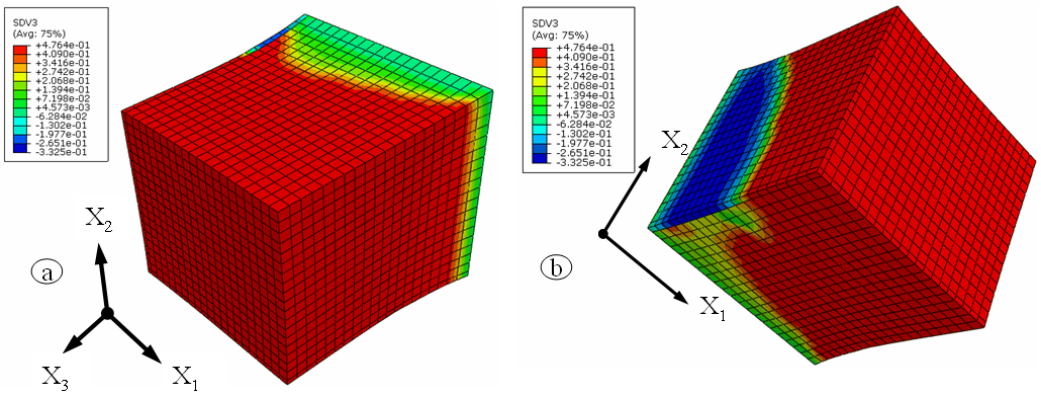

Figure 3.30: Full sintering of secondary imperfection: $\bar{b}_2 \simeq 0.5$ except at the bottom of the cluster for $\bar{E} = 3000$ and $\bar{R} = 1$.

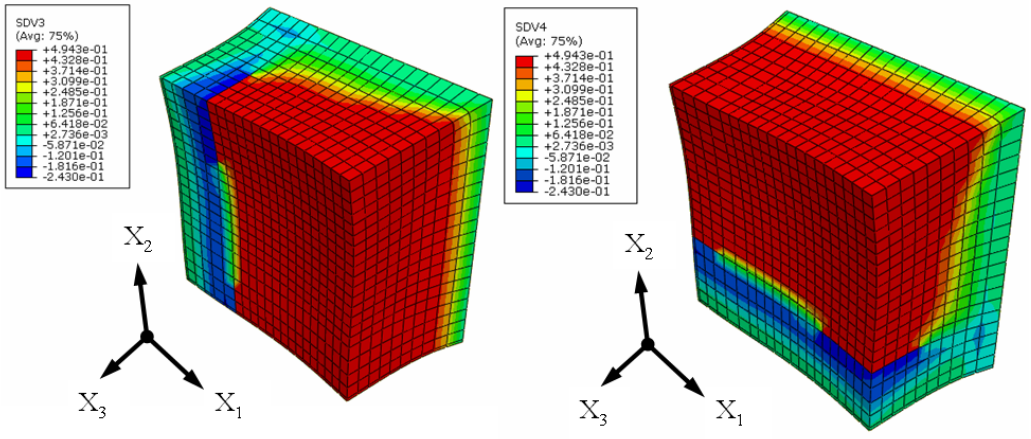

Figure 3.31: Fully developed crack close to secondary imperfection ($\bar{b}_1$) except at the bottom of the cluster for $\bar{E} = 3000$ and $\bar{R} = 2$.

($\bar{u}_1 > \bar{u}_1^{cr2} > \bar{u}_1^{cr}$) and geometrical properties of the coating, in the practical range of modulus of the coating. The Young's modulus of the ceramic coating itself is in the range 5-40GPa. From the micrographs of the EB-PVD coatings it can be seen that the wave length λ ranges from 0.2-2μm. These values correspond to a non-dimensional modulus range $\bar{E} = 1500 - 120000$. We explored the sintering response of the EB-PVD in this study in the range $\bar{E} = 300 - 7000$. Here, we are mainly interested in exploring the mud-cracking phenomenon. The key to this is the choice of appropriate contact model. Predicted saturated mud-crack spacing, CS, is in the range $1.5H \leq CS \leq 3H$, where H is the thickness of the coating. Experimentally

observed CS is in the range $3H \leq CS \leq 10H$ [40]. Crack spacing predicted in this study is consistent in the lower range of experimentally observed crack spacing. Results suggest that no further cracks can form below the saturated crack spacing size $\bar{R}$. Mud cracking may eventually lead to loss of structural integrity of the coating system. An advantage of the simple models over the computational models described in chapter 2 is that a wide range of geometric conditions with different material properties can be analysed efficiently.

Chapter 4

Axisymmetric Contact Computational Models

4.1 Abstract

In this study we focus on computational aspects of in-service sintering and the eventual inter-columnar mud-cracking of an EB-PVD top coat which comprises axisymmetric contact geometry between columns and examine the conditions under which inter-columnar cracks can develop within the coating. Here we assume that sintering is driven by changes in interface free energy of columns and the potential energy of the applied stress. We neglect much faster diffusion that occurs over the free surfaces of the asperities and assume that the rate of sintering of the contacting asperities is determined by diffusion along the interface between the contacting asperities to keep the formulation simple. Ignoring surface diffusion altogether is valid provided surface diffusion is more rapid than the grain boundary diffusion. We account for time dependent contact modulus in the formulation as a function of sintering strain. We develop a macroscopic constitutive model to perform finite element calculations in order to evaluate the sensitivity of the sintering response to imperfections in the coating.

4.2 Problem Statement

In the analyses of chapter 2 and 3 we assumed a simple 2-D trapezoidal profile for the evolving shape of the asperities between the contacting columns of the ePVD coating. This provides a dense distribution of contacts. In practice the contacts that form are axisymmetric, with an initial spacing that is much greater than the size of the asperities, as illustrated in the SEM image of Fig. 4.1 taken from Lughi et al [40]. In the previous chapters, we also assumed that the in-plane modulus is constant. In practice, the modulus depends on the stiffness of the columns and the stiffness of the contacts, which evolves as the size of the contacts grow as the TBC sinters. During the initial stages of sintering, the in-plane modulus is largely determined by the stiffness of the contacting asperities. As the asperities grow and the contact stiffness increases, the modulus approaches that of a fully dense solid. In this and the following chapter we modify the models described in chapters 2 and 3 to provide more realistic representation of size, shape, distribution and the stiffness of the evolving contacts. We evaluate the degree to which these additional effects modify the predictions presented in the previous chapters.

In this chapter we initially develop a constitutive model for a discrete distribution of axisymmetric asperities which take into account the influence of contact stiffness or the in-plane elastic properties. This model is then employed in a computational study of constrained sintering of a perfect TBC with the simulations compared with an analytical solution of intercolumnar sintering. We go on to study the influence of imperfections in the initial microstructure on the sintering response. As in chapter 3, we consider the behaviour of a TBC that contains an arbitrarily placed imperfection. Then we explore the sintering response when the TBC contains a family of imperfections to identify the conditions under which the imperfections grow into cracks.

Following the analyses of chapter 2 and 3 we idealise the top coat as a regular array of parallelepiped columnar grains of square cross-section of size $d \times d$, as illustrated in Fig. 4.2a. The contacts between columns are assumed to be axisymmetric as shown

in Fig. 4.2a. These contacts are discrete in the pre-sintered state. The mean centre to centre distance between contacts is s. The TBC layer is of height H and it is assumed that the TBC film is perfectly bonded to the substrate. We describe the response of the TBC in terms of a Cartesian co-ordinate system in which the x_1 and x_2 directions lie in the plane of the coating and are parallel to the sides of the columnar grains. The x_3 direction is perpendicular to the plane, and is in the direction of thickness of the coating with its origin at the interface with the substrate. In the pre-sintered state, asperities on columns are just in point contact. During service at higher temperature, sintering occurs due to diffusional flow of material into the gaps between contacts. As a result macroscopic sintering strains, $\varepsilon^s_{11}, \varepsilon^s_{22}$ evolve in the TBC. By considering the response of a representative volume element (RVE), we can develop a constitutive model for the sintering rate in terms of the microscopic geometric variables of the axisymmetric contacts and columns and the macroscopic stress experienced by the RVE. We initially perform a computational study of intercolumnar sintering of a constrained perfect film (Fig. 4.2.a). The results of finite element studies are compared directly with an analytical solution of constrained sintering of a perfect film which we present in the next chapter. We then use the computational model to evaluate the influence of imperfections. The resulting mud-cracked pattern is an idealisation of the patterns observed experimentally, for example by Lughi et al [40], see Fig. 4.2b. These simulations are used to guide the development of analytical models, which are described in chapter 5.

4.3 Computational Model

Consider a representative macroscopic volume element of the coating as shown in Fig. 4.3a and b. The element has a square cross section of size $d \times d$, made up of 4 quarter columns. These columns are in contact through axisymmetric asperities in the planes perpendicular to x_1 and x_2 axes. Let the height of the element be t_1. We envisage that the elastic response depends on the detailed structure of asperities across the interface between the columns. We consider the effect of asperity con-

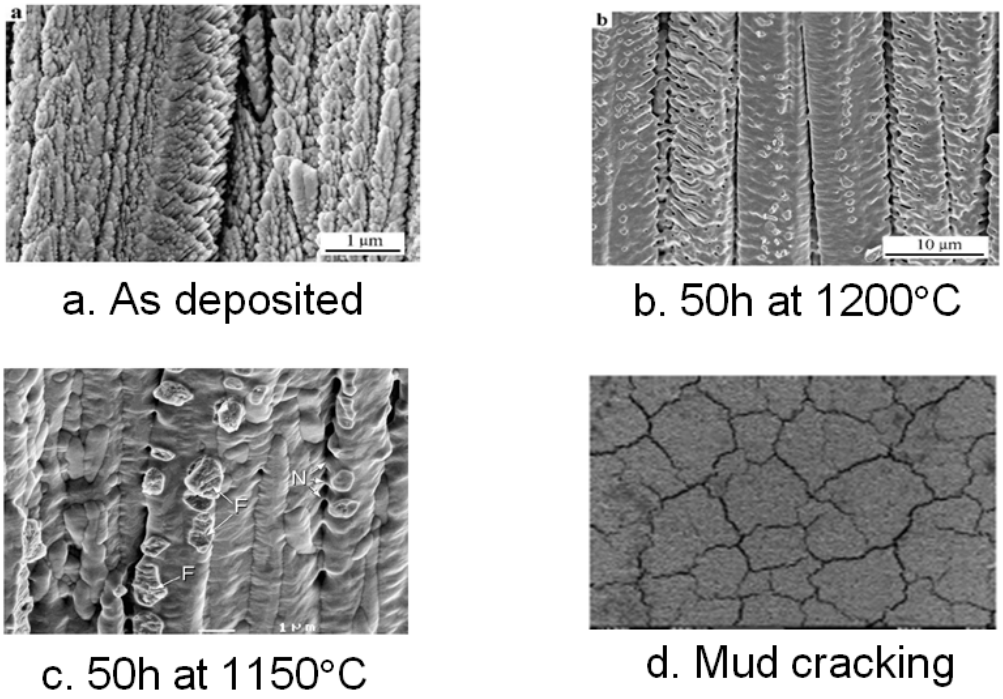

Figure 4.1: Experimental observations under isothermal sintering of ePVD coating: a. SEM image of ePVD coating in as deposited condition. b. Microstructure of TBC after 50h at 1200°C. c. Microstructure of TBC after 50h at 1150°C. d. Micrograph of mud-cracked TBC

tact stiffness in developing a constitutive model here. Inelastic deformation results from sintering and sliding between the asperities. We assume a simple linear viscous response for the sliding deformation. The inelastic strain-rates $\dot{\varepsilon}^s_{11}, \dot{\varepsilon}^s_{22}$ arise from diffusional rearrangement at the asperity scale on two independent planes. We can therefore model these processes independently and superimpose the results to give the full constitutive response.

We assume simple axisymmetric shapes for the evolving asperities and develop the constitutive model based the thermodynamic variational principle described by Cocks et al [45] and Suo [87]. This requires an identification of the different contributions to the functional

$$\Phi \;=\; \psi + \dot{G} \tag{4.1}$$

where ψ is a rate potential and $\dot{G}$ is the rate of change of Gibbs free energy of the

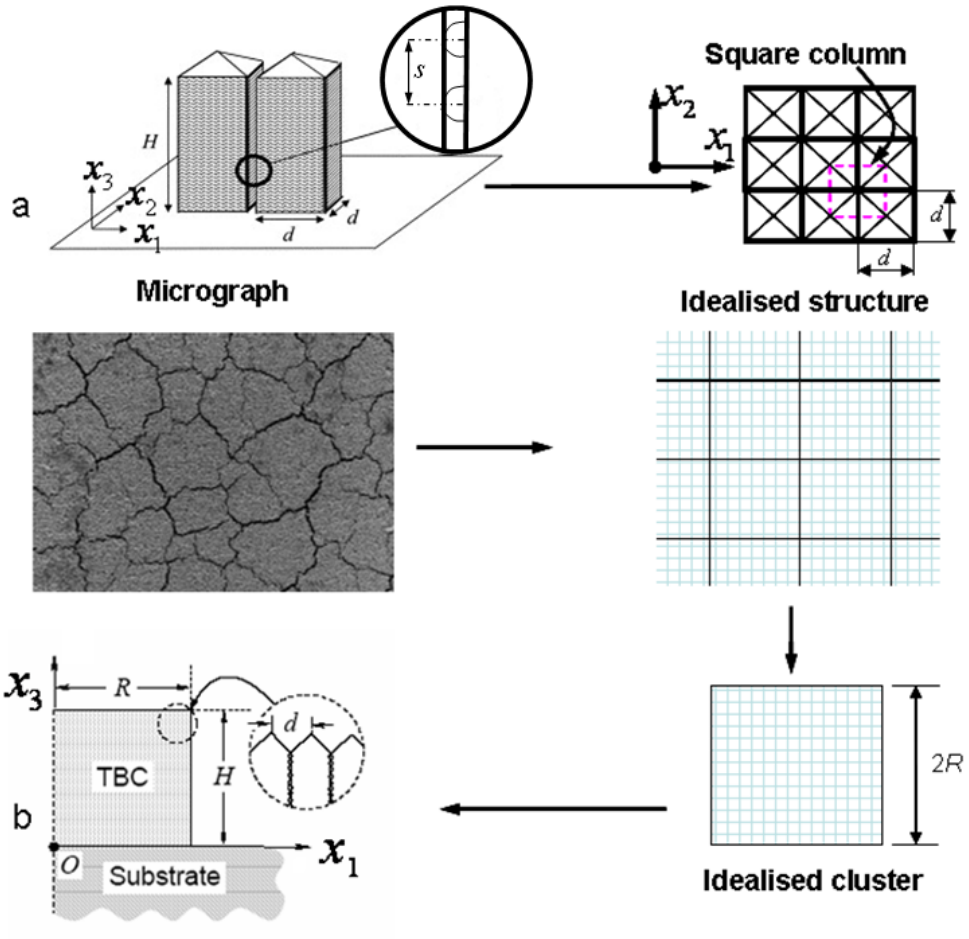

Figure 4.2: a. Sintering of neighbouring TBC columns, each of cross-section $d \times d$ perfectly bonded to the substrate. The distance between contacts is s. b. The mud-cracked TBC layer is idealized as an assembly of square clusters, each of height H and size $2R$. The clusters comprise columns which progressively sinter together

system. As in chapters 2 and 3 each of these quantities are expressed in terms of geometric rate quantities that describe the rate of evolution of the microstructure (ie the change in shape of the asperities). The actual combination of rates is that which minimises the functional Φ. We consider an isothermal situation here and solve for the evolution of the sintering strains ε^s_{11} and ε^s_{22} in the x_1 and x_2 directions respectively under fixed temperature T.

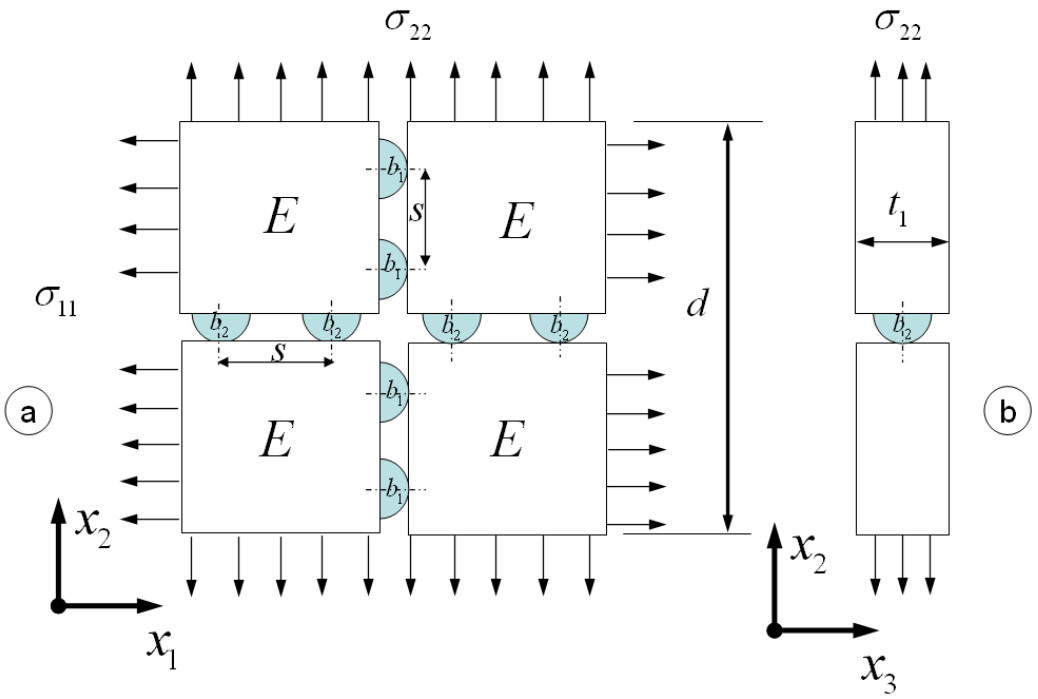

Figure 4.3: A representative macroscopic volume element of the coating. The element has a square cross section $d \times d$, made up of 4 quarter columns which are in contact. The height of the element is t_1. a. Plan view of the RVE b. Side view of the RVE.

4.3.1 Contact geometry

We assume the axisymmetric contact geometry shown in Fig. 4.4. Following the models described in chapters 2 and 3, we associate all the surface roughness with one of the contacting surfaces, while the other surface is treated as perfectly flat. It is convenient to define a reference configuration as illustrated in Fig. 4.4a. Note that the reference configuration is introduced for algebraic convenience only and may not be realized in practice. In practice, pre-sintering would have occurred during deposition itself to some degree. Initially, in the pre-sintered state as given by the reference configuration in Fig. 4.4a, the radius of the hemi-sphere is R_o and the volume of the asperity, $V = 2/3\pi R_o^3$. Note that initially $R_o = w_o$, where, w_o is the initial asperity height at the interface in the pre-sintered state. In their analysis of sintering of arrays of spherical particles Parhami et al [90] and Cocks et al [45] demonstrated that an accurate prediction of the sintering response can be obtained by assuming simple

geometric profiles of the evolving shape of the particles. We follow their approach here and assume that as the columns approach each other and the contacts grow, the shape of a particle can be represented by a truncated hemisphere connected to a cylindrical region. Parhami et al [90] allow for the radius of a spherical particle and cylindrical region to evolve during sintering, but as demonstrated by Cocks et al [45] the radius of the spherical particle remains essentially constant, allowing the evolving shape to be expressed in terms of a single degree of freedom, the contact radius b. As the contact grows, the size of the truncated sphere reduces, until it is consumed by the cylindrical region. We follow a similar description here for the evolving shape of an asperity. During the early stages of sintering, the configuration is as shown in Fig. 4.4b. Eventually this evolves into the cylindrical profile of Fig. 4.4c when $b = R_o$

Consider, initially, the configuration of Fig. 4.4b. Here, w is the asperity height at any instant. The semi-contact width is b. And the height of the cylinder formed at the interface at any instant is h. Volume is conserved during sintering. Therefore, the volume of the gray shaded portion in Fig. 4.5 must be equal to the volume of the cylinder of radius b and height h. From geometry, we can readily determine this volume:

$$V_{cap} = \frac{2}{3}\pi R_o^3 \left[1 - \frac{1}{2}\sqrt{1 - \left(\frac{b}{R_o}\right)^2}\left[2 + \left(\frac{b}{R_o}\right)^2\right]\right] \tag{4.2}$$

Equating this to the volume of the cylinder gives

$$\frac{2}{3}\pi R_o^3 \left[1 - \frac{1}{2}\sqrt{1 - \left(\frac{b}{R_o}\right)^2}\left[2 + \left(\frac{b}{R_o}\right)^2\right]\right] = \pi b^2 h \tag{4.3}$$

Rearranging the above equation gives

$$h = \frac{2}{3}\frac{R_o^3}{b^2}\left[1 - \frac{1}{2}\sqrt{1 - \left(\frac{b}{R_o}\right)^2}\left[2 + \left(\frac{b}{R_o}\right)^2\right]\right] \tag{4.4}$$

From the geometry shown in Fig. 4.5, we can also determine w:

$$w = R_o\sqrt{1 - \left(\frac{b}{R_o}\right)^2} + h \tag{4.5}$$

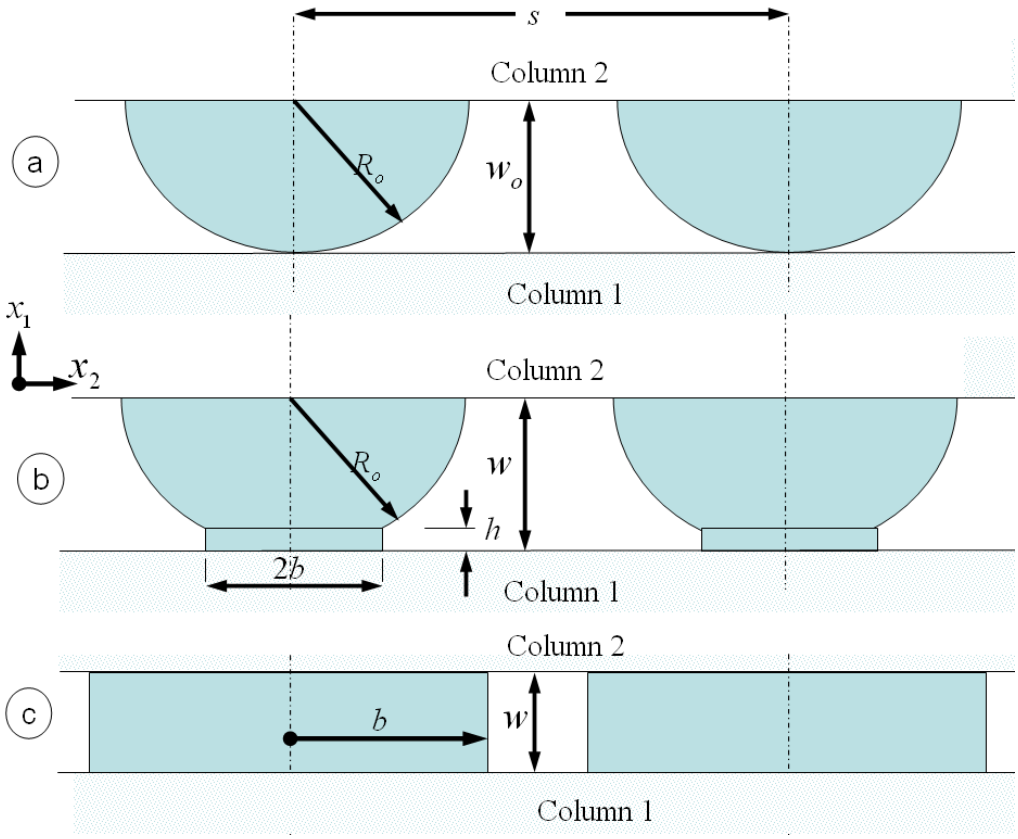

Figure 4.4: Axisymmetric contact geometry between neighbouring columns: a. Reference configuration (purely hemi-spherical asperity) b. Intermediate configuration, column 2 displaced by an amount $(w_0 - w)$. c. Configuration (purely cylindrical asperity) after prolonged sintering.

This simplification of contact geometry allows us to reduce the number of independent geometric variables and to formulate an analytical micromechanical model for the evolution of contact geometry. Consider the situation where the element of Fig. 4.3 is subjected to stresses σ_{11} and σ_{22} in the x_1 and x_2 directions. Let w_1,b_1,h_1 be the geometric variables of an asperity on a plane normal to the x_1 direction and w_2,b_2,h_2 be the geometric variables of an asperity on a plane normal to the x_2 direction. w_o^1 and w_o^2 are the initial heights of the asperities on the respective planes. Similarly, b_o^1 and b_o^2 are the initial values of b_1 and b_2 respectively. As sintering progresses, the contact width $2b_i$(where $i = 1, 2$) increases and the combined peak-to-peak amplitude of the undulations w_i decreases. Also the height of the cylinder h_i formed at the interface

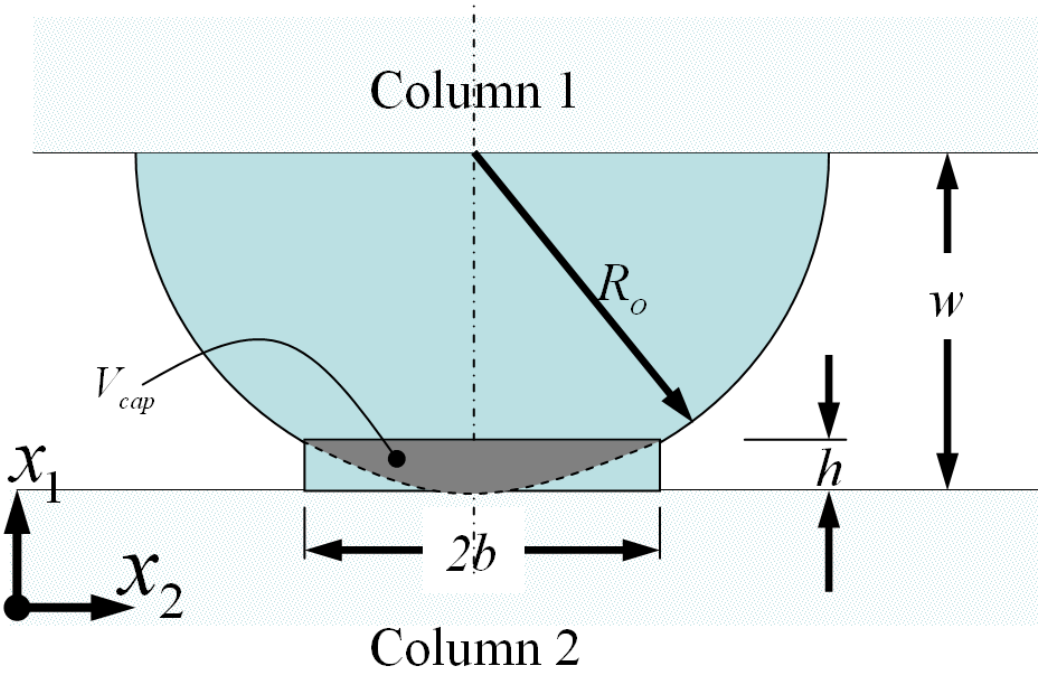

Figure 4.5: Current configuration any any instant. Volume of gray shaded portion is V_{cap}.

increases, while the radius of the asperity R_o remains the same. When $b_i \to R_o$, the asperity becomes a pure cylinder and $h_i \to w_i$. With further sintering, the cylinder flattens until $b_i \to s/2$. This is the instant of complete sintering of the TBC.

The task now is to solve for the local evolution of surface profile as characterized by b_i due to the interfacial diffusion of matter from the contacts into the gaps between the asperities. Interfacial diffusion is driven by the combined driving forces of the net reduction in interfacial energy, and the change in potential energy of the system.

The macroscopic sintering strain in the x_i direction ε^s_{ii} (where in the current context repeating a suffix does not imply summation) can be expressed in terms of the variable w_i which is the function of the primary unknown b_i.

$$\varepsilon^s_{ii} = \frac{w_i(b_i) - w^i_0}{d} \tag{4.6}$$

Note that w^i_0 is the initial value of state variable $w_i(b_i)$.

4.3.2 Local sintering at contacts

We further simplify the model by assuming that the rate controlling part of the dissipative process is diffusion along the boundary formed between the asperity and contacting column. Matter diffuses along the interface from the contacts, labelled OA in Fig. 4.6. Interfacial volumetric flux j per unit thickness (in units of m^2/s) is given by eqn. 2.5.

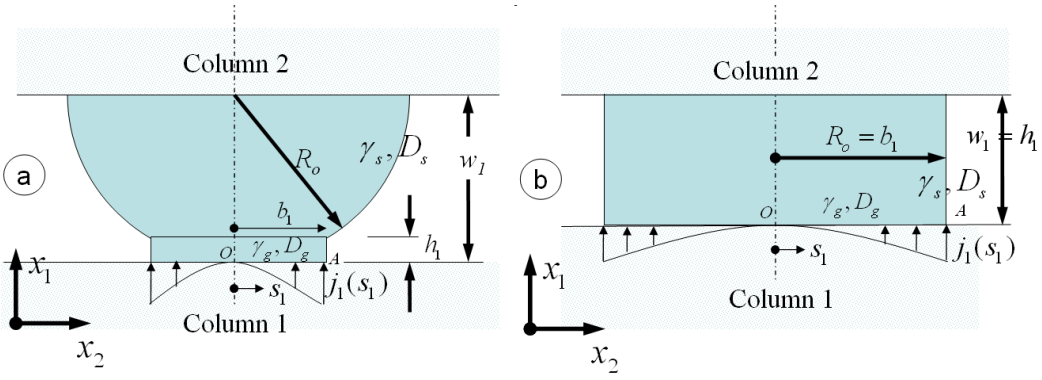

Figure 4.6: Definition of fluxes, surface energies and diffusivities at the contact geometry. a. $b_1 < R_o$ b. $b_1 \geq R_o$

Noting mass continuity at an interface given by eqn. 2.7, we can find the flux j, knowing the normal velocity of the evolving interface.

4.3.3 Thermodynamic variational principle (TVP)

Consider, intitially, the growth of contacts normal to the x_1 direction. At a given instant the state of the microstructure can be expressed in terms b_1. In order to derive the constitutive model we need to determine the rate of change of b_1 , ie $\dot{b}_1$. We get this by using the variational principle given by eqn. 4.1, which requires expressing ψ and $\dot{G}$ in terms of $\dot{b}_1$. By minimizing the functional Φ, we obtain $\dot{b}_1$.

Determination of Gibbs free energy

Consider a RVE of thickness t_1 and size $d \times d$ subjected to a stress σ_{11} in the x_1 direction as shown in Fig. 4.3. The Gibbs free energy is the sum of the interface

energy and the potential energy of the applied stress. The Gibbs free energy density is given by

$$G_1 \;=\; G_a N_{a1} + \sigma_{11}\frac{t_1 d(w_o^1 - w_1)}{t_1 d^2} \tag{4.7}$$

Where G_a is the interface energy per asperity and N_{a1} is the number of asperities per unit volume of the TBC on a plane normal to the x_1 direction.

Expressions for $b_1 \leq R_o$

In the initial stages of sintering $b_1 < R_o$ and the asperity takes the shape as shown in Fig. 4.6a. We can write the interface energy per asperity as

$$G_a \;=\; 2\pi R_o(w_1 - h_1)\gamma_s + 2\pi b_1 h_1 \gamma_s - \pi R_o^2 \gamma_s - \pi b_1^2 \gamma_s + \pi b_1^2 \gamma_g \tag{4.8}$$

and

$$N_{a1} \;=\; \frac{4}{\pi s^2 d} \tag{4.9}$$

Adopting the following normalisations

$$\bar{b}_1 = \frac{b_1}{R_o};\;\; \bar{w}_1 = \frac{w_1}{R_o};\;\; \bar{w}_o^1 = \frac{w_o^1}{R_o};\;\; \bar{s} = \frac{s}{R_o};\;\; \bar{d} = \frac{d}{R_o};\;\; \bar{h}_1 = \frac{h_1}{R_o};\;\; \bar{\gamma}_g = \frac{\gamma_g}{\gamma_s};\;\; \bar{\sigma}_{11} = \frac{\sigma_{11} R_o}{(1-\nu^2)\gamma_s}; \tag{4.10}$$

we can rewrite G_1 as

$$G_1 \;=\; \frac{4}{\bar{s}^2 \bar{d} R_o}\left[2(\bar{w}_1 - \bar{h}_1)\gamma_s + 2\bar{b}_1\bar{h}_1\gamma_s - \gamma_s - \bar{b}_1^2\gamma_s + \bar{b}_1^2\bar{\gamma}_g\gamma_s\right] + \frac{\bar{\sigma}_{11}(1-\nu^2)\gamma_s}{\bar{d}R_o}(\bar{w}_o^1 - \bar{w}_1) \tag{4.11}$$

Introducing $\bar{h}_1$ given by eqn. 4.4 and $\bar{w}_1$ as given by eqn. 4.5 into the 4.11 and differentiating the resulting expression for G_1 with respect to time, we obtain the rate of change of Gibbs energy density as

$$\dot{G}_1 \;=\; \frac{4\gamma_s}{\bar{s}^2\bar{d}R_o}\left[A_{11}(\bar{b}_1)\right]\dot{\bar{b}}_1 + \frac{\bar{\sigma}_{11}(1-\nu^2)\gamma_s}{\bar{d}R_o}\left[B_{11}(\bar{b}_1)\right]\dot{\bar{b}}_1 \tag{4.12}$$

where,

$$A_{11} \;=\; \frac{-2\bar{b}_1}{\sqrt{1-\bar{b}_1^2}} + \frac{4}{3}\left[\frac{-1}{\bar{b}_1^2} - \frac{1}{2}\sqrt{1-\bar{b}_1^2}\left(1 - \frac{2}{\bar{b}_1^2}\right) + \frac{1}{2}\left(\frac{2}{\bar{b}_1} + \bar{b}_1\right)\frac{\bar{b}_1}{\sqrt{1-\bar{b}_1^2}}\right] - 2\bar{b}_1 + 2\bar{b}_1\bar{\gamma}_g \tag{4.13}$$

and

$$B_{11} = \frac{\bar{b}_1}{\sqrt{1-\bar{b}_1^2}} - \frac{2}{3}\left[\frac{-2}{\bar{b}_1^3} + \frac{1}{2}\frac{\bar{b}_1}{\sqrt{1-\bar{b}_1^2}}\left(\frac{2}{\bar{b}_1^2+1}\right) + \frac{2}{\bar{b}_1^3}\sqrt{1-\bar{b}_1^2}\right] \tag{4.14}$$

Expressions for $b_1 \geq R_o$

When $b_1 \geq R_o$, the asperity adopts a cylindrical profile as shown in Fig. 4.6b. The expression for $\dot{G}_1$ has the same form as eqn. 4.12 but the functions A_{11} and B_{11} are now given below

$$A_{11} = \left[\frac{-2\bar{V}_1}{\pi\bar{b}_1^2} - 4\bar{b}_1 + 2\bar{b}_1\bar{\gamma}_g\right] \tag{4.15}$$

and

$$B_{11} = \frac{2\bar{V}_1}{\pi\bar{b}_1^3} \tag{4.16}$$

where, $\bar{V}_1$ is the non-dimensional volume of the cylindrical asperity at any instant and is equal to $\pi\bar{b}_1^2\bar{w}_1$.

Determination of rate potential

Let us now derive the macroscopic rate potential per unit volume of the TBC ψ_1 arising from diffusional flow of material over the asperities for the representative volume element of Fig. 4.3. We assume that grain boundary diffusion occurs along the local co-ordinate OA as shown in Fig. 4.6 and the energy dissipated by surface diffusion over the asperity is much smaller and can therefore be neglected. The rate potential per asperity is expressed in terms of the volumetric flux per unit depth j as given below.

$$\psi_a = \frac{1}{2D_g}\int_0^{b_1} 2\pi s_1 j_1^2(s_1)\, ds_1 \tag{4.17}$$

where D_g is the diffusion coefficient for interfacial diffusion along OA as specified by eqn. 2.6. The flux on OA can be obtained by considering mass conservation (eqn. 2.7). From the contact geometry, we can readily find the normal velocity of surface OA as

$$v_n = \dot{w}_1 \tag{4.18}$$

Upon invoking eqn. 2.7, the flux along interface OA is obtained as

$$j_1(s_1) = -\frac{1}{2}s_1\dot{w}_1 \tag{4.19}$$

The macroscopic potential per unit volume of the TBC is given by

$$\psi_1 \;=\; N_{a1}\psi_a \tag{4.20}$$

An explicit expression can be obtained for ψ_1 by integration of eqn. 4.17, using expressions for the flux and N_{a1} to give

$$\psi_1(\dot{b}_1) \;=\; \frac{4}{\pi s^2 d}\left[\frac{\pi \dot{w}_1^2 b_1^4}{16 D_g}\right] \tag{4.21}$$

Adopting normalisations given be eqn. 4.10 and normalising D_g such that $\bar{D}_g = D_g/D_g$, ψ_1 can be expressed as

$$\psi_1 \;=\; \frac{1}{4\bar{D}_g \bar{s}^2 \bar{d}}\frac{R_o^3}{D_g}\dot{\bar{w}}_1^2 \bar{b}_1^4 \tag{4.22}$$

$\dot{\bar{w}}_1$ in the above equation is obtained by differentiating eqn. 4.5 with respect to time and $\psi_1(\dot{\bar{b}}_1)$ can be re-written as

$$\psi_1(\dot{\bar{b}}_1) \;=\; \frac{1}{4\bar{D}_g \bar{s}^2 \bar{d}}\frac{R_o^3}{D_g}\bar{b}_1^4 C_{11}(\bar{b}_1)\dot{\bar{b}}_1^2 \tag{4.23}$$

where, $C_{11} = [-B_{11}]^2$. In the above expression for ψ_1, B_{11} comes either from eqn. 4.14 or eqn. 4.16 depending upon the current shape of the asperity.

Constitutive model

Substituting $\dot{G}_1$ given by eqn. 4.12 and ψ_1 given by eqn. 4.22 into eqn. 4.1 and minimising the resulting functional gives the rate of evolution of the microstructure $\dot{\bar{b}}_1$ as a function of the current state and applied stress. Here, the non-dimensional time is taken to be

$$\bar{t} \;=\; \frac{D_g \gamma_s t}{R_o^4} \tag{4.24}$$

The rate of evolution of $\bar{b}_1$ is then given by

$$\dot{\bar{b}}_1 \;=\; -\frac{2\bar{D}_g}{C_{11}\bar{b}_1^4}\left[4A_{11} + \bar{\sigma}_{11}(1-\nu^2)\bar{s}^2 B_{11}\right] \tag{4.25}$$

Differentiating eqn. 4.6, we get the sintering strain rate in the x_1 direction as

$$\dot{\varepsilon}_{11}^p \;=\; \frac{\dot{\bar{w}}_1}{\bar{d}} \tag{4.26}$$

Noting that $\dot{\bar{w}}_1 = (-B_{11})\dot{\bar{b}}_1$ and substituting $\dot{\bar{b}}_1$ given by eqn. 4.25 into the above equation, we can re-write the sintering strain rate $\dot{\varepsilon}^p_{11}$ as

$$\dot{\varepsilon}^p_{11} = \frac{2\bar{D}_g}{d\bar{b}_1^4 B_{11}}\left[4A_{11} + (1-\nu^2)\bar{s}^2\bar{\sigma}_{11}B_{11}\right] \equiv g_{11} \tag{4.27}$$

We can perform a similar analysis for a stress σ_{22} applied in the x_2 direction of the RVE to obtain

$$\dot{\varepsilon}^p_{22} = \frac{2\bar{D}_g}{d\bar{b}_1^4 B_{22}}\left[4A_{22} + (1-\nu^2)\bar{s}^2\bar{\sigma}_{22}B_{22}\right] \equiv g_{22} \tag{4.28}$$

The sintering strain rate in the x_1 direction, ε^p_{11}, is a function of the state variable $\bar{b}_1$ as given by eqn. 4.27 and the sintering strain in the x_2 direction, ε^p_{22}, is a function of the state variable $\bar{b}_2$ given by the eqn. 4.28. We assume that the only source of inelastic deformation is sintering and sliding of the asperity contacts. Therefore $\varepsilon^p_{33} = 0$. It is also demonstrated in the Appendix A that $\gamma^p_{13} = \gamma^p_{23} = 0$. We complete the model by specifying a relationship for the shear sintering strain rate in the 1-2 plane as

$$\dot{\gamma}^p_{12} = \frac{\sigma_{12}}{\eta} \tag{4.29}$$

Where η is the shear viscosity. $\dot{\gamma}^p_{12}$ is non-dimensionalised taking $\bar{\eta} = \frac{\eta D_g}{(1-\nu^2)R_o^3}$ and is given by

$$\dot{\gamma}^p_{12} = \frac{\bar{\sigma}_{12}}{\bar{\eta}} \tag{4.30}$$

As a consequence of assuming no shear in the 1-3 and 2-3 planes, the columns are not expected to slide in these planes. These equations have been coded into ABAQUS using the user subroutines. The Newton-Raphson implicit scheme employed to solve the system of equations is detailed in the following section. The developed code has been used to simulate the sintering response of a constrained TBC with axisymmetric asperities as detailed in the following sections.

Elastic properties of the RVE

The stiffness of the coating changes with the evolution of contacting asperities. Considering the RVE shown in Fig. 4.3 and accounting for displacement due to asperities

in addition to displacement of the columnar grains, we can now write the effective modulus as a function of state variable b. The effective modulus is expressed below by assuming that the columns and the asperities are considered to be springs connected in series. The effective modulus, E_1, in the x_1 direction is given by

$$\frac{1}{E_1} = \frac{1}{E} + \frac{1}{q_1(b_1)d} \tag{4.31}$$

where, E is the modulus of the bulk material of the coating. q_1 is the effective contact stiffness in the x_1 direction and is a function of b_1. Similarly we can write the effective modulus in the x_2 direction, E_2, as

$$\frac{1}{E_2} = \frac{1}{E} + \frac{1}{q_2(b_2)d} \tag{4.32}$$

q_2 is the effective contact stiffness in the x_2 direction and is a function of b_2. The effective shear modulus in the $x_1 - x_2$ plane of the coating can be written as

$$\frac{1}{G_{12}} = \frac{1}{G} + \frac{1}{2q_1(b_1)d} + \frac{1}{2q_2(b_2)d} \tag{4.33}$$

where, G is the shear modulus of the bulk material of the coating, ie columns. Note that the functional form of normal and shear displacements of the asperities are the same [91]. Shear deformation in the $x_2 - x_3$ and $x_1 - x_3$ planes of the coating is evaluated in the Appendix A, where the coating is modelled as a micropolar (or Cosserat type) continuum. The description effectively treats the columns as beams, which bend and slide over each other, with sliding accommodated by elastic shear deformation of the asperities. In the limit where the columns are slender and can readily bend the shear moduli in the $x_1 - x_3$ and $x_2 - x_3$ planes are given by

$$\frac{1}{G_{13}} = \frac{1}{G} + \frac{1}{2q_1(b_1)d} \tag{4.34}$$

$$\frac{1}{G_{23}} = \frac{1}{G} + \frac{1}{2q_2(b_2)d} \tag{4.35}$$

The effective stiffness for the asperities is determined by considering two extremes of topology for the asperities. First, consider small, widely spaced asperities and treat them as isolated circular junctions of radius b and spacing s bridging two parallel

planes under a nominal tensile traction T. The tensile load $P = \frac{\pi s^2 T}{4}$ is carried by each junction. The displacement due to asperity is deduced from the solution for normal indentation of a half-space by a frictionless, rigid punch of circular cross section and the resulting contact stiffness [46] is given by

$$k_1(b_1) = \frac{4b_1 E}{\pi s^2(1-\nu^2)} \tag{4.36}$$

Here, ν is the Poisson's ratio of the bulk material of the coating. Now consider other extreme topology where asperities almost bridge the gaps between the asperities. The resulting contact stiffness [46] for this case is

$$k_2(b_1) = \frac{3}{8s(1-\nu^2)}\left[1 - \frac{4b_1^2}{s^2}\right]^{-3/2} \tag{4.37}$$

An interpolation formula is needed for the effective contact stiffness q_1 between the values of k_1 at small b_1/s and k_2 at b_1/s close to 1/2. Following Fleck and Cocks [46], we assume an interpolation formula of the form:

$$q_1(b_1) \;=\; \frac{k_1(b_1)}{2}\left[1 + \cos\left(\frac{2\pi b_1}{s}\right)\right] + \frac{k_2(b_1)}{2}\left[1 - \cos\left(\frac{2\pi b_1}{s}\right)\right] \tag{4.38}$$

as this preserves the asymptotic behaviour except for mid-range values of b_1/s close to 1/4. The detailed derivation for obtaining the effective contact stiffness is given in Fleck and Cocks [46]. Similarly, we can write the effective contact stiffness in the x_2 direction as

$$q_2(b_2) \;=\; \frac{k_1(b_2)}{2}\left[1 + \cos\left(\frac{2\pi b_2}{s}\right)\right] + \frac{k_2(b_2)}{2}\left[1 - \cos\left(\frac{2\pi b_2}{s}\right)\right] \tag{4.39}$$

If we assume sticking contact at the interface, we use $E = 2G(1+\nu)$. However, at temperature, contacting asperities can slide as a result of sintering deformation. In this case the above relationship between E and G ceases to be valid and the $\frac{G}{E}$ becomes very small. Therefore we use the the following relationship so as to keep this $\frac{G}{E}$ ratio as small as possible.

$$\frac{G}{E} \;=\; \frac{(1-\rho)}{2(1-\nu^2)} \tag{4.40}$$

In principle, ρ can vary from ν to a value close to 1. When $\rho \to \nu$, $E \to 2G(1+\nu)$.

Integration scheme for constitutive model

In order to integrate the above system of equations we need to modify the integration scheme described in chapter 2 to take into account the change in elastic properties with sintering strain. As before, the constitutive relationships of eqns. 4.27, 4.28 and eqn. 4.30 can be written in incremental form as follows

$$\bar{G}_{ij} = \Delta\varepsilon^p_{ij} - \Delta\bar{t}\; g_{ij}\left(\bar{\sigma}_{ij} + \theta\Delta\bar{\sigma}_{ij}, \bar{b}_i + \theta\Delta\bar{b}_i\right) = 0 \qquad 0 < \theta \leq 1; \tag{4.41}$$

Note that the sintering stains ε^p_{11} and ε^p_{22} are functions of state variables $\bar{b}_1$ and $\bar{b}_2$ respectively and they can be written as

$$\varepsilon^p_{11} = h(\bar{b}_1); \qquad \varepsilon^p_{22} = h(\bar{b}_2); \tag{4.42}$$

Also, the increment in sintering strains $\Delta\varepsilon^p_{11}$ and $\Delta\varepsilon^p_{22}$ can be written as

$$\Delta\varepsilon^p_{11} = \frac{\partial h(\bar{b}_1)}{\partial\bar{b}_1}\Delta\bar{b}_1; \qquad \Delta\varepsilon^p_{22} = \frac{\partial h(\bar{b}_2)}{\partial\bar{b}_2}\Delta\bar{b}_2; \tag{4.43}$$

where $\Delta\varepsilon^p_{ij}$ is the increment of sintering strain over the time increment $\Delta\bar{t}$, with the rates determined at an instant $\theta\Delta\bar{t}$ in the increment. In the simulations presented here a value of $\theta = 0.5$ was chosen to ensure that the solution is unconditionally stable. The stress and strain increments must satisfy the following constitutive law

$$\bar{H}_{ij} = \bar{\sigma}_{ij} + \Delta\bar{\sigma}_{ij} - \bar{D}_{ijkl}(\bar{b}_1 + \Delta\bar{b}_1, \bar{b}_2 + \Delta\bar{b}_2)\left[\varepsilon_{ij} + \Delta\varepsilon_{ij} - (\varepsilon^p_{ij} + \Delta\varepsilon^p_{ij})\right] = 0 \tag{4.44}$$

at the end of the increment, where the stiffness matrix $\bar{D}_{ijkl}$ is now a function of state (ie inelastic strain). Eqns. 4.41 and 4.44 represent a set of non-linear equations in unknowns $(\Delta\varepsilon^p_{ij}, \Delta\bar{\sigma}_{ij})$. This system of equations can be solved using Newton's method. After i iterations within the increment the values of $(\Delta\varepsilon^p_{ij}, \Delta\bar{\sigma}_{ij})^i$ are given by

$$\begin{bmatrix} \Delta\varepsilon^p_{kl} \\ \Delta\bar{\sigma}_{kl} \end{bmatrix}^i = \begin{bmatrix} \Delta\varepsilon^p_{kl} \\ \Delta\bar{\sigma}_{kl} \end{bmatrix}^{i-1} - \left[\begin{bmatrix} \delta_{ik}\delta_{jl} - \Delta\bar{t}\theta\frac{\partial g_{ij}}{\partial\varepsilon^p_{kl}} & -\Delta\bar{t}\theta\frac{\partial g_{ij}}{\partial\bar{\sigma}_{kl}} \\ \bar{D}_{ijkl} - \frac{\partial\bar{D}_{ijmn}}{\partial\varepsilon^p_{kl}}[\varepsilon'_{mn} - \varepsilon'^{p}_{mn}] & \delta_{ik}\delta_{jl} \end{bmatrix}^{i-1}\right]^{-1} \begin{bmatrix} \bar{G}_{ij} \\ \bar{H}_{ij} \end{bmatrix}^{i-1}$$

where $\varepsilon'_{mn} = \varepsilon_{mn} + \Delta\varepsilon_{mn}$ and $\varepsilon'^{p}_{mn} = \varepsilon^p_{mn} + \Delta\varepsilon^p_{mn}$ and the superscript $i-1$ indicates that all functions are determined using quantities determined at the end of the $(i-1)^{th}$

iteration. The iterative process is continued until a prescribed tolerance in $\Delta\varepsilon^p_{kl}, \Delta\bar{\sigma}_{kl}$ is reached. Now we derive the explicit expressions for $\bar{G}_{ij}$ and $\bar{H}_{ij}$. The elastic normal stress-strain relationship in the x_1, x_2 and x_3 directions can be written as

$$\varepsilon_{11} - \varepsilon^p_{11} = \frac{\sigma_{11}}{E_1} - \frac{\nu}{E}(\sigma_{22} + \sigma_{33}) \tag{4.45}$$

$$\varepsilon_{22} - \varepsilon^p_{22} = \frac{\sigma_{22}}{E_2} - \frac{\nu}{E}(\sigma_{11} + \sigma_{33}) \tag{4.46}$$

$$\varepsilon_{33} = \frac{\sigma_{33}}{E} - \frac{\nu}{E}(\sigma_{11} + \sigma_{22}) \tag{4.47}$$

Note that the sintering strain in the x_3 direction is zero, ie, $\varepsilon^p_{33} = 0$. The elastic shear stress-strain relationship in different planes can be written as

$$\gamma_{12} - \gamma^p_{12} = \frac{\sigma_{12}}{G_{12}} \tag{4.48}$$

$$\gamma_{13} = \frac{\sigma_{13}}{G_{13}} \tag{4.49}$$

$$\gamma_{23} = \frac{\sigma_{23}}{G_{23}} \tag{4.50}$$

Inverting the set of equations given by eqns. 4.45, 4.46 and 4.47 and casting them in matrix form, we have

$$\begin{bmatrix} \sigma_{11} \\ \sigma_{22} \\ \sigma_{33} \end{bmatrix} = \begin{bmatrix} D_{11} & D_{12} & D_{13} \\ D_{21} & D_{22} & D_{23} \\ D_{31} & D_{32} & D_{33} \end{bmatrix} \begin{bmatrix} \varepsilon_{11} - \varepsilon^p_{11} \\ \varepsilon_{22} - \varepsilon^p_{22} \\ \varepsilon_{33} \end{bmatrix}$$

Explicit expressions for D_{ij} are given below.

$$\left[\ D_{ij}\ \right] = \frac{1}{M} \begin{bmatrix} (E - \nu^2 E_2)EE_1 & \nu(1+\nu)EE_2E_1 & \nu(\nu E_2 + E)EE_1 \\ \nu(1+\nu)EE_2E_1 & (E - \nu^2 E_1)EE_2 & \nu(\nu E_1 + E)EE_2 \\ \nu(\nu E_2 + E)EE_1 & \nu(\nu E_1 + E)EE_2 & (E^2 - \nu^2 E_2 E_1)E \end{bmatrix}$$

where

$$M \ = \ -2\nu^3 E_2 E_1 - \nu^2 E E_1 - \nu^2 E_2 E_1 + E^2 - \nu^2 E E_2 \tag{4.51}$$

Adopting the following normalisations for the Youngs modulus (E, E_1, E_2) and shear modulus $(G, G_{12}, G_{13}, G_{23})$ in addition to normalisations given by eqn. 4.10

$$\bar{E} = \frac{ER_o}{(1-\nu^2)\gamma_s}; \qquad \bar{G} = \frac{GR_o}{(1-\nu^2)\gamma_s} \tag{4.52}$$

we can write D_{ij} given above in non-dimensional form as

$$\left[\ \bar{D}_{ij}\ \right] = \begin{bmatrix} \bar{D}_{11} & \bar{D}_{12} & \bar{D}_{13} \\ \bar{D}_{21} & \bar{D}_{22} & \bar{D}_{23} \\ \bar{D}_{31} & \bar{D}_{32} & \bar{D}_{33} \end{bmatrix}$$

Explicit forms of eqns. 4.41 and 4.44 are given below.

$$\bar{G}_{11} = \Delta\varepsilon^p_{11} - \Delta\bar{t}\ g_{11}\left(\bar{\sigma}_{11} + \theta\Delta\bar{\sigma}_{11}, \bar{b}_1 + \theta\Delta\bar{b}_1\right) = 0 \tag{4.53}$$

$$\bar{G}_{22} = \Delta\varepsilon^p_{22} - \Delta\bar{t}\ g_{22}\left(\bar{\sigma}_{22} + \theta\Delta\bar{\sigma}_{22}, \bar{b}_2 + \theta\Delta\bar{b}_2\right) = 0 \tag{4.54}$$

$$\begin{aligned}\bar{H}_{11} &= \bar{\sigma}_{11} + \Delta\bar{\sigma}_{11} - \bar{D}_{11}(\bar{b}_1 + \Delta\bar{b}_1, \bar{b}_2 + \Delta\bar{b}_2)\left[(\varepsilon^{'}_{11} - \varepsilon^{'p}_{11})\right] \\ &\quad -\bar{D}_{12}(\bar{b}_1 + \Delta\bar{b}_1, \bar{b}_2 + \Delta\bar{b}_2)\left[(\varepsilon^{'}_{22} - \varepsilon^{'p}_{22})\right] - \bar{D}_{13}(\bar{b}_1 + \Delta\bar{b}_1, \bar{b}_2 + \Delta\bar{b}_2)\left[(\varepsilon^{'}_{33})\right] = 0\end{aligned} \tag{4.55}$$

$$\begin{aligned}\bar{H}_{22} &= \bar{\sigma}_{22} + \Delta\bar{\sigma}_{22} - \bar{D}_{21}(\bar{b}_1 + \Delta\bar{b}_1, \bar{b}_2 + \Delta\bar{b}_2)\left[(\varepsilon^{'}_{11} - \varepsilon^{'p}_{11})\right] \\ &\quad -\bar{D}_{22}(\bar{b}_1 + \Delta\bar{b}_1, \bar{b}_2 + \Delta\bar{b}_2)\left[(\varepsilon^{'}_{22} - \varepsilon^{'p}_{22})\right] - \bar{D}_{23}(\bar{b}_1 + \Delta\bar{b}_1, \bar{b}_2 + \Delta\bar{b}_2)\left[(\varepsilon^{'}_{33})\right] = 0\end{aligned} \tag{4.56}$$

$$\begin{aligned}\bar{H}_{33} &= \bar{\sigma}_{33} + \Delta\bar{\sigma}_{33} - \bar{D}_{31}(\bar{b}_1 + \Delta\bar{b}_1, \bar{b}_2 + \Delta\bar{b}_2)\left[(\varepsilon^{'}_{11} - \varepsilon^{'p}_{11})\right] \\ &\quad -\bar{D}_{32}(\bar{b}_1 + \Delta\bar{b}_1, \bar{b}_2 + \Delta\bar{b}_2)\left[(\varepsilon^{'}_{22} - \varepsilon^{'p}_{22})\right] - \bar{D}_{33}(\bar{b}_1 + \Delta\bar{b}_1, \bar{b}_2 + \Delta\bar{b}_2)\left[(\varepsilon^{'}_{33})\right] = 0\end{aligned} \tag{4.57}$$

$$\bar{G}_{33} = \Delta\gamma^p_{12} - \frac{\Delta\bar{t}}{\bar{\eta}}\left(\bar{\sigma}_{12} + \theta\Delta\bar{\sigma}_{12}\right) = 0 \tag{4.58}$$

$$\bar{H}_{44} = \bar{\sigma}_{12} + \Delta\bar{\sigma}_{12} - \bar{G}_{12}(\bar{b}_1 + \Delta\bar{b}_1, \bar{b}_2 + \Delta\bar{b}_2)\left[(\gamma_{12} + \Delta\gamma_{12}) - (\gamma^p_{12} + \Delta\gamma^p_{12})\right] = 0 \tag{4.59}$$

$$\bar{H}_{55} = \bar{\sigma}_{13} + \Delta\bar{\sigma}_{13} - \bar{G}_{13}(\bar{b}_1 + \Delta\bar{b}_1)\left[\gamma_{13} + \Delta\gamma_{13}\right] = 0 \tag{4.60}$$

$$\bar{H}_{66} = \bar{\sigma}_{23} + \Delta\bar{\sigma}_{23} - \bar{G}_{23}(\bar{b}_2 + \Delta\bar{b}_2)\left[\gamma_{23} + \Delta\gamma_{23}\right] = 0 \tag{4.61}$$

Note that $\varepsilon^{'}_{11} = \varepsilon_{11} + \Delta\varepsilon_{11}$, $\varepsilon^{'}_{22} = \varepsilon_{22} + \Delta\varepsilon_{22}$, $\varepsilon^{'}_{33} = \varepsilon_{33} + \Delta\varepsilon_{33}$; $\varepsilon^{'p}_{11} = \varepsilon^p_{11} + \Delta\varepsilon^p_{11}$ and $\varepsilon^{'p}_{22} = \varepsilon^p_{22} + \Delta\varepsilon^p_{22}$. The above material model has been coded in ABAQUS as a UMAT routine. ABAQUS also reqires specification of the Jacobian for use in the solution for the next increment. This can be determined using a similar procedure to that employed in chapter2.

Determination of Jacobian

The Jacobian is defined as

$$J_{ijkl} = \frac{\partial \Delta\bar{\sigma}_{ij}}{\partial \Delta\varepsilon_{kl}} \tag{4.62}$$

Note that $(\Delta\varepsilon^p_{ij}, \Delta\bar{\sigma}_{ij})$ are functions of the total strain increment $\Delta\varepsilon_{ij}$. Differentiating eqns. 4.41 and 4.44 with respect to $\Delta\varepsilon_{ij}$ then gives

$$d\bar{G}_{ij} = \delta_{ik}\delta_{jl}d\Delta\varepsilon^p_{ij} - \Delta\bar{t}\theta\frac{\partial g_{ij}}{\partial\bar{\varepsilon}^p_{kl}}d\Delta\varepsilon^p_{kl} - \Delta\bar{t}\theta\frac{\partial g_{ij}}{\partial\bar{\sigma}_{kl}}d\Delta\bar{\sigma}_{kl} = 0 \tag{4.63}$$

$$d\bar{H}_{ij} = \delta_{ik}\delta_{jl}d\Delta\sigma_{ij} + \bar{D}_{ijkl}d\Delta\varepsilon^p_{kl} - \frac{\partial\bar{D}_{ijkl}}{\partial\bar{\varepsilon}^p_{mn}}[\bar{\varepsilon}'_{kl} - \bar{\varepsilon}'^{p}_{kl}]d\Delta\varepsilon^p_{mn} - \bar{D}_{ijkl}d\Delta\varepsilon_{kl} = 0 \tag{4.64}$$

This set of equations can be cast in matrix form as follows

$$\begin{bmatrix} \delta_{ik}\delta_{jl} - \Delta\bar{t}\theta\frac{\partial g_{ij}}{\partial\bar{\varepsilon}^p_{kl}} & -\Delta\bar{t}\theta\frac{\partial g_{ij}}{\partial\bar{\sigma}_{kl}} \\ \bar{D}_{ijkl} - \frac{\partial\bar{D}_{ijmn}}{\partial\bar{\varepsilon}^p_{kl}}[\bar{\varepsilon}'_{mn} - \bar{\varepsilon}'^{p}_{mn}] & \delta_{ik}\delta_{jl} \end{bmatrix} \begin{bmatrix} \frac{\partial\Delta\varepsilon^p_{kl}}{\partial\Delta\varepsilon_{op}} \\ J_{klop} \end{bmatrix} = \begin{bmatrix} 0 \\ \bar{D}_{ijop} \end{bmatrix}$$

J_{klop} in the above matrix is the Jacobian. While computing the Jacobian using the above equations, all the quantities within the leading square matrices are determined using the values computed in the final iteration for the determination of stress increment.

4.4 Constrained sintering of a perfect TBC

In this section, we make use of the micro-mechanical material model described above and perform finite element studies on the sintering behaviour of a perfect coating constrained by its substrate and compare the results with that obtained through direct integration of the constitutive relationships for zero in-plane strain. We construct the finite element model considering a RVE of size $R \times R \times H$ as shown in Fig. 4.7a. Here H is the thickness of the coating in the x_3 direction. The FE model consists of C3D8 8-noded linear brick elements. The FE model is constrained all around the boundary in the normal direction and the bottom ($x_3 = 0$) is fixed in all three directions. An initial contact radius of contacting asperities in the planes normal to the x_1 and x_2 directions are assumed to be the same ($\bar{b}^1_0 = \bar{b}^2_0 = 0.9$). Unless otherwise stated, we

assume that $\nu = 0.3, \rho = 15/16, \bar{d} = 40, \bar{D}_g = 1, \bar{\gamma}_g = 0.68, \bar{s} = 5$ and $\bar{\eta} = 25$ for the finite element simulations presented in this chapter. We performed a number of FE simulations varying the modulus of bulk material of the coating, $\bar{E}$, and found that uniform sintering occurs in the entire coating. For smaller values of $\bar{E}$ (eg 90), the defect-free coating completely sinters i.e $\bar{b}^1 = \bar{b}^2 \to \bar{s}/2$. It has been observed that the coating completely sinters in the x_1 direction i.e $\bar{b}^1 \simeq 2.5$. Similarly, $\bar{b}^2 \to 2.5$ simultaneously in the x_2 direction. This is the instant of full densification of the coating. And for larger values of $\bar{E}$ (say, 550), sintering gets arrested in the coating in a relatively short time period. In this case the contact radius ($\bar{b}^1 = \bar{b}^2$) of the asperities does not grow beyond 0.932. It has also been observed that the response of perfect film is not influenced by the choice of ρ. Although, sintering gets arrested in the coating with axisymmetric contacts for small values of $\bar{E}$ compared to that of the coating with trapezoidal contacts, different normalisations are used in the two models. Also, $\bar{E}$ in axisymmetric contact models means the modulus of the bulk material of the coating, whereas in trapezoidal contact models, $\bar{E}$ means the modulus of the coating itself. For the parameters employed here and in chapter 2, $\bar{E}$ of axisymmetric contact model is approximately equal to one fourth of $\bar{E}$ of the trapezoidal contact model.

The computational results of the sintering response of a constrained perfect film are compared with the analytical solutions for different modulus values in Figs. 4.8 and 4.9. The average value of $\bar{b}_1$ or $\bar{b}_2$ from the FE model is used to compare with analytical results. It is clear from these figures that the computational scheme accurately captures the sintering response of the coating. It also suggests that the computational model can be used to further analyse the sintering response of the coatings with initial imperfections and to predict under what conditions these imperfections grow into cracks.

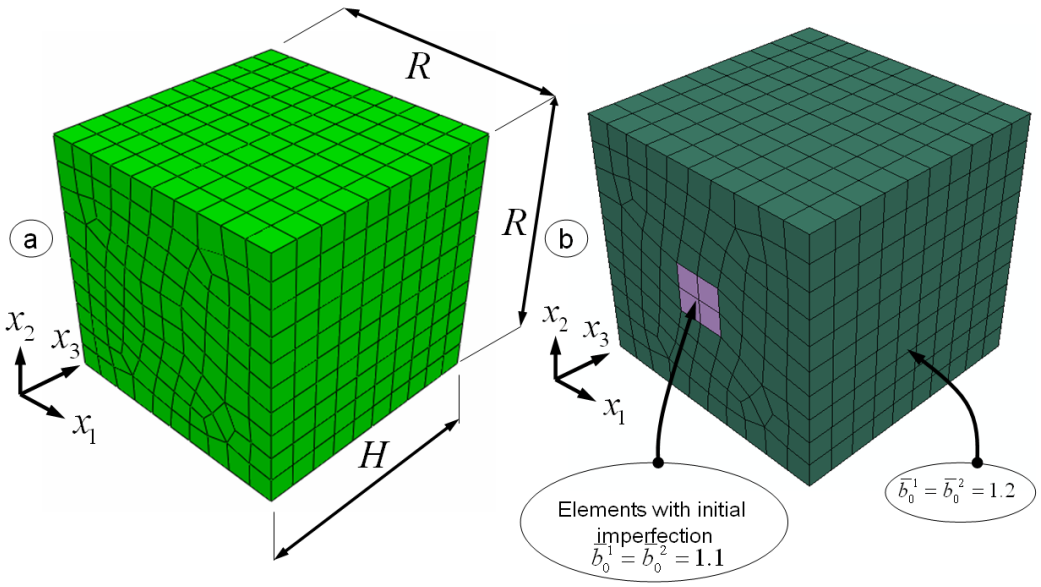

Figure 4.7: Axisymmetric model: a. Finite element model of size $R \times R \times H$. b. Finite element model of size $R \times R \times H$ of constrained film with imperfections. Imperfections exist over the entire height of the TBC (x_3-direction).

4.5 Constrained sintering of a TBC with an imperfection

Now we examine the sintering response of a constrained TBC which contains an array of imperfection. At the imperfection the initial contact radius of the asperities is less than the initial contact radius of the asperities in the remainder of the coating. The FE model of the RVE of the constrained film with an imperfection at the centre is shown in Fig. 4.7b. Symmetry conditions are imposed at all boundaries perpendicular to the x_1 and x_2 directions to create a square array of imperfections with spacing equal to the size of the RVE. The geometric and material parameters are kept the same. Elements at the middle of the model over the entire height of the TBC are treated as the imperfection. We take the initial condition of elements at the imperfection as $\bar{b}_0^1 = \bar{b}_0^2 = 1.1$ and the initial condition for the rest of the elements $\bar{b}_0^1 = \bar{b}_0^2 = 1.2$. We now assess the sintering response for different choices of $\bar{E}$. In the previous section, we demonstrated that a complaint coating can fully densify. It is shown here that for small values of $\bar{E}$, ie for complaint TBC, the coating is insensitive to the presence of

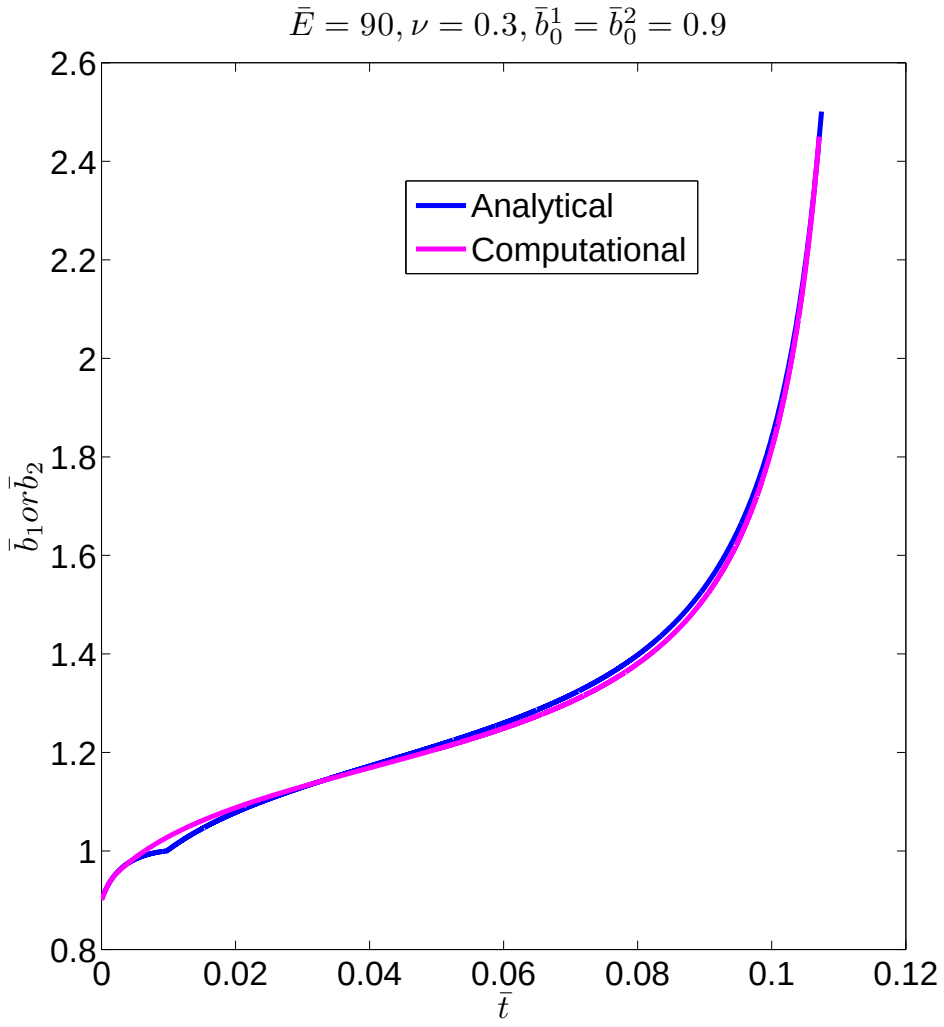

Figure 4.8: Axisymmetric model: Comparison of analytical and computational solution of sintering response of a perfect constrained film: Full sintering occurs for $\bar{E} = 90$.

small imperfections and the TBC fully densifies. This situation is shown in Figs. **??**a and **??**b for $\bar{E} = 90$. Note that both $\bar{b}_1$ and $\bar{b}_2$ simultaneously reach $\bar{s}/2$ (2.5). On the other hand, it has been observed through numerical simulations that the imperfection grows into crack for a stiff coating for the same set of initial conditions. For $\bar{E} = 1650$, FE analysis indicates that the imperfection and surrounding material densify initially at a rate similar to that for the perfect film although they start off with different initial conditions. With further sintering, the build up of elastic stored energy in the

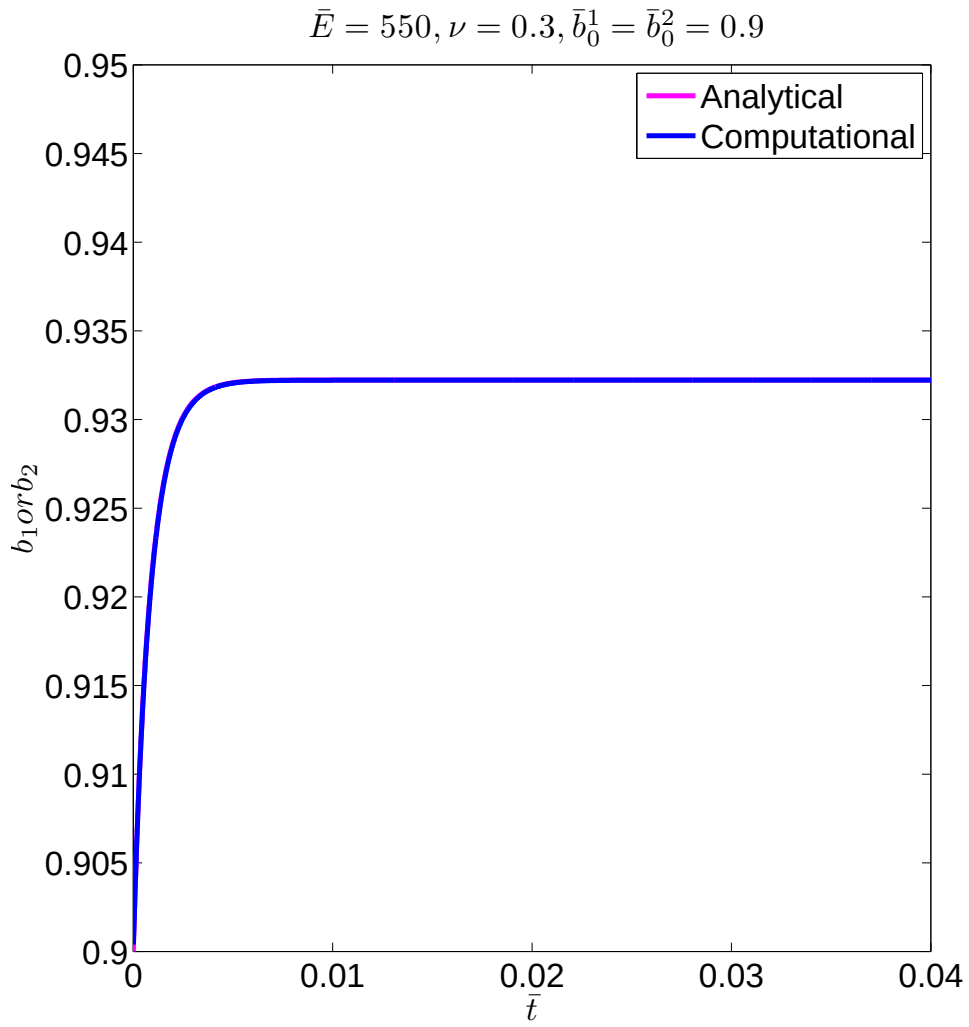

Figure 4.9: Axisymmetric model: Comparison of analytical and computational solution of sintering response of a perfect constrained film: Sintering gets arrested for $\bar{E} = 550$.

coating decelerates the rate of sintering. As the sintering is about be arrested, as in the case of a perfect coating, we observe a divergence in response between that at the imperfection and the remainder of the coating. This is illustrated in Fig. 4.10 which shows the evolution of contact radius ($\bar{b}_1$ or $\bar{b}_2$) at the imperfection and surrounding material in the top of the RVE, compared with that for the perfect film for $\bar{E} = 1650$. Now note that here the sintering response of the perfect film is different for different choices of initial condition. Desintering occurs at the site of the initial imperfection

initially, ie $\bar{b}_1$ or $\bar{b}_2$ decreases, for $\bar{t} > 1.1 \times 10^{-3}$. Desintering at the imperfection relaxes the constraint on the remaining material permitting the surrounding material to sinter faster. Therefore, the surrounding material starts densifying at a faster rate for $\bar{t} > 4 \times 10^{-3}$ as shown in Fig. 4.10. Eventually, $\bar{b}_1 = \bar{b}_2 \approx 0$ at the site of the imperfection. This means that a physical crack forms when $\bar{b}_1 \approx 0$ or $\bar{b}_2 \approx 0$. We terminate the computational analysis when $\bar{b}_1$ and/or $\bar{b}_2$ approaches zero for the sake of computational convenience. When we terminate the analysis before contact the radii reach zero at this zone, the constraint on the surrounding material is not completely relaxed since it still experiences a small tensile stress corresponding to the size of contact at the desintering zone. A fully developed crack that forms initially at the surface of the TBC then advances vertically towards the TGO and horizontally towards the axis of symmetry, where it meets with another crack spreading from the adjacent imperfection to form a band of desintered material. The developed crack reduces the constraint on the surrounding material, allowing it to sinter faster. Note that the rate of densification is more at the top of the desintered band of material than that at the material below it because more desintering occurs at the top of the coating. Figs. 4.11a and 4.11b indicate the contact radii $\bar{b}_1$ and $\bar{b}_2$ in the x_1 and x_2-directions respectively following the spread of the desintering region from the initial imperfection (ie at $\bar{t} = 0.0760$). Note that from these figures, $\bar{b}_1 \approx 0$ (Fig. 4.11a) and $\bar{b}_2 \approx 0$ (Fig. 4.11b) at the disinterred region. The radius of the contacting asperities can not have a value less than zero. Therefore, the physical separation between columns can be tracked by monitoring $\bar{w}_1$ and $\bar{w}_2$ at these locations. For this value of $\bar{E} = 1650$ the constraint on elements in the top of the RVE away from the defect is relaxed sufficiently to allow them to reach close to full density ($\bar{b}_1 \approx 2.5$ and $\bar{b}_2 \approx 2.5$) as shown in Figs. 4.10, 4.11a and 4.11b. Note that in Fig. 4.11a, $\bar{b}_1 \to 2.5$ and in Fig. 4.11b, $\bar{b}_2 \to 2.5$ at the top of the RVE in the surrounding material. For large value of modulus, say $\bar{E} = 9000$, we observe that sintering becomes arrested within the desintered band of material before it reaches fully density after the formation of cracks. Analyses of this sub-section indicate that a regular pattern of crack forms in

the coating from the initial regular pattern of imperfections.

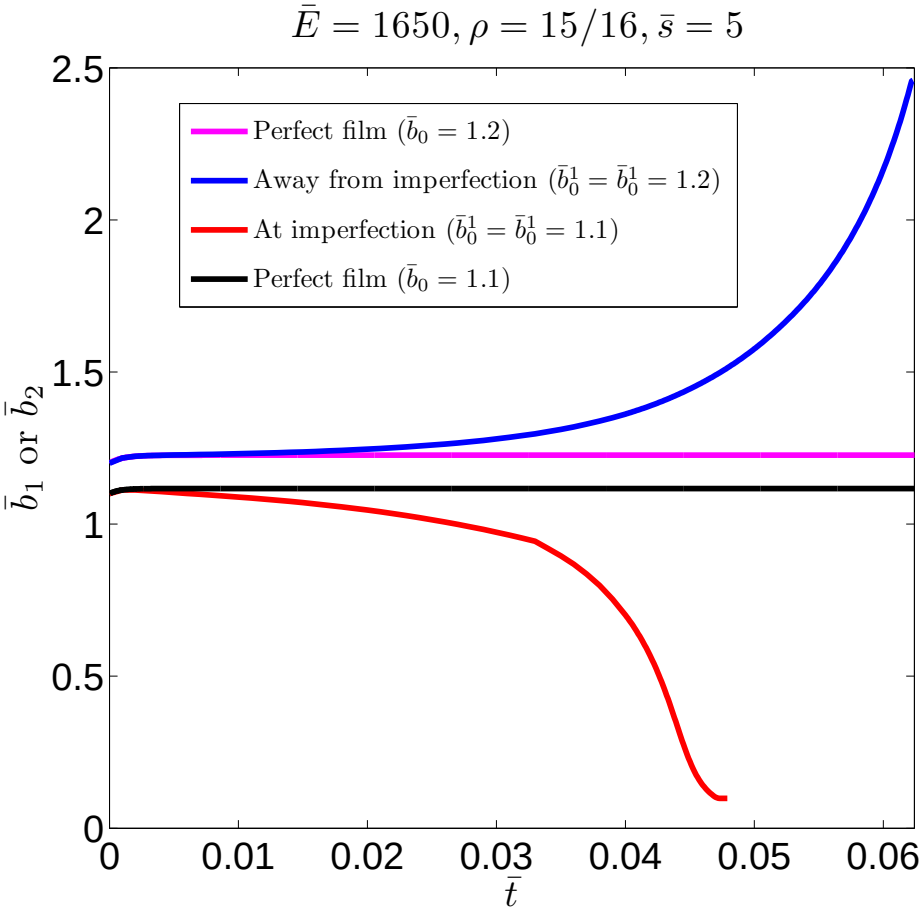

Figure 4.10: Crack development in a constrained TBC with an imperfection for $\bar{E} = 1650$

4.6 Influence of a family of imperfections

In the previous sub-section, we observed that a compliant coating is insensitive to the presence of small imperfections. Nevertheless, in stiff coatings, desintering occurs at the site of initial imperfections, leading to the formation of cracks on the surface of the coating. Then this crack advances towards the TGO. The previous analysis also indicates that a square pattern of crack forms in the stiff coatings. Following the approach adopted in chapter 2, we further investigate this by assessing the sintering response of the TBC when it has a square pattern of primary imperfections. Fig. 2.16

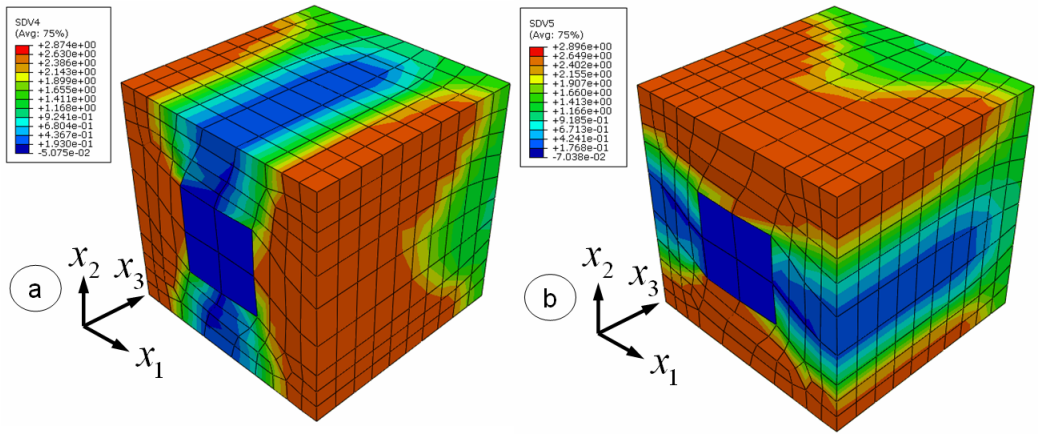

Figure 4.11: Full Sintering in the top portion of a constrained TBC with an imperfection for $\bar{E}$=1650: a. $\bar{b}_1 \simeq 2.5$ b. $\bar{b}_2 \simeq 2.5$

shows the idealised TBC comprising square clusters each of size $2R \times 2R$. The primary imperfections run along the boundaries of the cluster as shown in Fig. 2.16. To perform FE analysis, we consider a repeating cell of size $2R \times 2R \times H$ which contains primary imperfections over the entire height of the coating on its boundary as shown in Fig. 4.12a. The FE model was constructed using C3D8 uniform brick 8 noded elements. A typical FE model with cluster size, $\bar{R} = 1$ is shown in Fig. 4.13. The imperfection is considered to be an element wide. The elements with imperfections at the boundary of the FE model are shown in different colours and are marked by A, B and C. The initial condition for elements marked by A is $\bar{b}_0^1 = 1.2, \bar{b}_0^2 = 1.1$, for elements marked by B it is $\bar{b}_0^1 = 1.1, \bar{b}_0^2 = 1.2$ and for elements marked by C it is $\bar{b}_0^1 = \bar{b}_0^2 = 1.1$. The defect free elements are marked by D and their initial condition is $\bar{b}_0^1 = \bar{b}_0^2 = 1.2$. The nodes at the bottom the model ($x_3 = 0$) are fixed in all three directions and the normal displacements of the nodes on the boundaries of the model are constrained.

Now let us examine the sintering response of the TBC with a square pattern of primary imperfections (PIs) using this FE model by varying the cluster size $\bar{R}$ and modulus $\bar{E}$ of the coating with the same material parameters used earlier. For small values of $\bar{E}$, the sintering response is not sensitive the the presence of PIs and the coating reaches fully density, ie, complete sintering occurs both at the imperfections

and within the cluster irrespective of the cluster size $\bar{R}$ chosen. For instance, for $\bar{E} = 90$ and $\bar{R} = 1$ the contact radii $\bar{b}_1 \to 2.5$ and $\bar{b}_2 \to 2.5$ both at the imperfections and within the cluster as shown in Figs. 4.14a and 4.14b respectively at $\bar{t} = 0.035$. Material within cluster goes to full density before imperfections fully sinter as expected. Note that full densification happens in the coating with primary imperfections in a shorter time compared to perfect film for the same $\bar{E}$. For values of $\bar{E} > 90$, desintering occurs at the site of PIs and the PIs grow with further desintering, eventually developing into cracks. For $\bar{E} = 500$ and same cluster size ($\bar{R} = 1$), the PIs develop into cracks ($\bar{b}_1 \approx 0$ or $\bar{b}_2 \approx 0$) as shown in Figs. 4.15a ($\bar{b}_1 \approx 0$) and 4.15b ($\bar{b}_2 \approx 0$) at $\bar{t} = 0.0275$. Fig. 4.15a shows $\bar{b}_1$ and Fig. 4.15b shows $\bar{b}_2$. Note from these figures that at the PIs, $\bar{b}_1 \approx 0$ or $\bar{b}_2 \approx 0$ almost over the entire height of the cluster except at the bottom where it is constrained by the substrate. This desintering at PIs reduces constraint on the material within the cluster permitting it to sinter uniformly behaving like an insolated cluster to full density at $\bar{t} = 0.06$. Now let us examine the sintering response of the TBC with PIs in the practical range of modulus $\bar{E}$ (The practical range of E=45-87.5GPa. Also the radius of axisymmetric asperities can range from 0.1-1μm. Therefore the practical range of non-dimensional modulus of the columns of the coating, $\bar{E} = 4000 - 79000$). For $\bar{E} = 5000$ and the cluster size $\bar{R} = 2$, PIs develop into cracks but the accelerated sintering within the cluster soon after the formation of cracks eventually gets arrested before it reaches full density due to high stiffness of the material within the cluster. Figs. 4.16a and 4.16b show $\bar{b}_1$ and $\bar{b}_2$ respectively at $\bar{t} = 0.0634$ for $\bar{E} = 5000$ and $\bar{R} = 2$. The values of $\bar{b}_1$ or $\bar{b}_2$ close to zero indicates a crack emanated from the PIs. Note that from these figures that sintering gets arrested within the cluster with an average value of $\bar{b}_1$ or $\bar{b}_2 \approx 1.35$.

However, if we choose a large cluster $\bar{R} = 4$ for the same modulus ($\bar{E} = 5000$), PIs develop into cracks quickly and the sintering within the cluster gets arrested as before. But a larger cluster size reduces the extent of sintering within the cluster after the formation of the cracks. Figs. 4.17a and 4.17b show $\bar{b}_1$ and $\bar{b}_2$ respectively

at $\bar{t} = 0.0596$ for $\bar{E} = 5000$ and $\bar{R} = 4$. Note that the average value of $\bar{b}_1$ or $\bar{b}_2 \approx 1.25$ within the cluster. It can also be observed from Figs. 4.17a and 4.17b that more densintering occurs at the centre of the cracked cluster along the axes of symmetry and this indicates that further set of cracks might form within the cracked cluster if triggered by seeding another set of imperfections. This situation is explored in the next section by considering two families of imperfections.

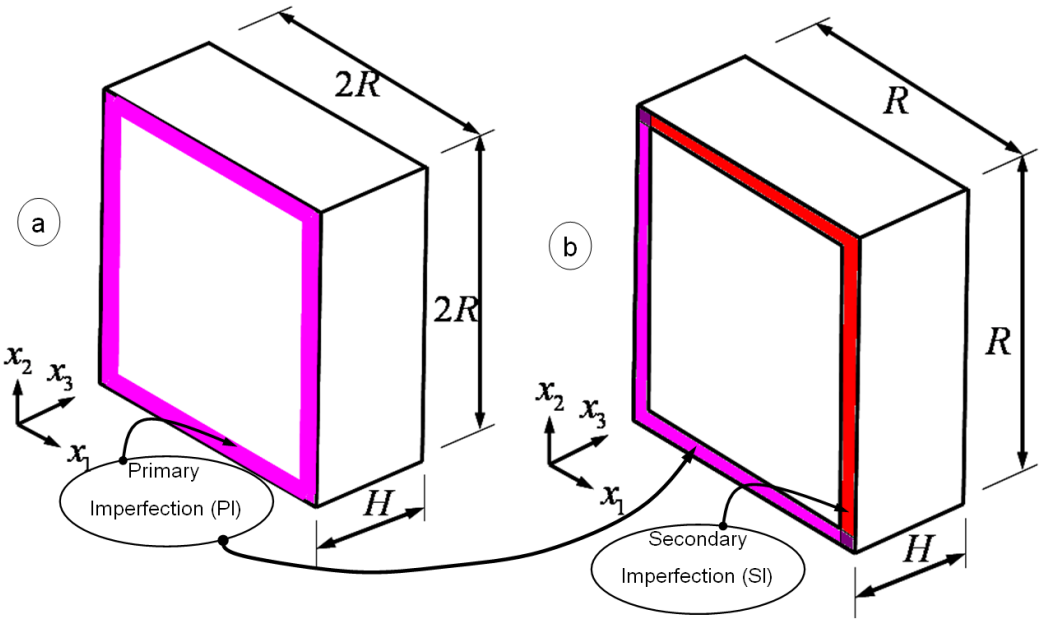

Figure 4.12: a. A RVE of size $2R \times 2R \times H$ which has primary imperfections on its boundary. b. A RVE of size $R \times R \times H$ which has primary and secondary imperfections on its boundary. Imperfections extend over the entire height H in the x_3 direction.

4.7 Influence of two families of imperfections

Analyses of TBCs with a single family of imperfections inidicate that for larger $\bar{E}$ and cluster size $\bar{R}$, the arrest of sintering within the cluster might lead to the formation of further set of cracks. Therefore, we now explore this by considering another family of square pattern of secondary imperfections (SIs) in addition to a family of primary imperfections. SIs run across the clusters as shown in Fig. 3.20. Now let us consider a repeating cell of size $R \times R \times H$ as shown in Fig. 4.12b which contains PIs and

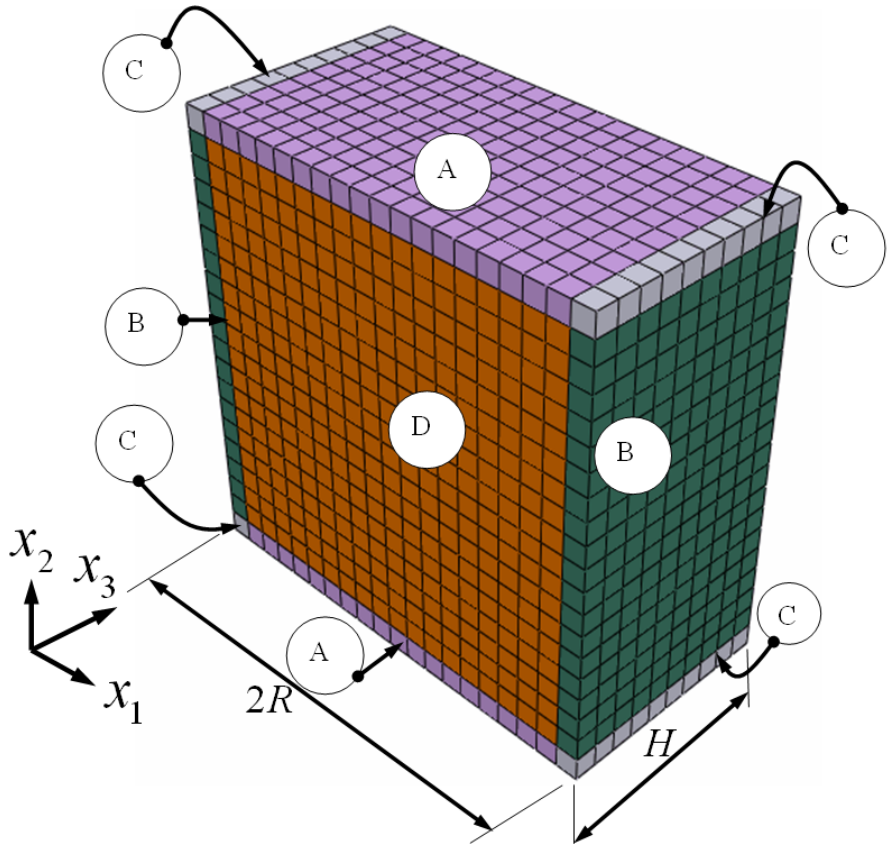

Figure 4.13: Finite element model of a repeating cluster with primary imperfection on its boundary for $\bar{R} = 1$: A-C elements with imperfection, D-Defect free elements, A: $\bar{b}_0^1 = 1.2, \bar{b}_0^2 = 1.1$; B: $\bar{b}_0^1 = 1.1, \bar{b}_0^2 = 1.2$; C: $\bar{b}_0^1 = \bar{b}_0^2 = 1.1$; D: $\bar{b}_0^1 = \bar{b}_0^2 = 1.2$.

SIs on its boundary. Both the imperfections extend over the entire height H of the cluster in the x_3 direction. The FE model of this RVE was constructed again using C3D8 uniform brick 8 noded elements. A typical FE model with PIs and SIs for cluster size $\bar{R} = 4$ is shown in Fig. 4.18. The imperfection is considered to be an element wide. The elements with imperfections at the boundary of the FE model are shown in different colours and are marked by A, B, C, D, E, F, G and H. The initial condition for elements marked by A is $\bar{b}_0^1 = 1.2, \bar{b}_0^2 = 1.15$, for elements marked by B it is $\bar{b}_0^1 = 1.1, \bar{b}_0^2 = 1.15$, for elements marked by C it is $\bar{b}_0^1 = 1.1, \bar{b}_0^2 = 1.2$, for elements marked by D it is $\bar{b}_0^1 = \bar{b}_0^2 = 1.1$, for elements marked by E it is $\bar{b}_0^1 = 1.1, \bar{b}_0^2 = 1.2$, for elements marked by F it is $\bar{b}_0^1 = 1.15, \bar{b}_0^2 = 1.1$, for elements marked by G it is $\bar{b}_0^1 = 1.15, \bar{b}_0^2 = 1.2$ and for elements marked by H it is $\bar{b}_0^1 = \bar{b}_0^2 = 1.15$. The defect free

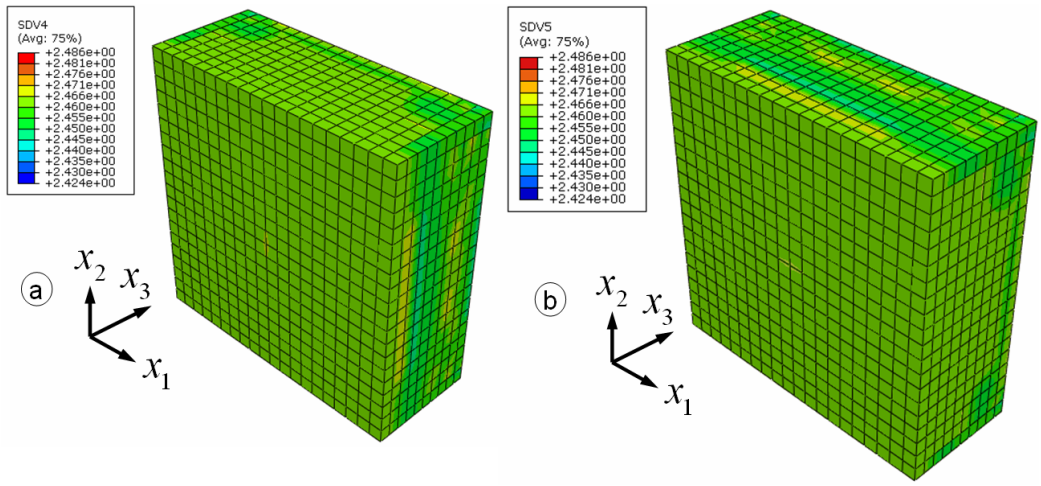

Figure 4.14: Full sintering both at the imperfections and within the cluster for $\bar{E} = 90$ and $\bar{R} = 1$. a. Contact radius $\bar{b}_1$ b. Contact radius $\bar{b}_2$

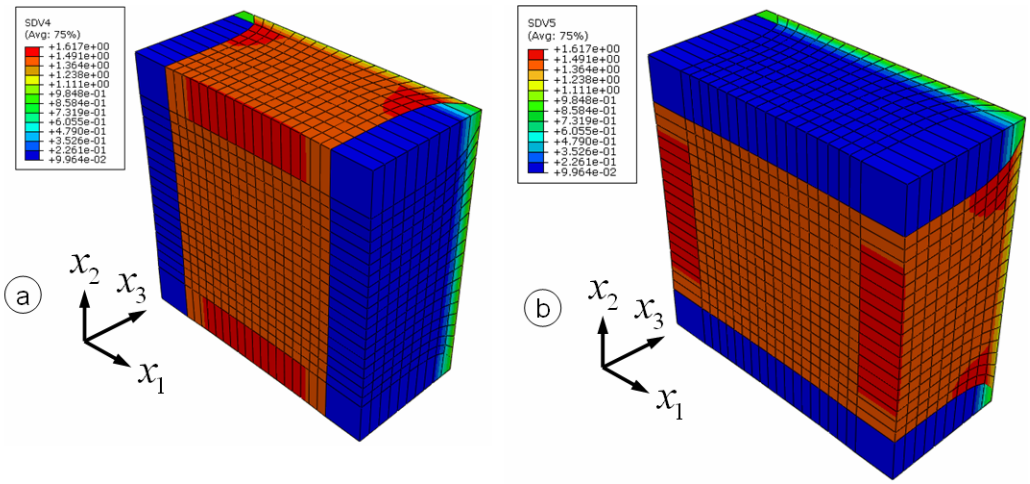

Figure 4.15: Fully developed primary crack at the imperfections and complete sintering within the cluster for $\bar{E} = 500$ and $\bar{R} = 1$. a. Contact radius $\bar{b}_1$ b. Contact radius $\bar{b}_2$.

elements are marked by I and their initial condition is $\bar{b}_0^1 = \bar{b}_0^2 = 1.2$. The normal displacements on all the boundary are constrained and the bottom ($x_3 = 0$) is fixed in all three directions.

Now we analyse the sintering response for $\bar{E} = 4000$ and $\bar{R} = 1.2$. The FE analysis indicates that PIs fully develop into cracks while the desintering at the SIs is not significant. Figs. 4.19a and 4.19b show $\bar{b}_1$ and $\bar{b}_2$ respectively. Note from

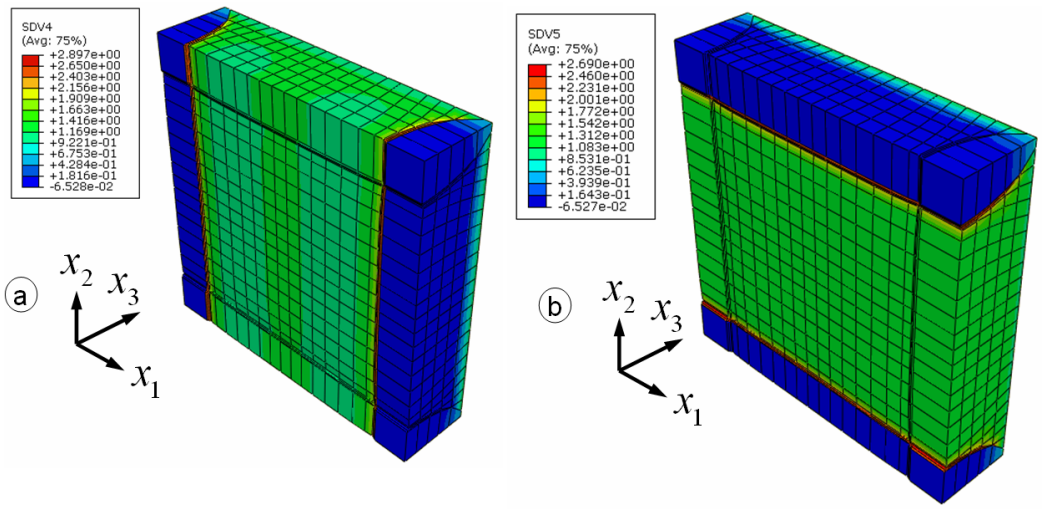

Figure 4.16: Fully developed primary crack at the imperfections and incomplete sintering within the cluster for $\bar{E} = 5000$ and $\bar{R} = 2$. a. Contact radius $\bar{b}_1$ b. Contact radius $\bar{b}_2$.

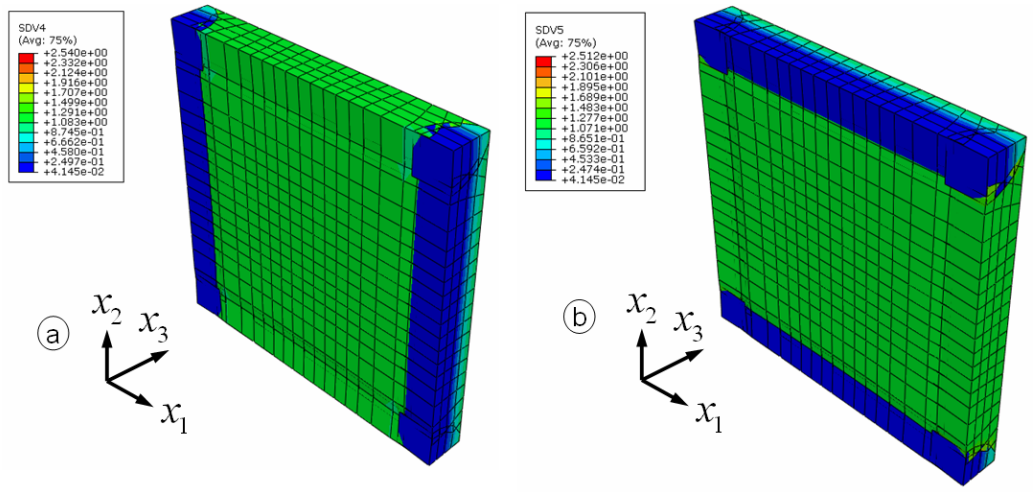

Figure 4.17: Fully developed primary crack at the imperfections and incomplete sintering within the cluster for $\bar{E} = 5000$ and $\bar{R} = 4$. a. Contact radius $\bar{b}_1$ b. Contact radius $\bar{b}_2$.

these figures that $\bar{b}_1 \approx 0$ at the PIs in the x_1 direction and $\bar{b}_2 \approx 0$ at the PIs in the x_2 direction almost over the entire height of the cluster indicating fully developed primary cracks. SIs do not desinter enough to develop into cracks. Both $\bar{b}_1$ at the SIs in the x_1 direction and $\bar{b}_2$ at the SIs in x_2 direction is approximately equal to 1.03. Sintering within the cluster ($2\bar{R} = 2.4$) subsequent to the formation of primary

cracks gets arrested with $\bar{b}_1 = \bar{b}_2 \approx 1.3$. On the other hand, if we consider a large cluster size $\bar{R} = 4$ for the same modulus ($\bar{E} = 4000$), both the imperfections develop into cracks. Figs. 4.20a and 4.20b show $\bar{b}_1 \approx 0$ at the PIs and SIs in the x_1 direction and $\bar{b}_2 \approx 0$ at the PIs and SIs in the x_2 direction respectively. Despite the formation of both the cracks, the extent of sintering within the cluster is much less than the previous case ($\bar{b}_1 = \bar{b}_2 \approx 1.25$) because of the larger cluster size ($\bar{R} = 4$).

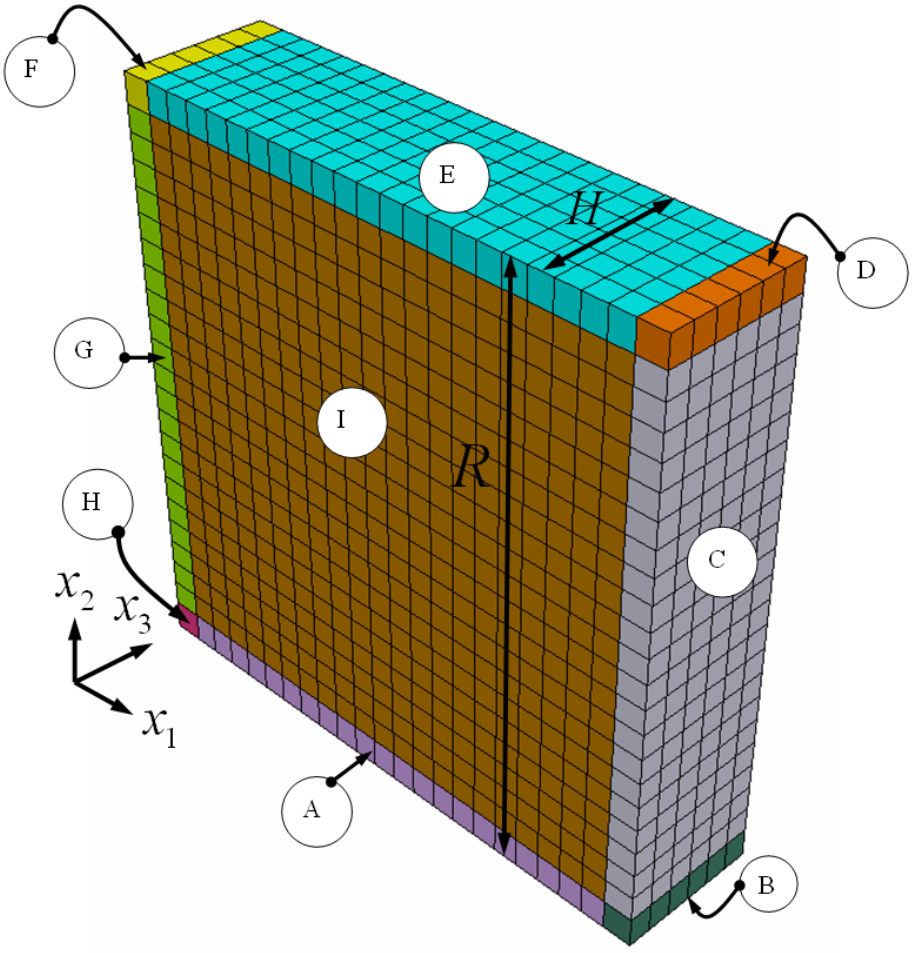

Figure 4.18: Finite element model of a repeating cluster with PIs and SIs on its boundary for $\bar{R} = 4$: A-H elements with imperfection, I-Defect free elements, A: $\bar{b}_0^1 = 1.2, \bar{b}_0^2 = 1.15$; B: $\bar{b}_0^1 = 1.1, \bar{b}_0^2 = 1.15$; C: $\bar{b}_0^1 = 1.1, \bar{b}_0^2 = 1.2$; D: $\bar{b}_0^1 = \bar{b}_0^2 = 1.1$; E: $\bar{b}_0^1 = 1.1, \bar{b}_0^2 = 1.2$; F: $\bar{b}_0^1 = 1.15, \bar{b}_0^2 = 1.1$; G: $\bar{b}_0^1 = 1.15, \bar{b}_0^2 = 1.2$; H: $\bar{b}_0^1 = \bar{b}_0^2 = 1.15$; I: $\bar{b}_0^1 = \bar{b}_0^2 = 1.2$.

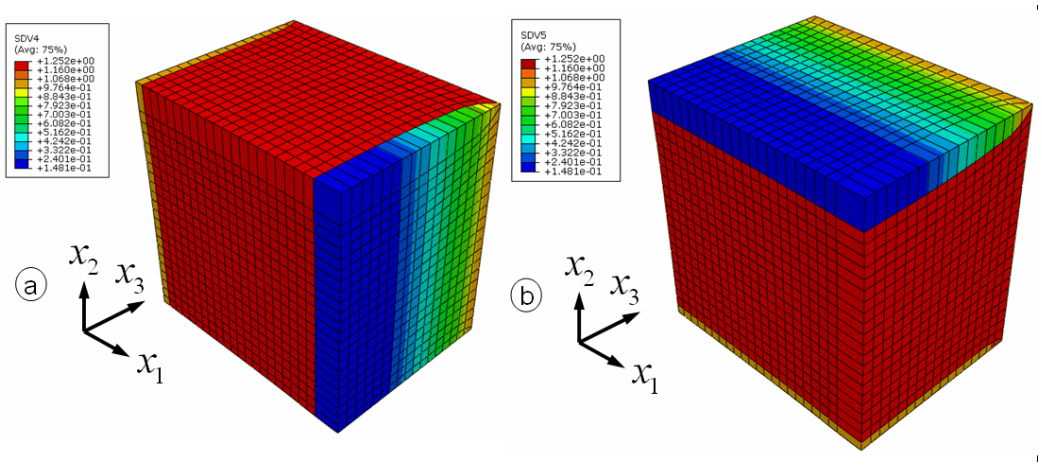

Figure 4.19: Fully developed primary cracks and incomplete sintering within the cluster for $\bar{E} = 4000$ and $\bar{R} = 1.2$. a. Contact radius $\bar{b}_1$ b. Contact radius $\bar{b}_2$.

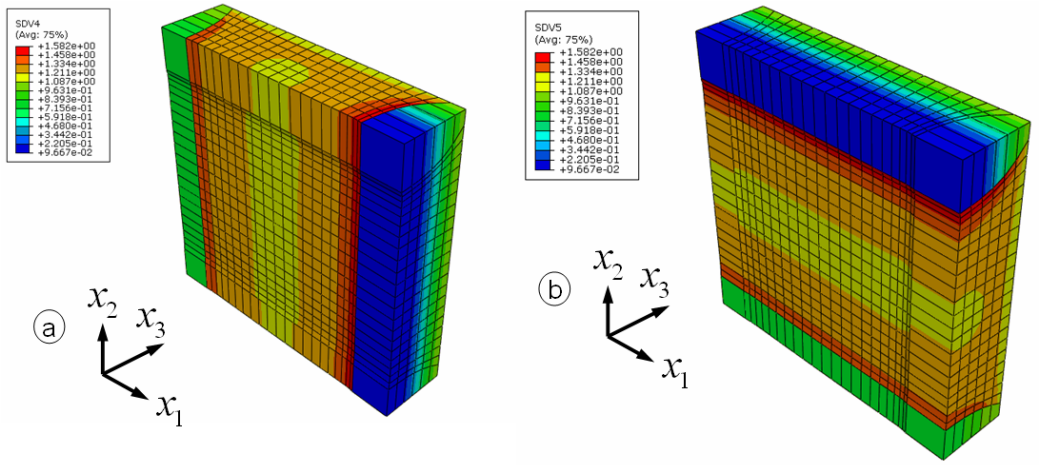

Figure 4.20: Fully developed primary and secondary cracks and incomplete sintering within the cluster for $\bar{E} = 4000$ and $\bar{R} = 4$. a. Contact radius $\bar{b}_1$ b. Contact radius $\bar{b}_2$.

4.8 Conclusion

In this chapter computational schemes have been presented for studying the sintering response of EB-PVD coatings and for identifying the conditions under which desintering occurs at imperfections, leading to formation of mud-cracks. A simple micromechanical material model has been developed assuming an axisymmetric contact geometry between columns and accounting for change of modulus during sintering.

Finite element studies have been performed using this constitutive model through a UMAT subroutine in Abaqus to assess the sintering response and to examine the sensitivity of the response to imperfections in the coating. Initially, we modelled the sintering response of a perfect coating and demonstrated that the results are in agreement with the analytical results. Then we went on to study the sintering response of a constrained TBC which contains an array of imperfections. This analysis indicates that the compliant coating is insensitive to the presence of small imperfections, whereas imperfections in stiff coatings can develop into a square pattern of cracks, which then advance towards the TGO. We explored this further by assessing the sintering response when the TBC contains a single family of square pattern of imperfections and identified the conditions under which they grow into cracks. We then considered another similar family of imperfections in addition to the PIs in order to explore whether subsequent set of cracks form within the cluster after the formation of primary set of cracks. These computational models predict the sintering response of the coating reasonably well in the practical range of modulus of the TBCs. However, these models take a considerable amount computational time to perform calculations over a wide range of modulus $\bar{E}$ and cluster size $\bar{R}$ in order to generate failure maps. Therefore, in the next chapter, we make use of the predictions of these models to develop simple analytical models which capture the major features of the effect of imperfections on the sintering response. Compared to the trapezoidal contact computational model presented in chapter 2, this axisymmetric computational model more accurately predicts the sintering response of the coating. The prediction using computational models of chapters 2 and 4 is more fully evaluated in chapter 6.

Chapter 5

Axisymmetric Contact Analytical Models

5.1 Abstract

Based on the detailed finite element studies carried out on the sintering response of the axisymmetric contact EB-PVD top coat in chapter 4, we develop simplified analytical micro-mechanical models to simulate in-service sintering and subsequent mud-cracking under isothermal conditions. With these models, we capture the evolution of microstructure and deformation of the coating. We assume that inter-columnar sintering is driven by the change in total free energy of the columns. We neglect much faster diffusion that occurs over the free surfaces of the asperities. The change of asperity stiffness with sintering is taken into account. It is further assumed that the columns are inextensible both elastically and plastically in the coatings's thickness direction. Initially, we present a model that simulates sintering of a perfect coating constrained by the rigid substrate. In a perfect coating, sintering gets arrested when the in-plane modulus exceeds a critical value. On the other hand, the sintering process becomes unstable if the coating contains imperfections in the microstructure. Imperfections grow due to instabilities in the sintering process. These imperfections in the coating can develop into cracks, which advance through the thickness of the coating, leading to a pattern of "mud cracks". Therefore, firstly, we modelled a two state variable analytical model to model the evolution of mud-cracks. This analyt-

ical model describes the sintering response and the growth of mud cracks in terms of the evolution of two degrees of freedom and therefore allow us to quickly identify the conditions under which imperfections develop into cracks. We also modelled a three state variable analytical model considering two families of imperfections in the coating to predict the average mud-crack spacing.

5.2 Problem description

This is essentially a repeat of the analysis presented in chapter 3, but with a different contact model. In this chapter we concentrate on developing analytical models to capture the computational sintering response of an EB-PVD ceramic TBC presented in chapter 4 and assess the conditions under which inter-columnar cracks can develop within the coating. In chapter 3, we assumed elastic incompressibility condition of the coating, in order to have simple form of displacement field, though not realistic. Therefore, here we assume that the columns are inextensible both elastically and plastically along the coating thickness, ie in the x_3 direction. This assumption is justified by the fact that during the early stages of sintering, there is small contact between asperities in the in-plane, ie $x_1 - x_2$ plane and the coating is very stiff in the x_3 direction compared to the in-plane directions. As the intercolumnar sintering progresses, the coating stiffness changes with the evolution of contact geometry and this change of stiffness of the coating with sintering is included in the analysis. The computational simulations presented in the previous chapter guide us to develop 2DOF and 3DOF analytical models, which capture the physics of the growth of imperfections, identify the conditions under which they develop into cracks and predict the saturated crack spacing in the coating.

In these models, we adopt the same geometric description of the EB-PVD coating and contacting asperities as considered in chapter 4, but follow the analytical approach of chapter 3 to provide a more comprehensive evaluation of the influence of imperfections on the sintering response. In the chapter 4, we compared the analytical results of constrained sintering of a perfect coating with the computational results

in order to demonstrate the accuracy of computational scheme, without presenting the model. Therefore, here, we initially present the analytical model of constrained sintering of a perfect EB-PVD TBC.

Problem A : A sintering model for an infinite TBC layer of columns upon a half-space, as shown schematically in Fig.4.2a.

In order to capture the essential features of the mud cracking phenomenon in EB-PVD TBCs due to in-service sintering between neighboring columns, the following models have been developed in this chapter.

Problem B : A model with axisymmetric contact for the evolution of a set of arbitrarily equi-spaced primary imperfections in an infinite TBC layer upon a half-space.

Problem C : A model for the evolution of two families of equi-spaced imperfections in an infinite TBC layer upon a half-space.

In all the problems, the TBC layer is of height H and it is assumed that the TBC film is perfectly bonded to the substrate. The layer contains columns of square cross-section, of dimension $d \times d$, aligned with the in-plane axes (x_1, x_2). The mean centre to centre distance between contacting asperities is s. The layer thickness is along the x_3 direction, with the origin located at the bottom of the columnar layer.

5.3 Problem A: Intercolumnar sintering of a constrained perfect film

In this section, a model is developed for the intercolumnar sintering of ceramic columns of EB-PVD coating. The wavy surfaces of the columns are idealised such that they have axisymmetric asperities between columns as shown in Fig. 4.4. It is assumed that the asperities are discrete and are widely spaced with mean centre to centre distance between the asperities being s. The modulus of the contacting asperities is considered to change during the sintering process. Fig. 4.4a shows the reference

configuration with initial asperity height w_o and spherical radius of the asperity R_o. Fig. 4.4b shows the deformed configuration of asperities at a typical instant during sintering process. In this configuration, column 2 is displaced by an amount $(w_o - w)$. Here, w is the current height of the asperity, h is the height of the cylindrical portion of the asperity at any instant formed as a result of the sintering and b is the contact radius at the interface between columns. As in chapter 4, it is assumed that only grain boundary diffusion at the contacts between columns is the dominant dissipative process.

We now consider the problem of progressive sintering of an infinite TBC layer of columns upon a half-space, as shown schematically in Fig. 4.2a. We impose isothermal conditions within the perfect TBC layer T which may be greater than or less than the deposition temperature T_D. The task now is to determine the time evolution of inter-columnar sintering at this uniform temperature T. The restraint of the substrate is included in the analysis. As the columns sinter together, and macroscopically uniform in-plane sintering strain ε^s evolves, overall strain compatibility with the substrate dictates the build-up of in-plane tensile stress.

In the plane of the coating, ε^s is matched by the uniform elastic strain ε^e when $\varepsilon^T = 0$ and is given by eqn. 3.29. As sintering proceeds, the contact radius b and the height of the cylindrical portion of the asperity h increase and the total asperity height w decreases, while the spherical radius of the asperity R_o remains constant. As sintering progresses further, at some stage, b reaches R_o. At this stage the asperity becomes a pure cylinder and h attains the value of w. With further sintering, the cylindrical asperity flattens until it touches the adjacent asperities. This is the state at which full densification is said to have occurred in the coating. At the point of full sintering, $b \to s/2$.

The problem posed is to solve for the local evolution of surface profile characterised by (b) due to the interfacial diffusion of matter from the contacts into the gaps between the asperities. Interfacial diffusion is driven by the combined driving forces of the net reduction in interfacial energy, and the potential energy of the TBC. Recall that both

h and w are expressed in terms of b as given by eqns. 4.4 and 4.5. The macroscopic sintering strain ε^s is related to the height of the asperity by

$$\varepsilon^s = \frac{w(b) - w_0}{d} \tag{5.1}$$

Note that w_0 is the initial value of variable $w(b)$. With this choice, ε^s equals zero immediately following deposition. As sintering progresses, w decreases and b increases while ε^s becomes increasingly negative. Considering a slice of thickness t_1 of the RVE of size $d \times d$ subjected to an equi-biaxial stress σ as shown in Fig. 5.1, we can write

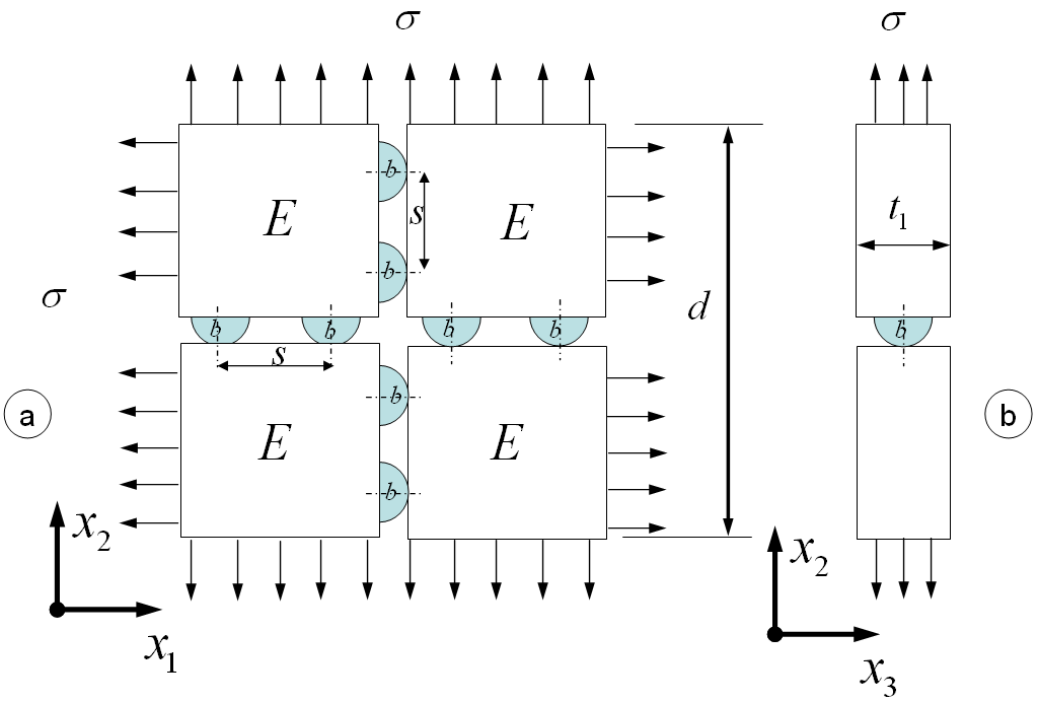

Figure 5.1: A representative macroscopic volume element of the coating subjected to an equi-biaxial stress σ. The element has a square cross section $d \times d$, made up of 4 quarter columns which are in contact. The height of the element is t_1. a. Plan view of the RVE b. Side view of the RVE.

the Gibbs free energy density in the perfect coating as

$$G = G_a N_a + \sigma \frac{(w_o - w)}{d} \tag{5.2}$$

where, G_a is the interface free energy per asperity and N_a is the number of asperities per unit volume of the TBC. G_a is of the same form of eqn. 4.8. Noting that the

contact radius, b, of the asperity in the x_1 and x_2 directions are the same for the perfect coating and adopting the same procedure described in the previous chapter we can write explicit expression for $\dot{G}$ as a function of the single state variable b in non-dimensional form as

$$\dot{G} \;=\; \frac{4\gamma_s}{\bar{s}^2\bar{d}R_o}\left[A(\bar{b})\right]\dot{\bar{b}} + \frac{\bar{\sigma}(1-\nu^2)\gamma_s}{\bar{d}R_o}\left[B(\bar{b})\right]\dot{\bar{b}} \tag{5.3}$$

where, $A(\bar{b})$ and $B(\bar{b})$ take the form of appropriate expressions for $A(\bar{b}_1)$ and $B(\bar{b}_1)$ given in chapter 4 depending upon the current shape of the asperity.

We can now derive the dissipation rate potential per unit volume of the TBC ψ arising from diffusional flow of material from contacts into the gaps between asperities considering the representative volume element of Fig. 5.1 and adopting the similar procedure described in the previous chapter and write ψ as a function of $\dot{\bar{b}}$

$$\psi(\dot{\bar{b}}) \;=\; \frac{1}{4\bar{D}_g\bar{s}^2\bar{d}}\frac{R_o^3}{D_g}\bar{b}^4 C(\bar{b})\dot{\bar{b}}^2 \tag{5.4}$$

where, $C(\bar{b}) = [-B(\bar{b})]^2$.

Constitutive model

The TVP for this problem can be written as

$$\Phi(\dot{b}) \;=\; \psi(\dot{b}) + \dot{G}(\dot{b}) \tag{5.5}$$

Using $\dot{G}$ given by eqn. 5.3 and ψ given by eqn. 5.4 into the TVP given by eqn. 5.5 and minimising the resulting functional gives the rate of evolution of the microstructure $\dot{\bar{b}}$ as a function of the current state $\bar{b}$ and applied stress $\bar{\sigma}$. Here, the non-dimensional time turns out to be same as eqn. 4.24. We get the rate of evolution of $\bar{b}$ as

$$\dot{\bar{b}} \;=\; -\frac{2\bar{D}_g}{C(\bar{b})\bar{b}^4}\left[4A(\bar{b}) + (1-\nu^2)\bar{\sigma}\bar{s}^2 B(\bar{b})\right] \tag{5.6}$$

Differentiating eqn. 5.1, we get the sintering strain rate in the x_1 or x_2 direction

$$\dot{\varepsilon}^p \;=\; \frac{\dot{\bar{w}}}{\bar{d}} \tag{5.7}$$

Noting that $\dot{\bar{w}} = [-B(\bar{b})]\dot{\bar{b}}$ and substituting $\dot{\bar{b}}$ given by eqn. 5.6 into the above equation, we can re-write the sintering strain rate $\dot{\varepsilon}^p$

$$\dot{\varepsilon}^p = \frac{2\bar{D}_g}{d\bar{b}^4 B(\bar{b})}\left[4A(\bar{b}) + (1-\nu^2)\bar{s}^2\bar{\sigma}B(\bar{b})\right] \tag{5.8}$$

Considering the Fig. 5.1, we write the elastic strain ε^e in the x_1 or x_2 direction accounting for bulk and asperity deformation

$$\varepsilon^e = \frac{(1-\nu)\sigma}{E} + \frac{\sigma}{q(b)d} \tag{5.9}$$

In the above equation, E and ν are modulus and Poisson's ratio of the bulk material respectively. The effective contact stiffness q can be given by the interpolation formula (eqn. 4.38) as a function of b. The effective modulus in the x_1 or x_2 direction, E_1 is therefore

$$\frac{1}{E_1} = \frac{(1-\nu)}{E} + \frac{1}{q(b)d} \tag{5.10}$$

Assuming ε^T to be zero and differentiating the eqn. 3.29 with respect to time, we get

$$\dot{\varepsilon}^e + \dot{\varepsilon}^s = 0 \tag{5.11}$$

Adopting similar normalisation procedure used in the previous chapter and differentiating ε^e given by the eqn. 5.9 with respect to time, we get the elastic strain rate

$$\dot{\varepsilon}^e = \frac{\dot{\bar{\sigma}}}{\bar{E}_1} - \frac{\bar{\sigma}}{\bar{E}_1^2}\frac{d\bar{E}_1}{d\bar{b}}\dot{\bar{b}} \tag{5.12}$$

Note that the sintering strain rate

$$\dot{\varepsilon}^s = \dot{\varepsilon}^p = \frac{-B(\bar{b})}{\bar{d}}\dot{\bar{b}} \tag{5.13}$$

Substituting $\dot{\varepsilon}^e$ given by eqn. 5.12 and $\dot{\varepsilon}^s$ given by eqn. 5.13 into eqn. 5.11, we get

$$\dot{\bar{\sigma}} = \bar{E}_1\left(\frac{\bar{\sigma}}{\bar{E}_1^2}\frac{d\bar{E}_1}{d\bar{b}} + \frac{B(\bar{b})}{\bar{d}}\right)\dot{\bar{b}} \tag{5.14}$$

The $\dot{\bar{b}}$ given by eqn. 5.6 and $\dot{\bar{\sigma}}$ given by eqn. 5.14 can be together integrated forward to obtain the evolution of $\bar{b}$ and $\bar{\sigma}$ noting that the initial conditions ($\bar{\sigma} = 0$ at $\bar{t} = 0$ and $\bar{b} = \bar{b}_o$ at $\bar{t} = 0$). In the simulations of perfect coating, we assume ν=0.3, $\bar{d}$=40, $\bar{\gamma}_g$=0.68, $\bar{D}_g$=1 and $\bar{s}$=5 unless otherwise stated.

5.3.1 Predictions of sintering response of a perfect TBC layer

The rate equations given by eqns. 5.6 and 5.14 are time integrated by a forward Euler scheme from an initial state of $\bar{b}_o$. The evolution of the surface profile ($\bar{b}$ and $\bar{w}$) and the sintering strain (ε^s) in the perfect coating were analysed for different values of $\bar{E}$ and initial conditions of $\bar{b}$. Two types of behaviour are observed depending upon $\bar{E}$. For small values of $\bar{E}$, elastic constraint retards rate of sintering but does not prevent full sintering. Fig. 5.2 shows the evolution of surface profile and sintering strain for a choice of $\bar{E}$=90 and vanishing thermal mismatch strain ε^T. Full sintering occurs over a finite time scale. It means that the $\bar{b} \rightarrow \bar{s}/2$, ie, 2.5 for the parameters used in the calculations. When $\bar{b} \rightarrow \bar{s}/2$, full sintering is said to have occurred although there is a small gap between a cluster of asperities. During densification, the asperity height $\bar{w}$ decreases monotonically, the neck size $\bar{b}$ attains the limiting value of $\bar{b}$, the height of of the cylindrical portion of the asperity $\bar{h}$ increases and the magnitude of the sintering strain ε^s increases to a saturated finite value with increasing time. The limiting value of sintering strain in this case is $\approx -1.6\%$. Note that beyond $\bar{b}$=1, $\bar{w} = \bar{h}$.

On the other hand, for a slightly larger value of $\bar{E}$, the build-up of in-plane tensile stress within the TBC layer prevents full sintering being achieved (since the sintering potential in this case is much smaller compared to the previous model presented in chapter 3), and the neck size $\bar{b}$ asymptotes to a value of less than 2.5. As a result, the asymptotic value of the sintering strain (-0.2%) does not attain the limiting value. The evolution of contact geometry and the sintering strain are shown in Fig. 5.3 for $\bar{E} = 140$. Note that the early stages of the sintering response are qualitatively similar for the choices $\bar{E} = 90$ and 140. However, the slightly higher modulus leads to an arrest of the sintering process prior to full densification. If the magnitude of tensile stress in the coating is sufficiently large it may lead to inter-columnar mud-cracking.

We performed a number of simulations with this model and observed that the overall sintering response of this coating is also very sensitive to the initial choice of neck size $\bar{b}_o$ and Poisson's ratio (ν). In order to understand the influence of the

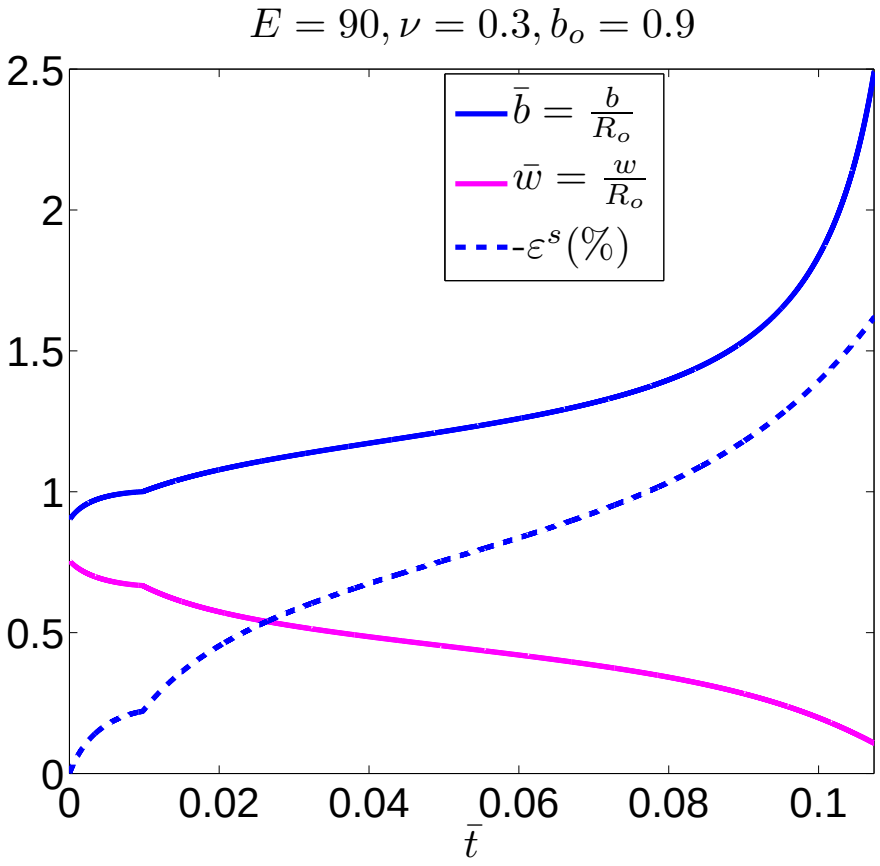

Figure 5.2: Perfect film: Evolution of contact geometry and sintering strain (%) for $\bar{E} = 90$. The initial condition $\bar{b}_o$=0.9. $\bar{t}$ is non-dimensional time.

modulus $\bar{E}$, initial choice of neck size $\bar{b}_o$ and Poisson's ratio ν on the sintering response, we compare the in-plane tensile stress $\bar{\sigma}$ generated in the coating with the sintering potential $\bar{\sigma}_s$. We now re-write the rate of change of $\bar{b}$ given by eqn. 5.6 as

$$\dot{\bar{b}} = f(\bar{b}) \left[\bar{\sigma}_s(\bar{b}) - \bar{\sigma}\right] \tag{5.15}$$

where, $\bar{\sigma}_s$ is the sintering potential and is a function of the state variable $\bar{b}$. The sintering potential is given by

$$\bar{\sigma}_s(\bar{b}) = \frac{-4A(\bar{b})}{(1-\nu^2)\bar{s}^2 B(\bar{b})} \tag{5.16}$$

Fig. 5.4 shows the sintering potential as a function of the geometric variable $\bar{b}$. In principle, $\bar{b}$ can vary from 0 to $\bar{s}/2$ (2.5 in this case). From Fig. 5.4, it can be

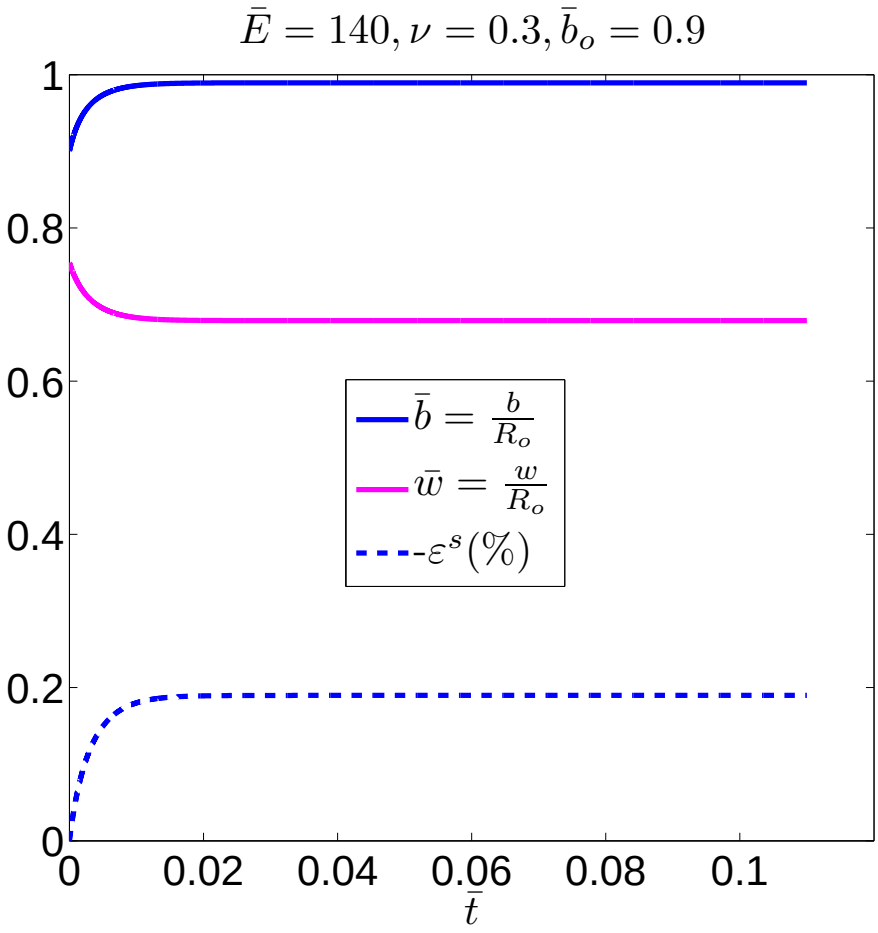

Figure 5.3: Perfect film: Evolution of contact geometry and sintering strain (%) for $\bar{E} = 140$. The initial condition $\bar{b}_o$=0.9. $\bar{t}$ is non-dimensional time.

observed that the sintering potential slightly decreases with increase of $\bar{b}$, until $\bar{b}$=1 and increases monotonicaly thereafter with the increase of $\bar{b}$. Note that the nature and magnitude of the sintering potential depends upon the contact model (contact geometry and its distribution) we employ and therefore, the sintering potential of this model is different from that of the the previous model. Since we assume widely spaced contacts between columns, the magnitude of the sintering potential is less in this case and the coating does not stiffen up quickly. Now for the choice of $\bar{E}$=90 and ν=0.3, sintering studies were performed for different values of initial neck size $\bar{b}_o$ and the resulting stress build-up in the coating compared with sintering potential in order to assess the sensitivity of initial neck size $\bar{b}_o$ to sintering response of the

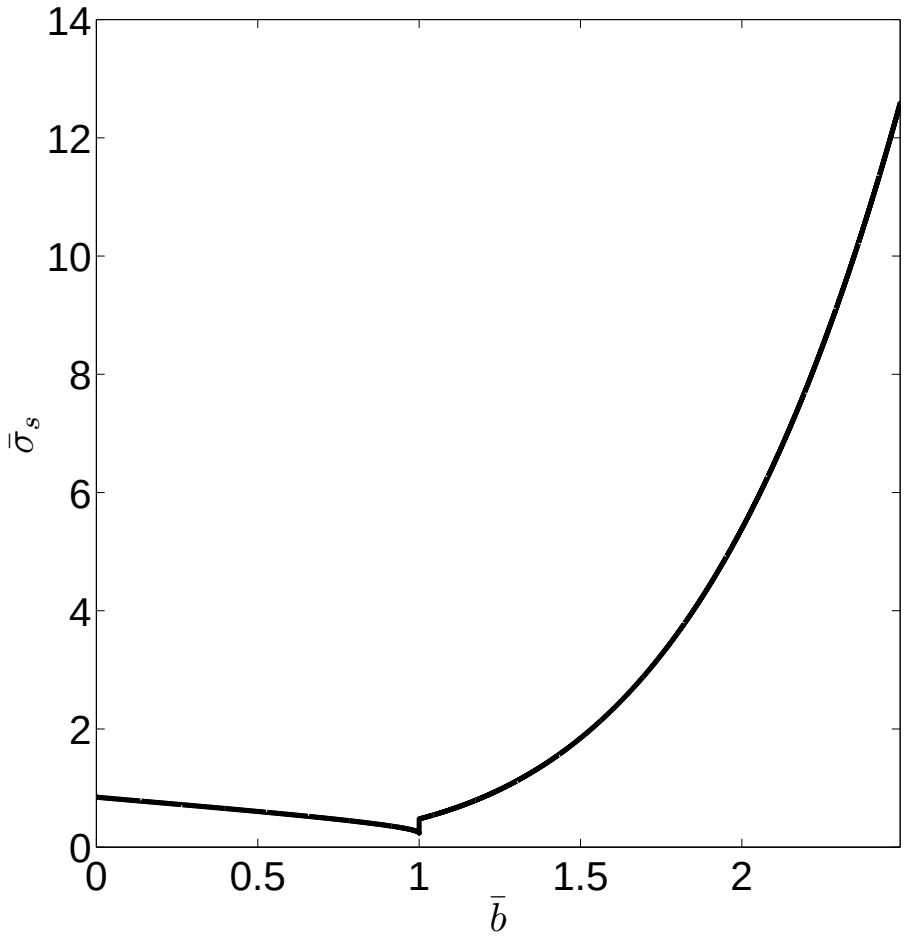

Figure 5.4: Sintering potential $\bar{\sigma}_s$ as a function of geometric variable $\bar{b}$. $\bar{b}$ is varied from 0.001 to $\bar{s}/2$ (2.5 in this case).

coating. Fig. 5.5 shows the in-plane stress produced in the coating for different initial conditions $\bar{b}_o$ along with the sintering potential. For small values of $\bar{b}_o$, say, less than 0.9, the stress generated in the coating due to sintering, attains the value of the sintering potential in the early stages itself. At this stage, sintering gets arrested and $\bar{b}$ does not evolve thereafter. In contrast, for values of $\bar{b}_o \geq 0.9$, the stress generated in the coating due to sintering never reaches the sintering potential and therefore sintering proceeds until full densification ($\bar{b}$=2.5). Now we will explore the influence of in-plane modulus $\bar{E}$ on sintering response for given initial $\bar{b}$ and ν. Fig. 5.6 shows

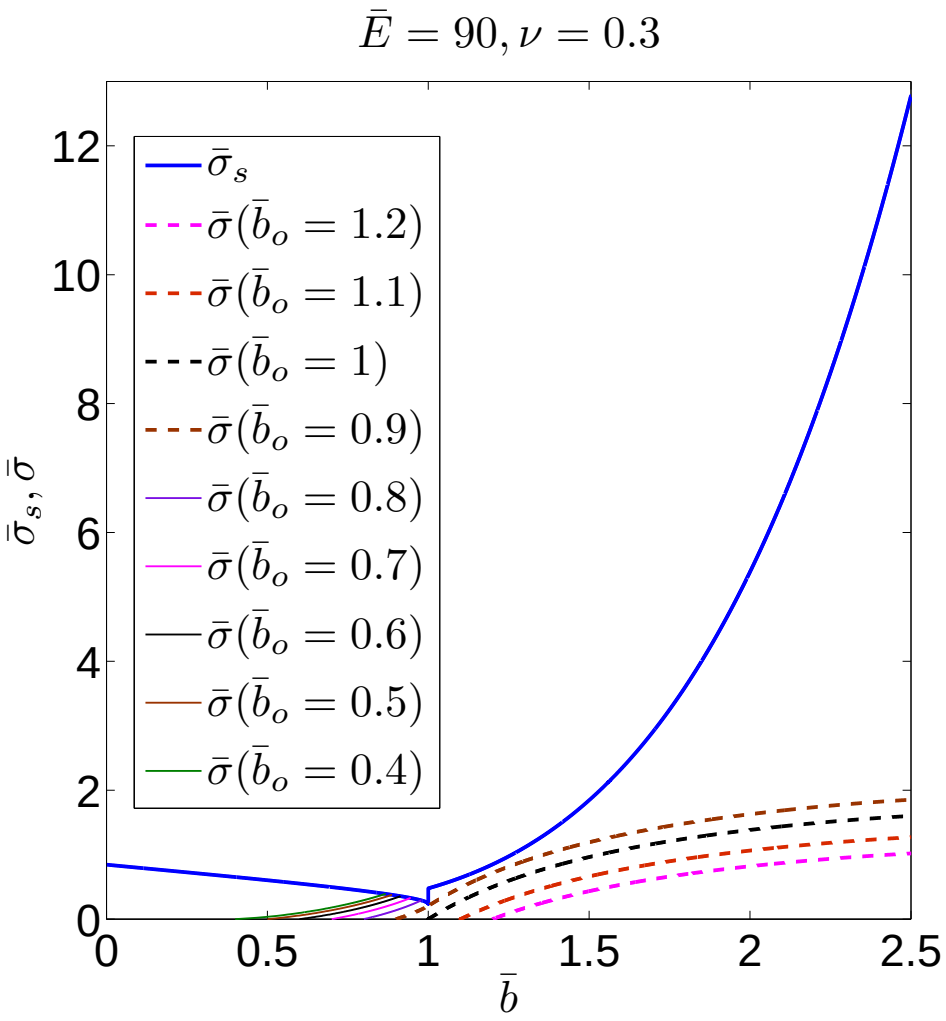

Figure 5.5: In-plane stress $\bar{\sigma}$ produced in the coating for different choices of initial neck size $\bar{b}_o$.

the comparison of in-plane stress produced in the coating with sintering potential for different values of $\bar{E}$. In these analyses, $\bar{b}_o$ is taken to be 1.2 and ν is taken to be 0.3. From Fig. 5.6, it is clear that for small values of $\bar{E}$ ie $\bar{E} < 330$, stress produced in the coating never reaches the value of the sintering potential, i.e, the stress generated in the coating is not sufficient enough to switch-off sintering and therefore the coating goes to full density. For $\bar{E} > 330$, stress produced in the coating reaches the value of the sintering potential and therefore sintering gets arrested prior to full densification. The Poisson's ratio ν also influences the sintering response of the perfect coating.

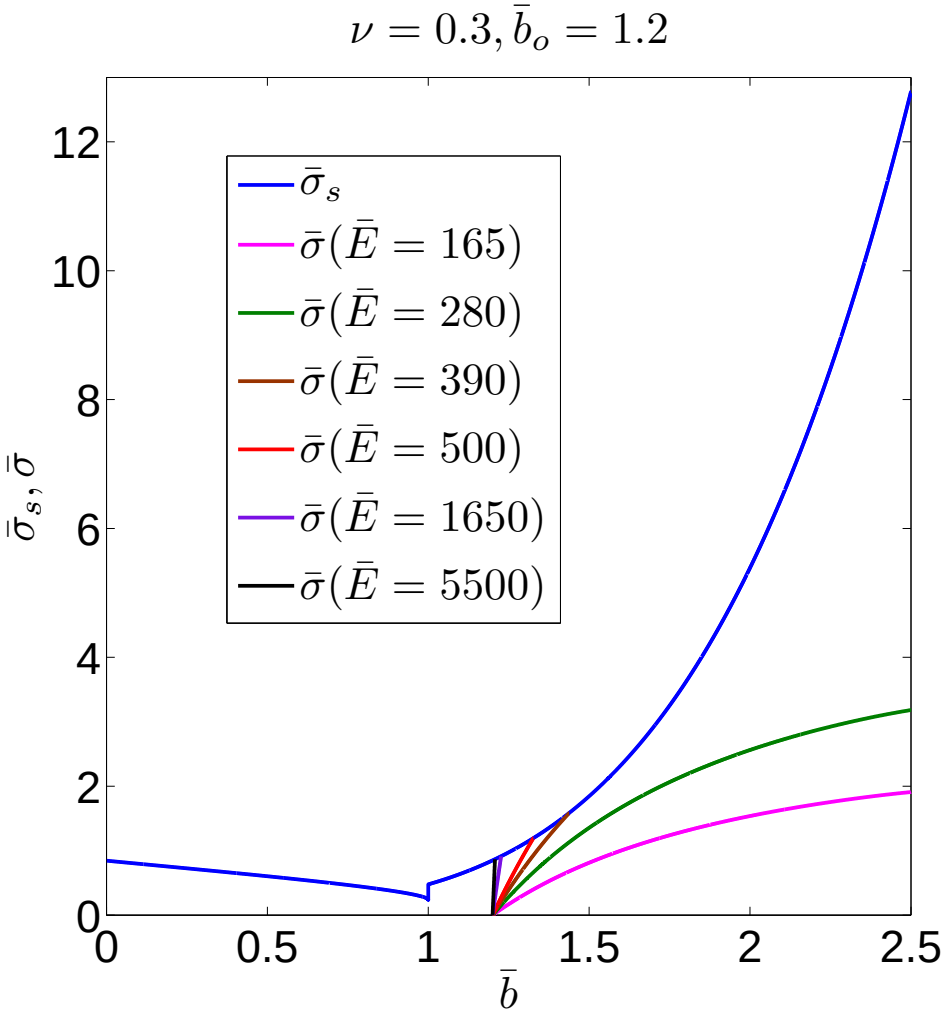

Figure 5.6: In-plane stress $\bar{\sigma}$ produced in the coating for different choices $\bar{E}$.

Fig. 5.7 shows the in-plane stress in the coating compared with sintering potential for different values of ν with a initial neck size $\bar{b}_o$=1.2 and $\bar{E}$=400. For smaller values of ν, $\bar{b}$ evolves to full possible value whereas it does not grow for larger values of ν as shown in Fig. 5.7.

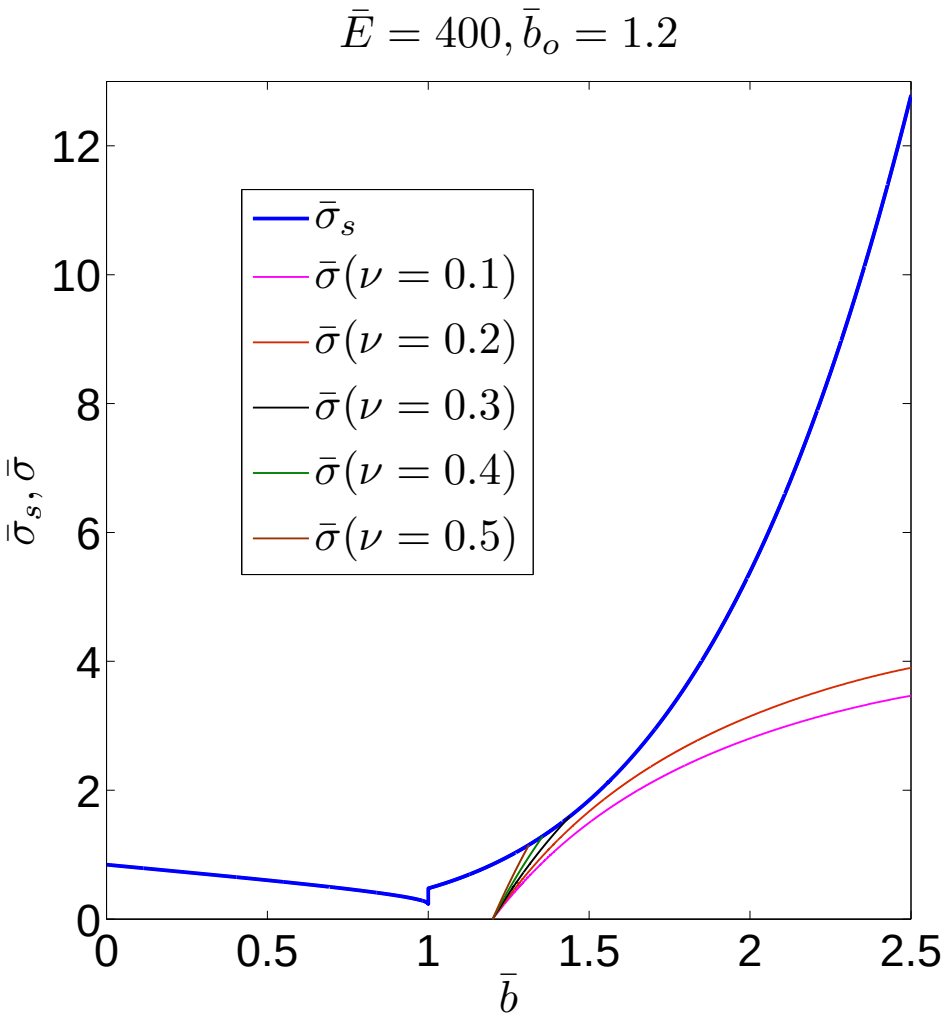

Figure 5.7: In-plane stress $\bar{\sigma}$ produced in the coating for different choices ν.

5.4 Problem B: Modelling evolution of primary imperfections

In the previous chapter, we performed finite element studies of the sintering response of the TBC comprising axisymmetric contacts between columns by seeding the coating with imperfections. In essence, the computational model indicates when mud-cracking can occur in practice. However, with the FE model a substantial amount of computational time is required to map out the failure behaviour in terms of geometric and material properties of the coating. Therefore, in this section we formulate a

simple analytical model following the sintering model discussed in the previous section to capture the sintering response of the TBC when it contains a single family of imperfections and conduct a range of calculations to generate a failure map for TBCs. Further, we can readily calibrate this analytical model using the computational model discussed in the previous chapter.

In this section we develop a two state variable Rayleigh-Ritz type model. In developing the model, it is assumed that the columns are inextensible both elastically and plastically in the x_3, i.e, the thickness direction. The change of coating stiffness during sintering is taken into account. We idealise the structure of a TBC as before (see Fig. 3.8) and consider a square grid of primary imperfections that exist at the boundaries of the clusters. At these imperfections, the initial contact radius of asperities is slightly less than within the cluster. These imperfections may grow during in-service sintering of the TBC depending upon geometric and material properties of the coating and the extent of assumed pre-sintering between neighbouring columns, and lead to mud-cracking.

In order to model the formation of mud-cracks, a representative repeating cell is chosen that has primary imperfections within it as shown in Fig. 3.8. For the computational studies, we assumed that the imperfection extended throughout a continuum element. As in the analysis of chapter 3, we assume that the imperfection exists along a single line of contacts between neighbouring columns. This is a more reasonable assumption. Isothermal conditions are imposed within the repeating cell which may be greater than or less than the deposition temperature T_D. The goal is to determine the time evolution of axisymmetric asperities within the clusters and at the primary imperfections and to identify conditions under which a fully developed primary crack forms due to the imposed thermal mismatch associated with T.

5.4.1 Global considerations

As inter-columnar sintering progresses in the TBC which contains a regular pattern of primary imperfections, an equi-biaxial sintering strain ε^s_{ij} evolves with time. As in

chapter 3, we assume that the sintering strain is uniform within the cluster. ε_{ij}^{s} can be decomposed into two fields (given by eqn. 3.28), one corresponding to sintering of a perfect TBC film with sintering strain ε_s^1 and thermal mismatch strain ε^T (given by eqn. 3.27) and the other corresponding to inter-columnar sintering of an isolated cluster with sintering strain ε_s^2 as shown in Fig. 3.9. The thermodynamic variational principle of Cocks et al [45] is used again here in order to calculate the time evolution of ε_s^1 and ε_s^2 based upon an assumed axisymmetric contact geometry between neighboring TBC columns. The contact geometry within the cluster and at the primary imperfections are shown in Fig.5.8. The subscripts $'cl'$ and $'cr'$ characterise the geometric parameters within the cluster and at the primary imperfections respectively. Note that the elastic deformation in field 1, $\varepsilon_{ij}^{e_1}$, is uniform and it is compatible with

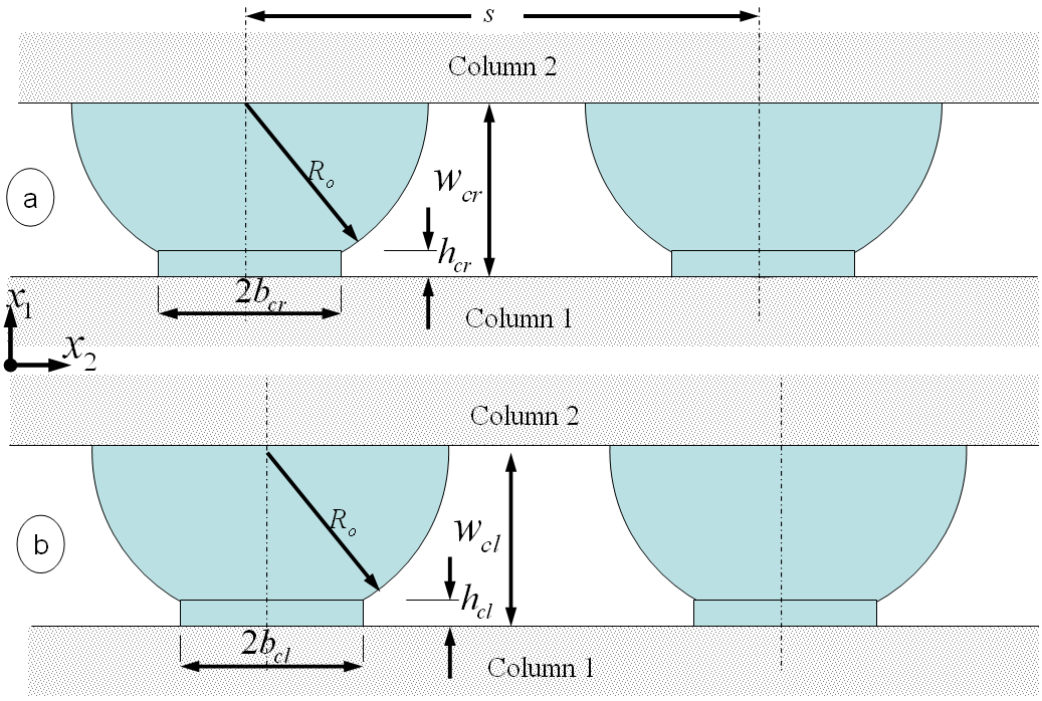

Figure 5.8: Idealisation of surface undulations. a. Current configuration at primary imperfection, where column 1 has displaced an amount $(w_1^{cr} - w_{cr})$ with respect to column 2 from the initial configuration. b. Current configuration within cluster, where column 1 has displaced an amount $(w_1^{cl} - w_{cl})$ with respect to column 2.

sintering strain in field 1, ε_{ij}^{s1} (given by eqn. 3.29). In field 2 of the repeating cluster,

we consider elastic constraint of the substrate up to a height ξ in the x_3 direction from the substrate. We consider the situations where, $\xi \leq H$ or $\xi \geq H$ (see Fig. 5.9 or Fig. 5.10). This elastic constraint alters the contact condition along the x_3 direction at the imperfections as shown in Fig. 5.9 or Fig. 5.10. Therefore, the following compatibility condition needs to be satisfied in field 2. The detailed form of field 2 is given later.

$$\left(\varepsilon_{ij}^{e_2}(x_3) + \varepsilon_{ij}^{s_2}\right) 2R - \Delta w_s(x_3) = 0 \tag{5.17}$$

Here, $\Delta w_s(x_3)$ is the net displacement across the primary imperfection.

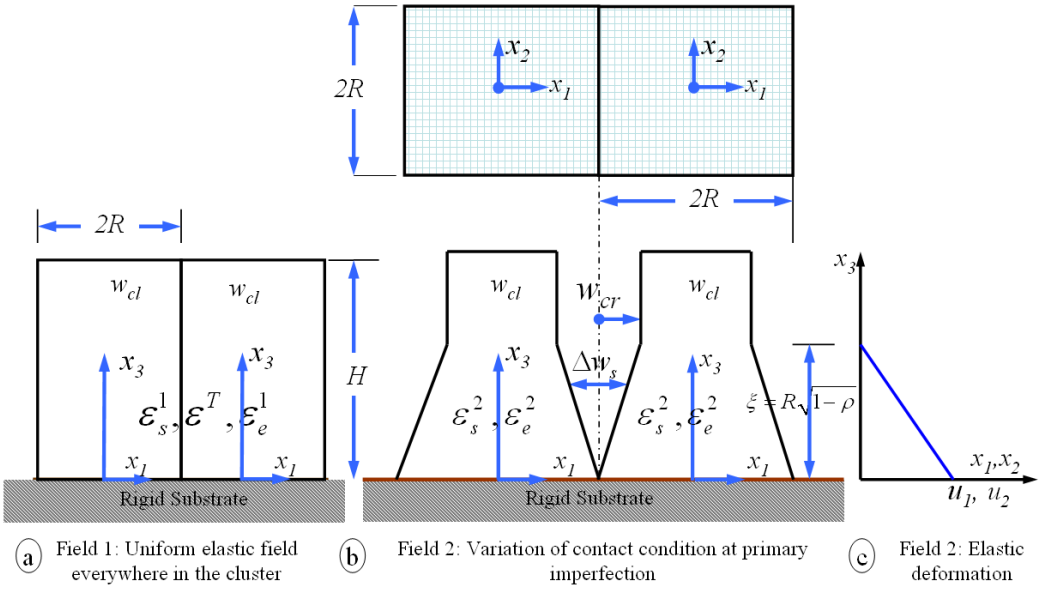

Figure 5.9: Variation of elastic field in the cluster. a. Field 1: Uniform elastic field exists over entire height H of the cluster. b. Field 2: Non-uniform elastic field in the bottom portion of cluster up to a height ξ from the substrate. c. Field 2: In-plane elastic deformation in the bottom portion of cluster

5.4.2 Local considerations

Contact geometry

The reference configuration is given in Fig. 4.4a. Considering only grain boundary diffusion at the interfaces, we can describe the contact geometry between columns at an imperfection at any instant during sintering by the geometric variable w_{cr} as shown

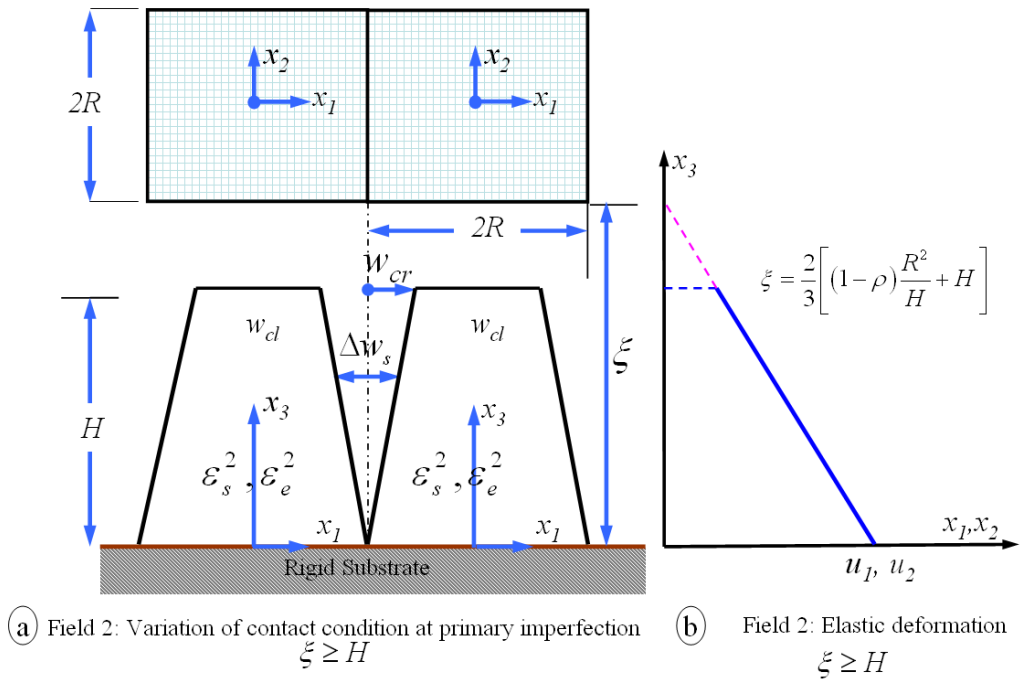

Figure 5.10: Variation of elastic field in the cluster: a. Contact condition changes from the bottom to top of the cluster b. In-plane elastic deformation of the cluster up to a height H from the substrate.

in Fig. 5.8a; and the contact geometry at a typical instant between columns within a cluster can be characterised by the geometric variable w_{cl} as shown in Fig. 5.8b. As sintering proceeds, the contact radius of the asperity within cluster b_{cl} and that at the imperfections b_{cr} increase and the total asperity height within cluster, w_{cl} and that at the imperfections w_{cr} decrease, while the centre to centre distance between asperities, s, remains the same. The height of the cylindrical portion of the asperities within cluster h_{cl} and that at the imperfections h_{cr} also increase with sintering. With further sintering, b_{cl} attains the value of R_o, this is the stage at which the asperity within cluster becomes a pure cylinder and h_{cl} reaches w_{cl}. With prolonged sintering, the cylindrical asperity flattens until it touches the neigbouring asperities. This is the state of full sintering. At this state $b_{cl} = s/2$. Similarly, full sintering can also happen at the imperfections in certain situations. However, when continued desintering occurs at imperfections, b_{cr} eventually becomes zero, this is the stage at

which physical separation occurs at interfaces.

The objective of the problem is to solve for the local evolution of surface profile within the repeating cluster as characterized by w_{cr} and w_{cl} due to the grain boundary diffusion of matter from the contacts into the gaps between asperities.

5.4.3 Geometric coupling between local and global scales

When $\xi \leq H$ as shown in Fig. 5.9

The uniform macroscopic sintering strain in field 1, ε_s^1 and in field 2, ε_s^2 are expressed in terms of the state variables (w_{cr}, w_{cl}) and their appropriate initial choices (w_1^{cr}, w_1^{cl}). The elastic strain in field 2 varies from the bottom to the top of the cluster due to the constraint of the substrate. Assuming a kinematically admissible in-plane elastic deformation of the cluster (field 2) up to a height ξ in the x_3 direction (see Fig. 5.9, $\xi \leq H$), we get

$$\Delta w_s(x_3) = \begin{cases} -2R\varepsilon_s^2 \, \frac{x_3}{\xi} & \text{if} \quad 0 \leq x_3 \leq \xi; \\ -2R\varepsilon_s^2 & \text{if} \quad \xi \leq x_3 \leq H. \end{cases}$$

The primary unknown at contacts within cluster w_{cl} is given by

$$w_{cl} \;=\; w_1^{cl} + \left(\varepsilon_s^1 + \varepsilon_s^2\right) d \tag{5.18}$$

The asperity height at the primary imperfection is given by

$$w_{cr}(x_3) \;=\; w_1^{cr} + \left(\varepsilon_s^1 + \varepsilon_s^2\right) d + \Delta w_s(x_3) \tag{5.19}$$

Noting that $w_{cr}(x_3)$ at $x_3 = \xi$ is w_{cr} and using appropriate expression for $\Delta w_s(x_3)$ in the above equation, we can write the state variable at the primary imperfection as

$$w_{cr} \;=\; w_1^{cr} + \left(\varepsilon_s^1 + \varepsilon_s^2\right) d - 2R\varepsilon_s^2 \tag{5.20}$$

Now manipulating the expression for w_{cr} with w_{cl} given by eqn. 5.18, we can express the sintering strains in the two fields as functions of two state variables (w_{cr}, w_{cl}) as follows

$$\varepsilon_s^1 \;=\; \frac{w_{cl} - w_1^{cl}}{d} - \left[\frac{(w_1^{cr} - w_1^{cl}) - (w_{cr} - w_{cl})}{2R}\right] \tag{5.21}$$

and

$$\varepsilon_s^2 = \left[\frac{(w_1^{cr} - w_1^{cl}) - (w_{cr} - w_{cl})}{2R}\right] \tag{5.22}$$

Note that w_1^{cr} and w_1^{cl} are the initial values of state variables w_{cr} and w_{cl} respectively soon after deposition.

When $\xi \geq H$ as shown in Fig. 5.10

As discussed above, we can similarly express ε_s^1 and ε_s^2 in terms of the state variables when $\xi \geq H$ as shown in Fig. 5.10. Assuming a kinematically admissible in-plane elastic displacement of the cluster (field 2) up to a height H as shown in Fig. 5.10, we get

$$\Delta w_s(x_3) = \begin{cases} -2R\varepsilon_s^2 \frac{x_3}{\xi} & \text{if} \quad 0 \leq x_3 \leq H. \end{cases}$$

Now the asperity height at the primary imperfection can be written as a function of x_3

$$w_{cr}(x_3) = w_1^{cr} + \left(\varepsilon_s^1 + \varepsilon_s^2\right) d - 2R\varepsilon_s^2 \frac{x_3}{\xi} \tag{5.23}$$

Note that $w_{cr}(x_3) = w_{cr}$ at $x_3 = H$ and the above equation reduces to

$$w_{cr} = w_1^{cr} + \left(\varepsilon_s^1 + \varepsilon_s^2\right) d - 2R\varepsilon_s^2 \frac{H}{\xi} \tag{5.24}$$

Now combining w_{cl} given by eqn. 5.18 and w_{cr} given by the eqn. 5.24, we can express ε_s^1 and ε_s^2 in terms of the state variables (w_{cr}, w_{cl}).

$$\varepsilon_s^1 = \frac{w_{cl} - w_1^{cl}}{d} - \left[\frac{(w_1^{cr} - w_1^{cl}) - (w_{cr} - w_{cl})}{2RH}\right] \xi \tag{5.25}$$

and

$$\varepsilon_s^2 = \left[\frac{(w_1^{cr} - w_1^{cl}) - (w_{cr} - w_{cl})}{2RH}\right] \xi \tag{5.26}$$

Note that the optimum height ξ in this case is different to the previous case and it is obtained by minimising the elastic stored energy in the cluster.

5.4.4 Thermodynamic variational principle(TVP)

We consider only grain boundary diffusion at contacts to model local sintering between neighbouring columns and go on to solve for the time evolution of geometric

variables (w_{cr}, w_{cl}) under a uniform temperature T. To solve this local sintering problem in a repeating cluster with primary imperfections, the thermodynamic variational principle is used to obtain the time evolution of (w_{cr}, w_{cl}) and this requires determination of the rate of change of Gibbs free energy density of the coating $\dot{G}$, and the rate potential density ψ arising from the local flux of matter at contacts. The Gibbs free energy density rate is derived as an explicit function of the rate of change of the state variables $(\dot{w}_{cr}, \dot{w}_{cl})$. The rate potential ψ is obtained as an explicit quadratic function of the rates of kinematic variables $(\dot{w}_{cr}, \dot{w}_{cl})$. For a given geometry of TBC columns and initial microstructure described by (w_1^{cr}, w_1^{cl}), it is shown below that the rate of evolution of the microstructure is given by the set of kinematic rates $(\dot{w}_{cr}, \dot{w}_{cl})$ that minimise the functional Φ.

$$\Phi(\dot{w}_{cr}, \dot{w}_{cl}) \;=\; \dot{G}(\dot{w}_{cr}, \dot{w}_{cl}) + \psi(\dot{w}_{cr}, \dot{w}_{cl}) \tag{5.27}$$

This gives two linear simultaneous equations for the rates that can be cast in matrix form:

$$\begin{bmatrix} \frac{\partial^2 \psi}{\partial \dot{w}_{cr}^2} & \frac{\partial^2 \psi}{\partial \dot{w}_{cr} \partial \dot{w}_{cl}} \\ \frac{\partial^2 \psi}{\partial \dot{w}_{cr} \partial \dot{w}_{cl}} & \frac{\partial^2 \psi}{\partial \dot{w}_{cl}^2} \end{bmatrix} \begin{bmatrix} \dot{w}_{cr} \\ \dot{w}_{cl} \end{bmatrix} = - \begin{bmatrix} \frac{\partial \dot{G}}{\partial \dot{w}_{cr}} \\ \frac{\partial \dot{G}}{\partial \dot{w}_{cl}} \end{bmatrix}$$

This matrix can be inverted algebraically to obtain $(\dot{w}_{cr}, \dot{w}_{cl})$ as a function of the current state (w_{cr}, w_{cl}). The time evolution of (w_{cr}, w_{cl}) is obtained by time integration of this set of nonlinear ODEs using a fourth-order Runge-Kutta (R-K4) method.

5.4.5 Determination of Gibbs free energy

The Gibbs free energy density, G, in the TBC is given by

$$G \;=\; G_i + U \tag{5.28}$$

where, G_i is the interfacial energy density and U is the elastic strain energy density of the TBC.

Determination of interface free energy

In this section, we estimate the interface energy density of the the TBC. The interfacial energy of the TBC has contributions from bulk contacts associated with w_{cl}

within the cluster and contacts associated with the primary imperfection $w_{cr}(x_3)$. Let G_i^{cl} be the interface energy density associated with bulk contact and G_i^{cr} be the interface energy density associated with primary imperfections of the TBC. Thus the interfacial energy density of the TBC is given by

$$G_i \;=\; G_i^{cl} + G_i^{cr} \tag{5.29}$$

The expressions for G_i^{cl} and G_i^{cr} for different choices of ξ are derived in Appendix B.

Determination of elastic stored energy; $\xi \leq H$

We derive now the elastic stored energy for $\xi \leq H$. The elastic strain energy in the potential cluster has contributions from field 1, field 2 and the interaction between them. The total elastic strain energy U_C in the cluster can be written as

$$U_C \;=\; \frac{1}{2}\int_V \left[\sigma_{ij}^1 \varepsilon_{ij}^{e_1} + \sigma_{ij}^2 \varepsilon_{ij}^{e_2} + 2\sigma_{ij}^1 \varepsilon_{ij}^{e_2}\right] dV \tag{5.30}$$

Here, i and j independently range over 1-3. Here, $\varepsilon_{ij}^{e_1}$ and $\varepsilon_{ij}^{e_2}$ are the the elastic strain tensor in field 1 and field 2 respectively. Similarly, σ_{ij}^1 and σ_{ij}^2 are the stresses associated with kinematically admissible strain fields 1 and 2, respectively. Since these fields are arbitrary the stresses do not necessarily satisfy equilibrium. The first two terms in the above equation are the strain energy in field 1 and field 2 respectively. The third term is the energy due to interaction between two fields.

The total elastic strain energy in the cluster is given by

$$U_C = \frac{4ER^2H\tilde{q}d}{(1-\nu^2)}(\varepsilon_s^1+\varepsilon^T)^2+\frac{4}{3}\frac{E\tilde{q}d}{(1-\nu^2)}(\varepsilon_s^2)^2R^2\xi+\frac{8}{3}G\tilde{q}d(\varepsilon_s^2)^2\frac{R^4}{\xi}+\frac{4E\tilde{q}d}{(1-\nu^2)}(\varepsilon_s^1+\varepsilon^T)\varepsilon_s^2R^2\xi \tag{5.31}$$

The optimal height ξ that minimises the total strain energy U_C is a function of ε_s^1 and ε_s^2. However, we take $\xi = R\sqrt{1-\rho}$ which minimises the strain energy in field 2 in order to keep the description of the evolving crack geometry simple. The factor ρ is related to $\frac{G}{E}$ ratio as given by eqn. 4.40. Note that when $\rho \to \nu$, $E \to 2G(1+\nu)$ and this relationship is valid for sticking condition of contacts. However, we expect sliding between asperities of the TBC at temperature. Therefore, we choose a value

of ρ close to 1 in our analysis so as to allow sliding between columns during sintering. Now the total strain energy density of the TBC is given by

$$U_T = \frac{E\tilde{q}d}{(1-\nu^2)}\left\{(\varepsilon_s^1+\varepsilon^T)^2 + \left[\frac{2}{3}(\varepsilon_s^2)^2 + (\varepsilon_s^1+\varepsilon^T)\varepsilon_s^2\right]\frac{R}{H}\sqrt{1-\rho}\right. \tag{5.32}$$

Taking, $\tilde{q} = \frac{4b_{cl}}{\pi s^2}$ and non-dimensionalising the above equation, we can express the strain energy density

$$U = \frac{4\bar{E}\bar{b}_{cl}\bar{d}}{\pi\bar{s}^2}\left(\frac{\gamma_s}{R_o}\right)\left\{(\varepsilon_s^1+\varepsilon^T)^2 + \left[\frac{2}{3}(\varepsilon_s^2)^2 + (\varepsilon_s^1+\varepsilon^T)\varepsilon_s^2\right]\bar{R}\sqrt{1-\rho}\right. \tag{5.33}$$

In eqn. B.38, the expression for $\bar{b}_{cl}$ depends upon the current shape of the asperity within the cluster. Using the expressions for ε_s^1 given by eqn. 5.21 and ε_s^2 given by eqn. 5.22 in terms of normalised state variables $(\bar{w}_{cr}, \bar{w}_{cl})$ in eqn. B.38, we can get $U(\bar{w}_{cr}, \bar{w}_{cl})$. Note that in this case, $\xi \leq H$. Therefore,

$$\bar{R} \leq \frac{1}{\sqrt{1-\rho}} \tag{5.34}$$

when ρ is close to 1, say, 15/16, $\bar{R} \leq 4$. Complete derivation of elastic stored energy is given in Appendix B.

Determination of elastic stored energy; $\xi \geq H$

Following the analysis of axisymmetric quantum dots of Gill and Cocks [89], we derive U as before assuming that $\xi \geq H$ as shown in Fig. 5.10. In this case, the elastic stored energy density in non-dimensional form is given by

$$\begin{aligned} U =& \frac{4\bar{E}\bar{b}_{cl}\bar{d}}{\pi\bar{s}^2}\left(\frac{\gamma_s}{R_o}\right)\left\{(\varepsilon_s^1+\varepsilon^T)^2 + \frac{1}{3}(\varepsilon_s^2)^2\left(\frac{\bar{H}}{\bar{\xi}}\right)^2 - (\varepsilon_s^2)^2\frac{\bar{H}}{\bar{\xi}}\right. \\ &\left. +(\varepsilon_s^2)^2 + \frac{(1-\rho)}{3}(\varepsilon_s^2)^2\left(\frac{\bar{R}\bar{H}}{\bar{\xi}}\right)^2 + 2(\varepsilon_s^1+\varepsilon^T)\varepsilon_s^2\left(1-\frac{\bar{H}}{2\bar{\xi}}\right)\right\} \end{aligned} \tag{5.35}$$

Using the expressions for ε_s^1 given by eqn. 5.25 and ε_s^2 given by eqn. 5.26 in terms of normalised state variables $(\bar{w}_{cr}, \bar{w}_{cl})$ in eqn. B.44, we obtain $U(\bar{w}_{cr}, \bar{w}_{cl})$. Note that

$$\bar{\xi} = \frac{2}{3}\bar{H}\left[(1-\rho)\bar{R}^2 + 1\right] \tag{5.36}$$

as $\xi \geq H$,

$$\bar{R} \geq \frac{1}{\sqrt{2(1-\rho)}} \tag{5.37}$$

For $\rho = 15/16$, $\bar{R} \geq 2.82$. Note that by comparing $\bar{R}$ given by the eqns. B.46 and B.39, we see that U is not continuous. Plotting U as a function of $\bar{R}$ for $\rho = 15/16$, reveals $U(\xi \leq H)$ is less than $U(\xi \geq H)$ between $\bar{R} = 2.82$ and $\bar{R} = 4$ and therefore $U(\xi \leq H)$ is valid for $\bar{R} \leq 4$ and $U(\xi \geq H)$ is valid for $\bar{R} \geq 4$. The elastic stored for this case is also derived in Appendix B. Now the Gibbs energy density of the TBC, G, given by eqn. B.1 can be re-written as

$$G \;=\; G_i^{cl}(\bar{w}_{cl}) + \int_0^{\bar{\xi}} G_i^{cr^b}(\bar{w}_{cr}, \bar{w}_{cl}, \bar{x}_3) d\bar{x}_3 + G_i^{cr^t}(\bar{w}_{cr}) + U(\bar{w}_{cr}, \bar{w}_{cl}); \qquad \xi \leq H \tag{5.38}$$

Note that in the above equation, $U(\bar{w}_{cr}, \bar{w}_{cl})$ is given by eqn. B.38 and

$$G \;=\; G_i^{cl}(\bar{w}_{cl}) + \int_0^{\bar{H}} G_i^{cr^b}(\bar{w}_{cr}, \bar{w}_{cl}, \bar{x}_3) d\bar{x}_3 + U(\bar{w}_{cr}, \bar{w}_{cl}); \qquad \xi \geq H \tag{5.39}$$

In this equation, $U(\bar{w}_{cr}, \bar{w}_{cl})$ is given by eqn. B.44

5.4.6 Determination of rate potential ψ

We now determine the macroscopic rate potential ψ per unit volume of the TBC. Considering only grain boundary diffusion along the local co-ordinate OA as shown in Fig. B.1, the macroscopic rate potential within the cluster per unit volume of the TBC is given by

$$\psi^{cl} \;=\; \frac{8}{\pi s^2 R}\left(\frac{R}{d} - \frac{1}{2}\right)\psi_a^{cl} \tag{5.40}$$

An explicit expression can be obtained for ψ^{cl} by integration of eqn. 4.17, using appropriate expressions for the flux to give

$$\psi^{cl} \;=\; \frac{1}{2s^2 R D_g}\left(\frac{R}{d} - \frac{1}{2}\right)\dot{w}_{cl}^2 b_{cl}^4 \tag{5.41}$$

ψ^{cl} in normalised form is given by

$$\psi^{cl} \;=\; \frac{1}{2\bar{D}_g \bar{s}^2 \bar{R}\bar{H}}\left(\frac{R_o^3}{D_g}\right)\left(\frac{\bar{R}\bar{H}}{\bar{d}} - \frac{1}{2}\right)\dot{\bar{w}}_{cl}^2 \bar{b}_{cl}^4 \tag{5.42}$$

$\bar{b}_{cl}$ in the above equation is a function of $\bar{w}_{cl}$ and depends upon the current shape of the asperity. Similarly, considering an asperity contact geometry at the primary imperfection as shown in Fig. B.2, the rate potential per unit volume of the TBC in the bottom portion of the imperfection up to height ξ from the substrate (note $\xi \leq H$) is given by

$$\psi^b_{cr} = \frac{4}{\pi s^2 RH} \int_0^{\xi} \frac{\pi}{16 D_g} (\dot{w}^b_{cr})^2 (b^b_{cr})^4 dx_3 \tag{5.43}$$

Adopting the normalisations discussed earlier we can write ψ^b_{cr} in non-dimensional form as

$$\psi^b_{cr} = \frac{1}{4\bar{s}^2 \bar{R} \bar{H}^2 \bar{D}_g} \left(\frac{R_o^3}{D_g}\right) \int_0^{\bar{\xi}} (\dot{\bar{w}}^b_{cr})^2 (\bar{b}^b_{cr})^4 d\bar{x}_3 \tag{5.44}$$

In the above equation,

$$\dot{\bar{w}}^b_{cr} = \left(1 - \frac{\bar{x}_3}{\bar{\xi}}\right) \dot{\bar{w}}_{cl} + \frac{\bar{x}_3}{\bar{\xi}} \dot{\bar{w}}_{cr} \tag{5.45}$$

Note that $\bar{b}^b_{cr}$ in eqn. 5.44 is a function of $\bar{w}^b_{cr}$ and it depends upon the current shape of the asperity at this location. And $\bar{w}^b_{cr}(\xi \leq H)$ is a function of $(\bar{w}_{cr}, \bar{w}_{cl}, \bar{x}_3)$. Now we will determine the macroscopic rate potential per unit volume of the TBC in the top portion of the imperfection where there is uniform contact

$$\psi^t_{cr} = \frac{4}{\pi s^2 RH} (H - \xi) \frac{\pi}{16 D_g} \dot{w}^2_{cr} b^4_{cr} dx_3 \tag{5.46}$$

Normalising the above equation, we get,

$$\psi^t_{cr} = \frac{(\bar{H} - \bar{\xi})}{4\bar{s}^2 \bar{R} \bar{H}^2 \bar{D}_g} \left(\frac{R_o^3}{D_g}\right) \dot{\bar{w}}^2_{cr} \bar{b}^4_{cr} d\bar{x}_3 \tag{5.47}$$

$\bar{b}_{cr}$ in the above equation is a function of $\bar{w}_{cr}$ and it depends on the current shape of the asperity. Now the total macroscopic dissipation potential per unit volume of TBC is given by the sum of eqns. 5.42, 5.44 and 5.47

$$\psi(\dot{\bar{w}}_{cr}, \dot{\bar{w}}_{cl}) = \psi^{cl}(\dot{\bar{w}}_{cl}) + \int_0^{\bar{\xi}} \psi^b_{cr}(\dot{\bar{w}}_{cr}, \dot{\bar{w}}_{cl}, \bar{x}_3) d\bar{x}_3 + \psi^t_{cr}(\dot{\bar{w}}_{cr}); \qquad \xi \leq H \tag{5.48}$$

Similarly we can derive the rate potential per unit volume of the TBC when $\xi \geq H$ and is give by

$$\psi(\dot{\bar{w}}_{cr}, \dot{\bar{w}}_{cl}) = \psi^{cl}(\dot{\bar{w}}_{cl}) + \int_0^{\bar{H}} \psi^b_{cr}(\dot{\bar{w}}_{cr}, \dot{\bar{w}}_{cl}, \bar{x}_3) d\bar{x}_3; \qquad \xi \geq H \tag{5.49}$$

5.4.7 Numerical solution of 2DOF system

Now differentiating G given by the eqn. B.47 with respect to time, we obtain $\dot{G}$ and using this together with ψ given by the eqn. 5.48, we construct the functional. Rendering the functional stationary gives a set of non-linear ODEs and the appropriate non-dimensional time scale turns out to be the same as eqn. 4.24. The non-dimensional form of $\dot{G}$ and ψ are

$$\dot{\bar{G}}(\dot{\bar{w}}_{cr}, \dot{\bar{w}}_{cl}) \;=\; \dot{\bar{G}}_i^{cl}(\dot{\bar{w}}_{cl}) + \int_0^{\bar{\xi}} \dot{\bar{G}}_i^{cr^b}(\dot{\bar{w}}_{cr}, \dot{\bar{w}}_{cl}, \bar{x}_3) d\bar{x}_3 + \dot{\bar{G}}_i^{cr^t}(\dot{\bar{w}}_{cr}) + \dot{\bar{U}}(\dot{\bar{w}}_{cr}, \dot{\bar{w}}_{cl}) \quad (5.50)$$

$$\bar{\psi}(\dot{\bar{w}}_{cr}, \dot{\bar{w}}_{cl}) \;=\; \bar{\psi}^{cl}(\dot{\bar{w}}_{cl}) + \int_0^{\bar{\xi}} \bar{\psi}_{cr}^{b}(\dot{\bar{w}}_{cr}, \dot{\bar{w}}_{cl}, \bar{x}_3)\, d\bar{x}_3 + \bar{\psi}_{cr}^{t}(\dot{\bar{w}}_{cr}) \quad (5.51)$$

The second term of eqn. 5.50 needs to be numerically evaluated at each time step. We use a Gaussian quadrature rule to get an approximation for the definite integral of this function. The integral over $[0, \bar{\xi}]$ must be changed into an integral over $[-1, 1]$ before applying the Gaussian quadrature rule. In order to do that, replace $\bar{x}_3$ and $d\bar{x}_3$ in the above function by

$$\bar{x}_3 \;=\; \frac{\bar{\xi}}{2}\,(\eta + 1)\,, \quad d\bar{x}_3 \;=\; \frac{\bar{\xi}}{2}\, d\eta \quad (5.52)$$

Now the function takes the following form

$$\dot{\bar{G}}_i^{cr^b} \;=\; \int_0^{\bar{\xi}} \dot{\bar{G}}_i^{cr^b}(\dot{\bar{w}}_{cr}, \dot{\bar{w}}_{cl}, \bar{x}_3) d\bar{x}_3 = M \int_{-1}^{1} \dot{\bar{G}}_i^{cr^b}(\dot{\bar{w}}_{cr}, \dot{\bar{w}}_{cl}, \eta)\, d\eta \quad (5.53)$$

The degree of the resulting polynomial function of η is 3 and therefore a two point (η_i with weights C_i) Gauss-Legendre formula will be good enough to exactly integrate it.

$$\dot{\bar{G}}_i^{cr^b} \;=\; M \int_{-1}^{1} \dot{\bar{G}}_i^{cr^b}(\dot{\bar{w}}_{cr}, \dot{\bar{w}}_{cl}, \eta)\, d\eta \;=\; M \sum_{i=1}^{2} C_i \dot{\bar{G}}_i^{cr^b}(\dot{\bar{w}}_{cr}, \dot{\bar{w}}_{cl}, \eta_i)\, d\eta \quad (5.54)$$

Similarly, the second term of eqn.5.51 needs to be numerically evaluated at each time step. This can be numerically integrated as given below

$$\bar{\psi}_{cr}^{b} \;=\; M \int_{-1}^{1} \bar{\psi}_{cr}^{b}(\dot{\bar{w}}_{cr}, \dot{\bar{w}}_{cl}, \eta)\, d\eta \;=\; M \sum_{i=1}^{2} C_i \bar{\psi}_{cr}^{b}(\dot{\bar{w}}_{cr}, \dot{\bar{w}}_{cl}, \eta_i)\, d\eta \quad (5.55)$$

The resulting non-linear ODEs are numerically solved prescribing initial conditions $(\bar{w}_1^{cr}(\bar{b}_1^{cr}), \bar{w}_1^{cl}(\bar{b}_1^{cl}))$ at $\bar{t} = 0$. We prescribe initial contact conditions in terms of $(\bar{b}_1^{cr}, \bar{b}_1^{cl})$. We can solve a similar problem when $\xi \geq H$ using appropriate expressions for ψ and $\dot{G}$. We take $\bar{d} = 40$, $\bar{D}_g = 1$, $\bar{\gamma}_g = 0.68$, $\varepsilon^T = 0$, $\bar{s} = 5$, ρ=15/16 and $\bar{H} = 400$ for the simulations described below.

5.4.8 Predictions of 2DOF system

Capped hemi-sphere asperity contact model: The system of nonlinear ODEs are solved with contact conditions $\bar{b}_1^{cr} = \frac{b_1^{cr}}{R_o} = 1.1$ and $\bar{b}_1^{cl} = \frac{b_1^{cl}}{R_o} = 1.2$. Note that the contact radii of the asperities at the primary imperfections are intentionally chosen different from the radii of asperities within the cluster to simulate initial primary defects in the coating. Three different types of behaviour are observed depending upon the value of modulus $\bar{E}$ and the size of the cluster $\bar{R}$ as shown in Fig. 5.11. For small values of $\bar{E}$, full sintering occurs both at the primary imperfections and within the cluster irrespective of the cluster size $\bar{R}$. This region is marked by A in Fig. 5.11. The sintering response in region A is the same as that of a perfect coating. For values of $\bar{E} > 100$, desintering occurs at the primary imperfections leading to the formation of cracks. Desintering at the imperfections relaxes the constraints on the material within the cluster allowing it to sinter faster. For values of $\bar{E}$ between 100-600, full sintering is achieved within the cluster if the size of the cluster $\bar{R}$ is relatively small. This region is marked by B in Fig. 5.11. However, for $\bar{E} > 600$, sintering gets arrested within the cluster and this is shown by the region marked by C. Note that in region C, the extent of densification within the cluster after the formation of cracks decreases with increase in cluster size $\bar{R}$ for a given $\bar{E}$. It has been observed through a number of simulations using this model that the sintering response of the TBC is sensitive to initial contact radii and also the difference in initial contact radii to some extent and therefore the boundaries of different regions in Fig. 5.11 slightly shift.

We employed the same capped hemi-sphere contact model for the computational studies presented in the previous chapter and demonstrated that this model accurately

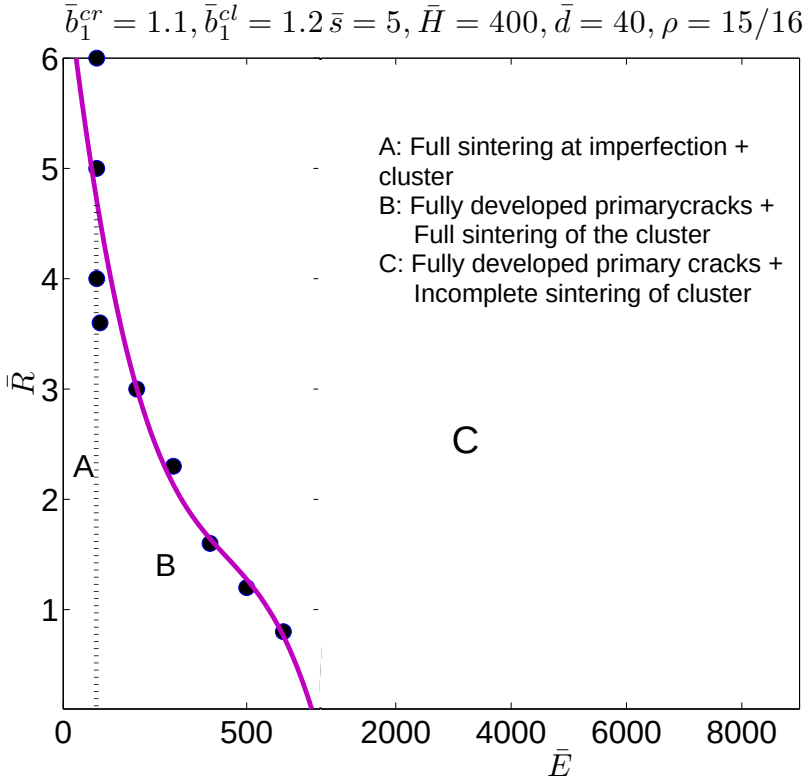

Figure 5.11: 2DOF Capped hemi-sphere contact model: Map showing different types of sintering behaviour of TBC

captures the physics of mud-cracking in the practical ranges of modulus of the coating. The sintering potential of the TBC depends upon the choice of the contact model. It means that the shape and distribution of asperities dictate the sintering potential of the TBC. The sintering potential plays key role in exploring the sintering response of the coating. The sintering potential for this capped hemi-spehere contact model is shown in Fig. 5.4 as a function of the contact radius $\bar{b}$ of the cylindrical cap of the asperity. Note from Fig. 5.4 that the sintering potential monotonically increases with $\bar{b}$ for $1 \leq \bar{b} \geq \bar{s}/2$. However, for $0 \leq \bar{b} \geq 1$, the sintering potential slightly decreases with increase in contact size $\bar{b}$. We observed through a number of computational simulations in chapter 4 that the sintering response of the coating is insensitive to the presence of imperfections if we choose an initial conditions in the range $0 \leq \bar{b} \geq 0.8$ for relatively larger values of $\bar{E}$. The analytical predictions of this model also

substantiates this observation. Therefore, we assumed purely cylindrical asperities instead of capped hemi-spheres between columns and analysed the 2DOF problem. In the capped hemi-sphere model, a fully developed crack occurs when the contact radius of the cylindrical cap at the imperfection diminishes to zero. On the other hand, in the cylindrical contact model, the radius of the asperity at the primary imperfections b_{cr} is allowed to shrink to a value less than R_o and a fully developed crack forms when $\bar{b}_{cr} \rightarrow 0$ and this happens when the height of the asperity at the primary imperfections $\bar{w}_{cr} \rightarrow \propto$.

Cylindrical asperity contact model: This is a subset of the capped hemi-sphere model. We solved the resulting system of nonlinear ODEs using the same initial contact conditions used in the capped hemi-sphere model, ie, $\bar{b}_1^{cr} = \frac{b_1^{cr}}{R_o} = 1.1$ and $\bar{b}_1^{cl} = \frac{b_1^{cl}}{R_o} = 1.2$. We observed the same three types of behaviour as in the capped hemi-sphere model but the boundaries of regions A, B and C have moved slightly as shown in Fig. 5.12. It has been observed that the initial conditions and also the difference in initial conditions influence the sintering response slightly.

Now let us explore sintering response of the TBC for various combinations of $\bar{E}$ and $\bar{R}$ using both models discussed above and compare them with the computational model presented in chapter 4. Full sintering occurs both at the primary imperfections and within the cluster irrespective of cluster size $\bar{R}$ for small values of $\bar{E}$ (region A in Figs. 5.11 and 5.12). An example of this situation is shown in Fig. 5.13 for $\bar{E} = 90$ and $\bar{R} = 1$. The contact radius at the imperfection $\bar{b}_{cr}$ and that within the cluster $\bar{b}_{cl}$ sinter to the maximum possible value of $\bar{s}/2$ (2.5). Analytical predictions of both contact models are exactly the same and they agree very well with computational results. Note that the material within the cluster goes to fully density before the imperfections since we assume a large difference in initial conditions. The TBC with primary imperfections fully densifies in about 30% of the time required for full densification in a perfect coating for the same modulus $\bar{E} = 90$. The displacement field that we assume for the primary imperfection varies linearly up to a height ξ, and then is constant with increasing height. This results in a variation of the contact radius of the asperities

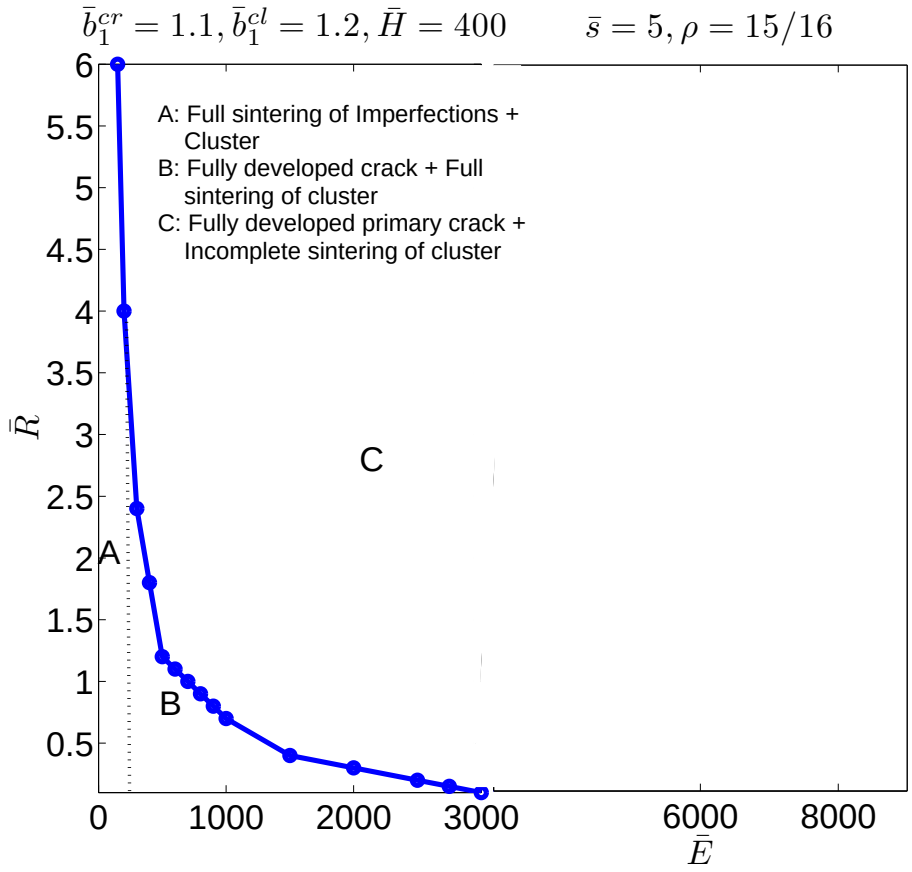

Figure 5.12: 2DOF Cylindrical contact model: Map showing different types of sintering behaviour of TBC

along the height of the imperfection. In subsequent figures the value of contact radius $\bar{b}$ in the uniform top section of the imperfection is plotted. Now let us examine the response of the TBC in the moderate range of $\bar{E}$ (region B), where the material within the cluster reaches full density after the formation of primary cracks for relatively small values of $\bar{R}$. The evolution of contact radius $\bar{b}$ for the cluster and imperfection for capped hemi-sphere and cylindrical contact models are shown in Fig.5.14 for $\bar{E} = 500$ and $\bar{R} = 1$ compared with FE results. In this case, significant in-plane tensile stress builds up in the coating initially which almost arrests sintering, the constraint is then relieved by desintering at the imperfections and by the development of cracks along the lines of the imperfections at about $\bar{t} = 0.023$. Developments of cracks at the imperfections promotes faster sintering within the cluster as shown in Fig.5.14.

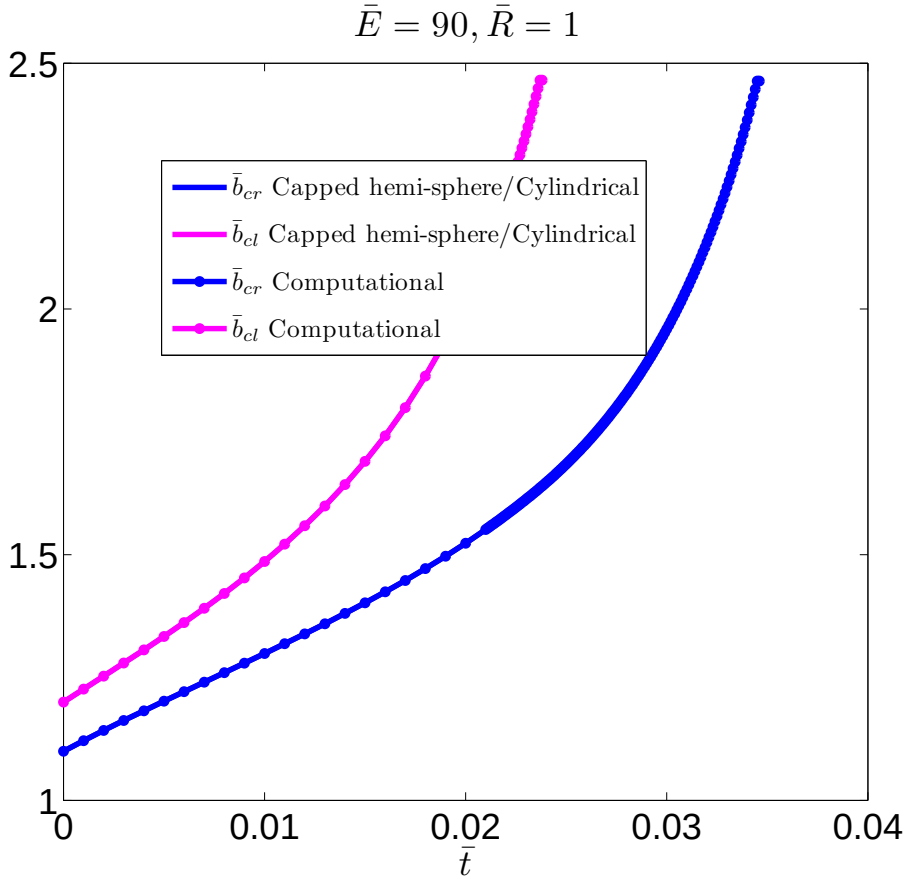

Figure 5.13: Full sintering both at the primary imperfections and within the cluster for $\bar{E} = 90$ and $\bar{R} = 1$.

Sintering is non-uniform in the cluster in the computational model and in this figure the average value within the cluster is plotted. In the computational model a fully developed crack is assumed to occur when $\bar{b}_{cr} \leq 0.09$ as we do not allow $\bar{b}_{cr}$ to decrease below this value for mathematical convenience. It can be seen from Fig.5.14 that the analytical models capture the desintering at the imperfections and the densification within the clusters reasonably well and are comparable to the computational results. It should be noted that the results of the capped hemi-sphere contact model matches more closely with the computational results than those of cylindrical contact model. For large values of $\bar{E}$ desintering occurs at the imperfections leading to the formation of cracks but the in-plane tensile stress generated in the TBC is sufficient to prevent

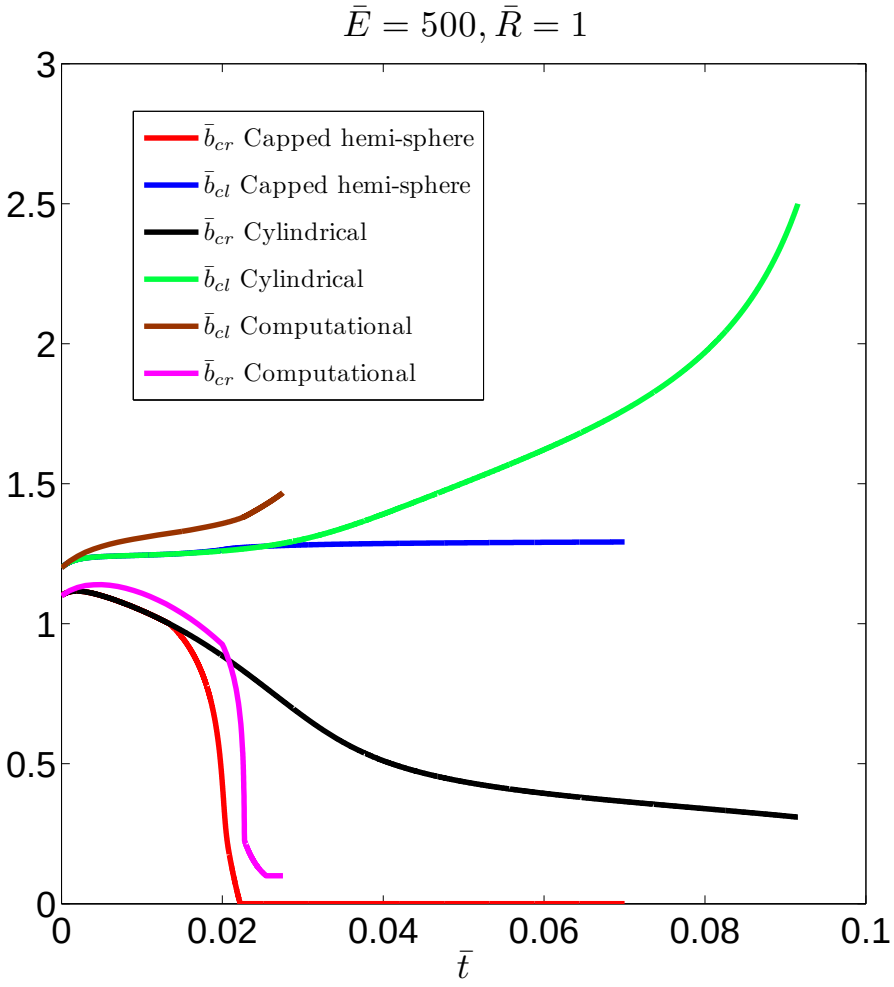

Figure 5.14: Fully developed primary crack at the imperfections and complete sintering within the cluster for $\bar{E} = 500$ and $\bar{R} = 1$.

full sintering being achieved within the cluster (region C). An example of this situation is shown Fig. 5.15. This figure shows the evolution of contact radius both at the imperfection and within the cluster compared with the computational results for $\bar{E} = 5000$ and $\bar{R} = 2$. Note that the fully developed crack forms ($\bar{b}_{cr} \leq 0.09$) at about $\bar{t} = 0.025$. It should be noted from Fig. 5.15 that the sintering response predicted by the cylindrical asperity contact model is much stiffer than that of the capped hemi-sphere contact model. On the other hand, if we choose $\bar{R} = 4$ for the same $\bar{E}$ (5000), a primary crack forms at about $\bar{t} = 0.04$ as shown in Fig. 5.16. For

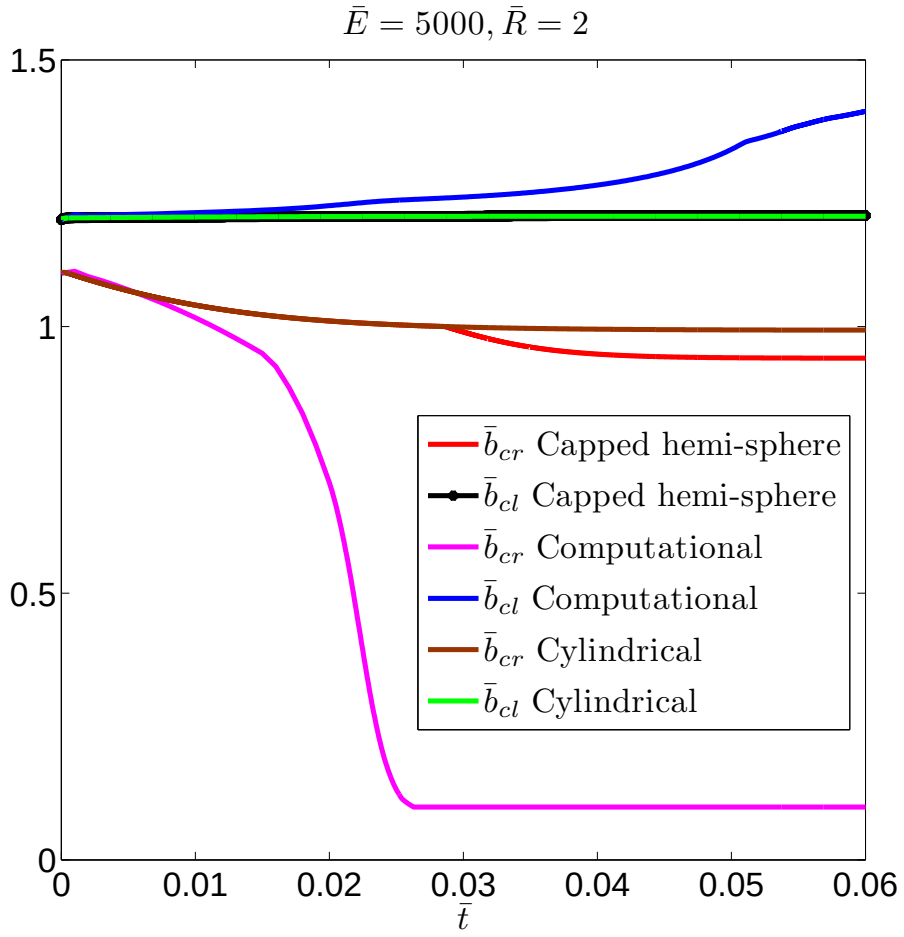

Figure 5.15: Fully developed primary crack at the imperfections and incomplete sintering within the cluster for $\bar{E} = 5000$ and $\bar{R} = 2$.

a combination of large $\bar{E}$ and $\bar{R}$, the sintering response of both analytical models are the same indicating that they behave equally stiff. In all the cases, the rate of densification within the cluster predicted by the computational model is much higher than that of analytical models. In the higher range of $\bar{E}$, (see Figs. 5.15 and 5.16), we can see fully developed primary cracks predicted by computational model. Though the analytical models can not predict the later stages of desintering at the imperfections, they capture accurately the early stages of desintering which is crucial in the formation of mud-cracks. The differences between computational and analytical models arise mainly because of the approximations employed in the analytical models,

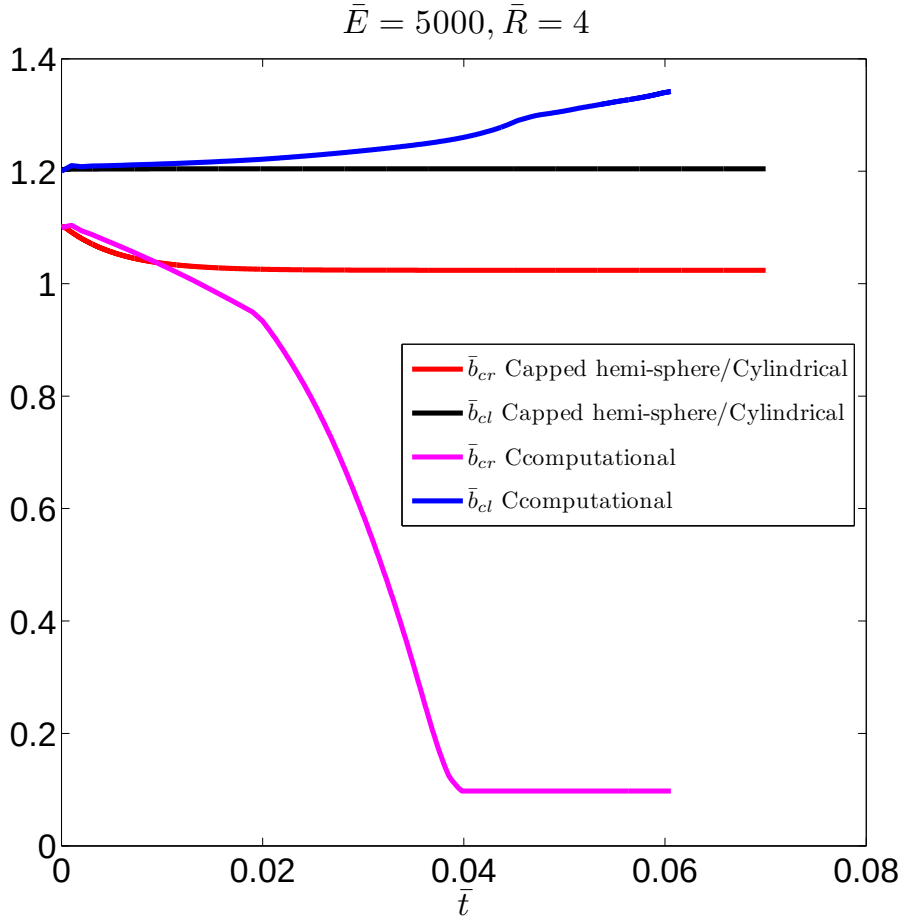

Figure 5.16: Fully developed primary crack at the imperfections and incomplete sintering within the cluster for $\bar{E} = 5000$ and $\bar{R} = 4$.

but it should also be noted that the imperfections are incorporated in different ways in these cases. In the analytical models, the imperfection is a line defect, whereas, in the computational model, the imperfection has a width equal to an element size. Also the response of the analytical models in the higher ranges of $\bar{E}$ is quite stiff as they have a small number of degrees of freedom (two here). Comparing Figs. 5.15 and 5.16, it can be seen that the extent of densification within the cluster reduces with increase in cluster size $\bar{R}$, ie the constraint on the sintering process increases with increase in $\bar{R}$ for a given $\bar{E}$. By carrying out a series of analytical simulations, we can determine the sintering response in terms of material and geometric parameters. Fig. 5.17 shows

the time for the initiation of desintering at the imperfections as a function of cluster size for $\bar{E} = 2000$ and $\bar{H} = 400$. This indicates that up to $\bar{R} = 4$, the wider the

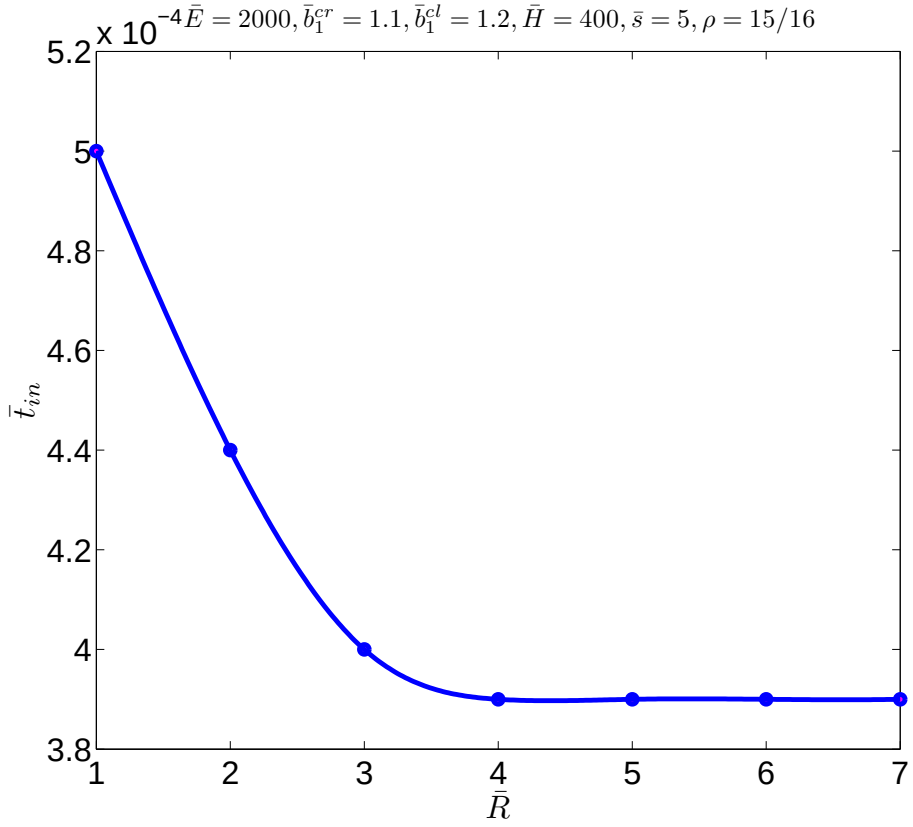

Figure 5.17: Time at crack initiation as a function of cluster size $\bar{R}$ for $\bar{E} = 2000$

spacing of the imperfections the earlier the instability occurs. Beyond this value of $\bar{R}$ the time to initiate the cracks is insensitive to the spacing of the imperfections. Although the time taken for the formation of cracks from imperfections increases with increase in $\bar{E}$ for a fixed cluster size $\bar{R}$, it also changes with change in $\bar{R}$ for a given $\bar{E}$. Fig. 5.18 shows the time at which primary cracks fully develop (i.e the columns loose contact at the top of the imperfection) as a function of cluster size for $\bar{E} = 2000$ and $\bar{H} = 400$ based on the cylindrical contact analytical model. It is clear from this plot that the mud-cracking time is minimum for a particular cluster size ($\bar{R} \approx 4$) as shown in Fig. 5.18. Based on the simulations presented here, we can identify the conditions under which mud-cracks will form in the TBC, but these

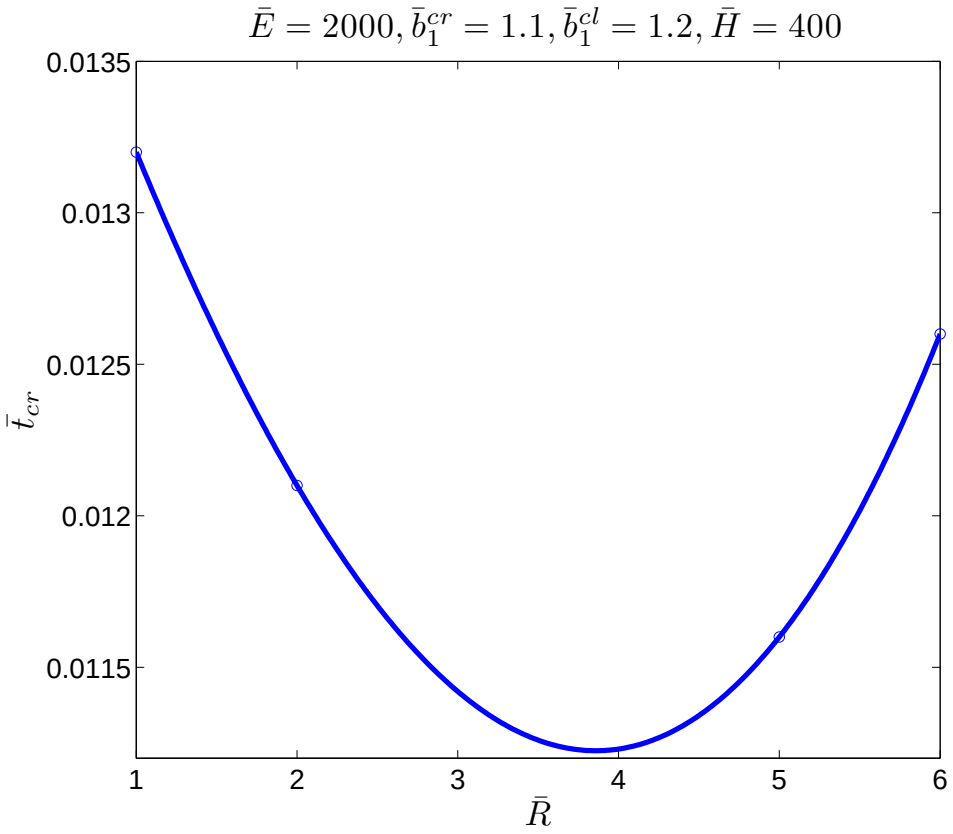

Figure 5.18: Time at which fully developed primary crack forms as a function of cluster size $\bar{R}$ for $\bar{E} = 2000$

models do not provide enough information about the saturated mud-crack spacing. In order to find the saturated crack density in the TBC, we consider another problem in the next section in which we seed the coating with a number of different families of imperfections and study the sintering response.

5.5 Problem C: Modelling of evolution of two families of imperfections

In the 2DOF problem, we have explored the sintering response in the practical ranges of modulus of the coating and generated failure maps which indicate the conditions under which a primary set of mud cracks can form during in-service sintering of the TBC. We now formulate a 3DOF problem considering two families of imperfections

(see Fig. 3.20) as we did in the chapter 3 in order to obtain information about the saturated mud crack spacing in the TBC. We choose a RVE as shown in Fig. 3.20 with primary and secondary imperfections and analyse the problem in a similar way to problem D of chapter 3. Macroscopic equi-biaxial sintering strain, ε^s is split into three fields (given by eqn. 3.78) as before and is shown in Fig. 3.21. Time evolution of ε_s^1, ε_s^2 and ε_s^3 is obtained assuming an axisymmetric contact geometry as shown in Figs. 5.8 and 5.19. The subscripts $'cr'$, $'cl'$ and $'cr_2'$ are used to characterize the geometric parameters at the primary imperfection, bulk contacts in the cluster and the secondary imperfection respectively. The compatibility conditions given by eqns. 3.29 and 5.17 are still valid for field 1 and field 2 respectively in this problem. The following compatibility condition needs to be satisfied in field 3 of each sub-cluster.

$$\left(\varepsilon_{ij}^{e_3}(x_3) + \varepsilon_{ij}^{s_3}\right) R - \Delta w_s^{cr_2}(x_3) = 0 \tag{5.56}$$

Here, $\Delta w_s^{cr_2}(x_3)$ is the net displacement across the secondary imperfection. This is due to elastic constraint of the substrate up to height ξ on each sub-cluster in the x_3 direction as shown in Fig. 5.20b as it alters the local contact condition at the secondary imperfection to vary linearly from the substrate up to ξ. The task now is to solve for the local evolution of surface profile within the RVE as characterized by $(w_{cr}, w_{cl}, w_{cr_2})$ (see Figs. 5.8 and Fig. 5.19).

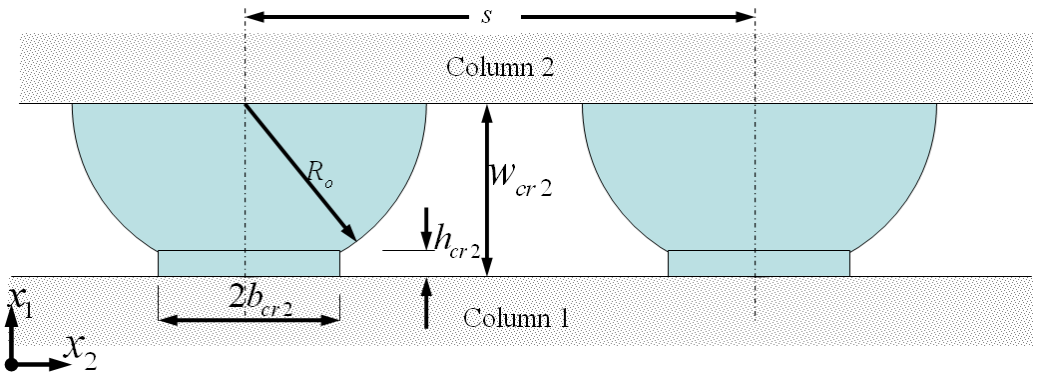

Figure 5.19: Contact geometry at secondary imperfection characterized by w_{cr_2}

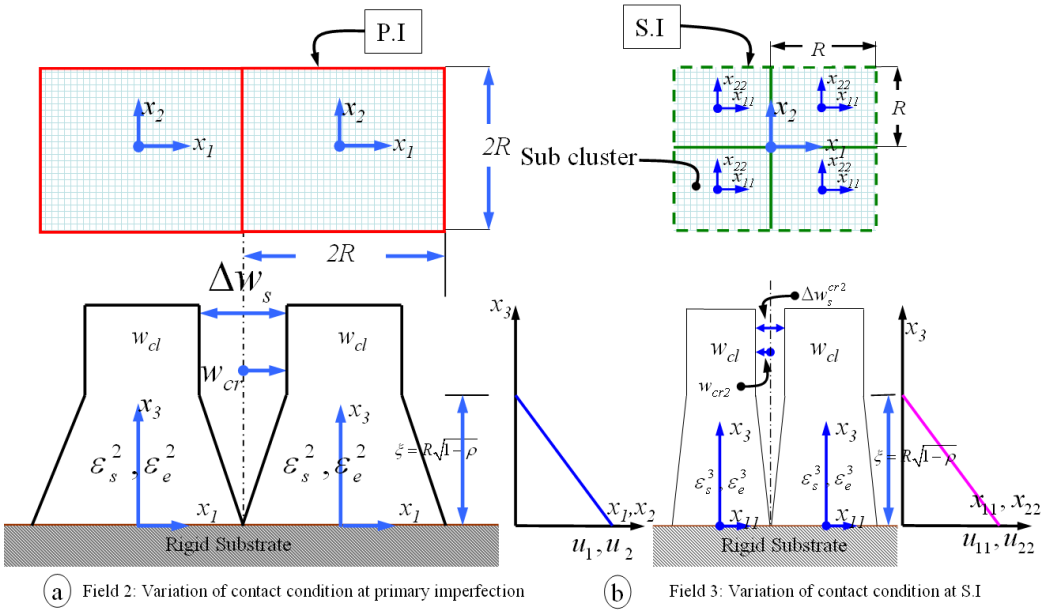

Figure 5.20: Variation of contact condition in the representative cluster. a. Field 2: Variation of contact condition at P.I; In-plane elastic deformation in the bottom portion of cluster up to a height ξ from the substrate. b. Field 3: Variation of contact condition at S.I; In-plane elastic deformation in the bottom portion of cluster up to a height ξ from the substrate.

5.5.1 Thermodynamic variational principle (TVP)

Again using the TVP, it is shown below that the rate of evolution of microstructure is given by the set of kinematic rates $(\dot{w}_{cr}, \dot{w}_{cl}, \dot{w}_{cr2})$ that minimise the following functional Φ.

$$\Phi(\dot{w}_{cr}, \dot{w}_{cl}, \dot{w}_{cr2}) \;=\; \dot{G}(\dot{w}_{cr}, \dot{w}_{cl}, \dot{w}_{cr2}) + \psi(\dot{w}_{cr}, \dot{w}_{cl}, \dot{w}_{cr2}) \tag{5.57}$$

The optimal choice for $(\dot{w}_{cr}, \dot{w}_{cl}, \dot{w}_{cr2})$ is obtained by minimising the functional Φ, ie

$$\delta\Phi(\dot{w}_{cr}, \dot{w}_{cl}, \dot{w}_{cr2}) \;= 0 \tag{5.58}$$

for arbitrary variations in $(\dot{w}_{cr}, \dot{w}_{cl}, \dot{w}_{cr2})$. This gives a set of simultaneous equations that can be cast in matrix

$$\begin{bmatrix} \frac{\partial^2\psi}{\partial\dot{w}_{cr}^2} & \frac{\partial^2\psi}{\partial\dot{w}_{cr}\partial\dot{w}_{cl}} & \frac{\partial^2\psi}{\partial\dot{w}_{cr}\partial\dot{w}_{cr2}} \\ \frac{\partial^2\psi}{\partial\dot{w}_{cr}\partial\dot{w}_{cl}} & \frac{\partial^2\psi}{\partial\dot{w}_{cl}^2} & \frac{\partial^2\psi}{\partial\dot{w}_{cl}\partial\dot{w}_{cr2}} \\ \frac{\partial^2\psi}{\partial\dot{w}_{cr}\partial\dot{w}_{cr2}} & \frac{\partial^2\psi}{\partial\dot{w}_{cl}\partial\dot{w}_{cr2}} & \frac{\partial^2\psi}{\partial\dot{w}_{cr2}^2} \end{bmatrix} \begin{bmatrix} \dot{w}_{cr} \\ \dot{w}_{cl} \\ \dot{w}_{cr2} \end{bmatrix} = - \begin{bmatrix} \frac{\partial\dot{G}}{\partial\dot{w}_{cr}} \\ \frac{\partial\dot{G}}{\partial\dot{w}_{cl}} \\ \frac{\partial\dot{G}}{\partial\dot{w}_{cr2}} \end{bmatrix}$$

This set of nonlinear ODEs are solved numerically to calculate the time evolution of $(w_{cr}, w_{cl}, w_{cr2})$ using a fourth order Runga-Kutta (R-K4) integration scheme.

5.5.2 Coupling between geometric scales

The macroscopic sintering strains, ε_s^1 in field 1, ε_s^2 in field 2 and ε_s^3 in field 3 of the repeating cluster are coupled to the microscopic state variables $(w_{cr}, w_{cl}, w_{cr2})$ and their appropriate initial choices $(w_1^{cr}, w_1^{cl}, w_2^{cr})$. Note that these sintering strains are uniform over the entire cluster. However, the elastic in-plane deformation field associated with field 2 and field 3 are non-uniform. Similar to field 2 in the cluster, we assume a kinematically admissible in-plane elastic deformation field that is compatible with ε_s^3 in the sub-clusters. This deformation field also varies linearly with height up to $x_3 = \xi$. This gives rise to a displacement across the secondary imperfection (see Fig. 5.20b).

$$\Delta w_s^{cr2}(x_3) = \begin{cases} -R\varepsilon_s^3 \, \frac{x_3}{\xi} & \text{if} \quad 0 \le x_3 \le \xi; \\ -R\varepsilon_s^3 & \text{if} \quad \xi \le x_3 \le H. \end{cases}$$

The state variable at bulk contacts within the cluster w_{cl} is given by

$$w_{cl} \;=\; w_1^{cl} + \left(\varepsilon_s^1 + \varepsilon_s^2 + \varepsilon_s^3\right) d; \qquad 0 \le x_3 \le H \tag{5.59}$$

The asperity height $w_{cr}(x_3)$ at the primary imperfection is given by

$$w_{cr}(x_3) \;=\; w_1^{cr} + \left(\varepsilon_s^1 + \varepsilon_s^2 + \varepsilon_s^3\right) d + \Delta w_s^{cr}(x_3) + \Delta w_s^{cr2}(x_3); \qquad \xi \le x_3 \le H \tag{5.60}$$

The asperity height at the secondary imperfection $w_{cr2}(x_3)$ is given by

$$w_{cr2}(x_3) \;=\; w_2^{cr} + \left(\varepsilon_s^1 + \varepsilon_s^2 + \varepsilon_s^3\right) d + \Delta w_s^{cr2}(x_3); \qquad \xi \le x_3 \le H \tag{5.61}$$

Now using $\Delta w_s^{cr}(x_3)$ and $\Delta w_s^{cr2}(x_3)$ in eqns. 5.60 and 5.61 and and noting that $w_{cr}(x_3) = w_{cr}$ and $w_{cr2}(x_3) = w_{cr2}$ at $x_3 = \xi$, we manipulate the resulting expressions for w_{cr} and w_{cr2} with w_{cl} given by eqn. 5.59 to express the sintering strains as functions of the state variables

$$\varepsilon_s^1 \;=\; \frac{w_1^{cl} - w_{cl}}{d} - \left[\frac{(w_1^{cr} - w_2^{cr}) - (w_{cr} - w_{cr})}{2R} + \frac{(w_{cl} - w_{cr2}) - (w_1^{cl} - w_2^{cr})}{R}\right] \tag{5.62}$$

$$\varepsilon_s^2 = \left[\frac{(w_1^{cr} - w_2^{cr}) - (w_{cr} - w_{cr})}{2R}\right] \tag{5.63}$$

and

$$\varepsilon_s^3 = \left[\frac{(w_{cl} - w_{cr2}) - (w_1^{cl} - w_2^{cr})}{R}\right] \tag{5.64}$$

5.5.3 Determination of Gibbs free energy

The Gibbs free energy density of the TBC is given by

$$G = G_i + U \tag{5.65}$$

where, G_i is the interface energy density of the the TBC. The interfacial energy of the TBC has contributions from bulk contacts associated with w_{cl} within the cluster and contacts associated with $w_{cr}(x_3)$ at the primary imperfection and contacts associated with $w_{cr2}(x_3)$ at the secondary imperfection. U is the strain energy density of the TBC.

Determination of interface free energy

In this section, we estimate G_i. The interfacial energy density of the TBC is given by

$$G_i = G_i^{cl} + G_i^{cr} + G_i^{cr2} \tag{5.66}$$

G_i^{cl} and G_i^{cr} are the energy density associated with bulk contacts within the cluster and the primary imperfections respectively and are the same as in 2DOF problem discussed in this chapter. We now derive the energy contribution from the secondary imperfections, G_i^{cr2}, considering an asperity contact geometry during early the stages of sintering (when $b_{cr2} < R_o$) as shown in Fig. 5.21a with the appropriate definition of fluxes, surface energies and diffusivities. We now derive an expression for G_i^{cr2} when $\xi \leq H$. It can be seen from Fig. 5.20b that the local contact at the secondary imperfection characterized by $w_{cr2}(x_3)$ is not uniform over the entire height of the cluster.

$$w_{cr2}(x_3) = \begin{cases} w_{cr2}^b = (w_2^{cr2} - w_1^{cl} + w_{cl})\left(1 - \frac{x_3}{\xi}\right) + w_{cr2}\,\frac{x_3}{\xi} & \text{if} \quad 0 \leq x_3 \leq \xi; \\ w_{cr}^t = w_{cr2} & \text{if} \quad \xi \leq x_3 \leq H. \end{cases}$$

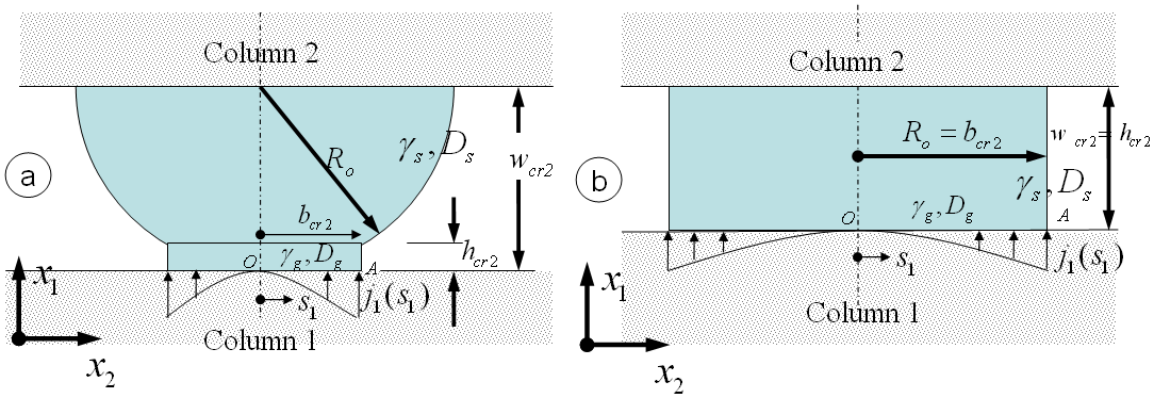

Figure 5.21: Contact geometry at the secondary imperfection a. Deformed asperity during early stages of sintering (when $b_{cr2} < R_o$) b. Deformed asperity during later stages of sintering (when $b_{cr2} \geq R_o$).

Therefore, in this case, G_i^{cr2} is the sum of the interface energy densities associated with linearly varying contact $w_{cr2}(x_3)$ in the bottom portion of the imperfection and that associated with uniform contact w_{cr2} in the top portion of the imperfection. The quantity G_i^{cr2} is given by

$$G_i^{cr2} = \int_0^{\xi} G_i^{cr2^b}\, dx_3 + G_i^{cr2^t} \tag{5.67}$$

When $b_{cr} < R_o$, the interfacial energy density in the bottom portion of the secondary imperfection where the contact radius varies is given by

$$G_i^{cr2^b} = \frac{4}{\bar{s}^2\bar{R}\bar{H}^2}\left(\frac{\gamma_s}{R_o}\right)\int_0^{\bar{\xi}} \left[2(\bar{w}_{cr2}^b - \bar{h}_{cr2}^b) + 2\bar{b}_{cr2}^b\bar{h}_{cr2}^b - 1 - (\bar{b}_{cr2}^b)^2 + (\bar{b}_{cr2}^b)^2\bar{\gamma}_g\right] d\bar{x}_3 \tag{5.68}$$

In the above expression for $G_i^{cr2^b}$, $\bar{h}_{cr2}^b$ can be expressed in terms of $\bar{b}_{cr2}^b$, which is of the same form as eqn. B.8 but a function of $\bar{w}_{cr2}^b$. Substituting $\bar{b}_{cr2}^b$ in $G_i^{cr2^b}$, we get the interfacial energy density in the bottom portion of the secondary imperfection in terms of $\bar{w}_{cr2}^b$. Note that $\bar{w}_{cr2}^b$ is a function of $\bar{w}_{cr2}$ and $\bar{w}_{cl}$ as discussed earlier. So, we now have, $G_i^{cr2^b}$ in terms of the state variables $(\bar{w}_{cr2}, \bar{w}_{cl})$ and the co-ordinate $\bar{x}_3$. The resulting expression needs to be integrated numerically. The interfacial energy density in the top portion of the imperfection is given by

$$G_i^{cr2^t} = \frac{4(\bar{H} - \bar{\xi})}{\bar{s}^2\bar{R}\bar{H}^2}\left(\frac{\gamma_s}{R_o}\right)\left[2(\bar{w}_{cr2} - \bar{h}_{cr2}) + 2\bar{b}_{cr2}\bar{h}_{cr2} - 1 - (\bar{b}_{cr2})^2 + (\bar{b}_{cr2})^2\bar{\gamma}_g\right] \tag{5.69}$$

In the above equation, $\bar{h}_{cr2}$ can be expressed in terms of $\bar{b}_{cr2}$, which in turn can be expressed in terms of the primary unknown $\bar{w}_{cr2}$. Now, $G_i^{cr2^t}$ is expressed only in terms of the primary unknown $\bar{w}_{cr2}$. Now considering the later stages of sintering at the secondary imperfection, ie, when $b_{cr2} \geq R_o$ as shown in Fig. 5.21b, we can derive expressions for $G_i^{cr2^b}$ and $G_i^{cr2^t}$ as detailed below.

$$G_i^{cr2^b} = \frac{4}{\bar{s}^2\bar{R}\bar{H}^2}\left(\frac{\gamma_s}{R_o}\right)\int_0^{\bar{\xi}}\left[2\bar{b}_{cr2}^b\bar{w}_{cr2}^b) - 2(\bar{b}_{cr2}^b)^2 + (\bar{b}_{cr2}^b)^2\bar{\gamma}_g\right]d\bar{x}_3 \tag{5.70}$$

where,

$$\bar{b}_{cr2}^b = \sqrt{\frac{\bar{V}}{\pi\bar{w}_{cr2}^b}} \tag{5.71}$$

$\bar{w}_{cr2}^b$ is a function of state variables $(\bar{w}_{cr2}, \bar{w}_{cl})$ and the co-ordinate $\bar{x}_3$ as discussed earlier which needs to be numerically integrated. Similarly, we can derive $G_i^{cr2^t}$:

$$G_i^{cr2^t} = \frac{4(\bar{H}-\bar{\xi})}{\bar{s}^2\bar{R}\bar{H}^2}\left(\frac{\gamma_s}{R_o}\right)\left[2\bar{b}_{cr2}\bar{w}_{cr2} - 2\bar{b}_{cr2}^2 + \bar{b}_{cr2}^2\bar{\gamma}_g\right] \tag{5.72}$$

where,

$$\bar{b}_{cr2} = \sqrt{\frac{\bar{V}}{\pi\bar{w}_{cr2}}} \tag{5.73}$$

Now we have the interfacial energy density in the top portion of the imperfection as a function of $\bar{w}_{cr2}$. Now the total interface energy density of the TBC, G_i is obtained by adding appropriate expressions for G_i^{cl}, $G_i^{cr^b}$, $G_i^{cr^t}$, $G_i^{cr2^b}$ and $G_i^{cr2^t}$ depending upon the current shape of the asperity.

$$\begin{aligned} G_i =& G_i^{cl}(\bar{w}_{cl}) + \int_0^{\bar{\xi}} G_i^{cr^b}(\bar{w}_{cr}, \bar{w}_{cl}, \bar{x}_3)d\bar{x}_3 + G_i^{cr^t}(\bar{w}_{cr}) \\ &+ \int_0^{\bar{\xi}} G_i^{cr2^b}(\bar{w}_{cr2}, \bar{w}_{cl}, \bar{x}_3)d\bar{x}_3 + G_i^{cr2^t}(\bar{w}_{cr}) \end{aligned} \tag{5.74}$$

Estimation of elastic stored energy

The elastic strain energy in the potential cluster has contributions from field 1, field 2 and field 3 and the interaction between them. The total elastic strain energy U_C in the cluster is given by

$$U_C = \frac{1}{2}\int_V \left[\sigma_{ij}^1\varepsilon_{ij}^{e_1} + \sigma_{ij}^2\varepsilon_{ij}^{e_2} + \sigma_{ij}^3\varepsilon_{ij}^{e_3} + 2\sigma_{ij}^1\varepsilon_{ij}^{e_2} + 2\sigma_{ij}^1\varepsilon_{ij}^{e_3} + 2\sigma_{ij}^2\varepsilon_{ij}^{e_3}\right]dV \tag{5.75}$$

Here, i and j independently range over 1-3. σ_{ij}^3 and $\varepsilon_{ij}^{e_3}$ are the stress and elastic strain tensor in field 3 respectively. The first three terms are the strain energies associated with field 1, field 2 and field 3 respectively. The fourth term is the energy due to interaction between fields 1 and 2. The fifth terms is the energy due to interaction between fields 1 and 3 and last term is the energy due to interaction between fields 2 and 3. The elastic strain energy in field 3 of the square sub-cluster U^{e_3} (third term in eqn. 5.75) is estimated by assuming a kinematically admissible displacement field within the sub-cluster. As in the 2DOF problem, we only consider asperity deformation which is dominant during the early stages of sintering and also use the inextensibility condition to determine the elastic strain tensor in the sub-cluster (field 3)

$$\varepsilon_{ij}^{e_3} = \begin{bmatrix} -\varepsilon_s^3(1-\frac{x_3}{\xi}) & 0 & \varepsilon_s^3\frac{(x_1-\frac{R}{2})}{2\xi} \\ 0 & -\varepsilon_s^3(1-\frac{x_3}{\xi}) & \varepsilon_s^3\frac{(x_2-\frac{R}{2})}{2\xi} \\ \varepsilon_s^3\frac{(x_1-\frac{R}{2})}{2\xi} & \varepsilon_s^3\frac{(x_2-\frac{R}{2})}{2\xi} & 0 \end{bmatrix}$$

The strain energy in field 3 is

$$U^{e_3} = \frac{1}{3}\frac{E\tilde{q}d}{(1-\nu^2)}(\varepsilon_s^3)^2R^2\left[4\xi + (1-\rho)\frac{R^2}{\xi}\right] \tag{5.76}$$

Similarly, we can determine the strain energy due to interaction between fields and 1 and 3

$$U^{e_1e_3} = \frac{4E\tilde{q}d}{(1-\nu^2)}(\varepsilon_s^1+\varepsilon^T)\varepsilon_s^3R^2\xi \tag{5.77}$$

and the strain energy due to interaction between fields 2 and 3 is given by

$$U^{e_2e_3} = \frac{2}{3}\frac{E\tilde{q}d}{(1-\nu^2)}\varepsilon_s^2\varepsilon_s^3R^2\left[4\xi + (1-\rho)\frac{R^2}{\xi}\right] \tag{5.78}$$

The total elastic strain energy in the cluster is the sum of U^{e_1}, U^{e_2}, U^{e_3}, $U^{e_1e_2}$, $U^{e_1e_3}$ and $U^{e_2e_3}$ given by eqns. B.24, B.33, B.35, 5.76, 5.77 and 5.78 respectively.

$$\begin{aligned} U_C =& \frac{4ER^2H\tilde{q}d}{(1-\nu^2)}(\varepsilon_s^1+\varepsilon^T)^2 + \frac{4}{3}\frac{E\tilde{q}d}{(1-\nu^2)}(\varepsilon_s^2)^2R^2\xi + \frac{8}{3}G\tilde{q}d(\varepsilon_s^2)^2\frac{R^4}{\xi} \\ &+ \frac{4E\tilde{q}d}{(1-\nu^2)}(\varepsilon_s^1+\varepsilon^T)\varepsilon_s^2R^2\xi + \frac{1}{3}\frac{E\tilde{q}d}{(1-\nu^2)}(\varepsilon_s^3)^2R^2\left[4\xi + (1-\rho)\frac{R^2}{\xi}\right] \\ &+ \frac{4E\tilde{q}d}{(1-\nu^2)}(\varepsilon_s^1+\varepsilon^T)\varepsilon_s^3R^2\xi + \frac{2}{3}\frac{E\tilde{q}d}{(1-\nu^2)}\varepsilon_s^2\varepsilon_s^3R^2\left[4\xi + (1-\rho)\frac{R^2}{\xi}\right] \end{aligned} \tag{5.79}$$

The optimal height ξ that minimises the total strain energy U_C is function of ε_s^1, ε_s^2 and ε_s^3. However, we take $\xi = R\sqrt{1-\rho}$ which minimises the strain energy in field 2 as in the 2DOF problem, in order to keep the description of the evolving crack geometry simple. Noting the relationship between ρ and $\frac{G}{E}$ as given by eqn. 4.40, the strain energy density of the TBC is given by

$$\begin{aligned} U_T =& \frac{E\tilde{q}d}{(1-\nu^2)}\left[(\varepsilon_s^1+\varepsilon^T)^2 + \frac{R}{H}\sqrt{1-\rho}\left[\frac{2}{3}(\varepsilon_s^2)^2 + \frac{5}{12}(\varepsilon_s^3)^2 + (\varepsilon_s^1+\varepsilon^T)\varepsilon_s^2\right.\right. \\ & \left.\left. +(\varepsilon_s^1+\varepsilon^T)\varepsilon_s^3 + \frac{5}{6}\varepsilon_s^2\varepsilon_s^3\right]\right] \end{aligned} \tag{5.80}$$

Taking, $\tilde{q} = \frac{4b_{cl}}{\pi s^2}$ and non-dimensionalising the above equation, we can express the strain energy density in the form

$$\begin{aligned} U =& \frac{4\bar{E}\bar{b}_{cl}\bar{d}}{\pi\bar{s}^2}\left(\frac{\gamma_s}{R_o}\right)\left[(\varepsilon_s^1+\varepsilon^T)^2 + \bar{R}\sqrt{1-\rho}\left[\frac{2}{3}(\varepsilon_s^2)^2 + \frac{5}{12}(\varepsilon_s^3)^2 + (\varepsilon_s^1+\varepsilon^T)\varepsilon_s^2\right.\right. \\ & \left.\left. +(\varepsilon_s^1+\varepsilon^T)\varepsilon_s^3 + \frac{5}{6}\varepsilon_s^2\varepsilon_s^3\right]\right] \end{aligned} \tag{5.81}$$

In eqn. 5.81, $\bar{b}_{cl}$ is given either by eqn. B.8 or eqn. B.10 depending upon the current shape of the asperity within the cluster. Using the expressions for ε_s^1 given by eqn. 5.62, ε_s^2 given by eqn. 5.63 and ε_s^3 given by eqn. 5.64 in terms of normalised state variables $(\bar{w}_{cr}, \bar{w}_{cl}, \bar{w}_{cr2})$ in eqn. 5.81, we get $U(\bar{w}_{cr}, \bar{w}_{cl}, \bar{w}_{cr2})$. Note that in this case, $\xi \leq H$. Therefore,

$$\bar{R} \leq \frac{1}{\sqrt{1-\rho}} \tag{5.82}$$

When ρ is close to 1, say, 15/16, $\bar{R} \leq 4$. Now the Gibbs energy density of the TBC, G, given by eqn. 5.65 can be re-written as

$$\begin{aligned} G(\bar{w}_{cr}, \bar{w}_{cl}, \bar{w}_{c2}) =& G_i^{cl}(\bar{w}_{cl}) + \int_0^{\bar{\xi}} G_i^{cr^b}(\bar{w}_{cr}, \bar{w}_{cl}, \bar{x}_3)d\bar{x}_3 + G_i^{cr^t}(\bar{w}_{cr}) \\ & + \int_0^{\bar{\xi}} G_i^{cr2^b}(\bar{w}_{cr2}, \bar{w}_{cl}, \bar{x}_3)d\bar{x}_3 + G_i^{cr2^t}(\bar{w}_{cr}) + U(\bar{w}_{cr}, \bar{w}_{cl}, \bar{w}_{cr2}) \end{aligned} \tag{5.83}$$

5.5.4 Determination of dissipation potential ψ

We now determine the macroscopic rate potential ψ per unit volume of the TBC when the TBC contains both primary and secondary imperfections. ψ has contributions

from bulk contacts within the clusters ψ^{cl}, primary imperfections ψ^{cr} and secondary imperfections ψ^{cr2}. ψ^{cl} (eqn. 5.42) and ψ^{cr} (sum of eqns. 5.44 and 5.47) are the same as in the 2DOF problem. We now derive ψ^{cr2} assuming grain boundary diffusion is the dominant energy dissipation process at the contacts as before. Consider an asperity contact geometry at the secondary imperfection as shown in Fig. 5.21. ψ^{cr2} has contributions from the bottom portion of the secondary imperfection where there is linearly varying contact up to height ξ from the substrate (note $\xi \leq H$) and the top portion of the secondary imperfection where there is uniform contact, ie, $\psi^{cr2} = \psi^{b}_{cr2} + \psi^{t}_{cr2}$. We obtain

$$\psi^{b}_{cr2} = \frac{4}{\pi s^2 RH} \int_0^{\xi} \frac{\pi}{16 D_g} (\dot{w}^{b}_{cr2})^2 (b^{b}_{cr2})^4 dx_3 \tag{5.84}$$

Adopting normalisations discussed earlier we write ψ^{b}_{cr2} in non-dimensional form

$$\psi^{b}_{cr2} = \frac{1}{4\bar{s}^2 \bar{R} \bar{H}^2 \bar{D}_g} \left(\frac{R_o^3}{D_g}\right) \int_0^{\bar{\xi}} (\dot{\bar{w}}^{b}_{cr2})^2 (\bar{b}^{b}_{cr2})^4 d\bar{x}_3 \tag{5.85}$$

In the above equation,

$$\dot{\bar{w}}^{b}_{cr2} = \left(1 - \frac{\bar{x}_3}{\bar{\xi}}\right) \dot{\bar{w}}_{cl} + \frac{\bar{x}_3}{\bar{\xi}} \dot{\bar{w}}_{cr2} \tag{5.86}$$

Note that $\bar{b}^{b}_{cr2}$ in eqn. 5.85 is a function of $\bar{w}^{b}_{cr2}$ and depends upon the current shape of the asperity. Also $\bar{w}^{b}_{cr2}(\xi \leq H)$ is a function of $(\bar{w}_{cr2}, \bar{w}_{cl}, \bar{x}_3)$ and

$$\psi^{t}_{cr2} = \frac{4}{\pi s^2 RH} (H - \xi) \frac{\pi}{16 D_g} \dot{w}^2_{cr2} b^4_{cr2} dx_3 \tag{5.87}$$

Normalising the above equation, we obtain

$$\psi^{t}_{cr2} = \frac{(\bar{H} - \bar{\xi})}{4\bar{s}^2 \bar{R} \bar{H}^2 \bar{D}_g} \left(\frac{R_o^3}{D_g}\right) \dot{\bar{w}}^2_{cr2} \bar{b}^4_{cr2} d\bar{x}_3 \tag{5.88}$$

$\bar{b}_{cr2}$ in the above equation is a function of $\bar{w}_{cr2}$ and it depends on the current shape of the asperity at this location. Now the total macroscopic rate potential per unit volume of TBC is given by the sum of eqns. 5.42, 5.44, 5.47, 5.85 and 5.88, ie

$$\begin{aligned} \psi \; =& \psi^{cl}(\dot{\bar{w}}_{cl}) + \int_0^{\bar{\xi}} \psi^{b}_{cr}(\dot{\bar{w}}_{cr}, \dot{\bar{w}}_{cl}, \bar{x}_3) d\bar{x}_3 + \psi^{t}_{cr}(\dot{\bar{w}}_{cr}) \\ &+ \int_0^{\bar{\xi}} \psi^{b}_{cr2}(\dot{\bar{w}}_{cr2}, \dot{\bar{w}}_{cl}, \bar{x}_3) d\bar{x}_3 + \psi^{t}_{cr2}(\dot{\bar{w}}_{cr2}) \end{aligned} \tag{5.89}$$

5.5.5 Numerical solution of three kinematic variables system

Now differentiating G given by eqn. 5.83 with respect to time, we get $\dot{G}$ and combining this with ψ given by eqn. 5.89, we construct the functional. Rendering the functional stationary gives a set of non-linear ODEs. The non-dimensional form of $\dot{G}$ and ψ are

$$\begin{aligned}\dot{\bar{G}} \;=\; & \dot{\bar{G}}_i^{cl}(\dot{\bar{w}}_{cl}) + \int_0^{\bar{\xi}} \dot{\bar{G}}_i^{cr^b}(\dot{\bar{w}}_{cr}, \dot{\bar{w}}_{cl}, \bar{x}_3) d\bar{x}_3 + \dot{\bar{G}}_i^{cr^t}(\dot{\bar{w}}_{cr}) \\ & + \int_0^{\bar{\xi}} \dot{\bar{G}}_i^{cr2^b}(\dot{\bar{w}}_{cr2}, \dot{\bar{w}}_{cl}, \bar{x}_3) d\bar{x}_3 + \dot{\bar{G}}_i^{cr2^t}(\dot{\bar{w}}_{cr2}) + \dot{\bar{U}}(\dot{\bar{w}}_{cr}, \dot{\bar{w}}_{cl}, \dot{\bar{w}}_{cr2})\end{aligned} \tag{5.90}$$

$$\begin{aligned}\bar{\psi} \;=& \bar{\psi}^{cl}(\dot{\bar{w}}_{cl}) + \int_0^{\bar{\xi}} \bar{\psi}_{cr}^{b}(\dot{\bar{w}}_{cr}, \dot{\bar{w}}_{cl}, \bar{x}_3)\, d\bar{x}_3 + \bar{\psi}_{cr}^{t}(\dot{\bar{w}}_{cr}) \\ & + \int_0^{\bar{\xi}} \bar{\psi}_{cr2}^{b}(\dot{\bar{w}}_{cr2}, \dot{\bar{w}}_{cl}, \bar{x}_3)\, d\bar{x}_3 + \bar{\psi}_{cr2}^{t}(\dot{\bar{w}}_{cr2})\end{aligned} \tag{5.91}$$

The second and fourth terms of eqns. 5.90 and 5.91 need to be numerically evaluated at each time step. We use a Gaussian quadrature rule as before to obtain an approximation for the definite integral of these functions as discussed in the 2DOF problem. The resulting non-linear ODEs are numerically solved prescribing initial conditions $(\bar{w}_1^{cr}(\bar{b}_1^{cr}), \bar{w}_1^{cl}(\bar{b}_1^{cl}), \bar{w}_2^{cr2}(\bar{b}_1^{cr2}))$ at $\bar{t} = 0$. We take $\bar{d} = 40$, $\bar{D}_g = 1$, $\bar{\gamma}_g = 0.68$, $\varepsilon^T = 0$, $\bar{s} = 5$, ρ=15/16 and $\bar{H} = 400$ for the simulations presented here.

5.5.6 Results and discussion

Capped hemi-sphere model: The set of nonlinear ODEs are solved and time integrated by a fourth order Runge-Kutta(RK-4) scheme from an initial state of $\bar{b}_1^{cr} = 1.1$, $\bar{u}_1^{cl} = 1.2$ and $\bar{b}_1^{cr2} = 1.15$. If $\bar{E} < 90$ complete sintering of the cluster and imperfections occurs independent of the choice of geometric and other material parameters. In the practical range of of the TBC, we observe two major different types of mud cracking behaviour, depending on the magnitude of $\bar{E}$ and the size of the cluster $\bar{R}$. We carried out a number of simulations to construct a failure map which clearly shows the two regimes of mud-cracking of a TBC. The solid blue curve in Fig. 5.22 demarcates the two mud-cracking situations. The region within the blue curve marked by pentagrams (stars) is where we only observe primary cracks. However, we observe both primary

and secondary cracks in the region marked by hexagrams. In the practical range of $\bar{E}$, we do not always observe both cracks but only in certain situations as shown in Fig. 5.22. Since the analytical models capture only the early stages of desintering of imperfections in the higher ranges of $\bar{E}$, we assume that the secondary cracks form when the decrease of $\bar{b}_{cr2}$ from its initial value is greater than or equal to 10%. The initial contact sizes and also the difference between them influence the sintering response slightly and as a result the position of the blue solid curve in Fig. 5.22 is sensitive to the choice of initial conditions. Cylindrical asperity contact model: For

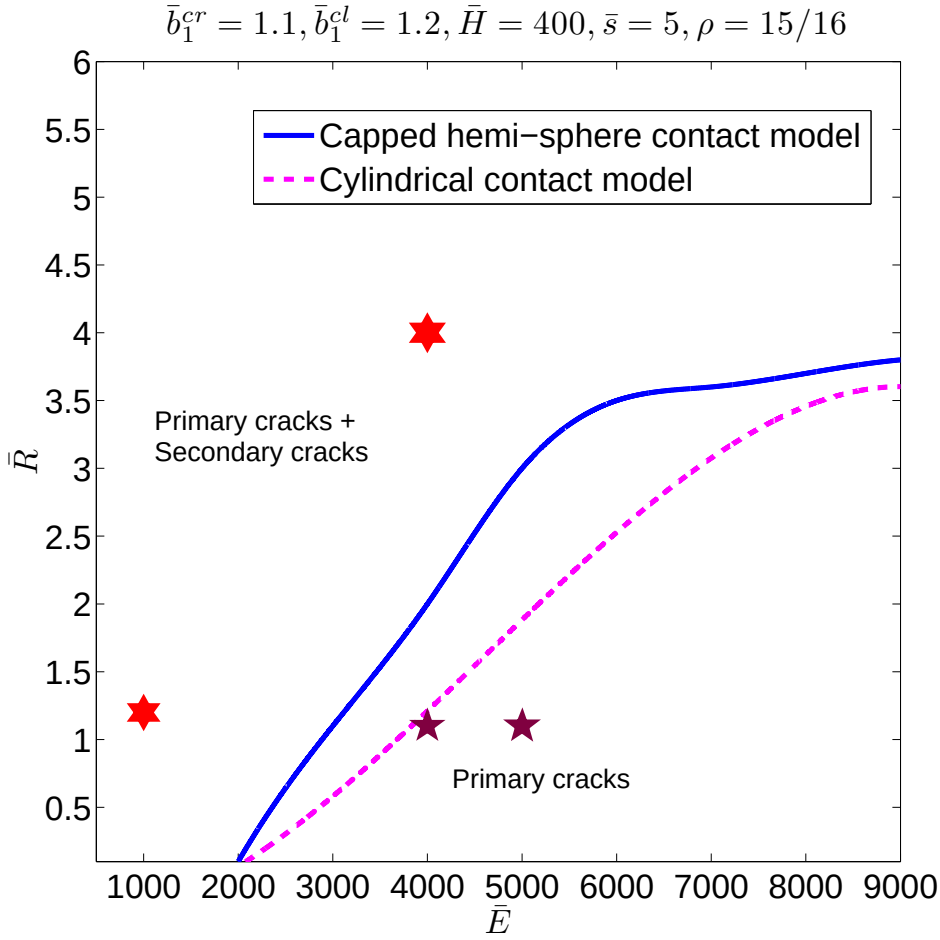

Figure 5.22: Failure map as a function of cluster size and modulus of coating

the reasons stated earlier in the 2DOF problem of this chapter, we have also solved another problem (which is a subset of the previous problem (capped hemi-sphere))

in which we assume purely cylindrical asperities between columns using the same set of initial conditions as in the capped hemi-sphere model. The sintering response of the TBC was observed over a wide range of $\bar{E}$ and $\bar{R}$ to construct a failure map as before. We invariably observed two different types of mud-cracking behaviour as before but now the dotted curve shown in Fig. 5.22 demarcates the two mud-cracking situations. It should be noted that in constructing this failure map, we assumed that the secondary cracks form when the decrease of $\bar{b}_{cr2}$ is greater than or equal to 5. This is justified by the fact that the average sintering response of this model is stiffer than the capped hemi-sphere model and therefore the early stages of desintering at imperfections predicted by this model is less than the capped hemi-sphere model. As in the previous model, the initial contact radii and the difference between them also influence the sintering response slightly.

Now let us explore the sintering response in these two regions for selected values of $\bar{E}$ and $\bar{R}$ marked on the Fig. 5.22 using both analytical models and compare them with computational results. For $\bar{E} = 1000$ and $\bar{R} = 1.2$, both primary and secondary imperfections develop into cracks and sintering is arrested in the cluster before full density is achieved as shown in Fig. 5.23. From Fig. 5.23, it can be seen that the predictions of computational model and the capped hemi-sphere model closely agree. The sintering in the cluster gets arrested before it reaches full density. However, if we choose a larger $\bar{E}$ for the same cluster size ($\bar{R} = 1.2$), we observe only fully developed primary cracks as shown in Figs. 5.24($\bar{E} = 4000$) and 5.25 ($\bar{E} = 5000$). Note from Fig. 5.24 that the secondary imperfection does not desinter enough to develop into a crack and sintering is completely prevented within the cluster ($\bar{b}_{cl} = 1.22$). It can also be seen from Fig. 5.24 that the sintering response of both analytical models are the same and this combination of large $\bar{E}$ and the large size of the cracked cluster ($2\bar{R} = 2.4$) make them behave too stiff. On the other hand, if we choose a large cluster size, say $\bar{R} = 4$ for the same $\bar{E} = 4000$, we observe fully developed primary and secondary cracks but the size of the cracked cluster ($\bar{R} = 2$) is smaller than in the previous case and therefore the extent of sintering is greater($\bar{b}_{cl} = 1.25$) as shown

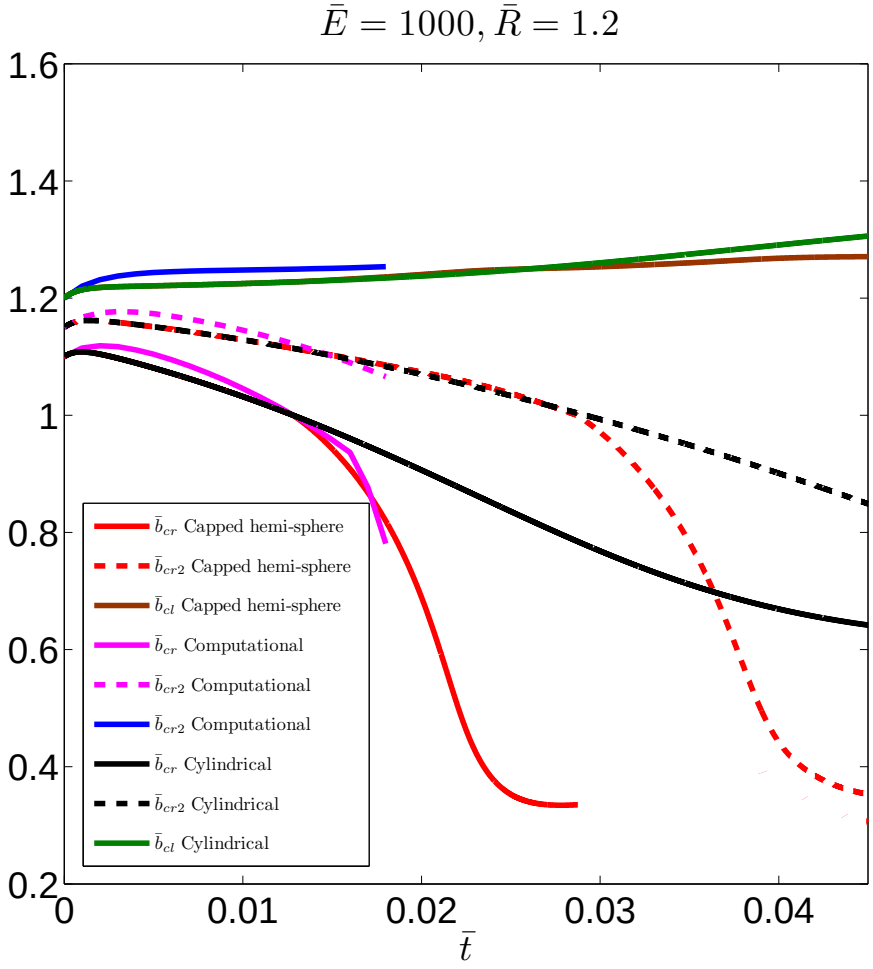

Figure 5.23: Fully developed primary and secondary cracks for $\bar{E} = 1000$ and $\bar{R} = 1.2$

in Fig. 5.26. In all these plots, we see that the analytical models capture the major features of desintering at the imperfections during the early stages of the sintering process.

From Fig. 5.22, we see that as $\bar{E}$ is increased the value of $\bar{R}$ at the transition between the two types of behaviour (ie the limiting crack spacing) increases (any model). This indicates that the higher the value of $\bar{E}$, the higher the constraint on sintering, which results in a smaller build up of elastic strain energy in the coating to drive the desintering and cracking process. Fig. 5.22 suggests that once the crack spacing has reduced to that represented by the solid or dotted line on the figure,

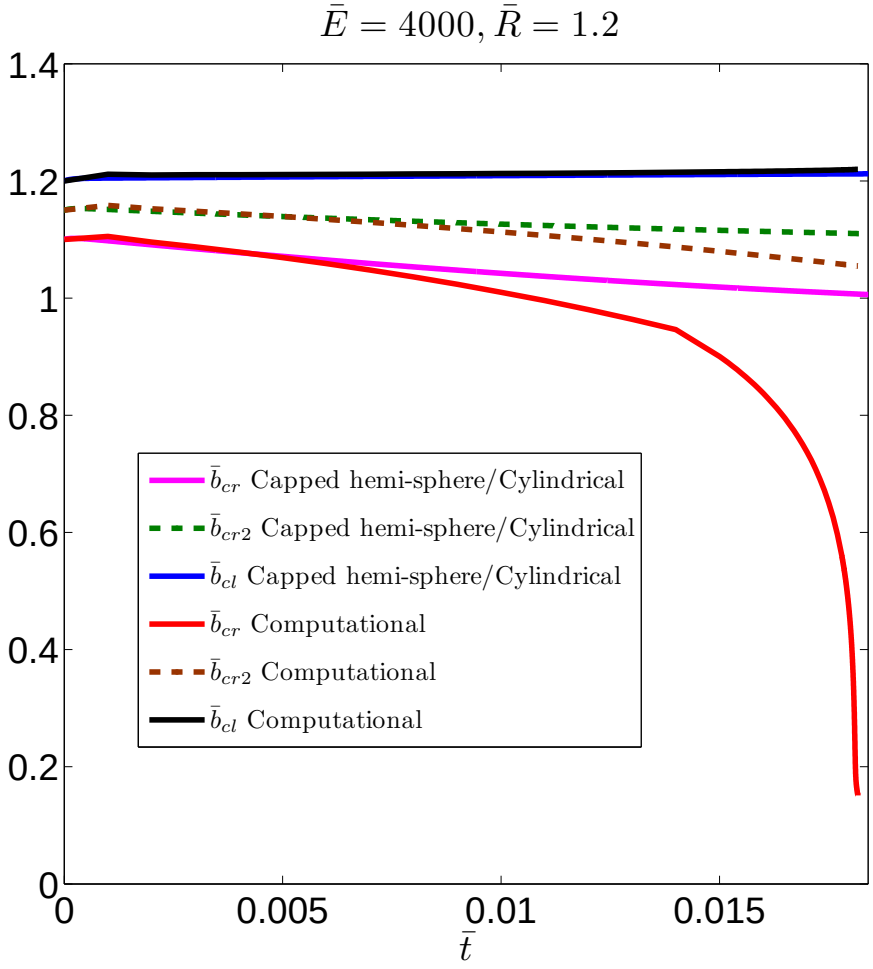

Figure 5.24: Fully developed primary cracks for $\bar{E} = 4000$ and $\bar{R} = 1.2$

no further cracking can occur. Thus either of these curves provide an indication of the value of $\bar{R}$ at which saturation of cracks occurs. From Fig. 5.22, we see that saturation of cracks occur approximately at $\bar{R} = 4$. Thus for a primary spacing of the imperfections slightly less than this value cracks will form with a spacing $2\bar{R} \approx 8$, while for a slightly larger value of $\bar{R}$ cracks will form at both the secondary and primary imperfections giving a crack spacing $\bar{R} \approx 4$. Thus in practice we would expect to see a pattern of cracks with spacing, CS , in the range $\bar{R} \leq CS \leq 2\bar{R}$. The crack spacing ($CS$), in terms of the coating thickness H, is in the range $4H \leq CS \leq 8H$. Lughi et al. [40] conducted isothermal and thermal cycling experiments to study the

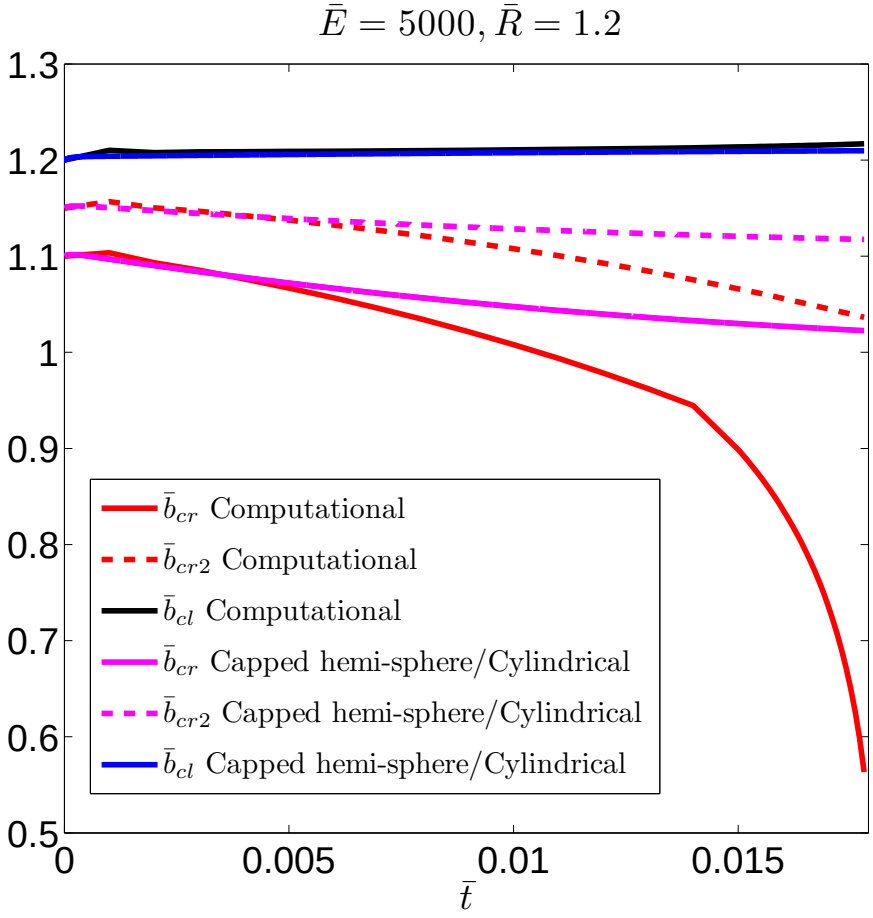

Figure 5.25: Fully developed primary cracks for $\bar{E} = 5000$ and $\bar{R} = 1.2$

sintering response of the coating of 10μm thickness and observed mud-crack spacing in the range of 30μm-100μm ($3H \leq CS \leq 10H$). Therefore, our prediction is consistent with the experimentally observed pattern of cracks as shown in Fig.2.2b.

5.6 Conclusion

A group of multiscale sintering models have been developed to capture the major features of the mud-cracking phenomenon in EB-PVD TBCs under isothermal conditions based on the information provided by computational models discussed in chapter 4. Initially, we studied the sintering response of an intact perfect TBC with a capped hemi-sphere contact model and demonstrated that the sintering gets arrested in the

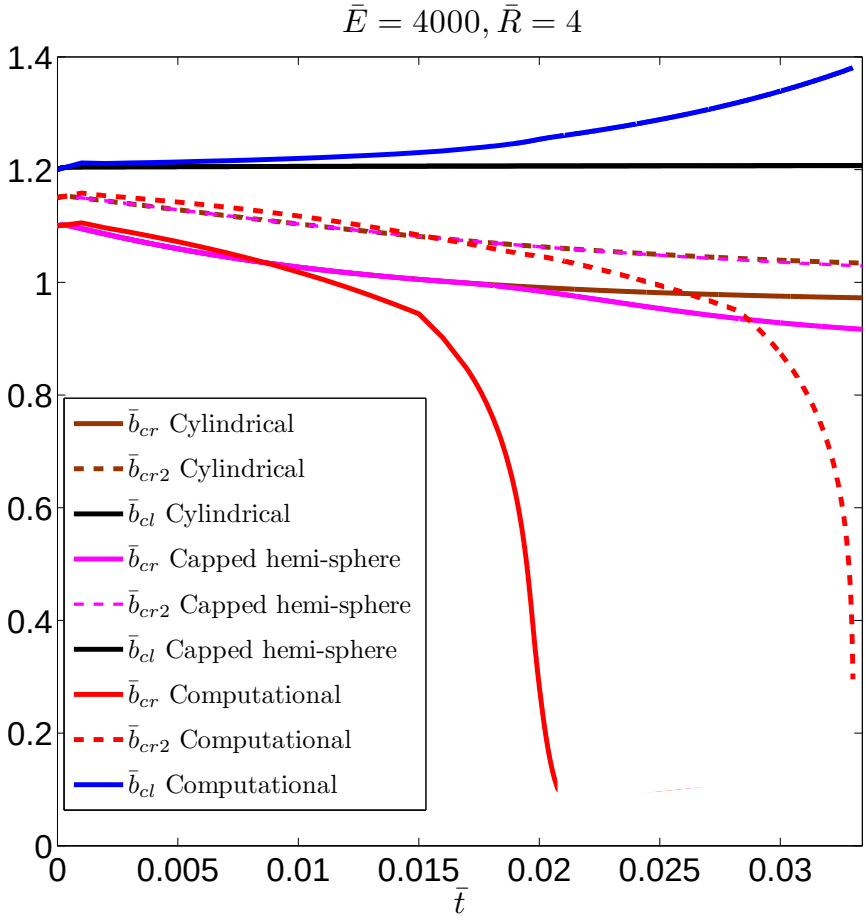

Figure 5.26: Fully developed primary and secondary cracks for $\bar{E} = 4000$ and $\bar{R} = 4$

TBC when the modulus exceeds a critical value. It was also observed from this model that the initial contact size and the Poisson's ratio also influence the sintering response. Then we went on to develop two, two state variable models, one using the same capped hemi-sphere contact model and the other based on purely cylindrical contact model (a subset of capped hemi-sphere contact model) to study the sintering response of the TBC when it contains a square pattern of primary imperfections and identified the conditions under which imperfections grow into mud-cracks. It was observed from these models that the wider the spacing of the imperfections the earlier the instability occurs up to $\bar{R}$=4. We then developed two 3DOF problems employing the same contact models to model the evolution of a further set of mud-cracks

within the mud-cracked islands of the TBC to predict the saturated mud-crack spacing. In these simulations the coating was seeded with two families of square patterns of imperfections. It was found from these 3DOF models that mud-cracking continues and eventually the crack density saturates to a constant value for given initial conditions ($\bar{b}_1^{cl} > \bar{b}_1^{cr2} > \bar{b}_1^{cr}$) and geometrical properties of the coating, in the practical range of modulus of the columns of the coating. We found from these two 3DOF models that saturation of transition from one family of imperfections developing into cracks to both families cracking occurs for a value of $\bar{R} = 4$. We used this value of $\bar{R}$ to estimate the final density of mud cracks in a coating. The density depends on the stiffness of the columns of the coating and results in a crack spacing, CS, in the range $4H \leq CS \leq 8H$. This is consistent with experimentally observed crack spacing range $3H \leq CS \leq 10H$ of Lughi et al. [40]. Compared to the trapezoidal contact analytical models presented in chapter 3, this axisymmetric contact analytical models presented in this chapter more accurately predicts the saturated mud crack spacing. The prediction using analytical models of chapters 3 and 5 is more fully evaluated in chapter 6. Mud cracking may eventually lead to spallation of the coating. The merit of these simple models over the computational models presented in chapter 4 is that we can analyse the sintering response of the TBCs over a wide range of geometric and material parameters efficiently.

Chapter 6

Conclusions

In this chapter, we summarise the work that has been described in this thesis and the main contributions. We analyse how far we have got with the modelling of sintering and mud-cracking in thermal barrier coatings. We then go on to describe future work that we propose in this area.

6.1 Summary

6.1.1 Trapezoidal contact models

Computational models: In chapter 2 computational approaches have been developed for determining the sintering response of an EBPVD columnar thermal barrier coating and for identifying the conditions under which instabilities can develop in the sintering process, leading to the formation of cracks. A simple constitutive model is developed which has been used in conventional finite element studies to model the sintering response and assess the sensitivity of the sintering response to the presence of imperfections in the coating. Initially, sintering of a perfect intact coating has been modelled using the constitutive model described above and demonstrated that the results are in exact agreement with the results of Hutchinson et al [42]. Then, we explored progressive sintering of columns within a mud cracked cluster and compared the results with analytical solutions. We went on to study the influence of an array of imperfections within the constrained TBC on the sintering response. This analysis indicates that in compliant systems the sintering response is not sensitive to

the presence of small imperfections, but if the system is stiff small imperfections can eventually develop into cracks, which advance towards the substrate. We explored this further by examining the sintering response when the coating contains a regular pattern of imperfections and identified conditions under which imperfections grow into cracks. We make use of the predictions of this computational model to guide the development of simple analytical models which capture the major features of the effect of imperfections on the sintering response and to predict the saturated mud-crack spacing in the coating in chapter 3.

Analytical models: Two micro-mechanical sintering models have been developed to capture the essential physics of the mud-cracking phenomenon in EB-PVD TBCs under isothermal conditions based on the information provided by trapezoidal contact computational models described in chapter 2. Initially, we studied the sintering response of a perfect constrained TBC and found that sintering gets arrested in the perfect coating when the in-plane modulus exceeds a critical value. Then we developed a two state variable model to model the evolution primary set of imperfections. In the 2DOF problem, it was observed that the build-up of in-plane tensile stress with progressive sintering triggers the development of a primary set of mud-cracks. Formation of a primary set of mud-cracks in turn partially relieves this stress and accelerates subsequent sintering within the mud-cracked island clusters. From this model, it was observed that the primary cracks can develop early if the spacing considered between the primary set of imperfections is larger. Mud-cracks can form in a coating under conditions where sintering in a perfect coating would be arrested before full density is achieved. As sintering is arrested, desintering can occur at the site of small imperfections within the coating, relaxing the constraint on the remaining material allowing it to sinter towards a lower energy state. We then modelled a 3DOF problem, which follows the evolution of a body which contains two families of imperfections. From the 3DOF model, it was observed that the build of tensile stress within the mud-cracked island clusters leads to further mud-cracking within mud-cracked clusters. This process of mud-cracking continues and eventually the crack

density saturates to a constant value for given initial conditions ($\bar{u}_1 > \bar{u}_1^{cr2} > \bar{u}_1^{cr}$) and mechanical properties of the coating. A coating can contain a large number of imperfections of different intensity, with cracks forming at different locations at different times during the sintering process. Eventually, the density of cracks will saturate. An assessment of the final crack density has been made using the three degree of freedom model. The transition from one family of imperfections developing into cracks to both families cracking is used to estimate the final density of mud cracks in a coating. The density depends on the stiffness of the coating and results in a crack spacing that scales with the thickness of the coating. The Young's modulus of the ceramic coating measured by in-situ experiments is in the range 5-40GPa. From the micrographs of the EB-PVD coatings it can be seen that the wave length λ ranges from 0.2-2μm. These values correspond to a non-dimensional modulus range $\bar{E} = 1500 - 120000$. We explored the sintering response of the EB-PVD in this study in range of modulus of the coating ($\bar{E} = 300 - 7000$). The predicted saturated mud-crack spacing, CS, is in the range $1.5H \leq CS \leq 3H$, where H is the thickness of the coating. Lughi et al. [40] conducted isothermal and thermal cycling experiments on a 10μm thickness coating and observed, CS, in the range $30\mu m \leq CS \leq 100\mu m$. This range in terms of the the thickness of the coating is $3H \leq CS \leq 10H$. Crack spacing predicted in this study is consistent in the lower range of experimentally observed crack spacing. We note from Fig. 3.25 that a higher modulus leads to higher limiting crack spacing. This indicates that we need to consider the higher piratical ranges of modulus of the coating to predict crack spacing accurately. This has been carried out in chapters 4 and 5. We validated the 3DOF analytical model by performing a few computational studies. These simpler models allow a wider range of conditions to be evaluated than can be achieved with computational models, and they can be readily extended to more complex distributions of initial imperfections.

Trapezoidal contact computational and analytical models predict mud-cracking scenarios and the saturated crack spacing accurately enough in the lower practical range of modulus of the coating. The limitation of these models in the higher practical

range of modulus of the coating is that their sintering response is too stiff. The stiff nature of these models is due the choice of the contact model and the approximations or assumptions employed. The way we idealise the geometrical features of the EB-PVD TBC and a number of other things make the model very stiff. So we hardly get any desintering at contacts in the analytical models in the higher range of modulus of the coating.

6.1.2 Axisymmetric contact models

The key assumptions in the trapezoidal contact models are the elastic incompressibility condition of columns and the constancy of modulus of the coating during sintering. To overcome the limitation of the earlier set of models, we proposed a model which contains a discrete distribution of axisymmetric contacts between columns. And also replaced a few unrealistic assumptions by sensible assumptions. In the axisymmetric contact analytical models, we assume elastic and plastic inextensibility condition of columns in the thickness direction of the coating. This inextensibility condition is justified by the fact that during the early stages of sintering (when contact between asperities is small), the response in the thickness direction is too stiff compared to that of in-plane directions. We also include the change of modulus of the coating as a function of sintering stain in the axisymmetric contact models. We also employed a micro-polar material model to determine the effective shear modulus G_e of the coating in the planes normal to the $x_1 - x_2$ plane, where inhomogeneous straining is expected.

Computational models: In chapter 4, computational schemes have been presented for studying the sintering response of EB-PVD coatings and for identifying the conditions under which desintering occurs at imperfections, leading to formation of mud-cracks. A simple micro-mechanical material model has been developed assuming an axisymmetric contact geometry between columns and accounting for change of modulus during sintering. Finite element studies have been performed using this constitutive model through a UMAT subroutine in Abaqus to assess the sintering response and to examine the sensitivity of the response to imperfections in the coating.

Initially, we modelled the sintering response of a perfect coating and demonstrated that the results are in agreement with the analytical results. Then we went on to study the sintering response of a constrained TBC which contains an array of imperfections. This analysis indicates that the compliant coating is insensitive to the presence of small imperfections, whereas imperfections in stiff coatings can develop into a square pattern of cracks, which then advance towards the TGO. We explored this further by assessing the sintering response when the TBC contains a single family of square pattern of imperfections and identified the conditions under which they grow into cracks. We then considered another similar family of imperfections in addition to the primary set of imperfections in order to explore whether a subsequent set of cracks form within the cluster after the formation of a primary set of cracks. These computational models predict the sintering response of the coating reasonably well in the entire practical ranges of modulus of the TBCs. However, these models take a considerable amount of computational time to perform calculations over a wide range of modulus $\bar{E}$ and cluster size $\bar{R}$ in order to generate failure maps. Therefore, in chapter 5, we make use of the predictions of these computational models to develop simple analytical models which capture the major features of the effect of imperfections on the sintering response. Compared to the trapezoidal contact computational models presented in chapter 2, axisymmetric contact computational models more accurately predict the sintering response of the TBC in the practical range of modulus (E=45-87.5GPa) of the dense material of the coating. This corresponds to non-dimensional modulus range of $\bar{E} = 100 - 79000$. Note that in the trapezoidal contact models, E is the modulus of the coating itself, whereas, in the axisymmetric contacts models, the modulus of the coating changes during sintering and E here means the modulus of the dense material (columnar grains) of the coating. Also note that the non-dimensional modulus of the axisymmetric contact model is approximately equal to one fourth of non-dimensional modulus of the trapezoidal contact model although the value of E in these models mean different things. This is because of the different normalisations and parameters used in the two models.

Analytical models: A group of multiscale sintering models have been developed to capture the major features of the mud-cracking phenomenon in EB-PVD TBCs under isothermal conditions based on the information provided by axisymmetric contact computational models discussed in chapter 4. Initially, we studied the sintering response of an intact perfect TBC with a capped hemi-sphere contact model and demonstrated that sintering gets arrested in the TBC when the modulus exceeds a critical value. It was also observed from this model that the initial contact size and Poisson's ratio also influence the sintering response. Then we went on to develop two, two state variable models, one using the same capped hemi-sphere contact model and the other based on a purely cylindrical contact model (a subset of capped hemi-sphere contact model) to study the sintering response of the TBC when it contains a square pattern of primary imperfections and identified the conditions under which imperfections grow into mud-cracks. It was observed from these models that the primary cracks develop early if the spacing considered between the primary set of imperfections is larger up to $\bar{R} = 4$. Because of the nature of sintering potential associated with capped hemi-sphere contact model, we found that the sintering response of the TBC is insensitive to imperfections when the initial contact size $\bar{b} < 0.8$ for relatively large values of $\bar{E}$. Therefore, we considered purely cylindrical asperities between columns and analysed the problem to generate a failure map. We then developed two 3DOF problems employing the set of contact models described above to model evolution of further set of mud-cracks within the mud-cracked islands of the TBC and to predict the saturated mud-crack spacing seeding the coating with two families of square patterns of imperfections. It was found from these 3DOF models that mud-cracking continues and eventually the crack density saturates to a constant value for given initial conditions ($\bar{b}_1^{cl} > \bar{b}_1^{cr2} > \bar{b}_1^{cr}$) and geometrical properties of the coating, in the practical range of modulus of the dense material of the coating. We found from these two 3DOF models that saturation of transition from one family of imperfections developing into cracks to both families cracking occurs for a value of $\bar{R} = 4$. We used this value of $\bar{R}$ to estimate the final density of mud cracks in a coating. The density

depends on the stiffness of the bulk material of the coating and results in a crack spacing, CS, in the range $4H \leq CS \leq 8H$. This is in good agreement with experimentally observed crack spacing range $3H \leq CS \leq 10H$ of Lughi et al. [40]. The Young's modulus of fully dense ceramic material is in the range, E_{fd}=90-175GPa. The modulus of the bulk material (columns) of the coating, $E = E_{fd}(1 - 2\rho)$, where ρ is the volume fraction of pores in the columns. Accounting for porosity ($\rho = 25\%$), we find the practical range of E=45-87.5GPa. Also the radius of axisymmetric asperities can range from 0.1-1μm. The practical range of non-dimensional modulus of the columns of the coating is $\bar{E} = 4000 - 79000$. In the axisymmetric models we explored the sintering response of the TBC in the range $\bar{E} = 90 - 9000$. Compared to the trapezoidal contact analytical models presented in chapter 3, the axisymmetric contact analytical models more accurately predict the saturated mud-crack spacing. The merit of these simple models over the computational models presented in chapter 4 is that we can analyse the sintering response of the TBCs over a wide range of geometric and material parameters and also under non-isothermal situations efficiently.

The choice of the contact model and in turn the sintering potential influences the sintering response of the TBC. Note that we are mainly interested in exploring the mud cracking phenomenon. With the choice of appropriate contact model, we can predict the mud-cracking of the TBC accurately even within the lower practical range of the modulus of the coatings. Matlab programs of the analytical models and Abaqus UMATs of the computational models are in a CD attached with this thesis

6.2 Future Work

6.2.1 EB-PVD coatings

Ceramic TBCs at temperature during service experience in-plane tension due to sintering and exhibits mud-cracking. The micro-mechanical models thus far developed capture the essential physics of this mud-cracking phenomenon in a ceramic EB-PVD TBC under isothermal conditions. Though formation of mud-cracks in a TBC does not mean complete loss of structural integrity of the coating system, it would eventu-

ally lead to TBC spallation. Therefore, it is indispensable to study how the evolved mud-cracks in the TBC lead to its spallation. To understand this, we first need to explore the effect of thermal cycling on mud-cracking. Let us first consider a simple isothermal case. Upon cool-down, under isothermal conditions, a TBC experiences in-plane compression and therefore further mud-cracks do not occur. Nonetheless, in-plane compression of TBC induces high mode I stress intensity at the mud crack tips which are yet to touch the TGO and mode II stress intensity at the mud crack tips already touching the interface/TGO. Mode I compressive stress intensity does not cause crack growth, but detailed study needs to be undertaken to observe how mode II stress intensity at the tips of mud-cracks touching TGO cause mud-cracks propagation and eventual coating spallation. On the other hand, upon cool down, under non-isothermal conditions (where temperature gradients are present), a mud cracked TBC may be subjected to residual tension which may cause further mud-cracking and extension of existing mud-cracks to reach the interface. In-plane tension in the TBC and the in-plane compression at the interface creates a mode II stress intensity at the mud crack tips already touching the interface/TGO. Again, we need to investigate how these mud cracks propagate and lead to delamination and/or spallation of the TBC under non-isothermal conditions.

The accuracy and reliability of these models however depend on how exactly we incorporate the active mechanisms and material behavior under near realistic loading conditions and therefore the following points may be worth considering to that end.

a. Grading microstructure inherent in EB-PVD TBCs leads to modulus, density, and hence stress gradients across the TBC thickness. This has a major implication on strain tolerance and hence mud-cracking of the TBC. Therefore, inclusion of anisotropic material properties owing to TBC sintering and degradation, in space, time and temperature would be appropriate. This requires experimental evaluation of basic TBC properties. b. Sintering is also influenced by the BC roughness and the applied mechanical strains (due to centrifugal or gas loads). c. Growth of TGO and its property change during service has significant influence on the failure. d. We ob-

served from the models presented in this thesis that the choice of contact model plays a key role in predicting the sintering response of the coating accurately. We assumed simple contact geometries to keep the number of independent variables as small as possible. However, we need to map out the effect of a range of variables to choose a contact geometry which closely reflects the behavior of real systems. Therefore, we can come up with improved contact models. Although the capped hemi-sphere model does the job well, we can still improve this by allowing the radius of the hemi-sphere to change. e. We can further improve the models by introducing more degrees of freedom.

Strain tolerance is not a property of the coating alone but the complete TBC system. Therefore, we can improve the strain tolerance by changing the coating architecture (e.g. having a functionally graded BC) and properties. We can study the effect of these on mud-cracking and coating failure. The microstructure and hence the performance of the coating can be controlled by controlling the process parameters such as the electron beam power, vapor incidence angle, and rotation speed. Influence of these parameters can be evaluated by suitably perturbing the initial contact conditions and coating properties in mud-cracking models.

During sintering of perfect coatings, columns need not bend, whereas, columns of the imperfect coating are subjected both bending and shearing as shown in Fig. A.1. In chapter 4, we developed a simple micro-polar model to determine the shear response of the coating in $x_2 - x_3$ and $x_1 - x_3$ planes where inhomogeneous staining expected and implemented that into the computational model. We later demonstrated that this computational model predicts the sintering response accurately. However, one can develop a fuller micro-polar model of the entire coating to more accurately predict the sintering response of the TBC. In the models described in the thesis, we just considered the TBC on a rigid substrate and developed models. Nevertheless, we need to consider the TBC as a system, including TGO, bond coat and the substrate with realistic properties to study how the mud-cracks from the top of the coating advance towards the substrate and lead to spallation of the coating.

6.2.2 APS coatings

In APS TBCs, initially, the highest crack density is parallel to the free surface. During ageing at temperature, these cracks sinter. Some of the vertical cracks fully sinter, while others open and grow. This situation is strong evidence for high in-plane tension and suggests a possible mechanism for mud crack development. Therefore, mud-cracking models for APS TBCs considering sintering of different microstructural features (e.g porosity, intersplat cracks and columnar grain structure of the splats) can be developed. Influence of isothermal and non-isothermal temperatures on mud-cracking under steady state and temperature cycling should also be explored as in EB-PVD TBCs. Time variation of coating material properties such as stiffness, thermal conductivity and toughness during service due to sintering may also be considered to improve the mud-cracking models. Mud-cracking models of APS TBCs can be compared with those of EB-PVD TBCs. The continuum state variable models thus developed for this coating can be incorporated in a commercial FE code such as Abaqus to analyse complex TBC systems as we did for EB-PVD coatings.

Appendix A

Micropolar Model

A.0.3 Micropolar theory of elasticity

In the main text the TBC is modelled as a conventional continuum. In this appendix, we develop an alternative model in which the TBC columns are treated as micro-beams. Asperity sintering can be accommodated by bending and shear deformation of the columnar beams as well as in-plane straining of the columns. Compatibility also requires shear deformation of the asperities to accommodate sliding of the columnar beams over each other as they bend. We do not attempt to develop a full model here, we concentrate on the shear deformation of an array of columnar grains and use the analysis to inform the choice of material parameters within the conventional continuum description employed in chapter 4. The resulting system of equations are equivalent to the Cosserat theory as described by Park and Lakes [92]. The micropolar theory of elasticity, also known as Cosserat elasticity or micropolar continuum mechanics, incorporates a local rotation of points as well as the translation assumed in classical elasticity. In the isotropic Cosserat solid or micropolar continuum, there are six elastic constants, in contrast to the classical elastic solid in which there are two, and the uniconstant material in which there is one. Cosserat elasticity may be viewed as a particular manifestation of nonlocality, but is not equivalent to the general nonlocal elasticity. It is more general than the gradient theory paradigm used to model size effects in plasticity [92].

In multiscale modelling, Cosserat effects are expected to appear as the consequence of the largest structural elements in the material. Consider the EB-PVD coating as shown in Fig. A.1a. The coating has columnar grains and has discrete contacts between columns. The size of the column is very large compared to the asperity size. In the $x_1 - x_2$ plane of the coating, we describe the response using conventional description of chapter 4, however, in the $x_1 - x_3$ and $x_2 - x_3$ planes, we expect Cosserat effects due to nonhomogeneous straining. Here, we are interested in the fundamental response of the coating to capture the Cosserat effects, in terms of the stresses, σ_{ij}, which give rise to strains, ε_{ij}, and the moments, M_{ij}, which give rise to micro-rotations, ϕ_i, where $\phi_{i,j}$ is the curvature. Consider a single column of the coating. This column is subjected shearing and bending in the $x_1 - x_3$ and $x_2 - x_3$ planes. Fig. A.1b shows the shearing and bending of a column in the $x_1 - x_3$ plane

during sintering.

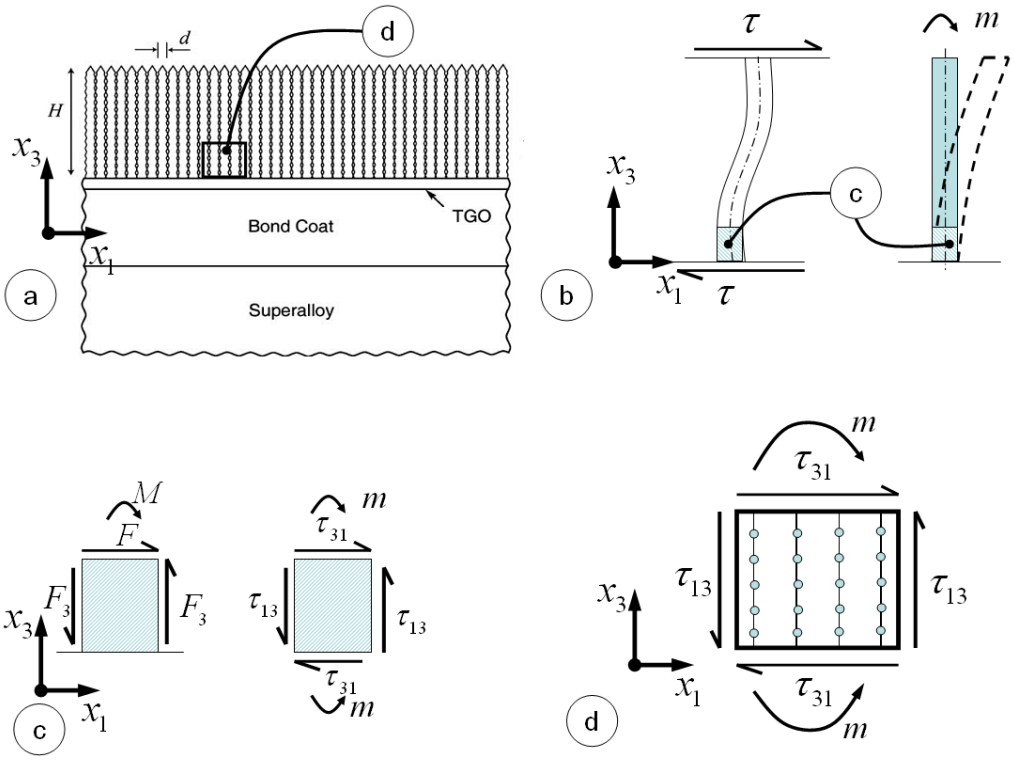

Figure A.1: a. Columnar grains of EB-PVD coating having discrete contacts between columns. b. A column of coating subjected to bending and shearing in the $x_1 - x_3$ plane during sintering. c. Left hand side figure shows the shear forces and the moments, M, on the shaded portion of a column and the right hand side figure shows the shear stresses and the moments m on the shaded portion of the column. Here M is the moment and m is moment per unit area. d. Micro-continuum response of Cosserat elastic material

Now consider a small element of the column (shaded portion) as shown in Fig. A.1b. Fig. A.1c shows the shear forces, moments and the stresses experienced by this element. However, we are interested in finding the macroscopic response of the coating in this plane. Therefore, consider a Cosserat element of the coating as shown in Fig. A.1d. This element is considered to be linear micropolar elastic medium which is macroscopically homogenous. In classical elasticity, $\tau_{13} = \tau_{31}$. However, as a consequence of considering microscopic moments carried by the columns, we have a non-classical response, ie $\tau_{13} \neq \tau_{31}$. This means that the shear modulus in the x_1 direction need not be equal to the shear modulus in the x_3 direction, ie $G_1 \neq G_3$. The objective here is to determine the effective shear modulus of this coating in the $x_1 - x_3$ plane, G_e. The column is of size $d \times d$, therefore the moment per unit area, $m = \frac{M}{d^2}$, where M is the moment. The curvature $\kappa = \frac{M}{EI}$, where, E is modulus of the columns and I, the moment of inertia of the column ($I = \frac{d^4}{12}$). Therefore, the moment

per unit area m is

$$m_{ij} = \frac{Ed^2}{12}\phi_{i,j} \tag{A.1}$$

here, $\beta = \frac{Ed^2}{12}$ and is the bending stiffness of the column per unit area. $\phi_{i,j}$ is the curvature. Following Lakes and Park [92], we can write constitutive equations for the element shown in Fig. A.1d.

$$\tau_{13} = G_1\varepsilon_{13}; \qquad \tau_{31} = G_3\varepsilon_{31}; \tag{A.2}$$

$$m = \beta\frac{\partial\phi}{\partial x_3} \tag{A.3}$$

and strain-displacements relations are

$$\varepsilon_{13} = \frac{\partial u_3}{\partial x_1} - \phi; \qquad \varepsilon_{31} = \frac{\partial u_1}{\partial x_3} + \phi; \tag{A.4}$$

here, u_1, u_2 and u_3 are the displacements in the x_1, x_2 and x_3 directions respectively. In these equations ϕ is treated as an internal parameter which is determined as part of the solution process. Considering pure bending of columns, ie $u_3 = 0$, $\phi = -\frac{\partial u_1}{\partial x_3}$ and the strain-displacement relations reduce to

$$\varepsilon_{31} = 0; \qquad \varepsilon_{13} = -\phi = \frac{\partial u_1}{\partial x_3}; \tag{A.5}$$

We can add the constitutive relationships for the normal straining of the columns and deformation of the asperities to give a full set of constitutive relationships for the coating. Here, however we simply analyse the shear response of an infinite film of TBC of height h subjected to a shear stress, $\tau^{\propto}$ at the surface. The above equations are sufficient to analyse the problem. It proves convenient to first analyse the limiting cases of an infinite bending stiffness (case I) and zero bending stiffness (case II) before analysing the full problem (case III).

Case I

Consider the material as shown in Fig. A.2a. The height of this element is h and is subjected to a macroscopic shear stress, $\tau^{\propto}$ at $x_3 = h$. This applied load produces a macroscopic shear strain, γ within the element. Let us initially explore the case in which the bending stiffness is very high, ie the columns of the coating are infinitely stiff in bending ($\beta \to \propto$). We assume that the coating deforms in simple shear such that

$$u_1 = ax_3; \qquad u_3 = 0; \tag{A.6}$$

There is a large energy penalty if the columns bend, and therefore $\phi = 0$ throughout the coating. We can now write the total potential energy (TPE) for unit area of the coating

$$\Omega = \int_V \frac{1}{2}[G_1\varepsilon_{13}^2 + G_3\varepsilon_{31}^2 + \beta\kappa^2]dV - \tau^{\propto}ah \tag{A.7}$$

Since $\phi = 0$, $\varepsilon_{13} = \frac{\partial u_3}{\partial x_1} = 0$; and $\varepsilon_{31} = \frac{\partial u_1}{\partial x_3} = a$. $\kappa = 0$. Now the TPE becomes,

$$\Omega = \frac{1}{2} G_3 a^2 h - \tau^{\propto} a h \tag{A.8}$$

Performing variational calculus on the above functional, we can show that $a = \frac{\tau^{\propto}}{G_3}$. Now the macroscopic shear strain γ in the element is

$$\gamma = a = \frac{\tau^{\propto}}{G_3} \tag{A.9}$$

Thus the effective shear modulus is the modulus of the columns.

Case II

Now let us consider another case in which the bending stiffness of the column, β is very small, or the columns are compliant, ie $\beta \to 0$. In this case, a column of the Cosserat material (Fig. A.2a) can kink at $x_3 = 0$ as shown in Fig. A.2b and again at $x_3 = h$, depending on the precise boundary condition at this location. We assume that away from these boundaries that ϕ, is constant, ie, independent of the position x_3; therefore $\phi = \phi_c$. As before we assume that the coating deforms in simple shear macroscopically, such that $u_1 = a x_3$ and $u_3 = 0$. Now the strain components in the Cosserat material shown in Fig. A.2a are

$$\varepsilon_{13} = \frac{\partial u_3}{\partial x_1} - \phi = -\phi_c \tag{A.10}$$

$$\varepsilon_{31} = \frac{\partial u_1}{\partial x_3} + \phi = a + \phi_c \tag{A.11}$$

Then the total potential energy Ω is given by

$$\Omega = \frac{1}{2}[G_1 \phi_c^2 + G_2 (a + \phi_c)^2] h - \tau^{\propto} a h \tag{A.12}$$

We choose the values of ϕ_c and a that minimise the functional, giving

$$\phi_c = -a \left[\frac{G_2 3}{G_1 + G_3} \right] \tag{A.13}$$

and

$$a = \tau^{\propto} \left[\frac{G_1 + G_3}{G_1 G_3} \right] \tag{A.14}$$

Therefore, the effective shear modulus G_e of this Cosserat continuum in the $x_1 - x_3$ plane is

$$\frac{1}{G_e} = \frac{1}{G_1} + \frac{1}{G_3} \tag{A.15}$$

Physically, this analysis demonstrates that the columns rotate to share the macroscopic deformation between the two modes, such that the total potential energy is

minimised. If $G_1 << G_3$ as shown in Fig. A.2c, $\phi_c = -a$, this means that the rotation is equal to the macroscopic shear strain. Now the strain $\varepsilon_{31} = 0$ and $\varepsilon_{13} = a = \gamma$, giving $G_e = G_3$. Thus the columns rotate to allow the material to shear in the most compliant mode. If the coating fully sinters, ie, the contacts fully flatten, $G_1 = G_3 = G$, $\phi_c = a/2$ and the effective shear modulus becomes

$$G_e = \frac{G}{2} \tag{A.16}$$

ie, the columns rotate to share the shear deformation equally between the two modes. This results in a stiffness that is half that for the situation where $\beta \to \propto$ and the beam elements are unable to rotate.

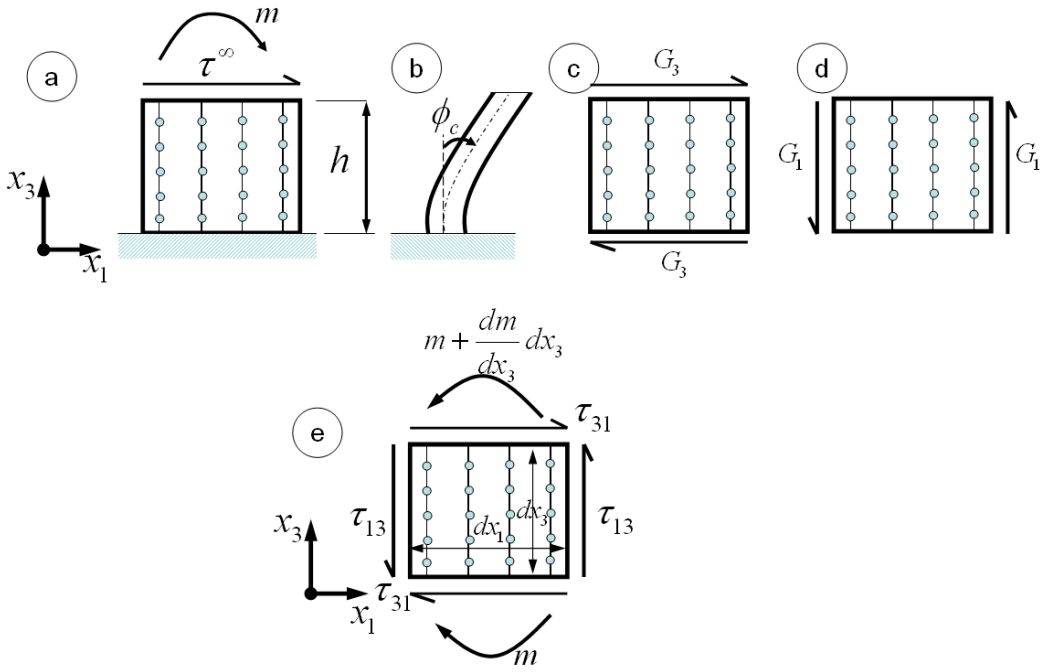

Figure A.2: a. Cosserat element of height h subjected to a moment m and the macroscopic shear stress, $\tau^{\propto}$ at $x_3 = h$. b. A column of the Cosserat element having a vertical kink ϕ_c at $x_3 = 0$ on account of sintering deformation. c. Cosserat element when $G_1 << G_3$. d. Cosserat element when $G_3 << G_1$

Case III

Now consider the case where β is infinite. Again consider unit area of a section of the coating of height h as indicated in Fig. A.2a. Considering force and moment equilibrium of an element of the coating shown in Fig. A.2e, we can write

$$\frac{d\tau_{31}}{dx_3} = 0 \tag{A.17}$$

$$\frac{dm}{dx_3} = (\tau_{31} - \tau_{13}) \tag{A.18}$$

For an infinite extent of coating the solution is independent of x_1. Further we assume that elements can only deform macroscopically in shear. Therefore $u_1 = f_1(x_3)$, $u_3 = 0$, where $f_1(x_3)$ is a function of x_3. Eqn. A.4 for the shear strains now become

$$\varepsilon_{13} = \frac{\partial u_3}{\partial x_1} - \phi = -\phi \tag{A.19}$$

$$\varepsilon_{31} = \frac{\partial u_1}{\partial x_3} + \phi \tag{A.20}$$

Symmetry also requires $\tau_{13} = f(x_3)$ and using the stress-strain relations given by eqn A.2, we can express eqn. A.19 in the form

$$\varepsilon_{13} = \frac{f(x_3)}{G_1} = -\phi \tag{A.21}$$

Using ϕ given by eqn A.21 in the eqn A.3 and differentiating m with respect to x_3 and plugging the resulting relationship into eqn A.18 and noting that $\tau_{31} = \tau^{\propto}$ at $x_3 = h$, we get the following differential equation

$$\frac{\beta}{G_1}\frac{\partial^2 f}{\partial x_3^2} - f + \tau^{\propto} = 0 \tag{A.22}$$

Taking,

$$\alpha^2 = \frac{\beta}{G_1}; \tag{A.23}$$

We can re-write the above differential equation

$$\alpha^2\frac{\partial^2 f}{\partial x_3^2} - f + \tau^{\propto} = 0 \tag{A.24}$$

The solution to the above equation is given by

$$f = A\exp\left(\frac{x_2}{\alpha}\right) + B\exp\left(-\frac{x_2}{\alpha}\right) + \tau^{\propto} \tag{A.25}$$

where A and B are constants of integration determined from the boundary conditions. We assume that the columnar beams are encastre at the base of the coating, ie $\phi = 0$; eqn A.21 then gives

$$f(x_3) = \left\{ \begin{array}{ll} 0 & \text{at} \quad x_3 = 0; \end{array} \right.$$

We can either assume that $m = 0$ at the top of the coating (if the beams are free to rotate at the surface) or $\phi = 0$ (if the shear deformation is applied by gripping the tips of the columns and preventing rotation). Here we assume the latter of these boundary conditions, such that

$$f(x_3) = \left\{ \begin{array}{ll} 0 & \text{at} \quad x_3 = h; \end{array} \right.$$

we then find

$$A = -\tau^{\propto}\left[\frac{\left[1-\exp\left(-\frac{h}{\alpha}\right)\right]}{\left[\exp\left(\frac{h}{\alpha}\right)-\exp\left(-\frac{h}{\alpha}\right)\right]}\right]; \quad B = \tau^{\propto}\left[\frac{\left(1-\exp\left(\frac{h}{\alpha}\right)\right)}{\left[\exp\left(\frac{h}{\alpha}\right)-\exp\left(-\frac{h}{\alpha}\right)\right]}\right]; \quad \text{(A.26)}$$

The strain $\varepsilon_{31} = \frac{\tau^{\propto}}{G_3}$ since $\tau_{31} = \tau^{\propto}$ at $x_3 = h$. Noting that $\phi = -\frac{f}{G_1}$ from eqn A.21 and using these in eqn A.20, we have

$$\frac{\partial u_1}{\partial x_3} = \frac{\tau^{\propto}}{G_3} + \frac{f(x_3)}{G_1} \quad \text{(A.27)}$$

Integrating the above equation plugging f given by eqn A.25 and using the BC, $u_1 = 0$ at $x_3 = 0$, we get u_1

$$u_1 = \frac{\tau^{\propto} x_3}{G_2} + \frac{A}{G_1}\alpha\exp\left(\frac{x_2}{\alpha}\right) - \frac{B}{G_1}\alpha\exp\left(-\frac{x_2}{\alpha}\right) + \frac{\tau^{\propto}}{G_1}x_2 + \frac{(B-A)}{G_1}\alpha \quad \text{(A.28)}$$

The macroscopic shear strain on the Cosserat element, $\gamma = \frac{u_1}{h}$, where, u_1 is obtained by evaluating expression given by the eqn A.28 at $x_3 = h$. Taking $\bar{h} = \frac{h}{\alpha}$, we can write

$$\gamma = \tau^{\propto}\left[\frac{1}{G_2} + \frac{1}{G_1} + \frac{1}{G_1\bar{h}}\left\{\frac{4-2\left(\exp(\bar{h})+\exp(-\bar{h})\right)}{\left(\exp(\bar{h})+\exp(-\bar{h})\right)}\right\}\right] \quad \text{(A.29)}$$

Therefore, the effective shear modulus, G_e, in the $x_1 - x_3$ plane is

$$\frac{1}{G_e} = \left[\frac{1}{G_2} + \frac{1}{G_1} + \frac{1}{G_1\bar{h}}\left\{\frac{4-2\left(\exp(\bar{h})+\exp(-\bar{h})\right)}{\left(\exp(\bar{h})+\exp(-\bar{h})\right)}\right\}\right] \quad \text{(A.30)}$$

If $\bar{h} \to \propto$, ie, $\beta \to 0$ and the above equation reduces to eqn. A.15

$$\frac{1}{G_e} = \frac{1}{G_1} + \frac{1}{G_3} \quad \text{(A.31)}$$

On the other hand, if $\bar{h} \to 0$, ie, ie, $\beta \to \propto$, the eqn A.30 reduces to eqn. A.9

$$\frac{1}{G_e} = \frac{1}{G_3} \quad \text{(A.32)}$$

The equations presented here can be used as the basis of a full micropolar model for the sintering of a TBC. We do not pursue this route here, but simply use the above analysis to facilitate the selection of suitable relationships for the shear response of the coating. In chapter 4 we assume that the columns of the coating are slender and the shear deformation can be determined from eqn. A.15. The shear modulus in the x_1 direction, ie G_1 of the Cosserat element has contributions from the shear modulus of the the columns, G, and also the stiffness of the asperities and is given by

$$\frac{1}{G_1} = \frac{1}{G} + \frac{1}{2q_1 d} \quad \text{(A.33)}$$

The shear modulus of the Cosserat element in the x_3 direction is

$$\frac{1}{G_3} = \frac{1}{G} \tag{A.34}$$

Therefore, using eqn. A.15, the effective shear modulus in the $x_1 - x_3$ plane is given by

$$\frac{1}{G_e} = \frac{2}{G} + \frac{1}{2q_1 d} \tag{A.35}$$

The effective shear modulus in the $x_2 - x_3$ plane can be determined in a similar way. Here, q_1 is the effective stiffness of the asperities in the x_1 direction and is given by eqn. 4.38. $q_1 = G\tilde{q}_1$, where, $\tilde{q}_1 = \frac{4b_1}{\pi s^2}$ and depends on the geometry of the asperities.

The above analysis can also be adapted to determine the linear viscous response of the coating. Using the elastic analogue we can simply replace strains by strain rates and shear modulus by viscosity in the above relationships. In the model of chapter 4 we assume that energy is only dissipated as a result of sintering and sliding at the asperity scale. Thus the bending viscosity of the columns is infinite and the analogue of case I applies with the effective shear viscosity given by $\eta_e = \eta_3$, where $\eta_3 \to \propto$. This is the shear viscosity of the columns. Thus the TBC is unable to deform in shear inelastically in the $x_1 - x_3$ and $x_2 - x_3$ planes, ie $\gamma^p_{13} = \gamma^p_{23} = 0$

Appendix B

2DOF Axisymmetric Contact Model

B.0.4 Determination of Gibbs free energy

The Gibbs free energy density, G, in the TBC is given by

$$G \;=\; G_i + U \tag{B.1}$$

where, G_i is the interfacial energy density and U is the elastic strain energy density of the TBC.

Determination of interface free energy

In this section, we estimate the interface energy density of the the TBC. The interfacial energy of the TBC has contributions from bulk contacts associated with w_{cl} within the cluster and contacts associated with the primary imperfection $w_{cr}(x_3)$. Let G_i^{cl} be the interface energy density associated with bulk contact and G_i^{cr} be the interface energy density associated with primary imperfections of the TBC. Thus the interfacial energy density of the TBC is given by

$$G_i \;=\; G_i^{cl} + G_i^{cr} \tag{B.2}$$

Now we derive G_i^{cl}. Consider an asperity contact geometry within the cluster during early stages of sintering (when $b_{cl} < R_o$) as shown in Fig. B.1a with the appropriate definition of fluxes, surface energies and diffusivities. When $b_{cr} < R_o$, the interfacial energy density associated with bulk contacts of the entire cluster is given by

$$G_i^{cl} \;=\; \frac{8}{\pi s^2 R}\left(\frac{R}{d} - \frac{1}{2}\right) G_a^{cl} \tag{B.3}$$

where, G_a^{cl} in the above equation is the interface energy per asperity within the cluster and is expressed in terms of the surface energy γ_s and interfacial energy γ_g

$$G_a^{cl} \;=\; 2\pi R_o(w_{cl} - h_{cl})\gamma_s + 2\pi b_{cl} h_{cl}\gamma_s - \pi R_o^2\gamma_s - \pi b_{cl}^2\gamma_s + \pi b_{cl}^2\gamma_g \tag{B.4}$$

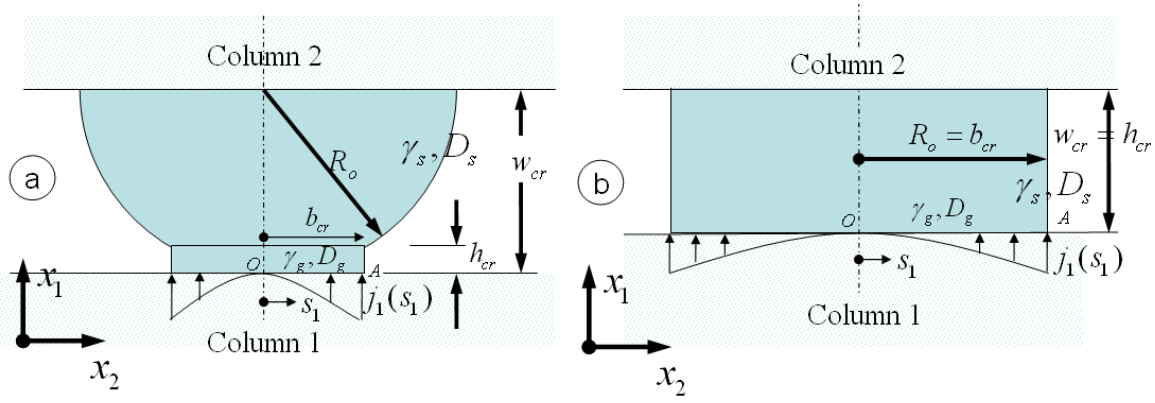

Figure B.1: Contact geometry within cluster a. Deformed asperity during early stages of sintering (when $b_{cr} < R_o$) b. Deformed asperity during later stages of sintering (when $b_{cr} \geq R_o$).

Normalising geometric and material parametrs as discussed in chapter 4, we get

$$G_i^{cl} = \frac{8}{\bar{s}^2 \bar{R}\bar{H}} \left(\frac{\bar{R}\bar{H}}{\bar{d}} - \frac{1}{2} \right) \left(\frac{\gamma_s}{R_o} \right) \left[2(\bar{w}_{cl} - \bar{h}_{cl}) + 2\bar{b}_{cl}\bar{h}_{cl} - 1 - \bar{b}_{cl}^2 + \bar{b}_{cl}^2 \bar{\gamma}_g \right] \tag{B.5}$$

Now G_a^{cl} is a function of $\bar{h}_{cl}$,$\bar{w}_{cl}$ and $\bar{b}_{cl}$. But we need G_a^{cl} in terms of $\bar{w}_{cl}$ in order to formulate the model in terms of the primary unknown $\bar{w}_{cl}$. In order to do this, we express $\bar{h}_{cl}$ and $\bar{w}_{cl}$ in terms of $\bar{b}_{cl}$ based on geometrical arguments to give

$$\bar{h}_{cl} = \frac{2}{3\bar{b}_{cl}^2} \left[1 - \frac{1}{2} \sqrt{1 - \left(\bar{b}_{cl}\right)^2} \left[2 + \left(\bar{b}_{cl}\right)^2 \right] \right] \tag{B.6}$$

$$\bar{w}_{cl} = \sqrt{1 - \left(\bar{b}_{cl}\right)^2} + \frac{2}{3\bar{b}_{cl}^2} \left[1 - \frac{1}{2} \sqrt{1 - \left(\bar{b}_{cl}\right)^2} \left[2 + \left(\bar{b}_{cl}\right)^2 \right] \right] \tag{B.7}$$

Plugging $\bar{h}_{cl}$ and $\bar{w}_{cl}$ in eqn. B.5, we get G_i^{cl} as a function of $\bar{b}_{cl}$ alone. However, the expression for $\bar{w}_{cl}$ needs to be inverted to express $\bar{b}_{cl}$ in terms of $\bar{w}_{cl}$. Now $\bar{b}_{cl}$ is given by

$$\bar{b}_{cl} = \frac{1}{2\sqrt{2}} \sqrt{12 - 9\bar{w}_{cl}^2 - \sqrt{3}\sqrt{(2 + \bar{w}_{cl})(-2 + 3\bar{w}_{cl})^3}} \tag{B.8}$$

Substituting $\bar{b}_{cl}$ given by eqn. B.8 into the final expression for G_i^{cl}, we get G_i^{cl} as a function of $\bar{w}_{cl}$ only. Now consider an asperity within the cluster during the later stages of sintering as shown in Fig. B.1b. Now the shape of the asperity is a pure cylinder. We can now express the interface energy per cylindrical asperity in terms of the surface energy γ_s and interfacial energy γ_g to get

$$G_i^{cl} = \frac{8}{\bar{s}^2 \bar{R}\bar{H}} \left(\frac{\bar{R}\bar{H}}{\bar{d}} - \frac{1}{2} \right) \left(\frac{\gamma_s}{R_o} \right) \left[2\bar{b}_{cl}\bar{w}_{cl} - 2\bar{b}_{cl}^2 + \bar{b}_{cl}^2 \bar{\gamma}_g \right] \tag{B.9}$$

where,

$$\bar{b}_{cl} = \sqrt{\frac{\bar{V}}{\pi \bar{w}_{cl}}} \tag{B.10}$$

$\bar{V}$ is the volume of the asperity in non-dimensional form and is equal to $\frac{2}{3}\pi$. G_i^{cr} changes with the choice of ξ and we now derive an expression for G_i^{cr} when $\xi \leq H$. It can be seen from Fig. 5.9b that the local contact at the primary imperfection characterized by $w_{cr}(x_3)$ varies linearly with x_3 from the substrate up to a height ξ and remains constant thereafter over the rest of the height of the cluster.

$$w_{cr}(x_3) = \begin{cases} w_{cr}^b = (w_1^{cr} - w_1^{cl} + w_{cl})\left(1 - \frac{x_3}{\xi}\right) + w_{cr}\ \frac{x_3}{\xi} & \text{if} \quad 0 \leq x_3 \leq \xi; \\ w_{cr}^t = w_{cr} & \text{if} \quad \xi \leq x_3 \leq H. \end{cases}$$

Therefore, in this case, G_i^{cr} is the sum of interface energy densities associated with linearly varying contacts $w_{cr}(x_3)$ in the bottom portion of the imperfection and that associated with uniform contact w_{cr} in the top portion of the imperfection. G_i^{cr} now is given by

$$G_i^{cr} \ = \ \int_0^{\xi} G_i^{cr^b}\, dx_3 + G_i^{cr^t} \tag{B.11}$$

Consider an asperity contact geometry at the primary imperfection during the early stages of sintering (when $b_{cr} < R_o$, see Fig. B.2a). When $b_{cr} < R_o$, the interfacial

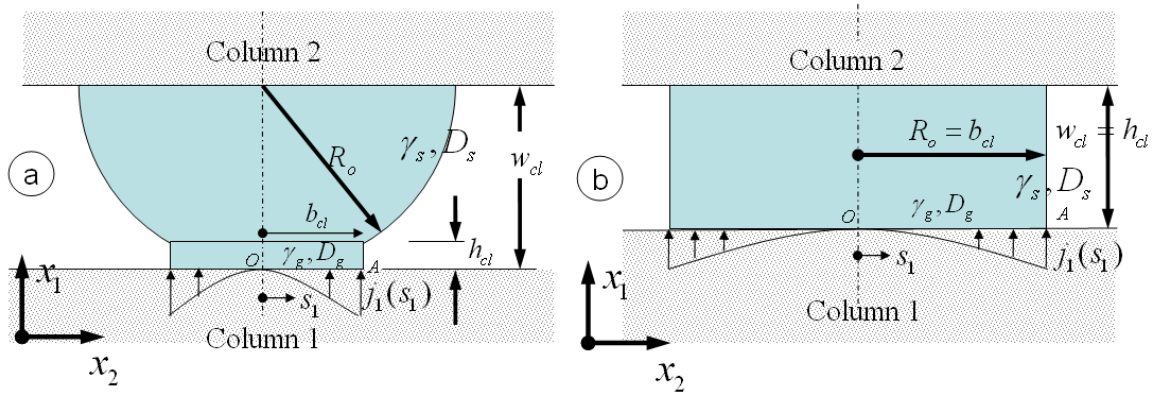

Figure B.2: Contact geometry at primary imperfection a. Deformed asperity during early stages of sintering (when $b_{cr} < R_o$) b. Deformed asperity during later stages of sintering (when $b_{cr} \geq R_o$).

energy density in the bottom portion of the primary imperfection where there is varying contact area is given by

$$G_i^{cr^b} = \frac{4}{\bar{s}^2 \bar{R} \bar{H}^2} \left(\frac{\gamma_s}{R_o}\right) \int_0^{\bar{\xi}} \left[2(\bar{w}_{cr}^b - \bar{h}_{cr}^b) + 2\bar{b}_{cr}^b \bar{h}_{cr}^b - 1 - (\bar{b}_{cr}^b)^2 + (\bar{b}_{cr}^b)^2 \bar{\gamma}_g\right] d\bar{x}_3 \tag{B.12}$$

In the above expression for $G_i^{cr^b}$, $\bar{h}_{cr}^b$ can be expressed in terms of $\bar{b}_{cr}^b$ and the $\bar{b}_{cr}^b$ is is of the same form as eqn. B.8 but a function of $\bar{w}_{cr}^b$. Substituting $\bar{b}_{cr}^b$ in $G_i^{cr^b}$, we get the interfacial energy density at the bottom portion of the primary imperfection in terms of $\bar{w}_{cr}^b$. Note that $\bar{w}_{cr}^b$ is a function of $\bar{w}_{cr}$ and $\bar{w}_{cl}$ as discussed earlier. So, we now have, $G_i^{cr^b}$ in terms of the state variables $(\bar{w}_{cr}, \bar{w}_{cl})$ and the co-ordinate $\bar{x}_3$, which needs to be integrated numerically. The interfacial energy density in the top portion of the imperfection is given by

$$G_i^{cr^t} = \frac{4(\bar{H}-\bar{\xi})}{\bar{s}^2\bar{R}\bar{H}^2}\left(\frac{\gamma_s}{R_o}\right)\left[2(\bar{w}_{cr}-\bar{h}_{cr})+2\bar{b}_{cr}\bar{h}_{cr}-1-(\bar{b}_{cr})^2+(\bar{b}_{cr})^2\bar{\gamma}_g\right] \tag{B.13}$$

In the above equation, $\bar{h}_{cr}$ can be expressed in terms of $\bar{b}_{cr}$ but $\bar{b}_{cr}$ can be expressed in terms of the primary unknown $\bar{w}_{cr}$. Now, $G_i^{cr^t}$ is expressed only in terms of the primary unknown $\bar{w}_{cr}$. Now considering the later stages of sintering at the primary imperfection, ie, when $b_{cr} \geq R_o$ as shown in Fig. B.2b, we can derive expressions for $G_i^{cr^b}$ and $G_i^{cr^t}$ as detailed below.

$$G_i^{cr^b} = \frac{4}{\bar{s}^2\bar{R}\bar{H}^2}\left(\frac{\gamma_s}{R_o}\right)\int_0^{\bar{\xi}}\left[2\bar{b}_{cr}^b\bar{w}_{cr}^b)-2(\bar{b}_{cr}^b)^2+(\bar{b}_{cr}^b)^2\bar{\gamma}_g\right]d\bar{x}_3 \tag{B.14}$$

where,

$$\bar{b}_{cr}^b = \sqrt{\frac{\bar{V}}{\pi\bar{w}_{cr}^b}} \tag{B.15}$$

$\bar{w}_{cr}^b$ is a function of state variables $(\bar{w}_{cr}, \bar{w}_{cl})$ and the co-ordinate $\bar{x}_3$ as discussed earlier. As before this expression needs to be numerically integrated. Similarly, we can derive the interfacial energy density in the top portion of the imperfection:

$$G_i^{cr^t} = \frac{4(\bar{H}-\bar{\xi})}{\bar{s}^2\bar{R}\bar{H}^2}\left(\frac{\gamma_s}{R_o}\right)\left[2\bar{b}_{cr}\bar{w}_{cr}-2\bar{b}_{cr}^2+\bar{b}_{cr}^2\bar{\gamma}_g\right] \tag{B.16}$$

where,

$$\bar{b}_{cr} = \sqrt{\frac{\bar{V}}{\pi\bar{w}_{cr}}} \tag{B.17}$$

Now we have $G_i^{cr^t}$ as a function of $\bar{w}_{cr}$. Now the total interface energy density of the TBC, G_i is obtained by adding the expressions for G_i^{cl}, $G_i^{cr^b}$ and $G_i^{cr^t}$, which depend upon the current shape of the asperities

$$G_i(\bar{w}_{cr}, \bar{w}_{cl}) = G_i^{cl}(\bar{w}_{cl}) + \int_0^{\bar{\xi}} G_i^{cr^b}(\bar{w}_{cr}, \bar{w}_{cl}, \bar{x}_3)d\bar{x}_3 + G_i^{cr^t}(\bar{w}_{cr}); \qquad \xi \leq H \tag{B.18}$$

Similarly, we can derive G_i, when $\xi \geq H$ as shown in Fig. 5.10, by noting that

$$w_{cr}(x_3) = \left\{ \; w_{cr}^b = (w_1^{cr} - w_1^{cl} + w_{cl})\left(1-\tfrac{x_3}{H}\right) + w_{cr}\;\tfrac{x_3}{H} \quad \text{if} \quad 0 \leq x_3 \leq H; \right.$$

ξ in this case is obtained by minimising the elastic stored energy when $\xi \geq H$. Using $w_{cr}(x_3)$ given above, we can derive an expression for G_i^{cr} depending upon the current shape of the asperities.

$$G_i(\bar{w}_{cr}, \bar{w}_{cl}) \;=\; G_i^{cl}(\bar{w}_{cl}) + \int_0^{\bar{H}} G_i^{cr^b}(\bar{w}_{cr}, \bar{w}_{cl}, \bar{x}_3) d\bar{x}_3; \qquad \xi \geq H \tag{B.19}$$

Determination of elastic stored energy; $\xi \leq H$

We derive now the elastic stored energy for $\xi \leq H$. The elastic strain energy in the potential cluster has contributions from field 1, field 2 and the interaction between them. The total elastic strain energy U_C in the cluster can be written as

$$U_C \;=\; \frac{1}{2} \int_V \left[\sigma_{ij}^1 \varepsilon_{ij}^{e_1} + \sigma_{ij}^2 \varepsilon_{ij}^{e_2} + 2\sigma_{ij}^1 \varepsilon_{ij}^{e_2} \right] dV \tag{B.20}$$

Here, i and j independently range over 1-3. Here, $\varepsilon_{ij}^{e_1}$ and $\varepsilon_{ij}^{e_2}$ are the the elastic strain tensor in field 1 and field 2 respectively. Similarly, σ_{ij}^1 and σ_{ij}^2 are the stresses associated with kinematically admissible strain fields 1 and 2, respectively. Since these fields are arbitrary the stresses do not necessarily satisfy equilibrium. The first two terms in the eqn. B.20 are the strain energy in field 1 and field 2 respectively. The elastic strain tensor in field 1 is obtained using the compatibility condition given by eqn. 3.29 and the inextensibility condition. Therefore, the elastic strain tensor in field 1 is given by

$$\varepsilon_{ij}^{e_1} \;=\; \begin{bmatrix} -(\varepsilon_s^1 + \varepsilon^T) & 0 & 0 \\ 0 & -(\varepsilon_s^1 + \varepsilon^T) & 0 \\ 0 & 0 & 0 \end{bmatrix}$$

Note that in field 1, $\varepsilon_{11}^{e_1} = \varepsilon_{22}^{e_1}$. We can express $\varepsilon_{11}^{e_1}$ or $\varepsilon_{22}^{e_1}$ by considering bulk and asperity deformations of the coating

$$\varepsilon_{11}^{e_1} \;=\; \frac{\sigma_{11}}{E} - \frac{\nu\sigma_{22}}{E} + \frac{\sigma_{11}(1-\nu^2)}{E\tilde{q}d} \tag{B.21}$$

The third term in the above equation is due to asperity deformation and is given by Johnson [91]. $\tilde{q}$ is a function of the geometry of asperities. The elastic strain energy in field 1 (perfect film) is given by

$$U^{e_1} \;=\; \frac{4ER^2H\tilde{q}d}{\tilde{q}d(1-\nu) + (1-\nu^2)} (\varepsilon_s^1 + \varepsilon^T)^2 \tag{B.22}$$

However, in developing the analytical model, we consider only asperity deformation which is dominant initially when the contacts are small. Therefore, we take $\varepsilon_{11}^{e_1}$ as,

$$\varepsilon_{11}^{e_1} \;=\; \frac{\sigma_{11}(1-\nu^2)}{E\tilde{q}d} \tag{B.23}$$

Consequently, the stress tensor and the elastic stored energy in field 1 are given by

$$\sigma_{ij}^{1} = \begin{bmatrix} -\frac{E\tilde{q}d}{(1-\nu^2)}(\varepsilon_s^1 + \varepsilon^T) & 0 & 0 \\ 0 & -\frac{E\tilde{q}d}{(1-\nu^2)}(\varepsilon_s^1 + \varepsilon^T) & 0 \\ 0 & 0 & 0 \end{bmatrix}$$

$$U^{e_1} = \frac{4ER^2H\tilde{q}d}{(1-\nu^2)}(\varepsilon_s^1 + \varepsilon^T)^2 \tag{B.24}$$

The elastic strain energy in field 2 of the square cluster U^{e_2} (second term in eqn. B.20) is estimated by assuming a kinematically admissible displacement field within the cluster and consequently the elastic strain tensor in the bottom portion of cluster (field 2) is given by

$$\varepsilon_{ij}^{e_2} = \begin{bmatrix} -\varepsilon_s^2(1-\frac{x_3}{\xi}) & 0 & \varepsilon_s^2\frac{x_1}{2\xi} \\ 0 & -\varepsilon_s^2(1-\frac{x_3}{\xi}) & \varepsilon_s^2\frac{x_2}{2\xi} \\ \varepsilon_s^2\frac{x_1}{2\xi} & \varepsilon_s^2\frac{x_2}{2\xi} & 0 \end{bmatrix}$$

The strain energy in field 2

$$U^{e_2} = \int_V \frac{1}{2}\left(\sigma_{11}^2\varepsilon_{11}^{e_2} + \sigma_{22}^2\varepsilon_{22}^{e_2} + \tau_{23}^2\gamma_{23}^{e_2} + \tau_{13}^2\gamma_{13}^{e_2}\right) dV \tag{B.25}$$

The normal strains in the x_1 and x_2 directions in field 2 are given by

$$\varepsilon_{11}^{e_2} = \frac{\sigma_{11}^2}{E} - \frac{\nu}{E}\sigma_{22}^2 + \frac{\sigma_{11}^2(1-\nu^2)}{E\tilde{q}d} \tag{B.26}$$

$$\varepsilon_{22}^{e_2} = \frac{\sigma_{22}^2}{E} - \frac{\nu}{E}\sigma_{11}^2 + \frac{\sigma_{22}^2(1-\nu^2)}{E\tilde{q}d} \tag{B.27}$$

Again, we consider only asperity deformation which is dominant initially when there is small contact between asperities. Therefore $\varepsilon_{11}^{e_2}$ and $\varepsilon_{22}^{e_2}$ are given by

$$\varepsilon_{11}^{e_2} = \frac{\sigma_{11}^2(1-\nu^2)}{E\tilde{q}d} \tag{B.28}$$

$$\varepsilon_{22}^{e_2} = \frac{\sigma_{22}^2(1-\nu^2)}{E\tilde{q}d} \tag{B.29}$$

The shear elastic strains in field 2 can be written as

$$\gamma_{23}^{e_2} = \frac{\tau_{23}^2}{G} + \frac{\tau_{23}^2}{2G\tilde{q}d} \tag{B.30}$$

$$\gamma_{13}^{e_2} = \frac{\tau_{13}^2}{G} + \frac{\tau_{13}^2}{2G\tilde{q}d} \tag{B.31}$$

Again considering only asperity deformation in the shear terms as well, we can write the elastic stored energy in the cluster (field 2)

$$U^{e_2} = (\varepsilon_s^2)^2 \int_{-R}^{R}\int_{-R}^{R}\int_{0}^{\xi} \left[\frac{E\tilde{q}d}{(1-\nu^2)} \left(1 - \frac{x_3}{\xi}\right)^2 + G\tilde{q}d \left[\left(\frac{x_2}{\xi}\right)^2 + \left(\frac{x_1}{\xi}\right)^2 \right] \right] dx_1 dx_2 dx_3 \tag{B.32}$$

This reduces to

$$U^{e_2} = \frac{4}{3}\frac{E\tilde{q}d}{(1-\nu^2)}(\varepsilon_s^2)^2 R^2 \xi + \frac{8}{3} G\tilde{q}d(\varepsilon_s^2)^2 \frac{R^4}{\xi} \tag{B.33}$$

Similarly, we can determine the strain energy due to interaction between field 1 and 2

$$U^{e_1 e_2} = \int_V \sigma_{ij}^1 \varepsilon_{ij}^2 \, dV \tag{B.34}$$

This gives

$$U^{e_1 e_2} = \frac{4E\tilde{q}d}{(1-\nu^2)}(\varepsilon_s^1 + \varepsilon^T)\varepsilon_s^2 R^2 \xi \tag{B.35}$$

The total elastic strain energy in the cluster is the sum of U^{e_1}, U^{e_2} and $U^{e_1 e_2}$ given by eqns. B.24, B.33 and B.35 respectively.

$$U_C = \frac{4ER^2 H\tilde{q}d}{(1-\nu^2)}(\varepsilon_s^1+\varepsilon^T)^2 + \frac{4}{3}\frac{E\tilde{q}d}{(1-\nu^2)}(\varepsilon_s^2)^2 R^2\xi + \frac{8}{3}G\tilde{q}d(\varepsilon_s^2)^2\frac{R^4}{\xi} + \frac{4E\tilde{q}d}{(1-\nu^2)}(\varepsilon_s^1+\varepsilon^T)\varepsilon_s^2 R^2\xi \tag{B.36}$$

The optimal height ξ that minimises the total strain energy U_C is a function of ε_s^1 and ε_s^2. However, we take $\xi = R\sqrt{1-\rho}$ which minimises the strain energy in field 2 in order to keep the description of the evolving crack geometry simple. The factor ρ is related to $\frac{G}{E}$ ratio as given by eqn. 4.40. Note that when $\rho \to \nu$, $E = 2G(1+\nu)$ and this relationship is valid for sticking condition of contacts. However, we expect sliding between asperities of the TBC at temperature. Therefore, we choose a value of ρ close to 1 in our analysis so as to allow sliding between columns during sintering. Now the total strain energy density of the TBC is given by

$$U_T = \frac{E\tilde{q}d}{(1-\nu^2)} \left\{ (\varepsilon_s^1 + \varepsilon^T)^2 + \left[\frac{2}{3}(\varepsilon_s^2)^2 + (\varepsilon_s^1 + \varepsilon^T)\varepsilon_s^2 \right] \frac{R}{H}\sqrt{1-\rho} \right. \tag{B.37}$$

Taking, $\tilde{q} = \frac{4\bar{b}_{cl}}{\pi \bar{s}^2}$ and non-dimensionalising the above equation, we can express the strain energy density

$$U = \frac{4\bar{E}\bar{b}_{cl}\bar{d}}{\pi\bar{s}^2}\left(\frac{\gamma_s}{R_o}\right) \left\{ (\varepsilon_s^1 + \varepsilon^T)^2 + \left[\frac{2}{3}(\varepsilon_s^2)^2 + (\varepsilon_s^1 + \varepsilon^T)\varepsilon_s^2 \right] \bar{R}\sqrt{1-\rho} \right. \tag{B.38}$$

In eqn. B.38, $\bar{b}_{cl}$ is given either by eqn. B.8 or eqn. B.10 depending upon the current shape of the asperity within the cluster. Using the expressions for ε_s^1 given by eqn. 5.21 and ε_s^2 given by eqn. 5.22 in terms of normalised state variables $(\bar{w}_{cr}, \bar{w}_{cl})$ in eqn. B.38, we can get $U(\bar{w}_{cr}, \bar{w}_{cl})$. Note that in this case, $\xi \leq H$. Therefore,

$$\bar{R} \leq \frac{1}{\sqrt{1-\rho}} \tag{B.39}$$

when ρ is close to 1, say, 15/16, $\bar{R} \leq 4$.

Determination of elastic stored energy; $\xi \geq H$

Following the analysis of axisymmetric quantum dots of Gill and Cocks [89], we derive U as before assuming that $\xi \geq H$ as shown in Fig. 5.10. In this case, U^{e_2} and $U^{e_1e_2}$ change as a result of this assumption.

$$U^{e_2} = \frac{E\tilde{q}d}{(1-\nu^2)}\left[\frac{4}{3}(\varepsilon_s^2)^2\left(\frac{R}{\xi}\right)^2 H^3 - 4(\varepsilon_s^2)^2\frac{R^2}{\xi}H^2 + 4(\varepsilon_s^2)^2R^2H\right] + \frac{8}{3}G\tilde{q}d\left[(\varepsilon_s^2)^2\frac{R^4}{\xi^2}H\right] \tag{B.40}$$

The optimum height ξ is obtained by minimising U^{e_2} alone

$$\xi \;=\; \frac{2}{3}\left[(1-\rho)\frac{R^2}{H} + H\right] \tag{B.41}$$

And the interaction energy

$$U^{e_1e_2} \;=\; \frac{2E\tilde{q}d}{(1-\nu^2)}(\varepsilon_s^1+\varepsilon^T)\varepsilon_s^2\left[4R^2H - 2R^2\frac{H^2}{\xi}\right] \tag{B.42}$$

The total elastic stored energy density in this case is given by

$$\begin{aligned} U_T =& \frac{E\tilde{q}d}{(1-\nu^2)}\left\{(\varepsilon_s^1+\varepsilon^T)^2 + \frac{1}{3}(\varepsilon_s^2)^2\left(\frac{H}{\xi}\right)^2 - (\varepsilon_s^2)^2\frac{H}{\xi}\right. \\ &\left. +(\varepsilon_s^2)^2 + \frac{(1-\rho)}{3}(\varepsilon_s^2)^2\left(\frac{R}{\xi}\right)^2 + 2(\varepsilon_s^1+\varepsilon^T)\varepsilon_s^2\left(1-\frac{H}{2\xi}\right)\right\} \end{aligned} \tag{B.43}$$

The elastic stored energy density in non-dimensional form is

$$\begin{aligned} U =& \frac{4\bar{E}\bar{b}_{cl}\bar{d}}{\pi\bar{s}^2}\left(\frac{\gamma_s}{R_o}\right)\left\{(\varepsilon_s^1+\varepsilon^T)^2 + \frac{1}{3}(\varepsilon_s^2)^2\left(\frac{\bar{H}}{\bar{\xi}}\right)^2 - (\varepsilon_s^2)^2\frac{\bar{H}}{\bar{\xi}}\right. \\ &\left. +(\varepsilon_s^2)^2 + \frac{(1-\rho)}{3}(\varepsilon_s^2)^2\left(\frac{\bar{R}\bar{H}}{\bar{\xi}}\right)^2 + 2(\varepsilon_s^1+\varepsilon^T)\varepsilon_s^2\left(1-\frac{\bar{H}}{2\bar{\xi}}\right)\right\} \end{aligned} \tag{B.44}$$

Using the expressions for ε_s^1 given by eqn. 5.25 and ε_s^2 given by eqn. 5.26 in terms of normalised state variables $(\bar{w}_{cr}, \bar{w}_{cl})$ in eqn. B.44, we obtain $U(\bar{w}_{cr}, \bar{w}_{cl})$. Note that

$$\bar{\xi} = \frac{2}{3}\bar{H}\left[(1-\rho)\bar{R}^2 + 1\right] \tag{B.45}$$

as $\xi \geq H$,

$$\bar{R} \geq \frac{1}{\sqrt{2(1-\rho)}} \tag{B.46}$$

For $\rho = 15/16$, $\bar{R} \geq 2.82$. Note that by comparing $\bar{R}$ given by the eqns. B.46 and B.39, we see that U is not continuous. Plotting U as a function of $\bar{R}$ for $\rho = 15/16$,

reveals $U(\xi \leq H)$ is less than $U(\xi \geq H)$ between $\bar{R} = 2.82$ and $\bar{R} = 4$ and therefore $U(\xi \leq H)$ is valid for $\bar{R} \leq 4$ and $U(\xi \geq H)$ is valid for $\bar{R} \geq 4$. Now the Gibbs energy density of the TBC, G, given by eqn. B.1 can be re-written as

$$G = G_i^{cl}(\bar{w}_{cl}) + \int_0^{\bar{\xi}} G_i^{cr^b}(\bar{w}_{cr}, \bar{w}_{cl}, \bar{x}_3) d\bar{x}_3 + G_i^{cr^t}(\bar{w}_{cr}) + U(\bar{w}_{cr}, \bar{w}_{cl}); \qquad \xi \leq H \quad \text{(B.47)}$$

Note that in the above equation, $U(\bar{w}_{cr}, \bar{w}_{cl})$ is given by eqn. B.38 and

$$G = G_i^{cl}(\bar{w}_{cl}) + \int_0^{\bar{H}} G_i^{cr^b}(\bar{w}_{cr}, \bar{w}_{cl}, \bar{x}_3) d\bar{x}_3 + U(\bar{w}_{cr}, \bar{w}_{cl}); \qquad \xi \geq H \qquad \text{(B.48)}$$

In this equation, $U(\bar{w}_{cr}, \bar{w}_{cl})$ is given by eqn. B.44

Bibliography

[1] D. R. Clarke and C. G. Levi. Materials design for the next generation thermal barrier coatings. *Anuual Review Materials Research*, 33:383–417, 2003.

[2] M. Peters, K. Fritscher, G. Staniek, W.A. Kaysser, and U. Schulz. Design and properties of thermal barrier coatings for advanced turbine engines. *Material Wissenschaft and Werkstofftechnik.*, 28:357–362, 1997.

[3] Manuel Belmonte. Advanced ceramic meterials for high temperature applications. *Advanced Engineering Materials*, 8(8):693, 2006.

[4] Jeanine T. DeMasi−Marcin and Dinesh K. Gupta. Protective coatings in the gas turbine engine. *Surface and coatings technology*, 68.

[5] C. T. Sims, N. S. Stoloff, and W. C. Hagel, editors. *Superalloys II.* Wiley, New York, 1987.

[6] A. G. Evans, D. R. Mumm, J. W. Hutchinson, G. H. Meier, and F. S. Pettit. Mechanisms controlling the durability of thermal barrier coatings. *Progress in Material Science*, 46:505–553, 2001.

[7] P. K. Wright and A. G. Evans. Mechanisms governing the performance of thermal barrier coatings. *Current Opinion in Solid State and Materials Science*, 4:255–265, 1999.

[8] Nitin P. Padtrue, Maurice Gell, and Eric H. Jordan. Thermal barrier coatings for gas-turbine engine applications. *Science*, 296:280–284, 2002.

[9] A. M. Karlsson. Modelling failures of thermal barrier coatings. *Key Engineering Materials*, 333:155–165, 2007.

[10] M. Gell, D. N. Duhl, D. K. Gupta, and K. D. Sheffler. Advanced superalloy airfoils. *J. Metals*, 39:11–15, 1987.

[11] F. H. Stott and G. C. Wood. Growth and adhesion of oxides scales on alumina forming alloys and coatings. *Material Science Engineering A*, 87:267–274, 1987.

[12] W. D. Kingery, H. K. Bowen, and D. R. Uhlmann. *Introduction to ceramics.* New York: Wiley and Sons, 1976.

[13] X. Q. Cao, R. Vassen, and D. Stoever. Ceramic materials for thermal barrier coatings. *Journal of European Ceramic Society*, 24:1–10, 2004.

[14] Carlos G. Levi. Emerging materials and processes for thermal barrier systems. *Current Opinion in Solid State and Materials Science*, 8:77–91, 2004.

[15] T. E. Strangman. *Thin Solid Films*, 127:93, 1985.

[16] M. W. Chen R. Ott, T. C. Hufnagel, P. K. Wright, and K. J. Hember. Microstructural evolution of platimnum modified nickel aluminide bond coat during thermal cycling. *Surface and Coatings Technology*, 163.

[17] D. D. Hass, Y. Marciano, and H. N. G. Wadley. Physical vapour deposition on cylindrical substrates. *Surface and coatings technology*, 185:283–291, 2004.

[18] R. A. Miller. Oxidation-based model for thermal barrier coating life. *Journal of American Ceramic Society*, 67:517–518, 1984.

[19] J. W. Hutchinson and A. G. Evans. On the delamination of thermal barrier coatings in a thermal gradient. *Surface and Coating Technology*, 149:179–184, 2002.

[20] J. L. Smialek, D. T. Jayne, J. C. Schaffer, and W. H. Murphy. Effects of hydrogen annealing, sulfur segregation and diffusion on cyclic oxidation resistance of superalloys: a review. *Thin Solid Films*, 253:285–292, 1994.

[21] C. H. Hsueh and S. Lee. Modelling of elastic thermal stresses in two materials joined by a graded layer. *Composites Part B: engineering*, 34:747–752, 2003.

[22] Y. C. Tsui and T. W. Clyne. An analytical model for predicting residual stresses in progressively deposited coatings part 1: Planar geometry. *Thin Solid Films*, 306:23–33, 1997.

[23] W. G. Mao, Y. C. Zhou, L. Yang, and X. H. Yu. Modelling of residual stresses variation with thermal cycling in thermal barrier coatings. *Mechanics of Materials*, 38:1118–1127, 2006.

[24] Igor Sevostianov and Mark Kachanov. Plasma-sprayed ceramic coatings: anisotropic elastic and conductive properties in relation to microstructute; cross-property correlations. *Material Science and Engineering A*, pages 235–243, 2001.

[25] A. Vasinonta and J.L. Beuth. Measurement of interfacial toughness in thermal barrier coating systems by indentation. *Engineering Fracture Mechanics*, 68:843–860, 2001.

[26] A. G. Evans and J. W. Hutchinson. On the mechanics of delamination and spalling in comressed films. *Int. J. Solids Structures*, 20(5):455–466, 1984.

[27] S. R. Choi, J. W. Hutchinson, and A. G. Evans. Delamination of multilayer thermal barrier coatings. *Mechanics of Materials*, 31:431–447, 1999.

[28] C. Mercer, S. Faulhaber, A. G. Evans, and R. Darolia. A delamination mechanism for thermal barrier coatings subject to calcium−magnesium−alumino−silicate (cmas) infiltration. *Acta Mater*, 53:1029–1039, 2005.

[29] D. Zhu and R. A. Miller. Investigation of thermal low cycle and high cycle fatigue mechanisms of thermal barrier coatings. *Surface and Coatings Technology*, 94.

[30] D. Zhu and R. A. Miller. Sintering and creep behaviour of plasma-sprayed zirconia and hafnia based thermal barrier coatings. *Surface and Coatings Technology*, 108:114–120, 1998.

[31] D. Zhu and R.A. Miller. Determination of creep behaviour of thermal barrier coatings under laser imposed thermal and stress gradient conditions. *Journal of Materials Research*, 14:146, 1999.

[32] I. O. Golosnoy, S. A. Tsipas, and T. W. Clyne. An analytical model for simulation of heat flow in plasma-sprayed thermal barrier coatings. *Journal of Thermal Spray Technology*, 14(2):205–214, 2005.

[33] K. W. Schlichting, N. P. Padture, and P. G. Klemens. Thermal conductivity of dense and porous yttria stabilised zirconia. *Journal of Material Science*, 36:3003, 2001.

[34] A. D. Jadhav, N. P. Padture, E. H. Jordan, M. Gell, P. Miranzo, and E. R. Fuller Jr. Low-thermal-conductivity plasma-sprayed thermal barrier coatings with engineered microstructures. *Mechanics of Materials*, 38:1118–1127, 2006.

[35] H. E. Eaton and R. C. Novak. Sintering studies of plasma-sprayed zirconia. *Surface and Coatings Technology*, 32:227, 1987.

[36] T. D. Bennett and Fengling Yu. A nondestructive technique for determining thermal properties of thermal barrier coatings. *Journal of Applied Physics*, 97(013520), 2005.

[37] F. Cernuschi, L. Lorenzoni, S. Ahmaniemi, P. Vuoristo, and T. Mäntylä. Studies of the sintering kinetics of thick thermal barrier coatings by thermal diffusivity measurements. *Journal of European Ceramic Society*, 25:393–400, 2005.

[38] K. Wada, Y. Ishiwata, N. Yamaguchi, and H. Matsubara. Strain tolerance and microstructure of thermal barrier coatings produced by eb-pvd process. *Materials Science Forum*, 522.

[39] D. Zhu, R. A. Miller, B. A. Nagaraj, and R. W. Bruce. Thermal conductivity of eb-pvd thermal barrier coatings evaluated by a steady-state laser heat flux technique. *Surface and Coatings Technology*, 138:1–8, 2001.

[40] V. Lughi, K. Tolpygo, and D. R. Clarke. Microstructural aspects of sintering of thermal barrier coatings. *Material Science Engineering A*, 368:212–221, 2004.

[41] R. K. Bordia and A. Jagota. Crack growth and damage in constrained sintering films. *Journal of American Ceramic Society*, 76:2475, 1993.

[42] R. G. Hutchinson, N. A. Fleck, and A. C. F. Cocks. A sintering model for thermal barrier coatings. *Acta Materiallia*, 54:1297–1306, 2006.

[43] A. Cipitria, I. O. Golosnoy, and T. W. Clyne. A sintering model for plasma-sprayed zirconia tbcs. part i: Free-standing coatings. *Acta Mater*, 57:980–992, 2009.

[44] A. Cipitria, I. O. Golosnoy, and T. W. Clyne. A sintering model for plasma-sprayed zirconia thermal barrier coatings. part ii: Coatings bonded to a rigid substrate. *Acta Mater*, 54:993–1003, 2009.

[45] A. C. F. Cocks, S. P. A. Gill, and J. Pan. Modelling microstructure evolution in engineering materials. *Advances in Applied Mechanics*, 36:81–161, 1999.

[46] N. A. Fleck and A. C. F. Cocks. A multi-scale constitutive model for the sintering of an air-plasma-sprayed thermal barrier coating, and its response under hot isostatic pressing. *Journal of Mechanics and Physics of Solids*, 57:689–705, 2009.

[47] A. C. F. Cocks and N. A. Fleck. Constrained sintering of an air-plasma-sprayed thermal barrier coating. *Acta Mater*, 58:4233–4244, 2010.

[48] R. G. Wellman, A. Dyer, and J. R. Nicholls. Nano and micro indentation studies of bulk zirconia and *eb−pvd* tbcs. *Surface and Coatings Technology*, 176:253–260, 2004.

[49] R. G. Wellman and J. R. Nicholls. On the effect of aging on the erosion rate of eb−pvd tbcs. *Surface and Coatings Technology*, 177.

[50] Xi Chen, J. W. Hutchinson, and A. G. Evans. Simulation of the high temperature impression of thermal barrier coatings with columnar microstructure. *Acta Materiallia*, 52:565–571, 2004.

[51] Adrian Bejan. How nature takes shape: extensions of constructal theory to ducts, rivers, turbulance, cracks, dentritic crystals and spatial economics. *Int Jl Thermal Science*, 38:653–663, 1999.

[52] D. C. Agrawal and R. Raj. Measurement of the ultimate shear strength of a metal-ceramic interface. *Acta Metall*, 37(4):1265–1270, 1989.

[53] C. H. Hsueh and M. Yanaka. Mutiple film cracking in film/substrate systems with residual stresses and unidirectional loading. *Journal of Material Science*, 38:1809–1817, 2003.

[54] C. H. Hsueh and A. A. Wereszczak. Multiple cracking of brittle coatings on strained substrates. *Jl. Applied Physics*, 96:3501–3506, 2004.

[55] M. D. Thouless. Crack spacing in brittle films on elastic substrates. *Journal of American Ceramic Society*, 73(7):2144–2149, 1990.

[56] M. D. Thouless, E. Olsson, and A. Gupta. Cracking of brittle films on elastic substrates. *Acta metal. mater.*, 40:1287–1292, 1992.

[57] M.S. Hu and A.G. Evans. The cracking and decohesion of thin films on ductle substrates. *Acta Metall*, 37(3):917–925, 1988.

[58] A. G. Evans and J. W. Hutchinson. A theoretical and numerical study of thin film delamination using the pull-off test. *Int. Jl. Solids and Structures*, 41:717–730, 2004.

[59] Z. Sun, Kai−Tak Wan, and David A. Dillard. The thermo mechanical integrity of thin films and multilayers. *Acta metal. mater*, 43(7):2507–2530, 1995.

[60] J. Liang, R. Huang, J.H. Prévost, and Z. Suo. Evolving crack patterns in thin films with extended finite element method. *Int. Jl. Solids and Structures*, 40:2343–2354, 2003.

[61] Juil Yoon, Zhen Zhang, Nanshu Lu, and Zhigang Suo. The effect of coating in increasing the critical size of islands on a compliant substrate. *Applied Physics Lettrs*, 90(211912), 2007.

[62] Marcin Bialas and Zenon Mróz. An energy model of segmentation cracking of thin films. *Mechanics of Materials*, 39:845–864, 2007.

[63] J. L. Beuth. Cracking of thin bonded films in residual tension. *Int. Jl. Solids and Structures*, 29(13):1657–1675, 1992.

[64] J. L. Beuth and N. W. Klingbeil. Cracking of thin films bonded to elastic-plastic substrates. *J.Mech.Phys.Solids*, 44(9):1411–1428, 1996.

[65] Z. P. Bazant and A. A. Wahab. Instability and spacing of cooling or shrinkage cracks. *Jl of Eng.Mech. Division*, 105(5):873–889, 1979.

[66] Yunan Li, , Ann P. Hong, and Z. P. Bazant. Initiation of parallel cracks from surface of elastichalf-plane. *Int. Jl Fracture*, 69:357–369, 1995.

[67] T. J. Lu and N. A. Fleck. The thermal shock resistance of solids. *Acta Mater*, 46(13):4755–4768, 1998.

[68] L. G. Zhao, T. J. Lu, and N. A. Fleck. Crack channelling and spalling in a plate to thermal shock loading. *Journal of Mechanics and Physics of Solids*, 48:867–897, 2000.

[69] Mark Kachanov. Elastic solids with many cracks: A simple method of analysis. *Int. Jl solids and Structures*, 23(1):23–43, 1987.

[70] I. Tsukrov and M. Kachanov. Stress concentrations and microfracturing patterns in a brittle elastic solid with interacting pores of diverse shapes. *Int. Jl solids and Structures*, 34(22):2887–2904, 1997.

[71] N. M. Ghoniem, E. P. Busso, N. Kioussis, and H. Huang. Multiscale modelling of nanomechanics and micromechanics: an overview. *Philosophical Magazine*, 83(31).

[72] W. J. Boettinger, J. A. Warren, C. Beckermann, and A. Karma. Phase-field simulation of solidification. *Annu Rev Mater Res*, 32:163–194, 2002.

[73] A. Karma, D. A. Kessler, and H. Levine. Phase-field model of mode iii dynamic fracture. *Physical Review Letters*, 87(4):045501, 2001.

[74] Yu U. Wang. Computer modelling and simulation of solid-state sintering: A phase field approach. *Acta Mater*, 54:953–961, 2006.

[75] M. F. Ashby, editor. *HIP 6.0*. Engineering Department, University of Cambridge, Cambridge, 1990.

[76] A. C. F. Cocks. Overview no. 117 the structure of constitutive laws for the sintering of fine grained materials. *Acta Metall*, 42(7):2191–2210, 1994.

[77] E. A. Olevsky. Theory of sintering from discrete to continuum. *Mater Sci Eng Rev*, pages 41–100, 1998.

[78] J. Pan and A. C. F. Cocks. A numerical technique for the analysis of coupled surface and grain-boundary diffusion. *Acta Metall Mater*, 43(4):1395–1406, 1995.

[79] J. Pan. Modelling sintering at different length scales. *Int Mater Rev*, 48(2):69–85, 2003.

[80] H. N. Ch'ng and J. Pan. Cubic spline elements for modelling microstructural evolution of materials controlled by solid state diffusion and grain-boundary migration. *J Comput Phys*, 196:725–750, 2004.

[81] J. Pan and A. C. F. Cocks. Sintering kinetics of large pores. *Mech Mater*, 37:705–721, 2005.

[82] E. A. Olevsky, V. Tikare, and T. Garino. Multi-scale study of sintering: A review. *J Am Cera Soc*, 89(6):1914–1922, 2006.

[83] R. K. Bordia, R. Zuo, O. Guillon S. M. Salamone, and J. Rödel. Anisotropic constitutive laws for sintering bodies. *Acta Mater*, 54:111–118, 2006.

[84] F. Li, J. Pan, O. Guillon, and A. Cocks. Predicting sintering deformation of ceramic film constrained by rigid substrate using anisotropic constitutive law. *Acta Mater*, page doi:10.1016/j.actamat.2010.07.05, 2010.

[85] D. J. Green, O. Guillon, and J. Rödel. Constrained sintering: A delicate balance of scales. *J Euro Ceram Soc*, 28:1451–1466, 2008.

[86] C. L. Martin and R. K. Bordia. The effect of a substrate on the sintering of constrained films. *Acta Mater*, 57:549–558, 2009.

[87] Z. Suo. Motions of microscopic surfaces in materials. *Advances in Applied Mechanics*, 33:193–294, 1997.

[88] A. Benallal, R. Billardon, and I. Doghri. An integration algorithm and the corresponding consistent tangent operator for fully coupled elastioplastic and damage equations. *Comm Applied Numerical Methods*, 4:731–740, 1988.

[89] S. P. A. Gill and A. C. F. Cocks. An analytical model for the energetics of quantum dots: beyond the small slope assumption. *Proc. R. Soc. A*, 462:3523–3553, 2006.

[90] F. Parhami, R. M. McMeeking, A. C. F. Cocks, and Z. Suo. A model for the sintering and coarsening of rows of spherical particles. *Mechanics of Materials*, 31:43–61, 1999.

[91] K. L. Johnson. *Contact Mechanics*. Cambridge University Press, 2003.

[92] H. C. Park and R. S. Lakes. Torsion of a micropolar elastic prism of square cross-section. *Int J Solids Structures*, 23(4):485–503, 1987.